ABSTRACT

Title of Document:                  NUMERICAL      AND     EXPERIMENTAL
                                    STUDY   OF   BIO-INSPIRED   VIBRATION
                                    SENSING   AND   ISOLATION   DEVICES:
                                    INTEGRATION OF BIOMIMETICS AND 3D
                                    PRINTING TECHNOLOGY

                                    Feng Shi, Doctor of Philosophy, 2015

Directed By:                        Professor, Yunfeng Zhang,
                                    Department of Civil and Environmental
                                    Engineering

Statocyst is the balancing and sensing organ of the cephalopods (octopus, squid and cuttlefish). Previous studies have shown the macula/statolith part of the statocyst is the linear acceleration sensing system of the water particle motion. Although a few differences primarily in gross morphology exist, the macula/statolith part of the statocyst shows a striking number of similarities in structure and function among different cephalopods. In this study, the macula/statolith part of the statocyst is investigated by means of mechanics method. Specifically, based on the geometry and material property of macula/statolith from three cephalopod species (*Octopus vulgaris, Sepia officinalis and Loligo vulgaris*), a second order dynamic oscillator model was used to simulate its frequency response to the water particle motion. The acceleration detection threshold spectra comparison between the modeling analysis

and the experiment data verifies that the cephalopods are sensitive to the water particle motion (acceleration) in the low (infrasound) frequency range.

As an integral part of this research, the characteristics of kinocilia bundle which is the mechanoreceptive part of macula/statolith are also studied by interpreting the interaction between kinocilia bundle and statolith in a fluid-structure-interaction (FSI) numerical model. A parametric study of the kinocilia/statolith numerical model is conducted to improve the understanding of the sensing mechanism of the kinocilia bundle interaction with the statolith. Inspired by this interaction phenomenon, a bio-inspired vibration sensor and a bio-inspired isolation element are conceptually developed and numerically studied. The numerical simulation result implies that the frequency response behavior observed in the kinocilia bundle model from FSI analysis is also seen in both engineering designs, and this behavior could be equivalently described by the Maxwell model and SLS model for these two designs, respectively.

Lastly, by taking advantage of 3D printing technology, a prototype bio-inspired vibration sensor was fabricated in the lab and subsequently tested to characterize its sensing behavior. A comparison between the experimental data and predictions from a theoretical model suggests that the frequency response of the bio-inspired sensor design is equivalent to the convolution of the frequency response of a $2^{nd}$-order oscillator and the sensor's inner beam. This unique feature enables the development of two potential motion sensor designs (jerk sensor and velocity sensor).

NUMERICAL AND EXPERIMENTAL STUDY OF BIO-INSPIRED VIBRATION
SENSING AND ISOLATION DEVICES: INTEGRATION OF BIOMIMETICS
AND 3D PRINTING TECHNOLOGY


By


Feng Shi


Dissertation submitted to the Faculty of the Graduate School of the
University of Maryland, College Park, in partial fulfillment
of the requirements for the degree of
Doctor of Philosophy
2015


Advisory Committee:
Professor Yunfeng Zhang, Chair
Professor Amde M. Amde
Professor Chung C. Fu
Professor M. Sherif Aggour
Professor Sung W. Lee

# Acknowledgements

I express my deep acknowledgment and gratitude to my supervisor Dr. Yunfeng Zhang for his inspiring guidance, helpful suggestions and continuous encouragement as well as close supervisions throughout the period of my Ph.D. study. His helpful advice and careful guidance are invaluable for me beyond this dissertation work.

I would like to thank the members of the committee, Dr. Amde M. Amde, Dr. Chung C. Fu, Dr. M. Sherif Aggour and Dr. Sung W. Lee, for carefully reading this dissertation and providing many constructive suggestions.

I would like to express my thanks to my lab mates, Zhen Li, Linjia Bai, Changjiang Zhou, Ruipeng Li and Noah C. Blum for their help during the period of my Ph.D. study. I also thank all my office mates in the EGL 0147 for cheerful discussions in the past four years.

I would like to extend my special thanks to my parents for their love and unwavering support. Special thanks also go to Yuan Xue, who is always supporting and encouraging me.

# Table of Contents

# List of tables

# List of figures

# Chapter 1: Introduction

## 1.1 Introduction

Nature has learned after billions of years of evolution what works, what is appropriate and what would last. Moreover, it learned how to use minimum resources to achieve maximal performance and came up with numerous lasting solutions (Gordon, 1985). By adapting mechanisms and capabilities from nature, scientific approaches helped humans understand the related phenomena and associated principles (Bar-Cohen, 2006). Among these approaches, biomechanics aims to explain the structure and function of biological systems by means of the methods of mechanics. From molecules to organisms, everything must obey the laws of mechanics. In order to understand any object in the living organisms, we must know its geometry and materials of construction, the mechanical properties of the materials involved, the governing natural laws, the mathematical formulation of specific problems and their solutions (Fung, 1990). Once understood, the concepts and methods of biology can be applied to solve real-world problems, which lead to the development of biological engineering in the past decades. By following this methodology, the cephalopod's balancing and underwater particle motion sensing system - statocyst is investigated for its morphology and sensing mechanism as well as potential application to innovative engineering design applications including bio-inspired sensor and vibration isolator in this study.

*1.2 Introduction of statocyst in cephalopod*

Cephalopods (octopus, cuttlefish, and squid) are the most highly evolved and intelligent of all invertebrates. Like other fast-moving marine life, cephalopods can sense water-borne vibrations (both linear and rotational motions) (Young, 1989; Packard et al., 1990; Williamson, 1991; Budelmann & Williamson, 1994; Kaifu et al., 2008; Hu et al., 2009). The statocyst is mainly responsible for the underwater particle motion detection.

Statocysts (see Figure 1.1) consist of two endolymph-filled cavities lying within the cranial cartilage, which are ventral and lateral to the brain. The left and right statocysts are mirror reversed with the precise shape of the cavity being species-specific, presumably influencing the hydrodynamics of the system and the overall response characteristics (Williamson & Chrachri, 2007). The morphological ultrastructure of various cephalopod statocysts has been reported by Young (1960), Barber (1966), Budelmann (1975, 1979) and Budelmann et al. (1973). The statocyst of octopus, cuttlefish and squid includes two main areas of sensory epithelium: the crista/cupula area and the macula/statolith area.

The crista/cupula system contains several strips of sensory epithelium that is distributed along the inner wall of the statocyst (Young, 1989; Williamson, 1991). The strip comprises of mechanosensory kinocilia/hair cells and afferent neurons, plus supporting cells, and is divided into segments: nine in octopuses and four in squids and cuttlefish (Williamson & Chrachri, 2007). Each crista segment is covered by a sail-like cupula that is deflected during rotational movement of the animal by the flow of endolymph relative to the statocyst wall. Through this deflection the underlying

kinocilia/hair cells are also deflected, providing transduction of the mechanical rotation to an electrical signal (Williamson, 1991).

The macula/statolith system, the subject in this study, consists of the overlying statolith and macula epithelium. When the cephalopod linearly moves its body, the relative displacement between the statolith and macula epithelium will deflect the kinocilia/hair cells through the endolymph, and the translational motion is transformed to an electrical signal (Budelmann & Bonn, 1982). The macula/statolith develops distinct forms among octopus (*O. vulgaris*), cuttlefish (*S. officinalis*) and squid (*L. vulgaris*). In *O. vulgaris*, the macula consists of a single plate of mechanosensory kinocilia/hair cells. In *S. officinalis* and *L. vulgaris*, the macula is divided into three parts located in three planes: the macula statica princeps, the macula neglecta anterior, and the macula neglecta. The macula statica princeps is similar to the octopus macula both in structure and function.

The majority of the hair cells in the macula and crista are secondary sensory cells (without an axon), but primary sensory hair cells (with an axon) exist in the crista. Unlike the vertebrate hair cell which carries one kinocilium (with the internal $9 \times 2 + 2$ tubules content) and 50-60 stereocilia, the cephalopod hair cell carries up to 150 kinocilia and no stereocilia. All kinocilia (see Figure 1.2) have the same diameter (0.25 µm) and the same length (about 6 µm) (Barber, 1966, 1968; Neumeister & Budelmann, 1997). Because the kinocilia in cephalopod hair cell are all of the same length, the well-known tip links of the vertebrate vestibular hair cells do not occur (Budelmann, 2000). Instead, the tight membrane junctions that connect the tips of the kinocilia over a length of up to 0.5 µm presumably play an important role in the

mechanical gating of ion channels at the tip or the side of kinocilia (Budelmann, 2000).

## 1.3 Development of bio-inspired design

Biologically inspired design is a nontraditional problem solving approach which often results in uniquely engineered solutions for complex practical problems (McConney, 2009). Furthermore, this approach can often work to catalyze development through the use of a bidirectional approach to solve the problem, where both the problem and potential solutions are analyzed simultaneously (Bar-Cohen, 2006). There are many examples in the engineering world where solutions are inspired from biological world. In structural engineering, a new strategy of structural stiffness has been proposed according to the curling and folding feature in monocotyledon leaves (King et al., 1996), and new smart structures have been inspired based on different biological systems (e.g. elastin, worm skin geometry, Venus fly trap, and spinning cellulose, etc.) (Vincent, 2000). In material engineering, studies on fiber orientation (Chaplin et al., 1983) and lotus leaf (Neinhuis & Barthlott, 1997) have led to the development of composite material and self-cleaning material technology, respectively; one drag reduction system inspired from the shark skin study has been applied to reduce the surface drag of airplane's wing and boat hulls (Bechert et al., 1985; Bechert, 1999).

Another field in which biological inspiration principles are widely employed is the biologically inspired sensor technology. Sensors convert physical signals into electrical signals acquired by digital data acquisition systems. Similar to sensors, many biological organs function as transducers that transform external stimulus

signals to ionic signal, which is further transmitted to subject's nervous system (if any) for information processing. By learning from this similarity, various bio-inspired sensor designs have been proposed.

One successfully developed bio-inspired sensor design is the hair-like air flow sensor, which is inspired by the sensory hairs situated on the back of the cricket's body. In the cricket, each of these hairs is lodged in a socket and held by an elastic material surrounding its base. When the air flows by the cricket body, the rotation of the hair base causes a neuron to be stimulated (see Figure 1.3) (Shimozawa et al., 1998) and the cricket is able to pinpoint low-frequency sound by using the combined neural information from all the sensory hairs (Landolfa & Jacobs, 1995). Based on these features, the artificial sensory hairs were realized in SU-8 on suspended $Si_xN_y$ membranes, in which the movement of the membranes is detected capacitively with the air flowing by the SU8-Hairs (see Figure 1.4). The successful frequency dependence and directional sensitivity measurements on fabricated sensor arrays confirmed the viability of this sensor (Dijkstra et al., 2005).

The hair-like structure is also found in fish. A lateral line system (see Figure 1.5) in fish consists of an array of neuromasts and each neuromast consists of a cluster of hair cells embedded in protective, gel-like domes (Fan et al., 2002). By measuring the deflection of different hair cells, Dambly et al. (2003) verified that the water particle motion could be detected by fish lateral line system. Combined with micro- and nanofabrication technology, an underwater flow sensor was invented by Fan et al. (2002) and Liu (2007). The structure of this sensor is shown in Figure 1.6, in which a horizontal cantilever is attached by a vertical cilium at the free end. When

external flow parallel to the sensor substrate imparts on the vertical cilium, a mechanical bending moment is transferred to the horizontal cantilever beam and the strain at the cantilever beam base is sensed by integrated piezoresistive sensors (Fan et al., 2002).

In addition to the development of the flow sensors, the hair-like structure was also investigated as tactile sensor. Instead of sensing the fluid environment, the tactile sensors found in insects and other arthropods are touching its surrounding solid environment. Wandering spiders like *cupiennius salei* are densely covered by tactile hairs and they use these hairs of their front legs as tactile feeler in darkness (Albert et al., 2001). The tactile hairs are easily identified from its surrounding hairs by its length and steep insertion angle (see Figure 1.7). The study on the selected hairs of the tarsus indicates its sensitivity to the deflection angle is on the order of $10^{-8}$ N·m/rad, which is about 10,000 times larger than the trichobothria's sensitivity in some insects (Albert et al., 2001). A finite element model conducted by Dechant et al. (2001) also demonstrated this tactile hair's high sensitivity (see Figure 1.8) and implied its application to artificial sensor technology.

The sensory hair in vertebrate's inner ear is another research field that has attracted growing attention from researchers. Inside the inner ear, a number of hair bundles form the key parts in the acoustic sensing system to detect a wider dynamic range and wider bandwidth of vibrations. Each hair bundle consists of many stereocilia and one kinocilium (see Figure 1.9), and the features of negative stiffness and automatically adaptation in the hair bundle significantly improve the performance of the sensing system (Hudspeth & Jacobs, 1979; Martin et al., 2000; Hudspeth,

1989). By taking advantage of these features, Lim & Park (2009) developed a biomimetic sensor model of stereocilia and fabricated the model at the macro scale. The model sensor consists of an inverted pendulum array with bistable buckled springs at its tips, which represent the mechanically gated ion channel between stereocilia (see Figure 1.10). Given a small input signal, the experimental data showed a remarkably increase of the pendulum deflection in the sensor and verified this sensor's amplification effectiveness (Lim & Park, 2009).

At present, bio-inspired sensors, especially the hair-like structure inspired sensor designs, are continually being studied. Depending on various hair-like configurations from both invertebrate and vertebrate, exploration in the biological world and learning from biological mechanisms will always provide abundant motivation to the sensor industry.

*1.4 Research motivation*

One interesting characteristic shown in cephalopods is its sensitivity to underwater particle motion in the infrasound frequency range. Cephalopods have an acute sensitivity to the low-frequency linear acceleration of water particles and this high sensitivity can be partly attributed to their statocysts (Kaifu et al., 2008). In the meanwhile, the experiments which investigate the water particle motion's effect on octopus, squid and cuttlefish (Kaifu et al., 2008; Packard, 1990; Hu, 2009), provides the actual detection threshold data points for three specific cephalopod species. By making use of these experiment data and configuration of the statocyst, a mechanics model of statocyst would be very helpful with understanding the frequency response characteristics of the cephalopod.

Furthermore, from the bio-inspiration standpoint, the hair-like structure in the animal kingdom provides a huge source to solve engineering problems. The hair-like structure is also found in the statocyst. The kinocilia bundle, which consists of up to 150 hair-like kinocilia, shows a different configuration as the hair on insect's body and vertebrate's inner ear. It is interesting to know what dynamic characteristics this kinocilia bundle is associated with and how this could be used to provide inspiration for innovative engineering design solutions.

## *1.5 Research objectives*

The first goal of this study is to determine a proper mechanics model of the statocyst to explain its sensing characteristics displayed in the experiments and subsequently use this model to predict the cephalopod's behavior under specific environmental impact. The second goal of this study is to investigate the dynamic response behavior of the kinocilia bundle and incorporate the bio-inspired features into engineering designs. To achieve these goals, the following analytical and experimental research tasks have been performed:

- A 2nd-order dynamic oscillator model is adopted to simulate the dynamic response behavior of the macula/statolith in the statocyst subjected to water particle motion induced excitation. The parameters of this model are discussed based on different cephalopod types. The acceleration detection threshold spectra is investigated for three specific cephalopod and the simulated results are compared with the reported experimental data.

- The dynamic response behavior of the kinocilia bundle interacting with the statolith is investigated by fluid-structure-interaction (FSI) numerical analysis

8

using the arbitrary Lagrangian-Eulerian based finite element analysis software. A series of parametric studies on the kinocilia bundle model is used to study the effect of dimensions and geometry on its frequency response characteristics.

- A bio-inspired vibration sensor design which has the similar configuration as the kinocilia bundle is proposed. The FSI numerical model of the sensor design is created and used to investigate the effect of control parameters. The prototype sensor is to be fabricated in the lab and the shake table test will be used to measure the sensor response signal under harmonic excitation at varying frequencies.

- Inspired by the kinocilia bundle in the macula part of the octopus's statocyst, a bio-inspired vibration isolation element is conceptually proposed. The isolation effect of this novel vibration isolation element design with built-in viscoelastic damping capacity is explored through FSI numerical simulation.

*1.6 Innovative aspects*

The proposed cross-disciplinary research work covers the areas of biology (morphological structures of octopus's statocyst through anatomy and imaging), dynamical system, fluid mechanics, signal processing, vibration testing and sensor technology. Specifically, this research has the following innovative aspects:

- Improving fundamental understandings of cephalopod's statocyst system by taking a multi-disciplinary approach, through iterations of multi-disciplinary steps – device characterization, anatomy and imaging, mechanics modeling. Through this new approach (as against the traditional single-disciplinary

approach in anatomy and physiology), many fundamental questions (e.g., how the statocyst in cephalopods help them detect weak underwater particle motion signal) can be better understood.

- Applying the kinocilia bundle's characteristics into practical engineering designs which are facilitated by the 3D printing manufacture procedure. One of the advantages of 3D printing lies in its ability to create complex geometrical shape that would be impossible to do with any other method of manufacturing. Given the complex and delicate configuration as the kinocilia bundle in statocyst, the 3D printing technology effectively realize the kinocilia bundle configuration in the proposed engineering designs for which the frequency band can be adjusted by changing the geometry design parameters.

*1.7 Organization of dissertation*

This dissertation consists of seven chapters, including an introduction presented in this chapter and the conclusions and future works summarized in Chapter 7. The remaining chapters are organized as follows,

Chapter 2 discusses the morphology structure of the statocyst in cephalopod and integrates the anatomy with the dynamic system knowledge to better understand the characteristics displayed in the cephalopod's life. By referring to the microscopy images of the macula/statolith in the octopus's statocyst taken by collaborating researchers from Shanghai Ocean University, China, a $2^{nd}$-order dynamic oscillator model was examined in order to simulate the octopus water particle motion sensing characteristics under the desired frequency range. Subsequent comparison with experimental data shows that this model could quantitatively explain some aspects of

the cephalopod's sensitivity to particle motion at lower frequency. Furthermore, potential applications of this model in assessing environmental impact on cephalopods, such as understanding the impact of environment noise on cephalopods' hearing ability, and detection of precursor signals, is also discussed in this chapter.

Chapter 3 presents the theoretical principle of FSI analysis used in the FEM numerical simulation. Because of the participation of endolymph fluid in the statocyst in motion sensing process, numerical simulation study on the macula/statolith system sensing behavior would require the FSI analysis. The arbitrary Lagrangian-Eulerian based FEM is introduced and discussed in this chapter. Next, three benchmark FSI models are used to demonstrate the ALE-FEM's high accuracy on the FSI problem with low Re number and large domain deformation.

The FEM numerical simulation of the kinocilia bundle interaction with the statolith is discussed in chapter 4. The dimensions and configuration of the kinocilia bundle and its surrounding parts are found to be key factors in affecting its frequency response characteristics. Based on this finding, the concept of a new bio-inspired sensor design is presented and its design parameters' effect is investigated in this chapter. The results of the FEM simulation study reveals that the sensing characteristics of the proposed bio-inspired sensor can be tuned by tuning the geometry-related parameters which could be physically realized by 3D printing technique.

Prototype bio-inspired sensor design is fabricated and its sensing characteristic is experimentally investigated in Chapter 5. By using the 3D printing and piezoelectric sensing technology, a fabrication procedure of the sensor is

presented in this chapter. The experimental test results of the bio-inspired sensor characterization with shake table tests demonstrate its agreement with the predictions from FSI simulation analysis. In the meanwhile, the features displayed in the experimental testing inspire two potential sensor designs: a jerk sensor and a velocity sensor. The characteristics of these two motion sensor designs are discussed in this chapter.

The concept of a bio-inspired vibration isolation element is presented in Chapter 6. This modular design of vibration isolation element is based on the configuration of each individual kinocilia bundle interacting with its surrounding environment and large scale isolation unit can be made up of arrayed modular vibration isolation element. Numerical simulation results for this vibration isolation element demonstrate its built-in viscoelastic feature which could be theoretically described by the Standard Linear Solid model. The transmissibility function of the modular vibration isolation element shows its promising performance across its design frequency range.
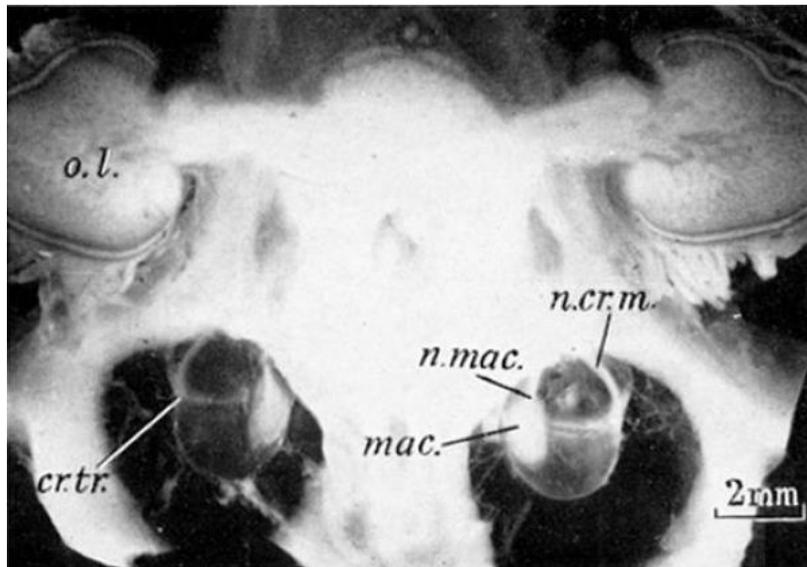
Figure 1.1 Section seen of the statocysts in relation to the horizontal plane. o.l., optic lobe; n.cr.m., middle crista nerve; n.mac., macular nerve; mac., macula; cr.tr., transverse crista (Young, 1960)
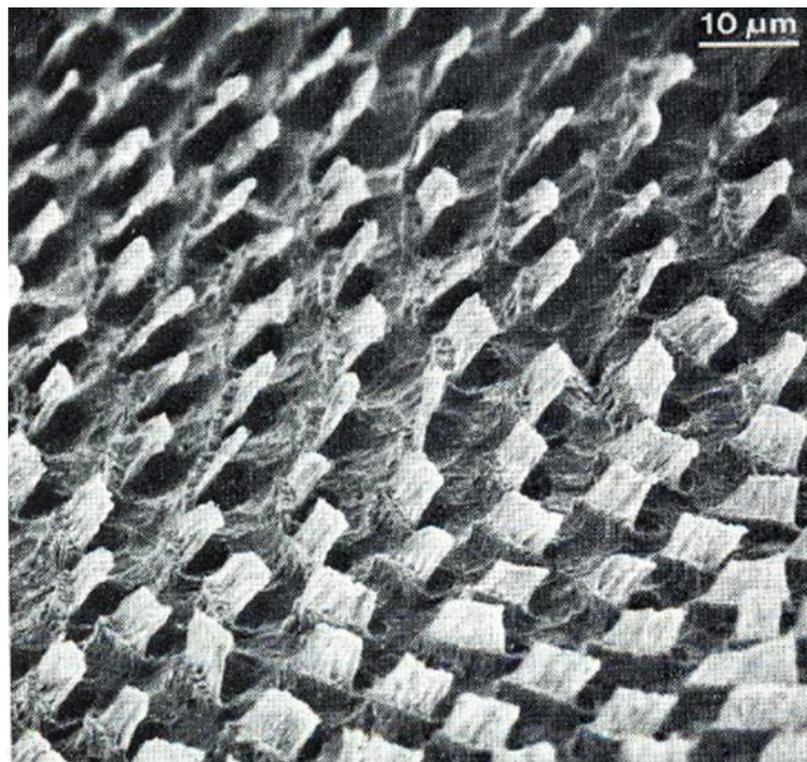


Figure 1.2 Part of the arrangement of the kinociliary groups of the hair cells. Inclination of kinocilia is toward the center of the epithelial surface. (Budelmann, 1979)
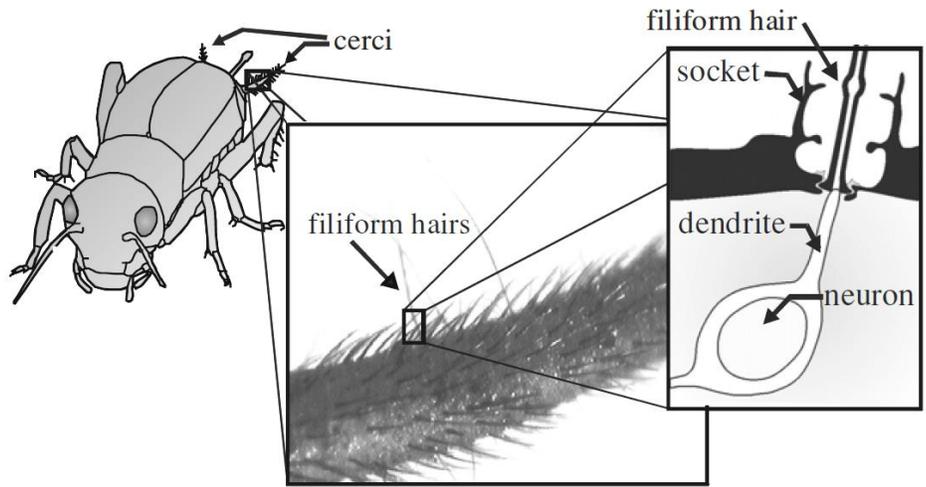
(a)
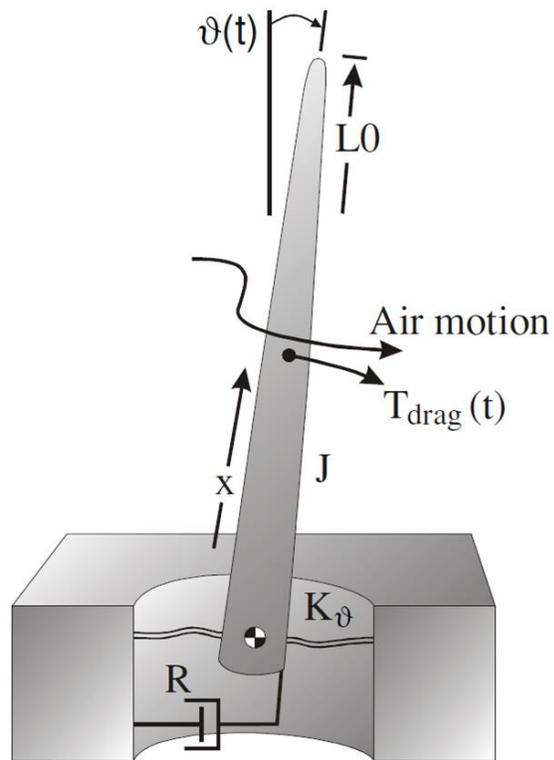


(b)

Figure 1.3 Flow sensitive receptor hairs of cricket: (a) filiform hairs on the cerci of cricket; (b) mechanical model used to describing filiform hairs (Shimozawa et al., 1998)
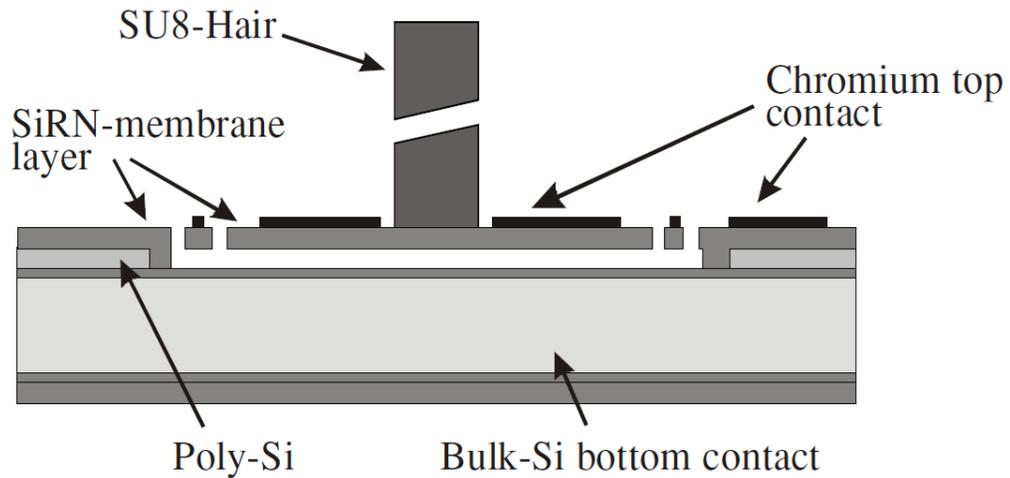
Figure 1.4 Schematic diagram of artificial sensory hairs based on the flow sensitive receptor hairs of crickets (Dijkstra et al., 2005)
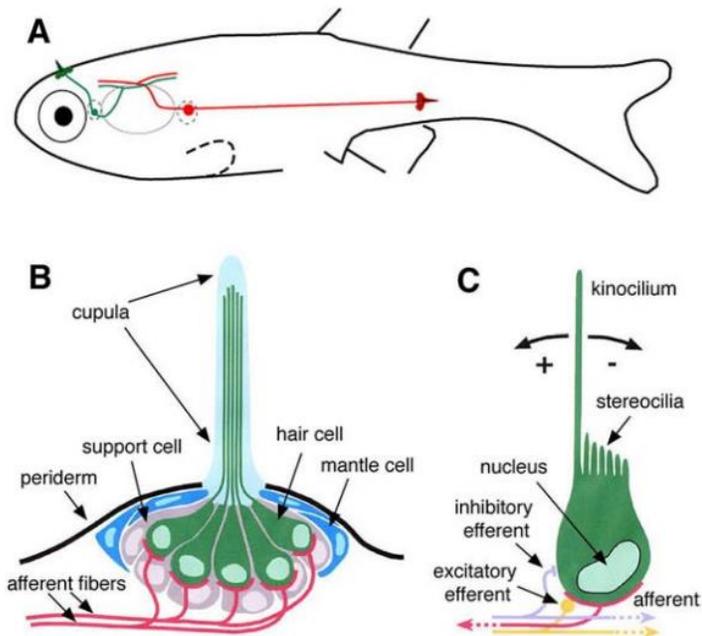


Figure 1.5 Lateral line of zebrafish: (A) Organization of the lateral line system; (B) Structure of a neuromast; (C) Function of the hair cell. (Dambly et al., 2003)
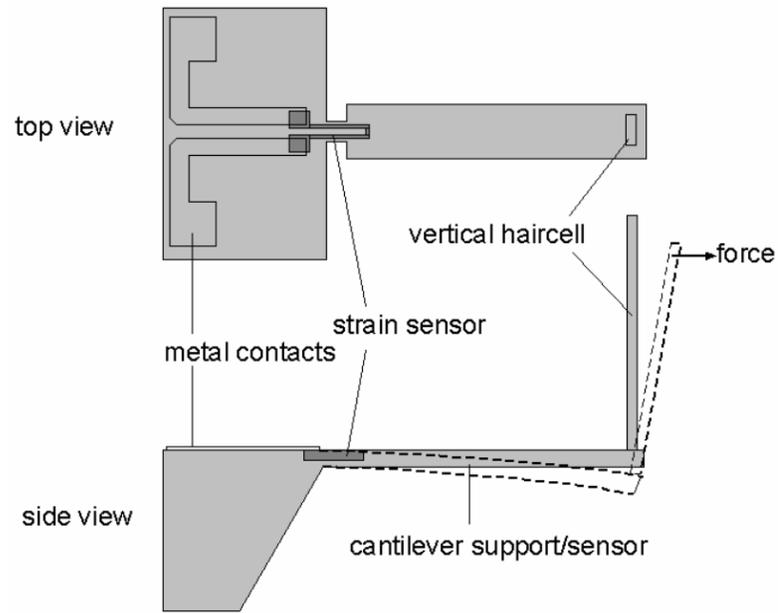
(a)
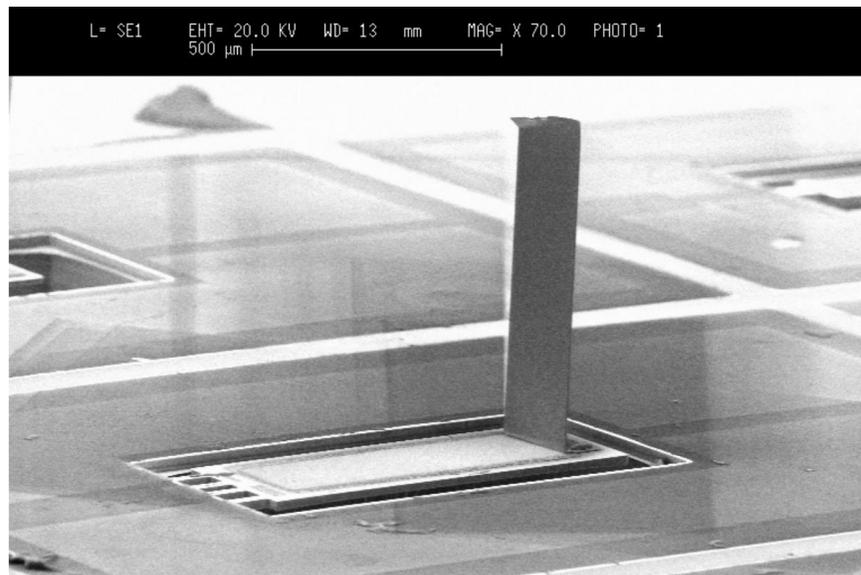


(b)

Figure 1.6 Artificial fish hair liquid flow sensor: (a) schematic diagram of a single artificial hair cell sensor; (b) SEM of single artificial hair cell sensor (Liu, 2007)
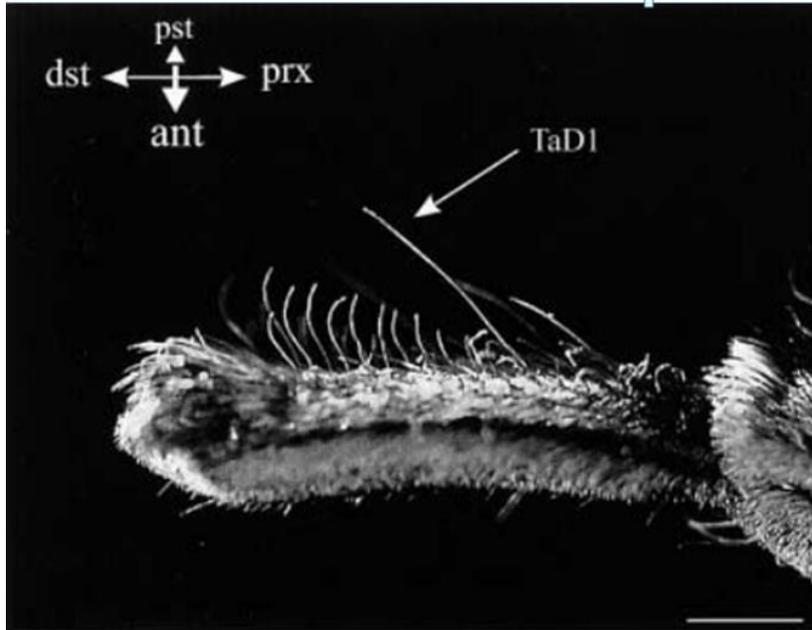
Figure 1.7 A tactile hair located dorsally on the spider leg tarsus (Albert et al., 2001)
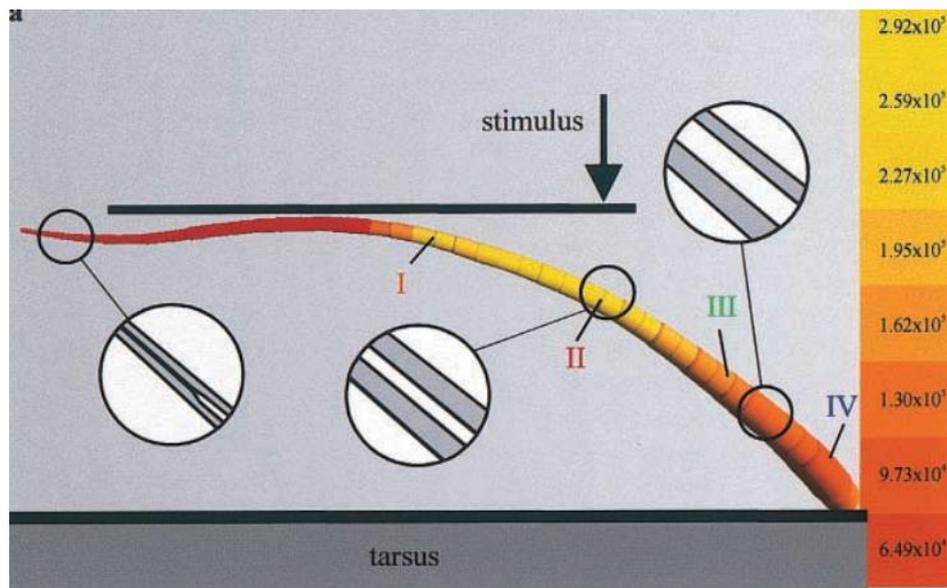


Figure 1.8 FE simulation of tarsal hair deflected by tactile simulation from above
(Unit: Pa) (Dechant et al., 2001)
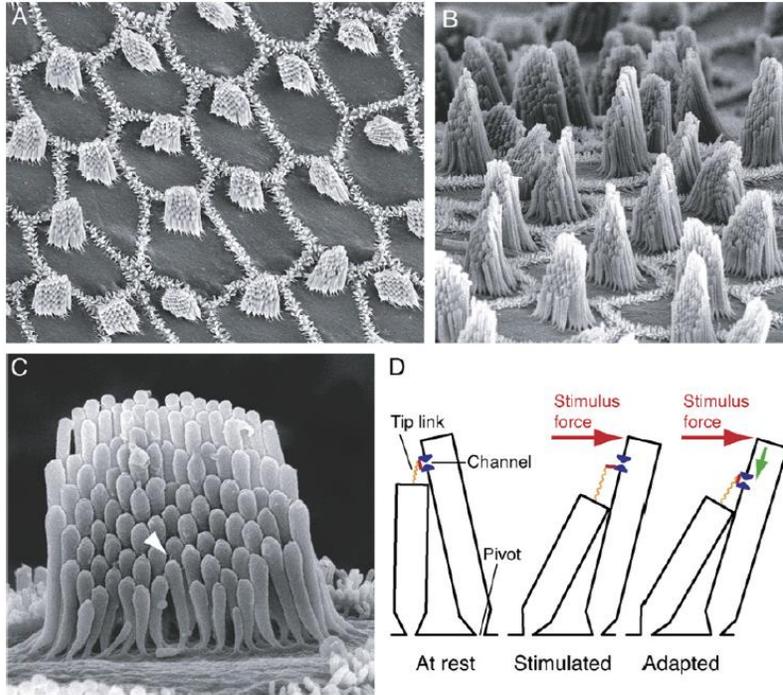
Figure 1.9 Hair cells of inner ear and their transduction process: (A) the sensory epithelium of the chicken cochlea; (B) a lateral view of hair bundle; (C) a higher-power view of a single hair bundle shows the orderly array of stereocilia; (D) the schematic depiction of the negative stiffness and automatic adaption in the hair cell (Hudspeth, 2008)
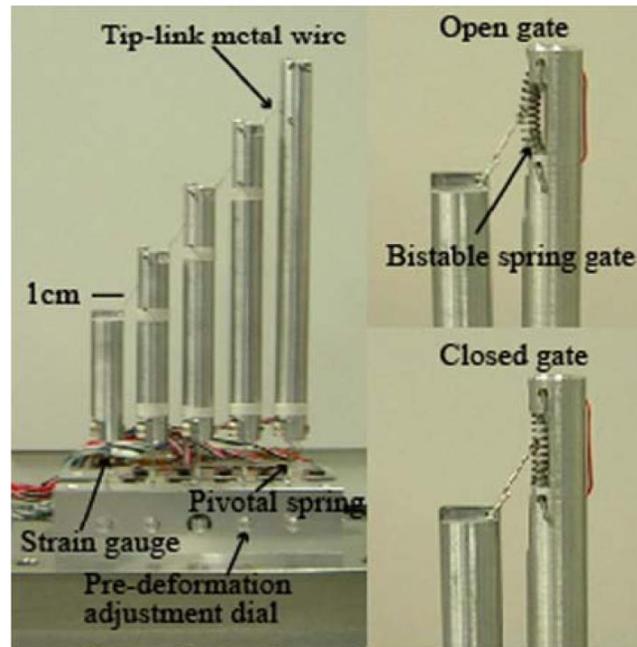


Figure 1.10 A stereocilia bundle inspired sensor and its mechanical fabrication (Lim & Park, 2009)

# Chapter 2: Hearing characteristics of cephalopods modeling study

## 2.1 Introduction

Cephalopod catches have increased to more than four million metric tons in 2007 (FAO, 2009). Cephalopods are sensitive to acoustic particle motion, especially at low frequencies in the order of 10 Hz (Packard et al., 1990; Williamson, 1991; Budelmann & Williamson, 1994; Kaifu et al., 2008). For example, the perception threshold of cuttlefish in the most sensitive frequency range is comparable to that of cod, reported by Sand and Karlsen (1986). Packard et al. (1990) shows that cephalopods can detect low frequency sounds and the statocyst is the sensory organ involved in hearing. An experimental study by Kaifu et al. (2008) also reveals that the cephalopod statocyst can detect particle motion. Combined with the morphology (Barber, 1966; Budelmann et al., 1973; Dilly, 1976), the cephalopod statocyst can be viewed as a particle motion sensor for both translational (displacement, velocity and acceleration) and angular motions.

In fisheries, sound has many uses, such as driving or attracting fishes into nets, or keeping fish away from certain areas (e.g. intakes of power plants) (Popper & Hawkins, 2012). However, few data on the hearing characteristics of cephalopods are presently available. A fundamental understanding of the underwater particle motion

detection and processing by the statocyst system in cephalopods can be achieved through an interdisciplinary modeling approach.

## *2.2 Morphology and sensing mechanism*

This chapter deals with quantitative modeling of the macula/statolith part in the statocyst of three cephalopod species: *Octopus vulgaris* Cuvier, 1797; *Sepia officinalis* Linnaeus, 1758; and *Loligo vulgaris* Lamarck, 1798. In the macula/statolith system, the statolith is made of crystalline subunits, namely the statoconia located over the sensory hair cells. The structural component aragonite has a specific gravity of 2.93 (Dilly, 1976); therefore, the statolith is very heavy compared with the surrounding endolymph. When the cephalopod body accelerates, the dense statolith would lag behind due to the mass inertia, creating deformation of the sensory kinocilia bundle, thus stimulating the underlying hair cells of the sensory epithelium. In this way, the macula/statolith part in cephalopods is directly sensitive to underwater particle motion.

Furthermore, all of the mechanosensory hair cells are morphologically and physiologically polarized such that they are excited by a deflection in a specific direction and inhibited by a deflection in the opposite direction (Williamson & Chrachri, 2007). Therefore, the kinocilia/hair cells are direction-sensitive displacement detectors, and the magnitude of the receptor current is dependent on the kinocilia bundle displacement (Budelmann, 1979; Budelmann & Williamson, 1994). It is the combined physical properties of these structures and the hair cells that determine the adequate stimulus, sensitivity and frequency range of the organ (Budelmann, 1979). The macula/statolith organs in cephalopods have been modeled

20

as harmonic oscillators, in which statolith movement is approximated as a force oscillator (Sand & Karlsen, 2000; Kaifu et al., 2011). In the present study, the macula/statolith system is modeled as a damped dynamic oscillator.

The proposed mechanical model can be used to investigate the effects of emerging environmental issues such as the influence of infrasonic noise on the particle motion sensing characteristics for *O. vulgaris*. Observations have been made in the past that the octopus is able to detect weak infrasound motion (low-frequency particle motion from 0.1 to 10.0 Hz) that often precedes imminent landslide events (Sand & Karlsen, 2000; Chadwick et al., 2012). Numerical simulation using the macula/statolith model and low frequency particle motion as the stimulus confirms this observation for *O. vulgaris*.

## *2.3 Materials and methods*

### 2.3.1 Histology

Statocysts from *O. vulgaris* (mass is 219 g) caught in the East China Sea near Shanghai, China, are used. The statocyst, together with a small portion of the surrounding cartilage, is dissected and fixed into 4 % neutral paraformaldehyde for two days. An eye surgery scissor is used to cut open the statocyst, and the statolith is removed with #5 Dumont forceps. The membranous substances are placed into 0.1 M phosphate buffer solution for 10 min, and rinsed twice to clean and displace the fixatives. The samples are transported to 1% $OsO_4$ solution for 30 min, and cleaned up again with 0.1 M phosphate buffer solution 3 times (15 min each time). The samples are dehydrated through graded alcohols and, finally, through critical point drying. After that the samples are attached carefully to aluminum stubs using

conducting resin. For scanning electron microscope viewing, samples are coated with a layer of gold in a sputter coating unit. The general morphology of the statocyst is viewed with a Zeiss optical microscope.

### 2.3.2 Modeling approach

The macula/statolith of the three types of cephalopods (*O. vulgaris*, *S. officinalis* and *L. vulgaris*) is believed to be responsible for sensing translational motion (displacement, velocity and acceleration). The macula/statolith is modeled here as a 2nd-order dynamic oscillator using parameters estimated from electron microscopy images of the macula/statolith system in individual species. The kinocilia bundles and underlying hair cells are coupled to a dense calcareous statolith through an interface mucus layer and the filling endolymph. The 2nd-order dynamic oscillator model (Figure 2.2) is used for modeling the macula/statolith system's sensing mechanism in this study.

Based on the 2nd-order dynamic oscillator model, the dynamic characteristics of the macula sensory organ can be described using the following equation of motion:

$$m_e \frac{d^2x}{dt^2} + c\frac{dx}{dt} + kx = -m_s a \cos \omega t + \rho_w Va \cos \omega t \tag{2.1}$$

where $x$ is the displacement of the statolith relative to its equilibrium position, $m_e$ is the effective mass of the statolith ($m_s$) plus the added mass ($m_{am}$) from acceleration of the surrounding fluid ($m_e = m_s + m_{am} = \rho_s \cdot V + \beta \cdot \rho_w \cdot V$, where $\beta$ is assumed to be equal to 1, according to de Vries [1950]). Thus, the statolith is an effective mass within the system (Dilly 1976). Continuing with Equation 2.1: $c$ is the viscous damping coefficient due to the viscous drag incurred by statolith movement within the

endolymph fluid, and $k$ is the stiffness mainly due to mucus layer; $a\cos(\omega t)$ represents the acceleration imparted to the cephalopod body; $\rho_w Va\cos(\omega t)$ is the acceleration caused by buoyancy. Because of the external particle motion excitation, $(-m_s a + \rho_w Va)\cos(\omega t)$ is the force exciting the macula statolith. A similar model has been adopted by Kaifu et al. (2011) in their work on the particle motion sensing characteristics of cephalopods.

Equation 2.1 is usually written in the standard form below:

$$\frac{d^2 x}{dt^2} + 2\zeta\omega_n \frac{dx}{dt} + \omega_n^2 x = -na\cos\omega t \tag{2.2}$$

where $\omega_n = \sqrt{k/m_e}$ is the natural frequency of the dynamic oscillator (i.e. the macula/statolith system); $\zeta = c/(2m_e\omega_n)$ is the damping ratio of this oscillator, which is assumed to be 0.7; and $n$ has the expression $n = \dfrac{\rho_s - \rho_w}{\rho_s + \rho_w}$.

Taking statolith $\rho_s$ as 2.93 g/cm$^3$, the value of $n$ is approximately equal to 0.491. By solving Equation 2.2, the acceleration imparted to the statolith is:

$$a\cos(\omega t - \phi) = -x(t) \cdot \frac{[(\omega_n/\omega - \omega/\omega_n)^2 + (2\zeta)^2]^{\frac{1}{2}} \omega_n^2}{(\omega_n/\omega) \cdot n} \tag{2.3}$$

where $\phi$ is the phase angle and $\omega$ is the angular frequency of particle motion of the cephalopod.

Based on Equation 2.3, when $x(t)$ exceeds the minimum displacement that the cephalopod can sense, the acceleration detection threshold for the cephalopod can be estimated at different excitation frequencies. Equation 2.3 is rewritten into the

following form to describe the relationship between the acceleration detection threshold $a_{min}$ and the minimum detectable displacement level $x_{min}$

$$a_{min} = x_{min} \frac{[(\omega_n / \omega - \omega / \omega_n)^2 + (2\zeta)^2]^{\frac{1}{2}} \omega_n^{2}}{(\omega_n / \omega) \cdot n} \qquad (2.4)$$

Equation 2.4 can be used to calculate the acceleration detection threshold spectrum for the cephalopod. According to structural dynamics, the parameters $x_{min}$ and $\omega_n$ play significant roles in this equation: the resonance frequency $\omega_n$ determines the lowest detection threshold and frequency; $x_{min}$ is proportional to the magnitude of $a_{min}$ under particle motion.

From Equation 2.4, it is seen that when the particle motion frequency $\omega$ is smaller than the natural frequency $\omega_n$, the acceleration threshold is at its lowest level, while the threshold value begins to increase rapidly after exceeding this $\omega_n$ value (Figure 2.3a). Therefore, the cephalopod is more sensitive to the low frequency particle motion in terms of acceleration.

Similarly, the jerk (time derivative of acceleration), velocity, and displacement detection thresholds can be expressed as:

$$j_{min} = a_{min} \omega = x_{min} \frac{[(\omega_n / \omega - \omega / \omega_n)^2 + (2\zeta)^2]^{\frac{1}{2}} \omega_n^{2} \omega}{(\omega_n / \omega) \cdot n} \qquad (2.5)$$

$$v_{min} = \frac{a_{min}}{\omega} = x_{min} \frac{[(\omega_n / \omega - \omega / \omega_n)^2 + (2\zeta)^2]^{\frac{1}{2}} \omega_n^{2}}{(\omega_n / \omega) \cdot n \cdot \omega} \qquad (2.6)$$

$$d_{min} = \frac{a_{min}}{\omega^2} = x_{min} \cdot \frac{[(\omega_n / \omega - \omega / \omega_n)^2 + (2\zeta)^2]^{\frac{1}{2}} \omega_n^{2}}{(\omega_n / \omega) \cdot n \cdot \omega^2} \qquad (2.7)$$

Compared with acceleration detection threshold, the sensitivity for jerk is decreasing with growing frequency and the decrease rate changes at the natural frequency $\omega_n$ (see Figure 2.3b). In contrast to the acceleration and jerk sensitivity, the greatest sensitivity for velocity is around the natural frequency $\omega_n$ (see Figure 2.3c), and displacement sensitivity keeps higher at high frequency range (see Figure 2.3d).

Strictly speaking, the cephalopod's statocyst only responds to underwater particle motion, not sound pressure; however, for the sole purpose of data comparison, the relation between the free-field sound pressure level (SPL) threshold and velocity threshold can be expressed as:

$$\mathrm{SPL}_{min} = 20\log\frac{p_{rms,min}}{p_{ref}} \tag{2.8}$$

$$p_{rms,min} = c_w \cdot \frac{v_{min}}{\sqrt{2}} \cdot \rho_w = \frac{c_w \rho_w}{\sqrt{2}} \cdot x_{min} \cdot \frac{\omega \cdot \sqrt{(\omega_n/\omega - \omega/\omega_n)^2 + (2\zeta)^2}}{(\omega_n/\omega) \cdot n} \tag{2.9}$$

where $p_{ref}$ is the reference pressure of 1 $\mu$Pa; $p_{rms}$ is the root-means-square sound pressure being measured; $c_w$ is the speed of sound in water; and $\rho_w$ is the water density. It should be noted here that cephalopods cannot sense underwater sound pressure like some fishes and mammals. The only reason to present the above relationship between the velocity and SPL spectra is purely for data comparison purposes because ambient ocean noise and manmade noises are usually measured with SPL instruments.

*2.4 Results analysis*

2.4.1 Particle motion detection threshold spectra

To verify this 2nd-order dynamic oscillator model, the particle motion detection threshold spectra for octopus, cuttlefish and squid are presented in this section along with experimental data.

2.4.1.1 Threshold spectra in Octopus

Using morphological data reported for the statocyst in the octopus (Young, 1960; Barber, 1966; Budelmann et al., 1973; Dilly, 1976), some model parameters are estimated and listed in Table 2.1. Another key factor is the displacement detection threshold by the statolith, $x_{min}$, in Equations (2.4) to (2.7). The experiments undertaken by Budelmann and Williamson (1994) reveal that the lowest displacement threshold is 0.4 μm (macula) peak-to-peak water displacement (calculated at the level of the hair cells) at 100 Hz. It is noted that this 0.4 μm is expressed in terms of the peak-to-peak water displacement instead of the statolith displacement considered here. In this study, the displacement detection threshold by the statolith, $x_{min}$, is assumed to be 1 μm for the octopus. The acceleration detection threshold spectra (Figure 2.4a) are derived from this model along with experimental data reported by Packard et al. (1990). The velocity detection threshold values were calculated to be 0.16, 0.64 and 1.28 mm/s at 10, 50 and 100 Hz, respectively (see Table 2.1). The results from modeling match reasonably well with the experimental data. Specifically, when the particle motion frequency is less than approximately 8 Hz (below resonance frequency), the acceleration detection threshold curve is flat. Once the particle motion

frequency exceeds this frequency, the acceleration detection threshold will increase with growing frequency.

### 2.4.1.2 Threshold spectra in Cuttlefish

The same modeling approach has been used to estimate the dynamic response characteristics in cuttlefish based on previous morphological data reported by Budelmann (1979). Only the macula princeps is modeled in this study. The following model parameters are estimated using the morphology data (see Table 2.2): mass of the statolith $m_s$ is 1.79e-6 kg; stiffness $k$ is equal to 4.4e-3 N/m and its natural frequency $f_n$ is equal to 7.8 Hz. The displacement detection threshold by the statolith, $x_{min}$, is also assumed to be 1.0 μm for the cuttlefish. The acceleration detection threshold spectrum of the cuttlefish follows a similar pattern as that of the octopus (see Figure 2.4b). The velocity detection threshold values are calculated to be 0.16, 0.64 and 1.30 mm/s at 10, 50 and 100 Hz, respectively.

### 2.4.1.3 Threshold spectra in Squid

The same modeling approach is used to estimate the dynamic response characteristics for the squid based on previous morphological data reported by Budelmann (1979). As with the cuttlefish, only the macula princeps is modeled in this study. The following parameter values are estimated using the morphology data (see Table 2.3): mass of the statolith $m_s$ is equal to 0.99e-6 kg; stiffness $k$ is set to 3.3e-3 N/m and its natural frequency $f_n$ is 7.9 Hz. The displacement detection threshold by the statolith, $x_{min}$, is also assumed to be 1.0 μm for the squid. The acceleration detection threshold spectrum is presented along with experimental data reported by

27

Packard *et al*. (1990) (see Figure 2.4c). The velocity detection threshold values are calculated to be 0.15, 0.63 and 1.3 mm/s at 10, 50 and 100 Hz, respectively.

Based on the modeling results, it could be concluded that the proposed model can be used to predict the particle motion detection threshold spectra of octopus, cuttlefish and squid. Therefore, it is reasonable to use this model to consider environmental impacts on particle motion detection by these cephalopods.

### 2.4.2 Model application

Using the above proposed model, the impact of environment noise on cephalopods' hearing ability could be better understood because very little field data are available about hearing, use of sound, or the effects of manmade sound on these species. For example, the impacts of near-shore wind farms on marine life could be examined. Specifically, noise produced by these generators could interfere with normal activities of these cephalopods, such as food searching, predator avoidance, mating and reproduction. Based on the noise measurement data from near-shore wind farms by Andersson (2011), a continuous broad-band sound (1 to 1000 Hz) with a few sharp tones (100 to 200 Hz) is propagated into the water. The lower end of the broad-band frequency range overlaps with the hearing frequency range for cephalopods.

### 2.4.2.1 Damaging particle motion level

One question asked by Popper and Hawkins (2012) in their report on the effect of noise on marine life is: "Is there evidence that intense sound can have acute impacts on fish and invertebrates or that lower levels of continuous sound may lead to

chronic effects?" Because the macula/statolith part of the statocyst behaves like a dynamic oscillator, severe particle motion could potentially cause irreparable damage in the cephalopod statocyst at short range. Andre et al. (2011) show that if the noise exceeding the critical level lasts for a sufficiently long period of time, it could severely damage the statocyst of *L. vulgaris*, *S. officinalis*, *O. vulgaris* and *Illex coindetii*.

The proposed model is used here to explain the damaging particle motion level by analyzing the statolith displacement from its equilibrium position when subjected to underwater particle motion. The statolith peak displacement response under sinusoidal excitation with various frequencies (peak excitation acceleration = 9.8 m/s$^2$; frequency range 10 to 1000 Hz) was calculated using the same model as reported in Table 2.1 for the octopus (see Figure 2.5). It is seen that the peak displacement values vary significantly under particle motion excitation with these frequencies. Specifically, the statolith displacement response is approximately 1 mm at 10 Hz; with increasing frequencies, the displacement response begins to decrease quickly in peak amplitude. When the excitation frequency increases to 400 Hz, the peak displacement is less than 1 μm. In other words, the statolith displacement responses at lower frequencies are much larger than those at higher frequencies if the particle motion amplitude is kept constant while frequency is changed.

From the morphological structure of the macula/statolith system, it is possible that large statolith displacement would cause damage to the macula. For illustration purposes, the damaging acceleration level is estimated to be approximately 0.27 m/s$^2$ (Figure 2.6) and the corresponding statolith displacement is approximately 44 μm at 8

Hz. Under such large displacement, the top of the kinocilia bundle would be deflected by several micrometers, which translates into large rotation of the kinocilia bundle. It is reasonable to conclude that large rotation would damage the macula, especially under repeated action. Accordingly, once the underwater particle motion level approaches this acceleration level, the macula of *O. vulgaris* could be damaged.

It is interesting to ask whether cephalopods would ever encounter an underwater particle motion of 0.27 m/s$^2$. Because particle motion is near field, it generally attenuates very rapidly from the source. To get these levels in the free field would require signals from the most intense sources, such as pile driving or seismic air guns. It is clear from this study that the damaging level for cephalopods is so high that it is a rare event for marine life.

2.4.2.2 Detection of landslide precursor signals

One interesting feature about cephalopods is that they are reported to leave an area before landslides occur. This phenomenon could also be interpreted by this model. A volcano-induced landslide reported by La Rocca et al. (2004) produced seismic signals whose frequency was concentrated in the band of 0.1−5.0 Hz with a duration of several minutes. The work by Chadwick et al. (2012) also shows similar results for submarine landslide signals, which have dominant energy below 10 Hz, with SPL of 160–180 dB re: 1 μPa. The cephalopod's most sensitive frequency band is close to this frequency band. However, the landslide signal data acquired by Chadwick et al. (2012) with an *in-situ* hydrophone are presented as power spectrum density rather than SPL. Therefore, conversion from the spectrum level to SPL (in root mean square level) has to be done first. For example, one empirical approach for

this conversion is to derive the SPL by adding 10–30 dB to the power spectrum density data depending on the actual bandwidth used for the data collection.

The SPL threshold values at this frequency range (below 10 Hz) are between the perception and damaging level (Figure 2.7), which means that the cephalopod could sense this landslide signal. This phenomenon only occurs in the low frequency range and vanishes at relatively high frequencies because the landslide signal is much weaker at higher frequencies. Based on these findings, a low frequency sensor (inspired by the cephalopod statocyst sensing mechanism) could be developed to monitor the precursor signals from imminent landslide events.

*2.5 Conclusion*

The octopus macula/statolith system is modeled here as a 2nd-order dynamic oscillator using parameters estimated from microscopy images. The modeling results agree reasonably well with the experimental audiograms (acceleration threshold) of the three cephalopod species, but discrepancy between the experimental data and model predictions are also seen in certain frequency range, especially in low frequency range. This suggests that the 2nd-order dynamic oscillator model may have limitations and further research should be performed to understand what may cause the discrepancy in following study. Insights made from quantitative modeling and simulating the sensing mechanism of cephalopods elucidates their hearing sensitivity and selectivity in underwater particle motion detection. The particle motion sensing characteristic of the cephalopod's macula/statolith organ can be quantitatively described using the proposed model. Observations have been made in the past that the octopus is able to detect weak infrasound motion signals: low-frequency particle

motion from 0.1 to 10 Hz that often precedes imminent landslide events. Numerical simulation results using the statolith/macula model of *O. vulgaris* confirms this observation. The modeling results are also used to explain the potential impacts of near shore wind farms on octopus.

Table 2.1 Estimated parameter values of the model for *Octopus vulgaris*

| | Model value (this study) | Experimental value (Packard 1990; Budelmann et al. 1973) |
|---|---|---|
| Fundamental frequency (Hz) | 8.5 | Approximately 10 |
| Statolith mass, $m_s$ (mg) | 1.39 | Varying (from 0.5 to 3 mg) |
| Stiffness ($10^{-3}$ N/m) | 5.6 | NA |
| Kinocilia length (μm) | 5 | 5 |
| Macula area (oval shape, mm$^2$ ) | 0.58 | 0.58 |
| Number of hair cells in macula | 5200 | 5138 |
| Acceleration threshold (mm/s$^2$) at 10, 50, 100 Hz | 9.8, 201.0, 803.9 | 13.66, NA, 485.3 |
| Velocity threshold (mm/s) at 10, 50, 100 Hz | 0.16, 0.64, 1.28 | NA |
| Displacement threshold (μm) at 10, 50, 100 Hz | 1 | NA |

Table 2.2 Estimated parameter values of the model for *Sepia officinalis*

| | Model value (this study) | Experimental value (Packard 1990; Budelmann et al. 1973) |
|---|---|---|
| Fundamental frequency (Hz) | 7.8 | Approximately 7 |
| Statolith mass, $m_s$ (mg) | 1.79 | Varying (from 0.2 to 2 mg) |
| Stiffness ($10^{-3}$ N/m) | 4.4 | NA |
| Kinocilia length (μm) | 5 | 5 |
| Macula (princeps) area (mm$^2$) | 0.47 | 0.47 |
| Number of hair cells in macula | 3000 | 3454 |
| Acceleration threshold (mm/s$^2$) at 10, 50, 100 Hz | 9.3, 197.0, 789.0 | 8.1, 460, 1100 |
| Velocity threshold (mm/s) at 10, 50, 100 Hz | 0.16, 0.64, 1.30 | NA |
| Displacement threshold (μm) at 10, 50, 100 Hz | 1 | NA |

Table 2.3 Estimated parameter values of the model for *Loligo Vulgaris*

| | Model value (this study) | Experimental value (Packard 1990; Budelmann et al. 1973) |
|---|---|---|
| Fundamental frequency (Hz) | 7.9 | NA |
| Statolith mass, $m_s$ (mg) | 0.99 | Varying (from 0.2 to 2 mg) |
| Stiffness ($10^{-3}$ N/m) | 3.3 | NA |
| Kinocilia length (μm) | 5 | 5 |
| Macula (princeps) area (mm$^2$) | 0.35 | 0.35 |
| Number of hair cells in macula | 1700 | 1881 |
| Acceleration threshold (mm/s$^2$) at 10, 50, 100 Hz | 9.4, 197.0, 789.1 | NA, 110, 1900 |
| Velocity threshold (mm/s) at 10, 50, 100 Hz | 0.15, 0.63, 1.30 | NA |
| Displacement threshold (μm) at 10, 50, 100 Hz | 1 | NA |

(a)

(b)

(c)

(d)

(e)
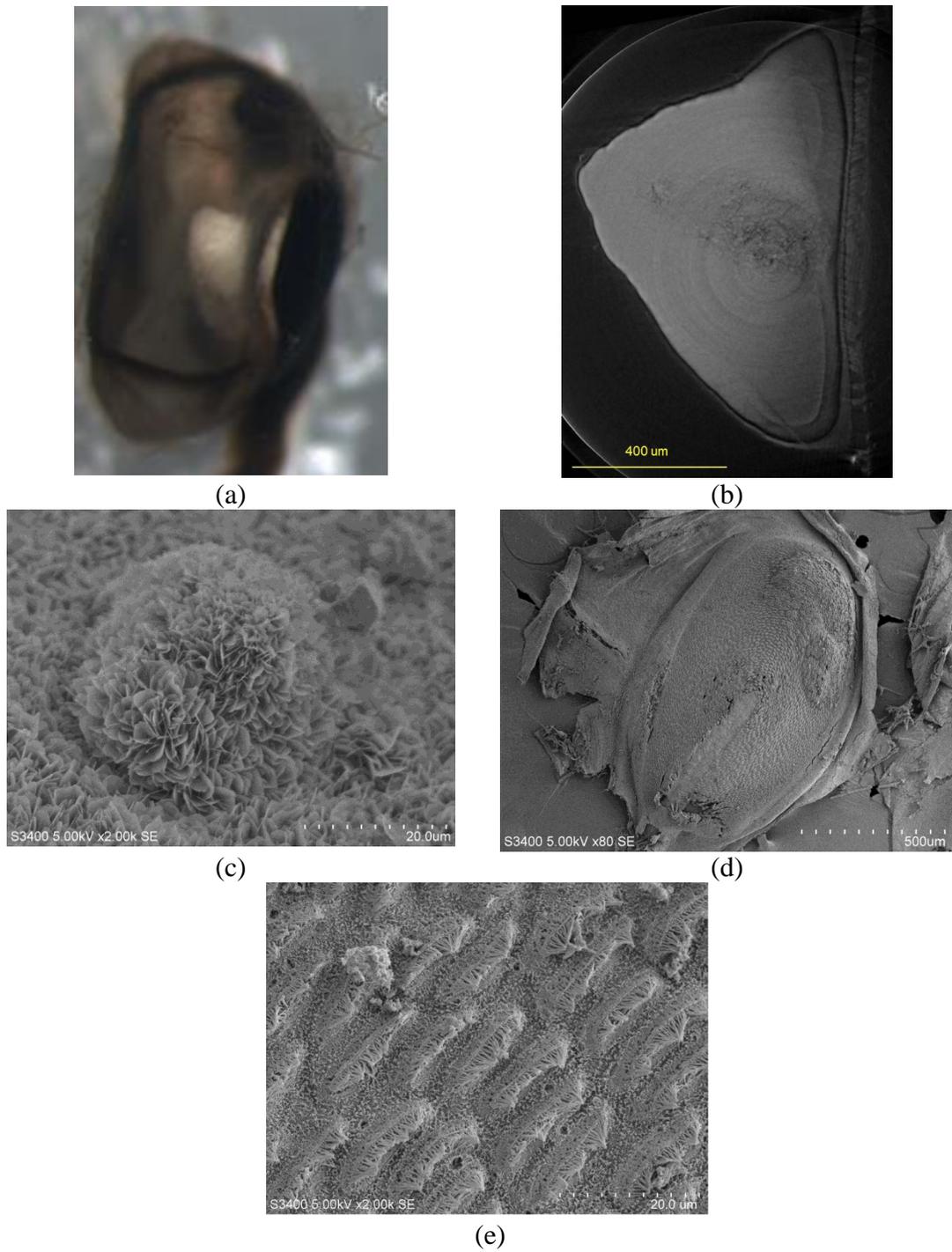
Figure 2.1 (a) Light micrograph of statocyst (white object is statolith and dark area left of the statolith is macula dyed with 1% $OsO_4$ solution); (b) radiography of statolith sitting on epithelium (c) scanning electron micrograph in part of statolith; (d) scanning electro micrograph of macula (statolith is removed); (e) scanning electro micrograph of kinicilia bundle in macula (courtesy of Professor Jiakun Song, Shanghai Ocean University, China)
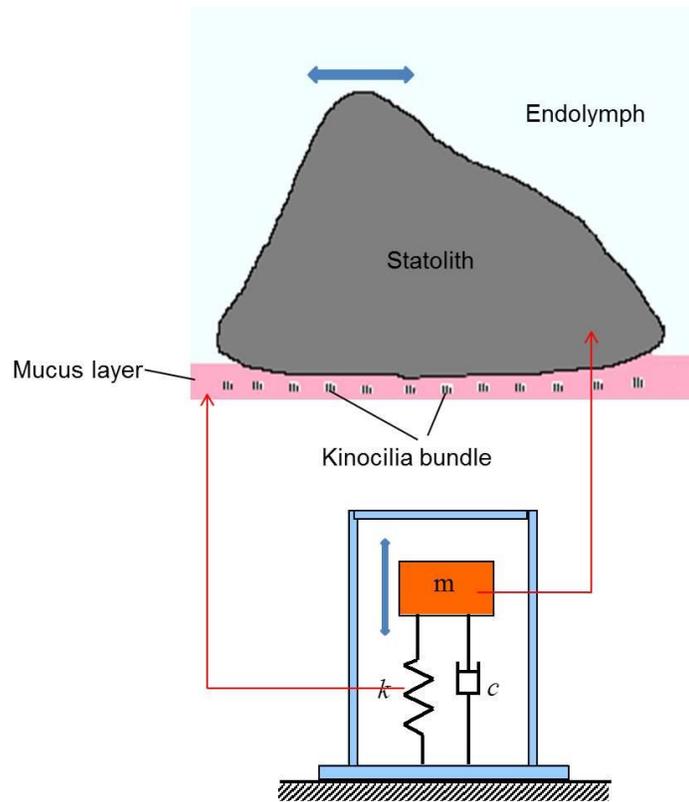
Figure 2.2 Schematics of the sensory macular structure in octopus statocyst
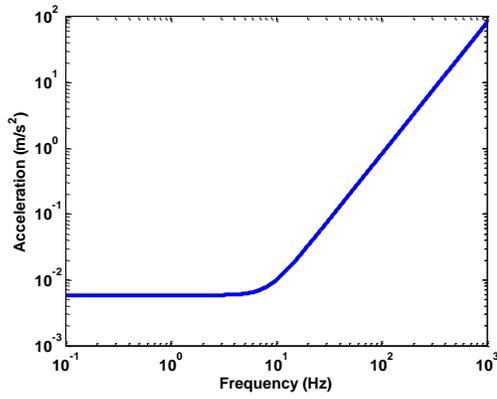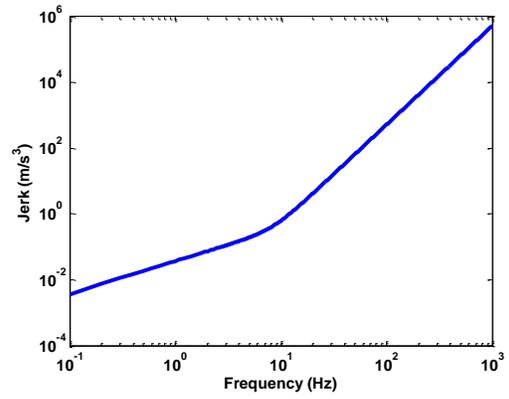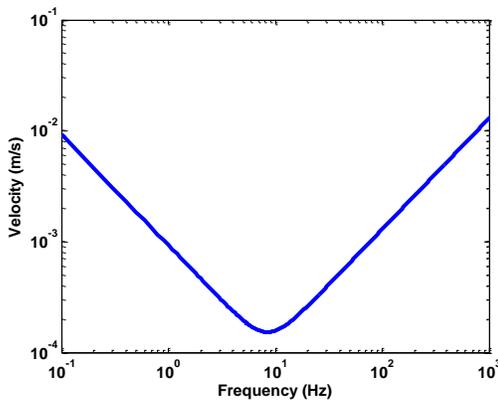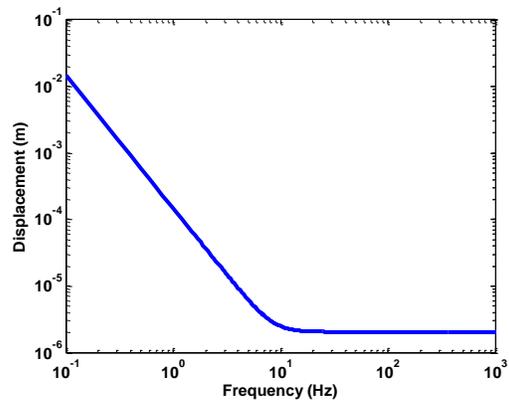
Figure 2.3 Typical detection threshold spectrums of *Octopus vulgaris*: (a) acceleration detection threshold; (b) jerk detection threshold; (c) velocity detection threshold; (d) displacement detection threshold
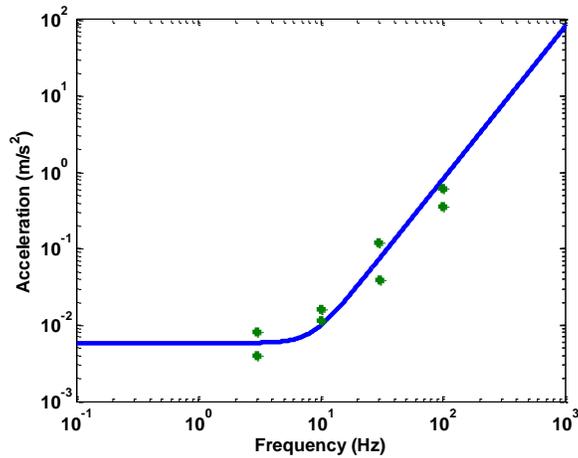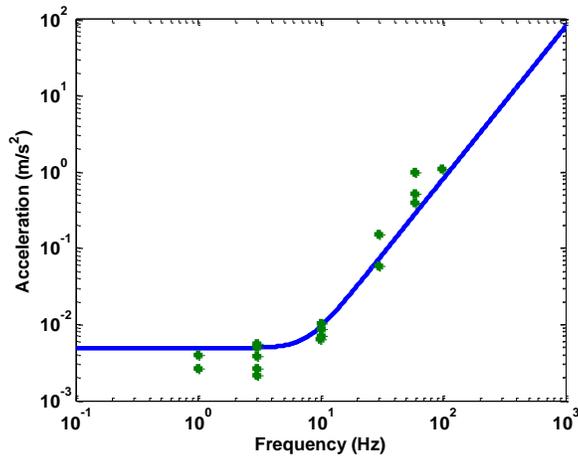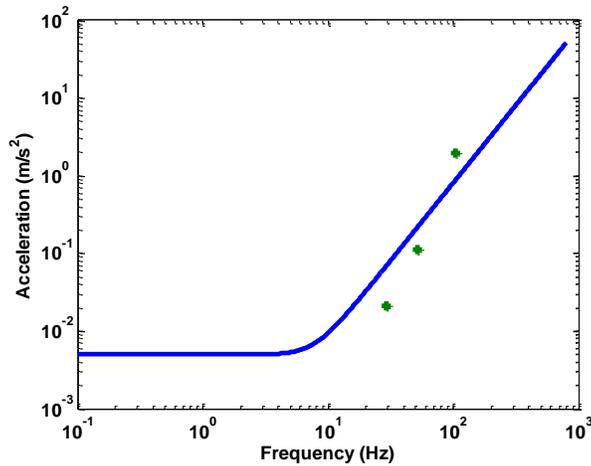
Figure 2.4 Acceleration detection threshold spectrums of cephalopods: (a) *Octopus vulgaris* (experimental data in green dots from Packard et al. 1990); (b) *Sepia officinalis* (experimental data from Packard et al. 1990); (c) *Loligo vulgaris* (experimental data from Packard et al. 1990)
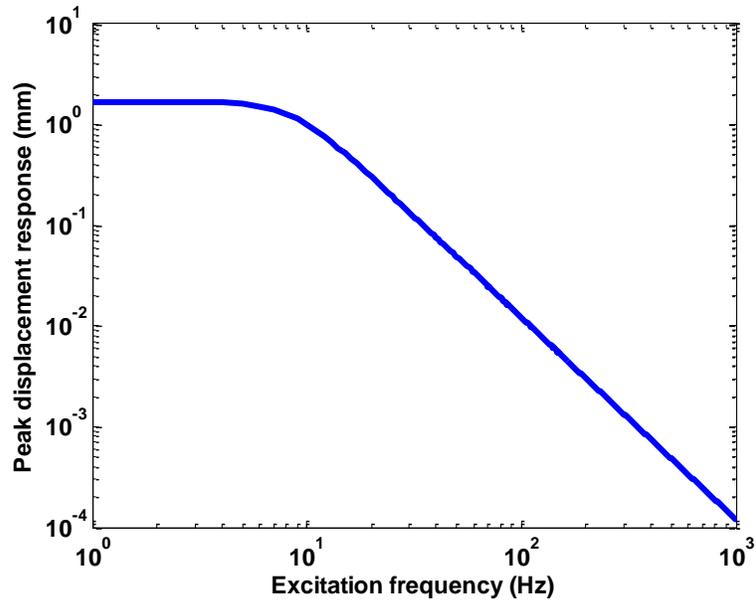
Figure 2.5 Peak displacement response of the octopus statolith to harmonic particle motion with varying frequencies (Peak excitation acceleration is 9.8 m/s$^2$)
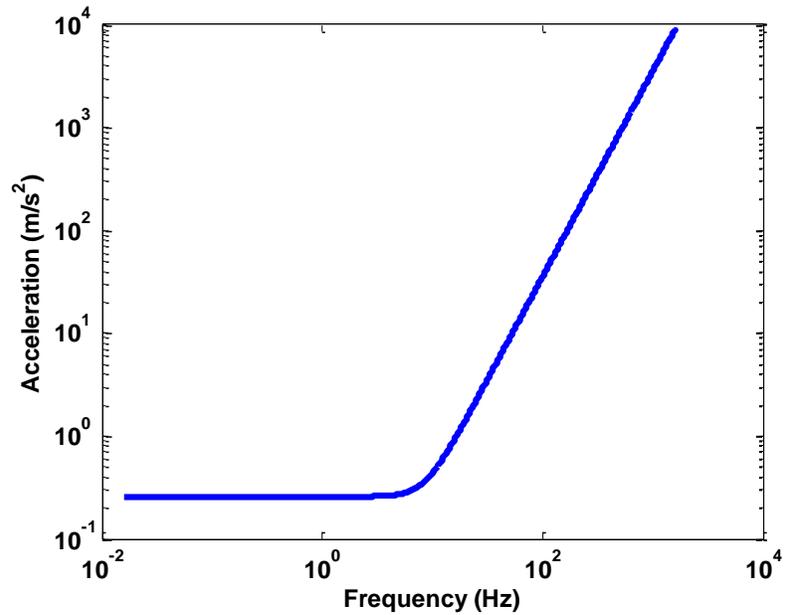


Figure 2.6 Damaging acceleration levels at various particle motion frequencies for octopus corresponding to statolith displacement of 44 μm at 8 Hz
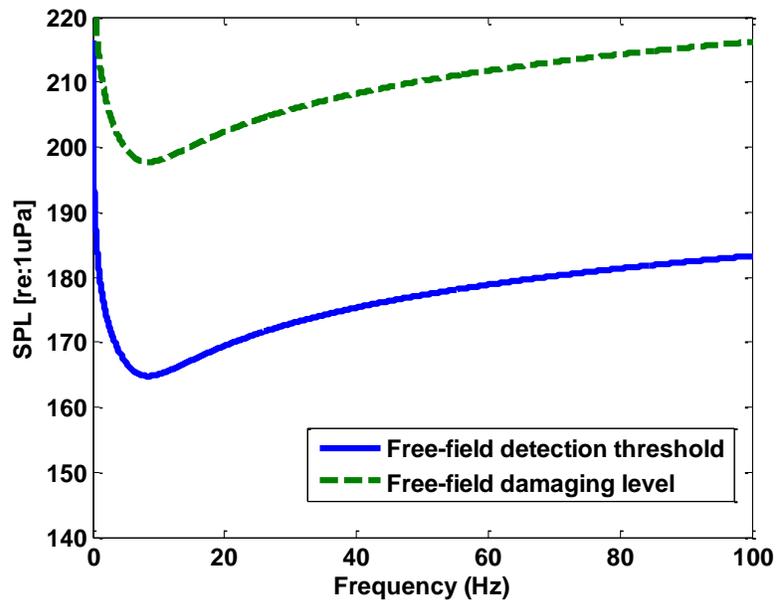
Figure 2.7 Free-field sound pressure level (SPL) detection and damaging threshold levels for octopus

# Chapter 3: FSI analysis theory

## *3.1 Introduction to the fluid-structure interaction*

Fluid-structure interaction (FSI) is a class of engineering problems dealing with the interaction of the movable or deformable structure with an internal or surrounding fluid flow. Because of the disparate mathematics used to describe fluid and solid regions, it is difficult to computationally model this problem. The first computational FSI model appears in the 1970s (Belytschko & Mullen, 1976; Hughes & Liu, 1978). Only in recent decades, with the advancement of computer technology, significant advances have been made in FSI analysis (Bathe & Zhang, 2004; Unger et al., 2007; Lee et al., 2007). The applications of FSI analysis are extended to a variety of industries, such as automobile (Shangguan & Lu, 2004), spacecraft (Takizawa et al., 2011), wind turbine (Bazilevs et al., 2011), and biomedical industries (Bazilevs et al., 2006). As the computational procedures become more efficient, the field of application will further expand (Bathe et al., 2007).

Since FSI has been more extensively explored, a variety of approaches have been proposed. One of the most widely used methods (Donea et al., 1982) is the arbitrary Lagrangian-Eulerian (ALE) formulation which is also adopted by a commercial FSI software – INTESIM. INTESIM is the software tool used in this study. This chapter first presents the theoretical formulation of the ALE FSI simulation algorithm. Specifically, Section 3.2 provides the mathematical foundation for key governing equations and initial conditions for the FSI in ALE format. Section

3.3 discusses the discretization of the governing equations and their numerical implementation in INTESIM. In order to demonstrate the technical capability of the adopted FSI software INTESIM, three benchmark FSI problems and associated solutions are presented in Section 3.5.

## *3.2 FSI: Theoretical background*

Continuum mechanics provides a mathematical framework that describes the behavior of materials, both solid and fluid, in the form of partial differential equations. This section presents the mathematical background necessary to formulate the governing equations in FSI analysis (Holzapfel, 2000; Anderson, 1995; Reddy & Gartling, 2001; Donea et al., 2004).

### 3.2.1 Kinematics and ALE description

Kinematics provides descriptions for the movement of bodies (Holzapfel, 2000). The algorithms of continuum mechanics usually make use of two classical description of motion (Donea et al., 2004): Lagrangian description and Eulerian description. Lagrangian description is mainly used in structural analysis, which allows an easy tracking of free surfaces and interfaces between different materials. In this description, each node of computational mesh follows the associated material particle during motion (see Figure 3.1a). Its weakness is its inability to follow large distortions of the computational domain without recourse to frequent re-meshing operations. In contrast, Eulerian description is widely used in fluid dynamics, in which the computational mesh is fixed and continuum moves with respect to the grid (see Figure 3.1b). Eulerian description can handle large distortions in the continuum

motion relatively easily at the expense of precise interface definition and the resolution of flow details.

Because of the shortcomings of purely Lagrangian and purely Eulerian descriptions, a technique has been developed that succeeds in combining the best features of both Lagrangian and Eulerian approaches (Donea et al., 2004). Such a technique is known as arbitrary Lagrangian-Eulerian (ALE) description. In the ALE description, the nodes of the computational mesh may be moved with the continuum in normal Lagrangian fashion, or be held fixed in Eulerian manner, or, as suggested in Figure 3.1c, be moved in some arbitrarily specified way to give a continuous rezoning capability. Because of this freedom in moving the computational mesh offered by the ALE description, greater distortions of the continuum can be handled than would be allowed by a purely Lagrangian method, with more resolution than is afforded by a purely Eulerian approach (Donea et al., 2004). The combined benefits of the ALE description, including sharp interface definition, time-dependent tracking, and accuracy over large deformations from Lagrangian and Eulerian descriptions, make it very promising for the FSI analysis.

3.2.2 Balance principles

In the continuum mechanics, there are three balance principles: mass conservation, momentum balance principles, and energy balance principles. These balance laws have a similar format in both Lagrangian description and Eulerian description. For the sake of brevity, they are presented in Eulerian description here. The mass conservation law is expressed in the following form,

$$\frac{\partial \rho}{\partial t} + \text{div}(\rho \boldsymbol{v}) = 0 \tag{3.1}$$

where $\rho$ is material's mass density, $\boldsymbol{v}$ is the velocity in Eulerian description, and $\text{div}$ is the divergence function. The second principle - the balance of momentum, involves the balance of linear and angular momentum. For the linear momentum balance, it can be expressed as,

$$\rho \frac{D\boldsymbol{v}}{Dt} = \rho \frac{\partial \boldsymbol{v}}{\partial t} + \rho(\text{grad}\,\boldsymbol{v})\boldsymbol{v} = \text{div}\,\boldsymbol{\sigma} + \rho\mathbf{b} \tag{3.2}$$

where $\mathbf{b}$ is the body force, $\boldsymbol{\sigma}$ is the Cauchy stress tensor. Material time derivative $\frac{D\boldsymbol{v}}{Dt}$ is expressed as $\frac{\partial \boldsymbol{v}}{\partial t} + \rho(\text{grad}\,\boldsymbol{v})$ and $\text{grad}\,\boldsymbol{v} = \frac{\partial \boldsymbol{v}}{\partial \mathbf{x}}$ is the spatial gradient of velocity. When the Cauchy stress tensor $\boldsymbol{\sigma}$ is symmetric, it automatically meets the requirements of angular momentum balance.

In this study, it is assumed that only mechanical energy shall be considered while other forms of energy, such as thermal, electric, magnetic, or chemical, are neglected. Due to this assumption, the balance of energy results naturally from the balance of linear momentum.

### 3.2.3 Governing equations

By combining the constitutive relations with the balance principles, the governing equations can be derived for FSI analysis. Since the solid and the fluid have different constitutive relations, the derived governing equations are different from each other. For the solid part, the Lagrangian description is adopted. For the governing equations in the fluid domain, it is first expressed in the Eulerian description and is then extended to the ALE description.

3.2.3.1 Governing equations for solid

In present research, linear elastic solid material is used while hyperplastic material is used in one of the three benchmark models presented in this chapter. Thus, both material theories are presented here. The governing equations for the elastic solid begin with the balance of linear momentum cast in Lagrangian description,

$$\rho \frac{D\mathbf{V}}{Dt} = \mathrm{div}\,\mathbf{P} + \rho\mathbf{B} \tag{3.3}$$

where $\mathbf{V}$ is the material velocity, $\mathbf{P}$ is the first Piola-Kirchhoff stress tensor, and $\mathbf{B}$ is the body force. The first Piola-Kirchhoff stress tensor is given by

$$\mathbf{P} = \mathbf{FS} \tag{3.4}$$

where $\mathbf{S}$ is the second Piola-Kirchhoff stress tensor and $\mathbf{F}$ is the deformation gradient from Lagrangian description to Eulerian description.

For the linear isotropic elastic material model, the constitutive relation is usually expressed as,

$$\mathbf{S} = \lambda\,\mathrm{tr}(\mathbf{E})\mathbf{I} + 2u\mathbf{E} \tag{3.5}$$

where $\mathbf{E}$ is the strain tensor known as Green-Lagrange strain tensor, $\mathbf{I}$ is the identity tensor, and $tr$ is the trace function. $\lambda$ is Lamé's first parameter and $u$ is the shear modulus or Lamé's second parameter. These parameters relate to the Poisson's ratio $v$ and Young's modulus $E$ as $v = \lambda/(2(\lambda+u))$ and $E = u(3\lambda+2u)/(\lambda+u)$. After introducing the displacement field $\mathbf{U}$,

$$\frac{D\mathbf{U}}{Dt} - \mathbf{V} = 0 \tag{3.6}$$

the strain tensor $\mathbf{E}$ can be expressed in terms of the displacement material gradient $\mathrm{Grad}\,\mathbf{U}$,

$$E = \frac{1}{2}(F^T F - I) = \frac{1}{2}(\text{Grad}^T U + \text{Grad}^T U) + \frac{1}{2}\text{Grad}^T U \, \text{Grad} \, U \qquad (3.7)$$

After substituting the Equations 3.4, 3.5 and 3.7 into Equation 3.3, Equations 3.3 and 3.6 become the governing equations for the solid with respect to the displacement field $U$ and the velocity field $V$.

For hyperelastic model material, strain-energy function is often used to get the constitutive relation. The strain-energy function is a scalar function of the strain tensor, whose derivative with respect to a strain component determines the corresponding stress component. Based on the hyperelastic material used in the benchmark model at this chapter, the strain energies can be expressed as a set of independent strain invariants of the symmetric Cauchy-Green tensor $C = 2E + I$, through $I_a = I_a(C)$, a = 1, 2, and 3, respectively (Holzapfel, 2000),

$$\psi = \psi[I_1(C) + I_2(C) + I_3(C)] \qquad (3.8)$$

Then the second Piold-Kirchhoff stress tenor is shown in the form of strain-energy function:

$$S = 2\frac{\partial \psi(C)}{\partial C} = 2[(\frac{\partial \psi}{\partial I_1} + I_1\frac{\partial \psi}{\partial I_2})I - \frac{\partial \psi}{\partial I_2}C + I_3\frac{\partial \psi}{\partial I_3}C^{-1}] \qquad (3.9)$$

Similarly, after substituting these expressions (Equations 3.4, 3.5, 3.7, 3.8 and 3.9) into Equation 3.3, Equations 3.3 and 3.6 are formulated solely in terms of the displacement $U$ and the velocity $V$.

### 3.2.3.2 Navier-stokes in Eulerian description

The governing equations derived from the balance principles in fluid dynamics are known as the Navier-Stokes Equations (NSEs), named after two

researchers who formulated these equations independently in the 19th century (Temma, 1984). In this research, the fluid is treated as the Newtonian fluid and the incompressible flow condition is automatically satisfied with the low Reynolds number. The governing equations of this incompressible Newtonian fluid flow are reviewed in Eulerian description in this section.

For the mass conservation, Equation 3.1 reduces to the divergence free velocity condition because of the incompressible flow condition,

$$\text{div}\,\mathbf{v} = 0 \tag{3.10}$$

The balance of momentum is unchanged,

$$\rho \frac{D\mathbf{v}}{Dt} = \rho \frac{\partial \mathbf{v}}{\partial t} + \rho(\text{grad}\,\mathbf{v})\mathbf{v} = \text{div}\,\boldsymbol{\sigma} + \rho\mathbf{b} \tag{3.11}$$

The Newtonian fluid has the following constitutive relation:

$$\boldsymbol{\sigma} = -p\mathbf{I} + \mu(\text{grad}\,\mathbf{v} + \text{grad}^T \mathbf{v}) \tag{3.12}$$

where $\mu$ is the fluid's dynamic viscosity and $p$ is the pressure, and the other variables are defined in the same way as previous ones. After substituting Equation 3.12 into 3.11, Equations 3.10 and 3.11 are collectively known as the Navier-Stokes equations for incompressible Newtonian flow in Eulerian description.

### 3.2.3.3 Navier-stokes in ALE description

As mentioned earlier in the chapter, the ALE description provides a unified way to solve FSI problems. In ALE description of motion, neither the material configuration (Lagrangian description) nor the spatial configuration (Eulerian description) is taken as the reference frame. The third configuration $\kappa$ is introduced to identify the grid points (see Figure 3.1c).

To derive the governing equations in the ALE description, the following equations are needed to perform this transformation (Holzapfel, 2000; Donea et al., 2004),

$$\operatorname{grad} \boldsymbol{\upsilon} = \operatorname{Grad} \boldsymbol{\upsilon}_\kappa \mathbf{F}_m^{-1} \tag{3.13}$$

$$\operatorname{div} \boldsymbol{\sigma} = \operatorname{Div} \boldsymbol{\sigma}_\kappa \mathbf{F}_m^{-T} \tag{3.14}$$

$$\frac{\partial \boldsymbol{\upsilon}}{\partial t} = \frac{\partial \boldsymbol{\upsilon}_\kappa}{\partial t} - (\operatorname{Grad} \boldsymbol{\upsilon}_\kappa \mathbf{F}_m^{-1}) \boldsymbol{\upsilon}_m \tag{3.15}$$

where $\boldsymbol{\upsilon}_m$ is the fluid domain velocity, defined as $\boldsymbol{\upsilon}_m = \partial \kappa / \partial t$, and the subscript $\kappa$ denotes variables transformed into the ALE description. $\mathbf{F}_m$ is the deformation gradient from ALE description to Eulerian fluid description. Substituting Equations 3.13, 3.14, and 3.15 into the Navier-Stokes equations, the governing equations are transformed into the following forms,

$$\rho \frac{\partial \boldsymbol{\upsilon}_\kappa}{\partial t} + \rho (\operatorname{Grad} \boldsymbol{\upsilon}_\kappa \mathbf{F}_m^{-1})[\boldsymbol{\upsilon}_\kappa - \boldsymbol{\upsilon}_m] + \operatorname{Div}(\boldsymbol{\sigma}_\kappa \mathbf{F}_m^{-T}) = \rho \mathbf{b}_\kappa \tag{3.16}$$

$$\mathbf{F}_m^{-1} : \operatorname{Grad} \boldsymbol{\upsilon}_\kappa^T = 0 \tag{3.17}$$

where : is the double dot product sign. The transformed Cauchy Stress $\boldsymbol{\sigma}_\kappa$ is expressed as,

$$\boldsymbol{\sigma}_\kappa = -p_\kappa \mathbf{I} + \mu (\operatorname{Grad} \boldsymbol{\upsilon}_\kappa \mathbf{F}_m^{-1} + \mathbf{F}_m^{-T} (\operatorname{Grad} \boldsymbol{\upsilon}_\kappa)^T) \tag{3.18}$$

Equations 3.16 and 3.17 are the Navier-Stokes equations expressed in ALE description.

### 3.2.4 Boundary condition

Boundary conditions are related to the specific problem in concern, while independent of the description employed. Therefore, the same boundary conditions in Eulerian or Lagrangian descriptions can be used in ALE formulation. Usually, two types of boundary conditions are formalized in any FSI problem,

$$\mathbf{v} = \mathbf{v}_D, \quad \text{on } \Gamma_D \tag{3.19}$$

$$\mathbf{n} \cdot \boldsymbol{\sigma} = \mathbf{t}, \quad \text{on } \Gamma_N \tag{3.20}$$

where $\mathbf{v}_D$ and $\mathbf{t}$ are the prescribed boundary velocities and traction respectively; $\mathbf{n}$ is the outward unit normal to $\Gamma_N$. $\Gamma_D$ and $\Gamma_N$ are two subsets: Dirichlet and Neumann boundaries of computational domain.

In FSI problem, part of the boundary could be composed of a material surface with unknown position, for which the following two conditions are required: (a) no particles can cross it; (b) stress must be continuous across the surface.

To satisfy condition (a), the enforcement of kinematic requirement is applied for the velocity. In addition, extra conditions for the displacement are needed to ensure that the fluid and structural domains will not detach or overlap during the motion (Donea et al., 2004). So, for a viscous fluid, the coupling between fluid and structure requires the velocities or displacement coincide along the interface:

$$\mathbf{v}_\kappa = \mathbf{V}, \qquad \text{Continuities of velocity} \tag{3.21}$$

$$\mathbf{u}_m = \mathbf{U}, \qquad \text{Continuities of displacement} \tag{3.22}$$

In practice, one fluid node and one structural node are placed at each point of the interface. This is achieved by constraining the mesh velocity $\mathbf{v}_m$ of the fluid nodes at the interface to be equal to the material velocity $\mathbf{V}$ of the structural nodes. Permanent alignment of nodes at the ALE interface facilitates the flow of the information between the fluid and structure domain (Donea et al., 2004).

To satisfy condition (b), the stress acting on the structure needs to be equal to the stress in the fluid at the interface. When the behavior of fluid is governed by the linear Stokes law, this condition is expressed as,

$$-p_\kappa \mathbf{n} + \mathbf{n} \cdot \mu (\operatorname{Grad} \mathbf{v}_\kappa \mathbf{F}_m^{-1} + \mathbf{F}_m^{-T} (\operatorname{Grad} \mathbf{v}_\kappa)^T) = \mathbf{n} \cdot \mathbf{T} \qquad (3.23)$$

where $\mathbf{T}$ is the stress tensor acting on the structure.

## *3.3 Finite element formulation of fluid-structure interaction problem*

This section is adapted from the corresponding chapter in the reference by Sheldon (2012). The advantages of FEM and the formulation of FSI problem will also be discussed in this section.

### 3.3.1 Advantages of FEM in FSI problem

For the governing equations formulated above for FSI problems, two common methods can be used for solving the partial differential equations: finite element method (FEM) and finite volume method (FVM). These two methods both involve discretizing the governing partial differential equations over a computational domain to reduce them to ordinary differential equations in time (Sheldon, 2012).

In the FVM, "finite volume" refers to the small volume surrounding each node point on a mesh, resulting from discretization of the body. Using the divergence

theorem, volume integrals in a partial differential equation that contain a divergence term are converted to surface integrals. These terms are then evaluated as fluxes at the surfaces of each finite volume. Because the flux entering a given volume is identical to that leaving the adjacent volume, these methods are conservative (LeVeque, 2002). The FVM is used in many computational fluid dynamics (CFD) software packages, in which it has an advantage in memory usage and solution speed, especially in high Reynolds number turbulent flows.

The FEM discretizes the computational domain into individual elements with interpolating basis functions. These basis functions are members of a function space, which approximate the values of a quantity in the element. The data at any point in the element can be interpolated using these basis functions. The FEM is favorable in structural analysis of solids, but is also applicable to fluids. Compared with FVM, FEM requires more memory and has slower solution process than FVM. However, the ease in obtaining higher order accuracy and the ease of implementation of boundary conditions form its advantages in CFD (Anderson, 1995). With boundary accuracy desired over the solution speed in the present low Reynolds number FSI simulation, the FEM is chosen as the solution technique in the following analysis.

3.3.2 Weak formulation

The FEM does not look for the solution of the partial differential equation itself, but looks for a solution of an integral form of the partial differential equation. By transforming the differential equation to its integral weak formulation, the second derivatives can be simplified as first derivatives format (Cook, 2007). One general

weak formulation is the weighted residual method (Cook, 2007). In solid analysis, Equation 3.3 can be written in the form of weighted residual,

$$\int \rho \frac{\partial \mathbf{V}}{\partial t} \cdot \hat{\mathbf{V}} d\Omega_S - \int \text{Div}\mathbf{P} \cdot \hat{\mathbf{V}} d\Omega_S - \int \rho \mathbf{B} \cdot \hat{\mathbf{V}} d\Omega_S = 0 \tag{3.24}$$

where $\hat{\mathbf{V}}$ is the arbitrary weight function with units of velocities and the solid domain is denoted as $\Omega_S$. Using integration by parts, the first Piola-kirchhoff term is written as

$$\int \text{Div}\mathbf{P} \cdot \hat{\mathbf{V}} d\Omega_S = \int \mathbf{T} \cdot \hat{\mathbf{V}} d\Gamma_S - \int \mathbf{P} \cdot \text{Grad} \hat{\mathbf{V}} d\Omega_S \tag{3.25}$$

where $\mathbf{T}$ is the traction force on the boundary $\Gamma$. Substituting this into Equation 3.24 yields,

$$\int \rho \frac{\partial \mathbf{V}}{\partial t} \cdot \hat{\mathbf{V}} d\Omega_S + \int \mathbf{P} \cdot \text{Grad} \hat{\mathbf{V}} d\Omega_S - \int \mathbf{T} \cdot \hat{\mathbf{V}} d\Gamma_S - \int \rho \mathbf{B} \cdot \hat{\mathbf{V}} d\Omega_S = 0 \tag{3.26}$$

Similarly, the other governing equation in solid analysis (Equation 3.6) can be written as

$$\int \frac{\partial \mathbf{U}}{\partial t} \cdot \hat{\mathbf{U}} d\Omega_S - \int \mathbf{V} \cdot \hat{\mathbf{U}} d\Omega_S = 0 \tag{3.27}$$

where $\hat{\mathbf{U}}$ is the arbitrary weight function with units of displacements. The weak form of the Navier-Stokes equations in Eulerian description is obtained for Equations 3.10 and 3.11 as,

$$\int \text{div}\,\boldsymbol{v} \cdot \hat{p} d\Omega_F = 0 \tag{3.28}$$

$$\int \rho \frac{\partial \boldsymbol{v}}{\partial t} \cdot \hat{\boldsymbol{v}} d\Omega_F + \int \rho(\text{grad}\,\boldsymbol{v})\boldsymbol{v} \cdot \hat{\boldsymbol{v}} d\Omega_F + \int \boldsymbol{\sigma} \cdot \text{grad}\,\hat{\boldsymbol{v}} d\Omega_F$$
$$= \int \rho \mathbf{b} \cdot \hat{\boldsymbol{v}} d\Omega_F + \int \mathbf{t} \cdot \hat{\boldsymbol{v}} d\Gamma_F \tag{3.29}$$

where $\overset{\wedge}{p}$ and $\overset{\wedge}{\boldsymbol{v}}$ are the arbitrary weight function with units of pressures and velocities; $\Omega_F$ and $\Gamma_F$ are the fluid domain and boundary, and $\mathbf{t}$ is the traction force on the boundary $\Gamma_F$. The integral term $\int \boldsymbol{\sigma} \cdot \operatorname{grad} \overset{\wedge}{\boldsymbol{v}} d\Omega_F$ and $\int \mathbf{t} \cdot \overset{\wedge}{\boldsymbol{v}} d\Gamma_F$ are derived from $\int \operatorname{div} \boldsymbol{\sigma} \cdot \overset{\wedge}{\boldsymbol{v}} d\Omega_F$ after integration by parts.

To transform the Navier-Stokes equations from the Eulerian format to the ALE format, the following transformation connects between the Eulerian description fluid domain $\Omega_F$ and the ALE description fluid domain $\Omega_{F\kappa}$ (Holzapfel, 2000),

$$\int_{\Omega_F} f(\mathbf{x}) dx = \int_{\Omega_{F\kappa}} f_\kappa(\mathbf{X}) J dX \tag{3.30}$$

where $J$ is the determinant of deformation gradient $\mathbf{F}_m$ and it is also known as volume ratio. Substituting Equation 3.30 into the ALE Navier-Stokes equations (Equation 3.16 and Equation 3.17) results in its weak forms as

$$\int J\rho \frac{\partial \boldsymbol{v}_\kappa}{\partial t} \cdot \overset{\wedge}{\boldsymbol{v}}_\kappa d\Omega_{F\kappa} + \int J\rho (\operatorname{Grad} \boldsymbol{v}_\kappa \mathbf{F}_m^{-1})[\boldsymbol{v}_\kappa - \boldsymbol{v}_m] \cdot \overset{\wedge}{\boldsymbol{v}}_\kappa d\Omega_{F\kappa}$$
$$+ \int J\boldsymbol{\sigma}_\kappa \mathbf{F}_m^{-T} \cdot \operatorname{Grad} \overset{\wedge}{\boldsymbol{v}}_\kappa d\Omega_{F\kappa} - \int J\rho \mathbf{b}_\kappa \cdot \overset{\wedge}{\boldsymbol{v}}_\kappa d\Omega_{F\kappa} - \int J\mathbf{t}_\kappa \cdot \overset{\wedge}{\boldsymbol{v}}_\kappa d\Gamma_{F\kappa} = 0 \tag{3.31}$$

$$\int J\mathbf{F}_m^{-1} : \operatorname{Grad} \boldsymbol{v}_\kappa^T \cdot \overset{\wedge}{p} d\Omega_{F\kappa} = 0 \tag{3.32}$$

3.3.3 Discretization

Spatial discretization breaks a continuous domain up into discrete piecewise-continuous subdomains which are termed as elements in FEM. In each element, the primary variables can be approximated by nodal values multiplied by basis functions, which allows for interpolation anywhere in the element. These approximations are given as

54

$$\overline{\mathbf{u}} \approx \sum_{j=1}^{n} \overline{\mathbf{N}}_u{}^j \overline{\mathbf{U}}{}^j, \quad \overline{\mathbf{v}} \approx \sum_{j=1}^{n} \overline{\mathbf{N}}_\upsilon{}^j \overline{\mathbf{V}}{}^j, \quad \overline{p} \approx \sum_{j=1}^{n} \overline{N}_p{}^j \overline{P}{}^j \qquad (3.33)$$

The over bar "-" indicates the general description, for instance, $\overline{\mathbf{v}}$ is corresponding to $\mathbf{V}$ in Lagrangian description, $\mathbf{v}$ in Eulerian description, and $\mathbf{v}_\kappa$ in ALE description. The parameter $n$ is the node number. $\overline{\mathbf{N}}_u{}^j$, $\overline{\mathbf{N}}_\upsilon{}^j$ and $\overline{N}_p{}^j$ are the j$^{\text{th}}$ interpolation basis functions, and $\overline{\mathbf{U}}{}^j$, $\overline{\mathbf{V}}{}^j$ and $\overline{P}{}^j$ are the j$^{\text{th}}$ nodal primary variables. In this study, the Galerkin method is adopted, in which the weight function is chosen the same as basis function (Cook, 2007) as shown below,

$$\overset{\wedge}{\overline{\mathbf{u}}}{}^j = \overline{\mathbf{N}}_u{}^j, \quad \overset{\wedge}{\overline{\mathbf{v}}}{}^j = \overline{\mathbf{V}}_u{}^j, \quad \overset{\wedge}{\overline{p}}{}^j = \overline{P}_u{}^j \qquad (3.34)$$

After spatial discretization, the governing equations can be expressed in general ordinary differential equations in terms of time. Several time integration methods are available to discretize the general ordinary differential equations, such as Predictor/multi-corrector algorithm (PMA), Newmark-Beta scheme, Generalized-Alpha scheme, Bathe scheme, Backward-Euler scheme and so on. For current research, the PMA algorithm is used because of its accuracy in nonlinear transient analysis. Details of PMA can be found from the book by Hughes (2012).

### 3.3.4 Fluid-structure interaction equations

Because body forces are prescribed to be zero in all governing equations and traction forces do not have residual contribution on Dirichlet boundaries for FSI interface, the residual can be further reduced.

In solid domain:

$$R_U^i = \int \frac{\partial \mathbf{U}}{\partial t} \cdot \hat{\mathbf{U}}^i \, d\Omega_S - \int \mathbf{V} \cdot \hat{\mathbf{U}}^i \, d\Omega_S \tag{3.35}$$

$$R_V^i = \int \rho_s \frac{\partial \mathbf{V}}{\partial t} \cdot \hat{\mathbf{V}}^i d\Omega_S + \int \mathbf{P} \cdot \operatorname{Grad} \hat{\mathbf{V}}^i d\Omega_S - \int -\boldsymbol{\sigma}_\kappa [J\mathbf{F}_m^{-T} \mathbf{n}_f] \cdot \hat{\mathbf{V}}^i \, d\Gamma \tag{3.36}$$

In ALE fluid domain:

$$R_p^i = \int (J\mathbf{F}_m^{-1} : \operatorname{Grad} \mathbf{v}_\kappa^T) \cdot \hat{p}^i \, d\Omega_{F\kappa} \tag{3.37}$$

$$\begin{aligned}
R_{v_\kappa}^i &= \int J\rho_f \frac{\partial \mathbf{v}_\kappa}{\partial t} \cdot \hat{\mathbf{v}}_\kappa^i \, d\Omega_{F\kappa} + \int J\rho_f (\operatorname{Grad} \mathbf{v}_\kappa \mathbf{F}_m^{-1})[\mathbf{v}_\kappa - \mathbf{v}_m] \cdot \hat{\mathbf{v}}_\kappa^i \, d\Omega_{F\kappa} \\
&\quad + \int J\boldsymbol{\sigma}_\kappa \mathbf{F}_m^{-T} \cdot \operatorname{Grad} \hat{\mathbf{v}}_\kappa^i \, d\Omega_{F\kappa}
\end{aligned} \tag{3.38}$$

For mesh domain, since there is no physical meaning for the mesh domain, it can be built in any arbitrary form. We choose linear elastic material constitutive relation as its governing equation as $\mathbf{P} = \lambda_m tr(\mathbf{E})\mathbf{I} + 2u_m \mathbf{E}$. The parameter $\lambda_m$ and $u_m$ can be determined for any arbitrary material, which leads to the mesh residual as:

$$\begin{aligned}
R_{u_m}^i &= \int \lambda_m \operatorname{Div} \mathbf{u}_m \cdot \operatorname{Div} \hat{\mathbf{u}}_m^i \, d\Omega_{F\kappa} \\
&\quad + \int \mu_m (\operatorname{Grad} \mathbf{u}_m + \operatorname{Grad}^T \mathbf{u}_m) \cdot \operatorname{Grad} \hat{\mathbf{u}}_m^i \, d\Omega_{F\kappa}
\end{aligned} \tag{3.39}$$

By choosing these parameters properly, large element distortion can be prevented. For example, the parameter $\lambda_m$ and $u_m$ can be used to define high stiffness mesh domain near the interface and low stiffness away from interface.

### 3.4 Numerical approaches for fluid-structure interaction problem

The numerical procedures to solve the FSI problems may be broadly classified into two approaches: the monolithic approach (Michler et al., 2004; Ishihara et al., 2005; Yoon, 2010) and the partitioned approach (Rosis et al., 2014; Wall et al., 2007;

Kassiotis, 2009; Yamada & Yoshimura, 2008). Monolithic approach treats the fluid and structure dynamics in the same mathematical framework to form a single system equation for the entire problem, in which the interfacial conditions are implicit in the solution procedure. In contrast, the partitioned approach treats the fluid and the structure as two computational fields which can be solved separately, in which the interfacial conditions are used explicitly or implicitly to communicate information between the fluid and structure solutions (Hou et.al, 2012).

3.4.1 Partitioned approach

In case of time-dependent nonlinear fluid models like the Navier-Stokes equations, which are coupled with linear or nonlinear elastic structures, the interface conditions in partitioned approach between the fluid and structure are solved through loosely or strongly coupled algorithms.

In loosely coupled algorithms, separate solvers for fluid and structure are applied once per time step and the interface conditions are explicitly coupled. A flow chart demonstrating the partitioned coupling method is shown in Figure 3.2. In this algorithm, the boundary conditions and interface conditions are applied to the fluid domain first; the velocity on the interface is equal for solid and fluid, and so a constraint is added to strongly enforce this. Fluid residuals and Jacobians are assembled and solved through iterations until convergence conditions are satisfied. The program moves on to the solid domain which also begins with applying boundary and interface conditions. The interface conditions on the solid are weakly enforced and needs to be added into the residual. Once the solid solution has converged, the program moves to the mesh motion domain, where the interface condition is defined

as the equal displacement on the interface between mesh and solid, and the boundary condition is defined as no normal fluxes on the boundaries. After applying these conditions and solving the equations in mesh domain, the solution is passed back to the fluid domain. Based on the updated mesh, the fluid has the new output through the iterations, and then puts it to solid and gets it solved. At this point, the convergence check is made, and the whole process repeats until the interface meets the tolerance requirement. When this convergence check is satisfied, the final solution of this time step is recorded and the program advances to next time step. The whole process is terminated when the time termination condition is met.

This loosely coupled method, which is widely used due to its simplified coupling procedure, is appropriate for weak interactions between fluid and structure (Felippa & Park, 1980; Oñate et al., 1998; Farhat & Lesoinne, 2000). However, because of the explicit coupling algorithms, the choice of time-step size is restricted and the divergence could exist in solving the large deformation problems (Hübner, 2004). To overcome the problem in explicitly coupled algorithms, Deparis et al. (2003) stated the coupling algorithms to solve the fluid, geometry, and the interface explicitly and the structure implicitly, but the unstable issues exist when the structure is light in this method (Tang, 2014). By applying a few correction iterations, some improvements have been made to solve the stability issues in explicit coupling algorithms (Nobile et al., 2012; Burman et al., 2007), in which higher order accuracy could be achieved at the expense of extra numerical effort (Hübner, 2004).

For strongly coupling algorithms, the geometry and interface coupling is treated implicitly (Čanić et al., 2006). In last decade, many researchers (Kalro et al.,

2000; Le Tallec et al., 2001; Ramm et al., 2001; Rugonyi et al.,2001), provide strongly coupling algorithms which show a satisfactory convergence behavior. Similarly as explicit coupling algorithms, extra numerical effort need to be considered in strongly coupling methods, too.

In both loosely and strongly coupling algorithms, sub-cycling is possible, for example, if the time scales in the flow field are much smaller than structural time scales. Another advantage of the partitioned solution approach is the application of existing appropriate and sophisticated solvers for each subsystem, which may be replaced with little effort (Hübner, 2004).

### 3.4.2 Monolithic approach

To minimize the problematic interface treatment when the fluid and structure are solved separately in partitioned approach, the monolithic approach is provided to treat the FSI problem as a single continuum with coupling automatically taking care of the internal interface (Hron & Mádlík, 2006; Hron & Turek, 2006).

The general procedure of the monolithic approach is shown in Figure 3.3: first, the boundary conditions and interface conditions are applied in the system; then, the program assemble appropriate residuals and Jacobians of fluid, solid and mesh terms into the global system; lastly, the program moves to the interface class which assembles the off-diagonal terms into the global system of equations. In monolithic approach, the solution by Newton method is utilized since it yields a powerful and rapidly converging scheme (Heil, 2004). Once the Newton-Raphson iterations converge, the present time step is fully solved and time is advanced to the next time. This process is repeated until the last time step is reached or a termination condition

is met. Since repeated assembly of Jacobian matrix and the solution associated with the linear systems for Newton corrections contributed to the computational cost, efficient preconditioning technique that allows the rapid iterative solution instead of applying the Newton method have been developed in the last decades (Heil et al., 2008; Hübner et al., 2004).

The computational cost per time step in the monolithic approach is higher than the partitioned approach (Michler, 2004), which does not show monolithic scheme's advantages in weak interaction problems. However, in case of strong interaction, the monolithic approach may be preferable in order to ensure stability and to accelerate convergence of the coupled solution. Specifically, monolithic approach appears to be unconditionally stable and considerable more accurate. As a consequence, larger time steps can be used than for partitioned scheme for the same level of accuracy, or the higher accuracy can be achieved by choosing the same time steps. According to Michler's test (2004), the results from monolithic approach are ten times more accurate, but the computational cost is only three to four times higher than those of the partitioned methods. Besides, the number of fluid-structure iterations required by a monolithic approach can be further reduced by means of prediction techniques, which reserve the potential for reducing their computational cost in monolithic approach.

In this research where the strong fluid-structure interaction exists, the use of explicit partitioned approach turns out to be problematic where stability is concerned, particularly due to the added mass effect. Furthermore, the implicit partitioned algorithms are also affected by the added mass effect in terms of convergence and

special treatment of interface conditions needs to be considered (Badia et al., 2008; Causin et al., 2005; Fernández et al., 2006). Therefore, the monolithic approach is applied in this research.

### *3.5 Software INTESIM*

There are several general purpose commercial CAE software packages available on the market that possess FSI capability, e.g., ANSYS-CFX®, ABAQUS® with StarCD or Fluent® through MpCCI, ALGOR®, ADINA®-FSI, etc. Some of these FSI products are limited to the partitioned coupling method, which make it ill equipped to solve strongly coupled highly nonlinear FSI problem.

Since high nonlinearity and large fluid domain changes are involved, the monolithic coupling method based software INTESIM was selected for this study. INTESIM consists of strong interface coupling methods that can deal with not only the compatible but also incompatible mesh discretization across physics interfaces. It also provides an advanced morphing technology to move the interior nodes in fluid domain according to the interface movement. Furthermore, Laplace equation or elasticity equation with adjustable mesh stiffness is employed for solving the moving boundary problem and the mesh deformation of the fluid element can be controlled to achieve good quality in INTESIM. To verify its effectiveness, three benchmark FSI models were built in INTESIM and the simulation results were compared with the solutions provided by leading CFD researchers in this section.

3.5.1 Benchmark FSI model #1

As the current FSI analysis are based on ALE finite element method, the first benchmark FSI model is intended to test its accuracy in the prediction of pressure and flow velocities as the fluid mesh experiences large deformation. As shown in Figure 3.4, this benchmark problem involves a stiff moving wall that pushes fluid into a channel with a sudden contraction. The fluid is modeled with 8-node 3D fluid element. The fluid density is 1000 kg/m$^3$ and dynamic viscosity is equal to 1 Pa-sec. The maximum Reynolds number based on the contracted channel diameter is 50.

As the wall moves, the deformation exists in the fluid domain (see Figure 3.5). Specifically, the fluid mesh between the moving wall and the contraction channel is severely squeezed and the consequent pressure and velocity change happen during this process.

The values of pressure along axisymmetric axis were compared at 40.0 sec, 100.0 sec, and 160.0 sec (see Figure 3.6a, Figure 3.7a, and Figure 3.8a). It can be seen that the pressure along axisymmetric axis keeps at a constant level before the fluid enters the contraction. In contrast, the fluid nodal pressure near the contraction channel experiences a severe decrease and the maximum pressure gradient happens at the contraction. By passing through this sudden contraction area, the pressure along axisymmetric axis keeps decreasing until the pressure drops to zero near the outlet of the channel. The velocity along axisymmetric axis is displayed at 40.0 sec, 100.0 sec, and 160.0 sec (see Figure 3.6b, Figure 3.7b, and Figure 3.8b) and the velocity comparison indicates that the maximum velocity gradient located at the contraction area. The pressure and velocity distribution of fluid is shown in Figure 3.6c, Figure

3.7c and Figure 3.8c, which further proves the maximum pressure and maximum velocity happens near the moving wall and outlet respectively, and the sudden changes for both variables exist around the contraction area.

By comparing with the ADINA simulation results by Bathe (Bathe & Zhang, 2004), it can be seen that the pressure and velocity results matches very well between the presented results and Bathe's results. Therefore, the accuracy of pressure and velocity under large deformation can be proved in this demonstration model.

### 3.5.2 Benchmark FSI model #2

In this benchmark model, the FSI problem is solved in a steady analysis. The dimension and mesh details of this fluid flow model is shown in Figure 3.9. The flexible cantilever beam is fixed at its base in the flow channel. The cantilever beam is modelled using 20-node 3D solid elements with Young's modulus E equal to 1.0e7 and Poisson's ratio equal to 0.3. The simulations of flow are carried out by setting different values for the fluid velocity $v$, dynamic viscosity $\mu$ and fluid density $\rho$ (Case 1: $Re = 1$, $v = 1$, $\mu = 1$, $\rho = 0.5$; Case 2: $Re = 100$, $v = 1$, $\mu = 1$, $\rho = 50$). The fluid is modelled using 8-node fluid element. The boundary conditions in the x-y plane are shown in Figure 3.9 and symmetric condition is applied along the z direction. With increasing Reynolds number, both the flow velocity and cantilever displacement will change in the process.

As Reynolds number is set to 1 at first case, the fluid velocity contour is shown in Figure 3.10a. Because of the existence of the flexible cantilever beam, the fluid flow velocity arrives at the maximum value near the top of the cantilever beam. During this whole process, the fluid field exhibits the feature of laminar flow: there is

no cross-currents perpendicular to the direction of flow, nor eddies or swirls of fluids. The Figure 3.10b shows the deformation of the cantilever beam under this flow condition, and the maximum displacement 0.093 happens at the tip of beam.

With Reynolds number increasing to 100, the fluid field is not laminar flow anymore. Figure 3.11a displays the fluid velocity distribution and exhibits the existence of fluid distortion by passing the cantilever beam. Because of this change and the increased velocity, the interaction between the fluid and cantilever beam is intensified. As a result, the maximum displacement at the beam top increases from 0.093 to 0.422.

The results in both cases prove that the Reynolds number's influence on the FSI analysis. Compared with the solution given by Bathe & Zhang (2004), it can be seen that the deformation of the cantilever beam at low Reynolds case is the same as Bathe's results. In Case 2, the tip displacement of the cantilever beam is 10.6% different from the Bathe's solution. This comparison implies that the accuracy of the FSI analysis is influenced by the Reynolds number: the results of the FSI solution at low Reynolds number more accurate compared with high Reynolds number case. Since the Reynolds number of the FSI problem in this research is much smaller than 1, the results are reliable.

### 3.5.3 Benchmark FSI model #3

This third benchmark FSI model is categorized as a strong FSI transient problem, as described by Hübner (2004) and Bathe (2007). In this model, the coupling between the fluid and the structure is strong, which makes the solution a valuable test for FSI analysis. For the solid part, the compressible Mooney-Rivlin

material model is used. A Mooney-Rivlin solid is a hyperelastic material model where the strain energy density function is a linear combination of two invariants of left Cauchy-Green deformation tensor. The strain energy density function for an incompressible Mooney-Rivlin material is

$$\psi = C_1(I_1 - 3) + C_2(I_2 - 3) \tag{3.40}$$

where $C_1$ and $C_2$ are empirically determined material constants, $I_1$ and $I_2$ are the first and the second invariant of the unimodular component of the left Cauchy-Green deformation tensor. The density of the material is assumed to be 0 kg/m$^3$, and two constant C1 and C2 are 1.6667 Pa and 0 Pa (Wang et al, 2004). The solid part is modeled with 8-node 3D solid element. On the other hand, the fluid's density is 1.0 kg/m$^3$ and dynamic viscosity is 1 Pa-sec. The fluid is modeled with 8-node 3D fluid element (see Figure 3.12).

Figure 3.13 displays the pressure field and fluid mesh deformation at 0.0 sec, 3.0 sec, 6.0 sec and 9.5 sec. Because of the softness of solid material, the pressure field experienced significant changes in both time and space, and the FSI effect can be clearly seen in the change of velocity and pressure. In Figure 3.14c, the pressure of the interface experienced two peaks during the investigated time, and they are corresponding to two velocity increase rate in Figure 3.14b. By comparing with the solution given by Bathe (2007), it can be seen that the displacement of interface is very close; the differences of maximum velocity and maximum acceleration are only 2.7% and 6.1% respectively. Clearly, the technical ability of INTESIM can be verified by this benchmark model.

## 3.6 Conclusion

This chapter presents the theory background to solve the FSI problem, in which ALE finite element formulation is employed to discretize the governing differential equations. Two coupling methods are described to solve these equations: monolithic coupling and partitioned coupling method. In terms of its accuracy towards FSI problem with low Re number and large deformation flow, the monolithic coupling based software package INTESIM is selected to perform the FSI simulation in this study. The simulation results from three carefully selected benchmark FSI models are verified with the solution given by leading FSI researchers.
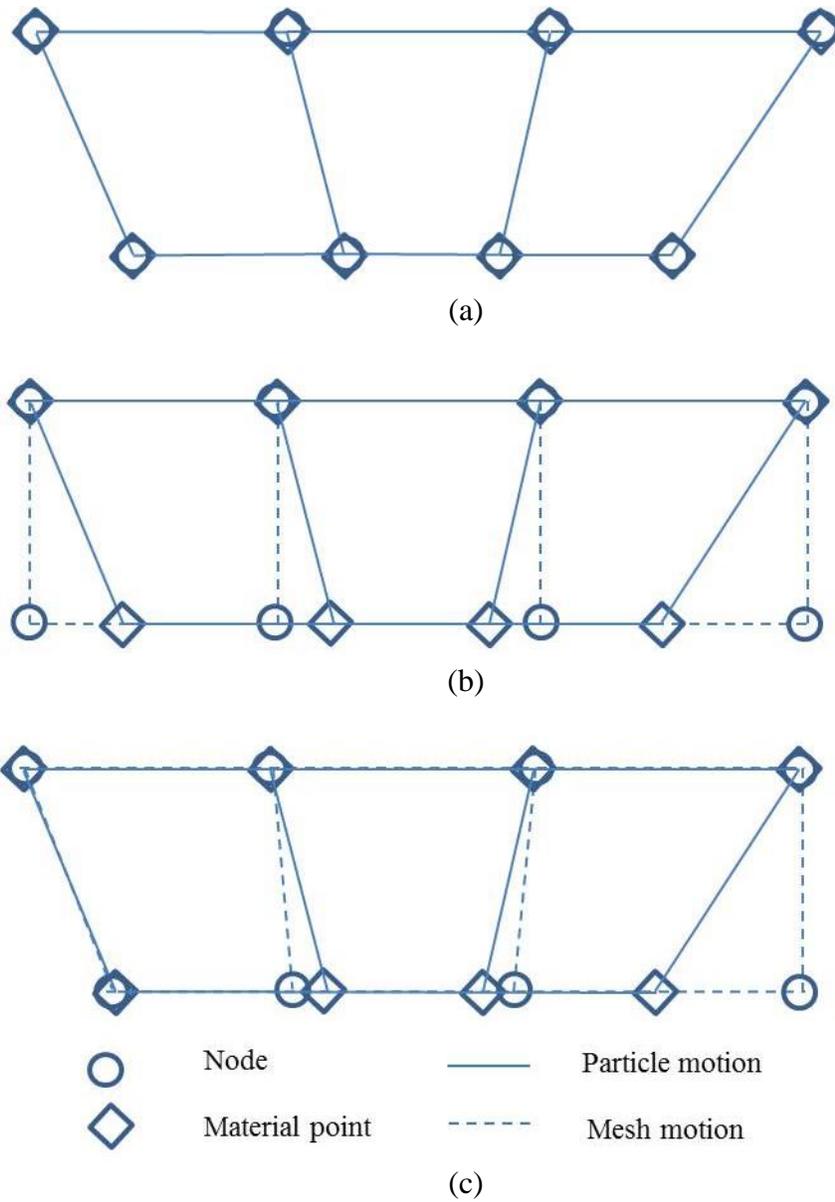
Figure 3.1 One-dimensional example of Lagrangian, Eulerian and ALE mesh and particle motion: (a) Lagrangian description; (b) Eulerian description; (c) ALE description (adapted from Donea, 1982)
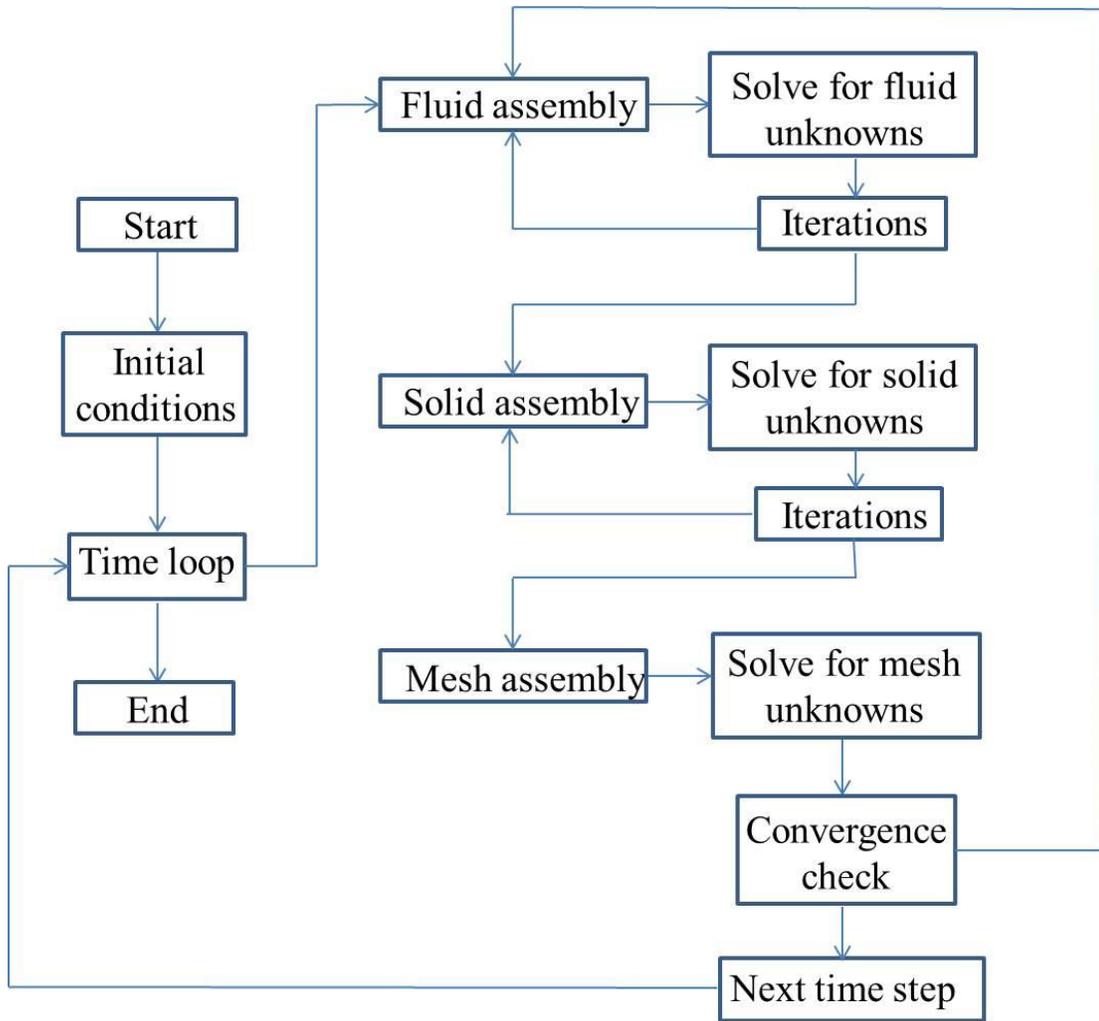
Figure 3.2 Flowchart demonstrating the partitioned coupling in FSI analysis (adapted from Sheldon, 2012)
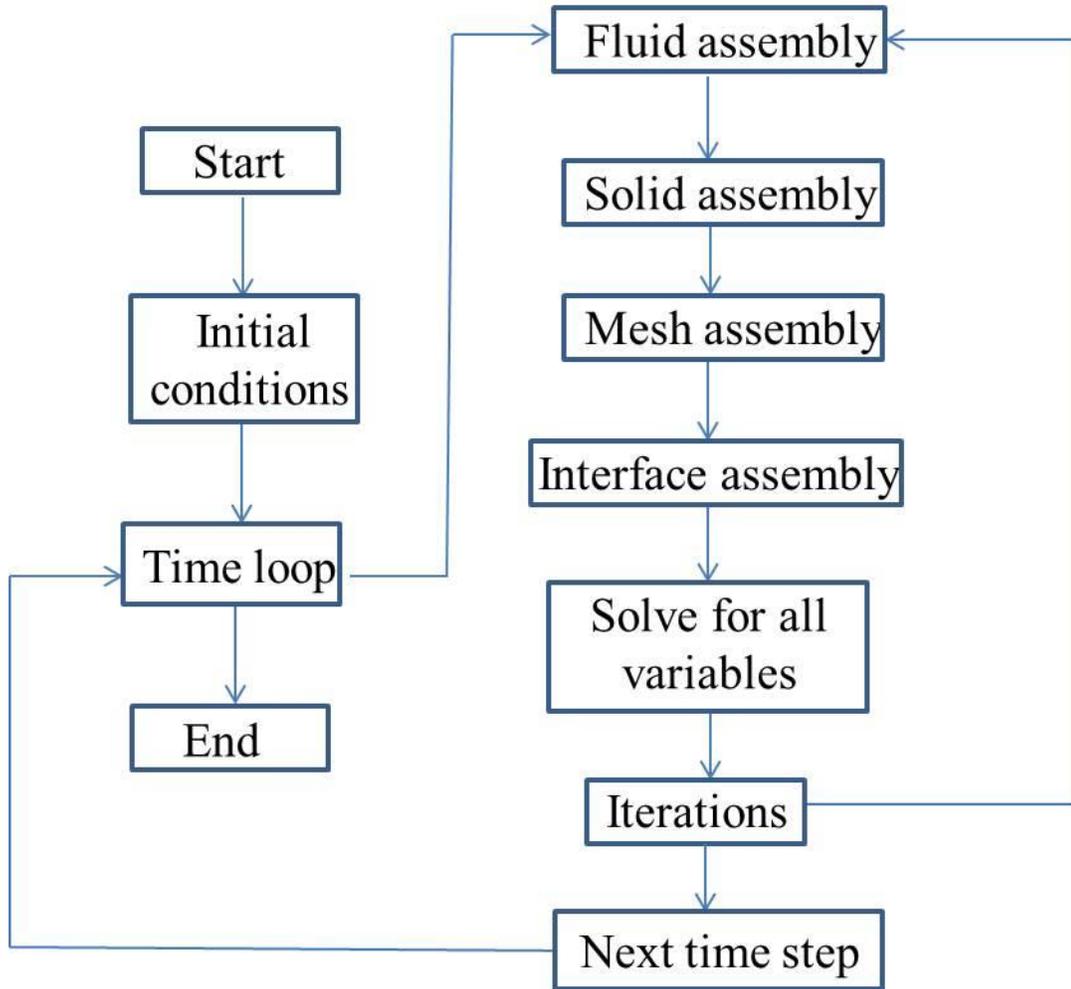
Figure 3.3 Flowchart demonstrating the monolithic coupling in FSI analysis (adapted from Sheldon, 2012)

2m 1m

0.1m

0.4m

$\tau \cdot \mathbf{n} = 0$

wall

Wall displacement
z(t)=0.01t m

Symmetry plane
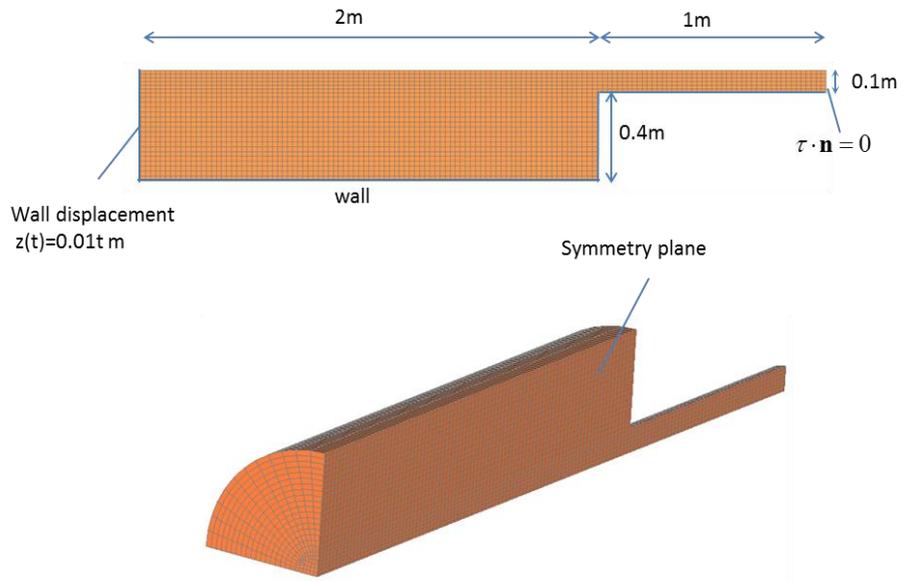
Figure 3.4 ALE low Re flow test: 3D model



Time=1.0s    Time=40.0s    Time=100.0s    Time=160.0s    Time=195.0s
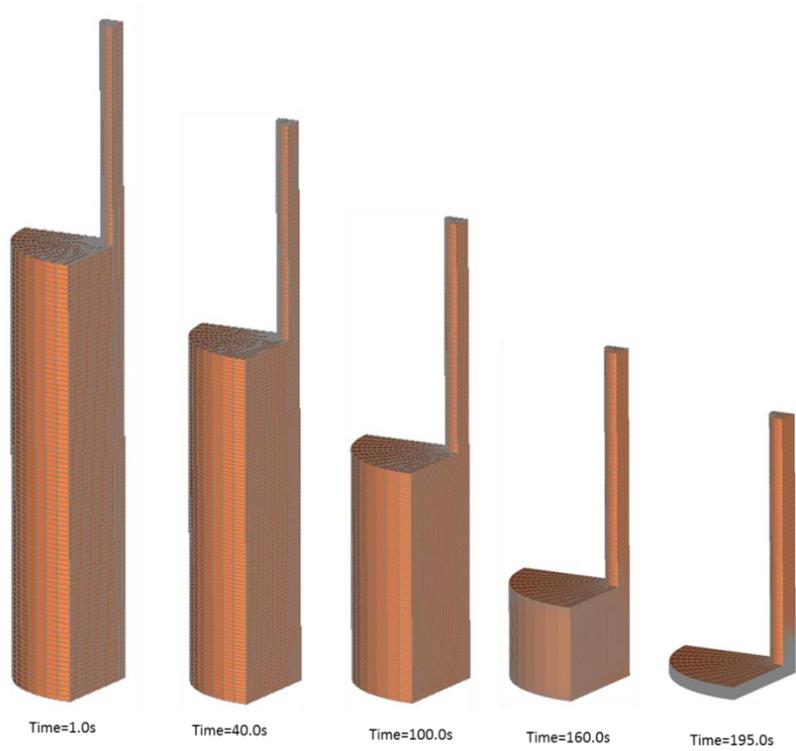
Figure 3.5 ALE low Re flow test: deformation history of the 3D mesh
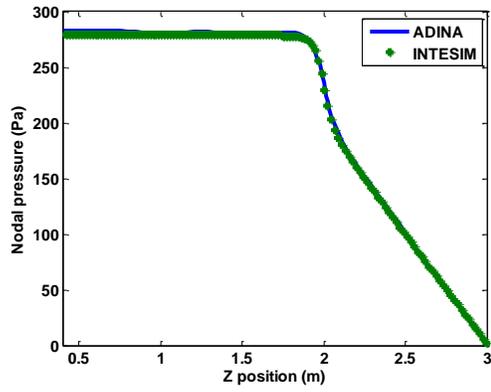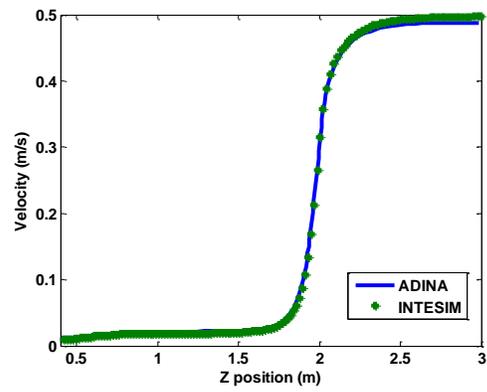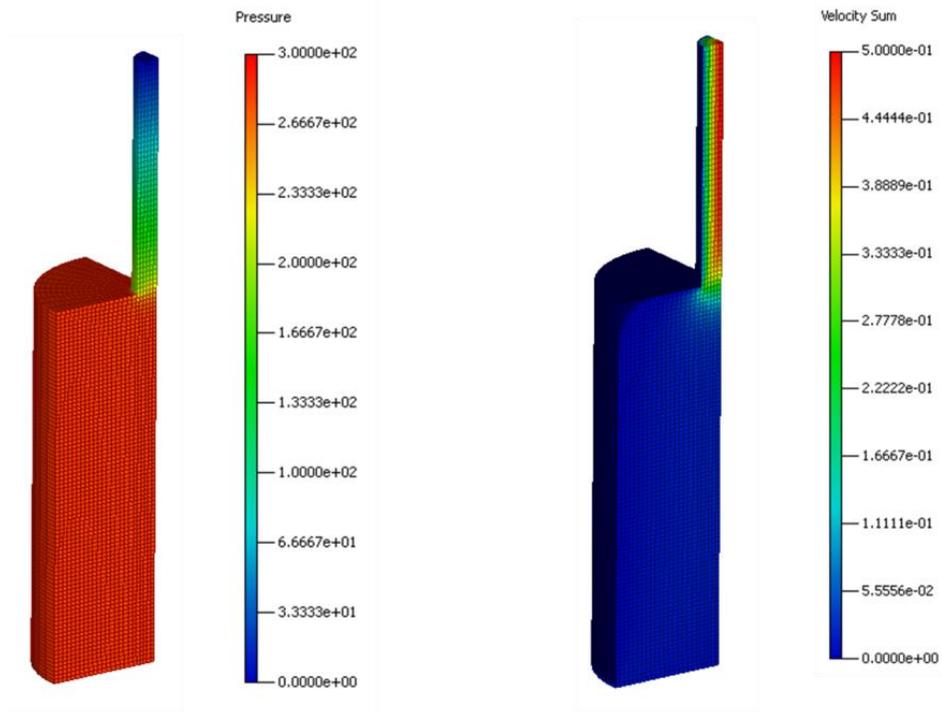
Figure 3.6 Fluid pressure and velocity distribution from low Re flow test at the time point of 40.0 s (ADINA data are from Bathe [2007]): (a) pressure along axisymmetric axis; (b) velocity along axisymmetric axis; (c) color contour plot of pressure and velocity distribution
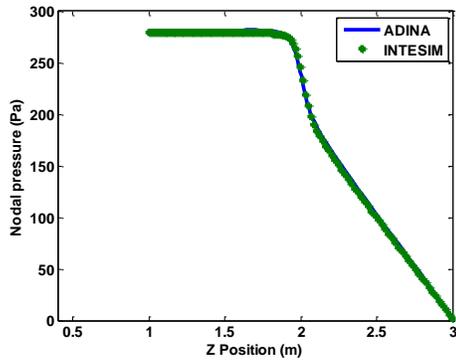
(a)
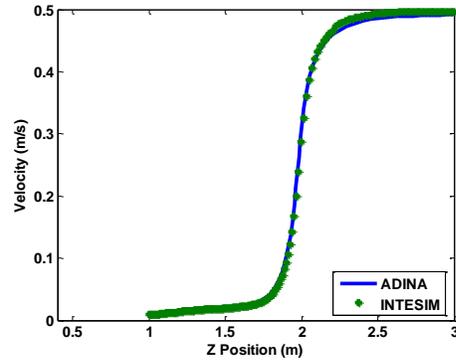
(b)
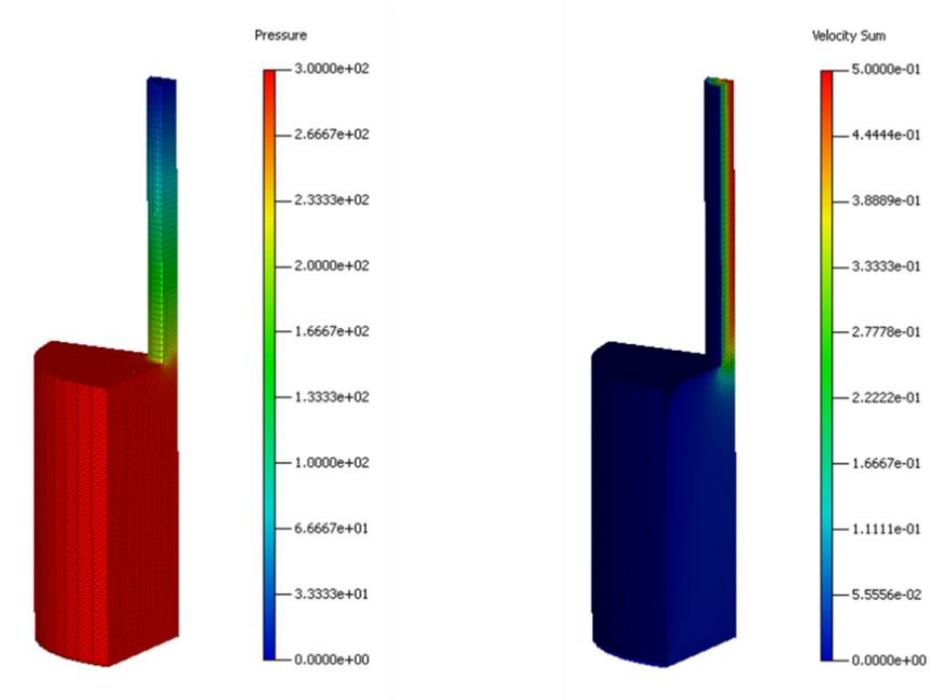
(c)

Figure 3.7 Fluid pressure and velocity distribution from low Re flow test at the time point of 100.0 s (ADINA data are from Bathe [2007]): (a) pressure along axisymmetric axis; (b) velocity along axisymmetric axis; (c) color contour plot of pressure and velocity distribution
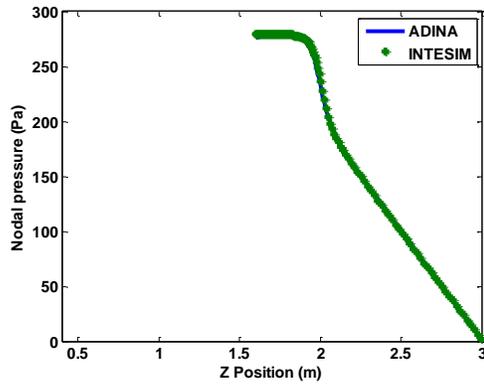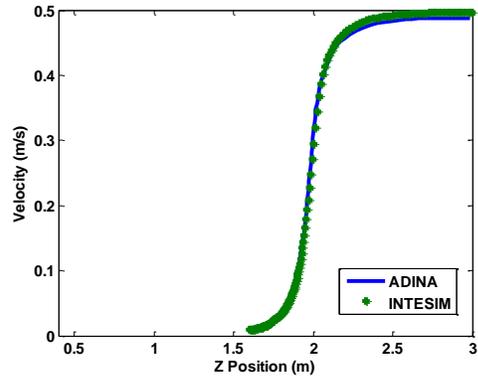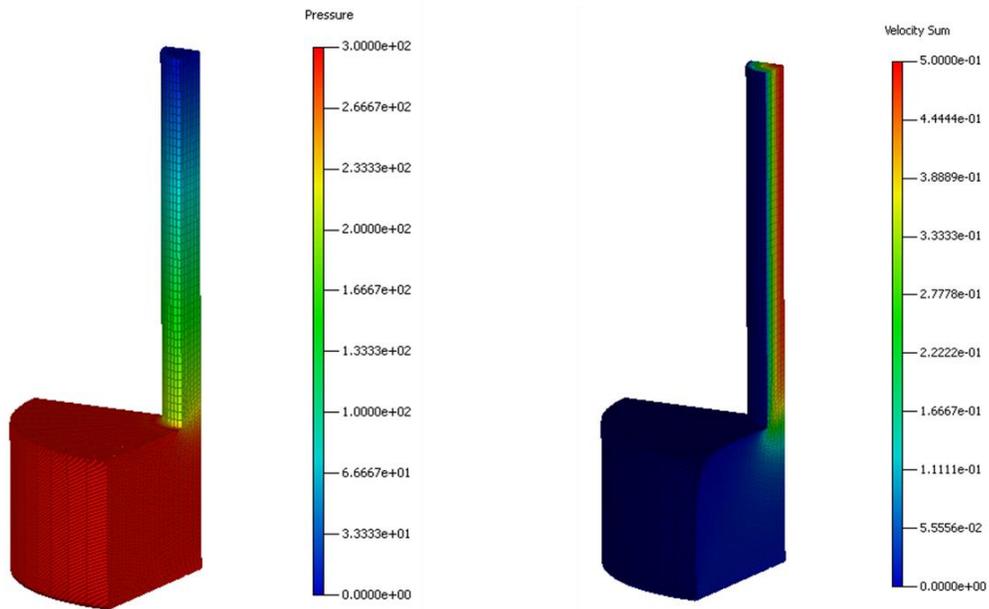
Figure 3.8 Fluid pressure and velocity distribution from low Re flow test at the time point of 160.0 s (ADINA data are from Bathe [2007]): (a) pressure along axisymmetric axis; (b) velocity along axisymmetric axis; (c) color contour plot of pressure and velocity distribution
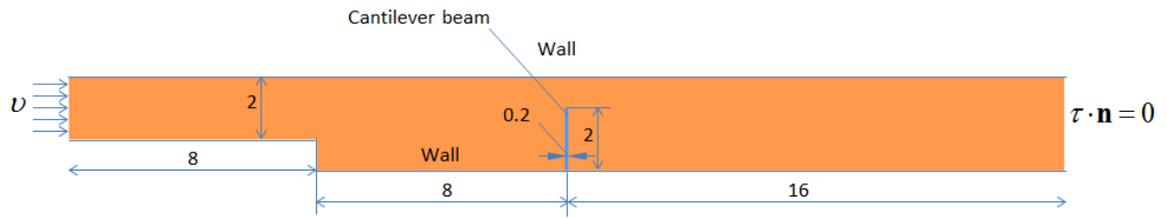
(a)
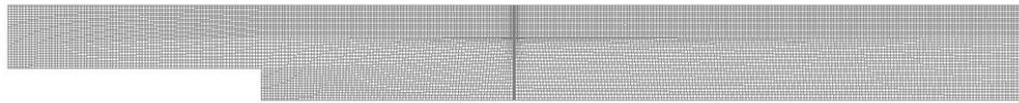


(b)

Figure 3.9 FSI steady test model: (a) model dimensions; (b) finite element model mesh scheme
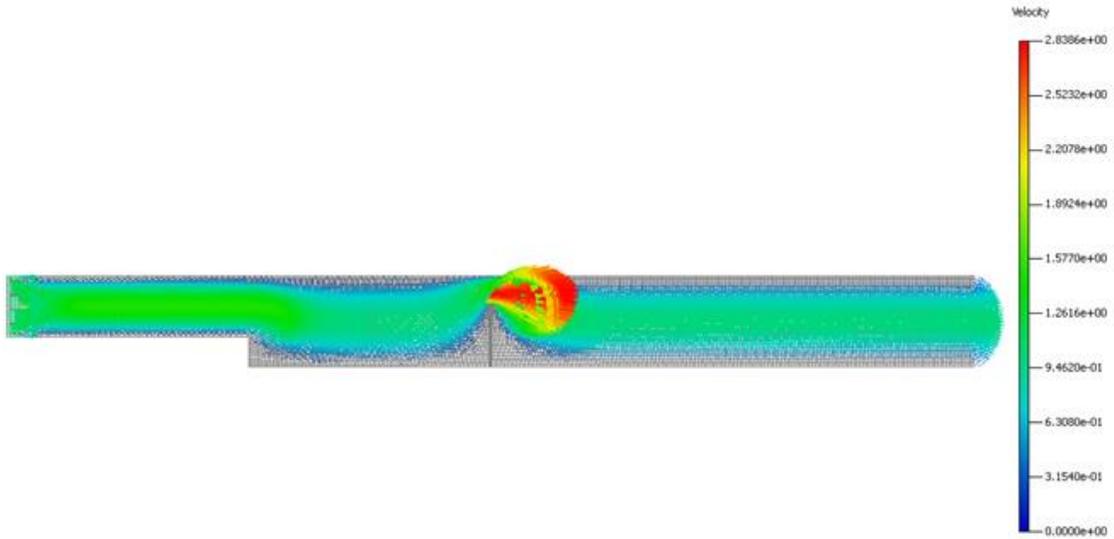
(a)
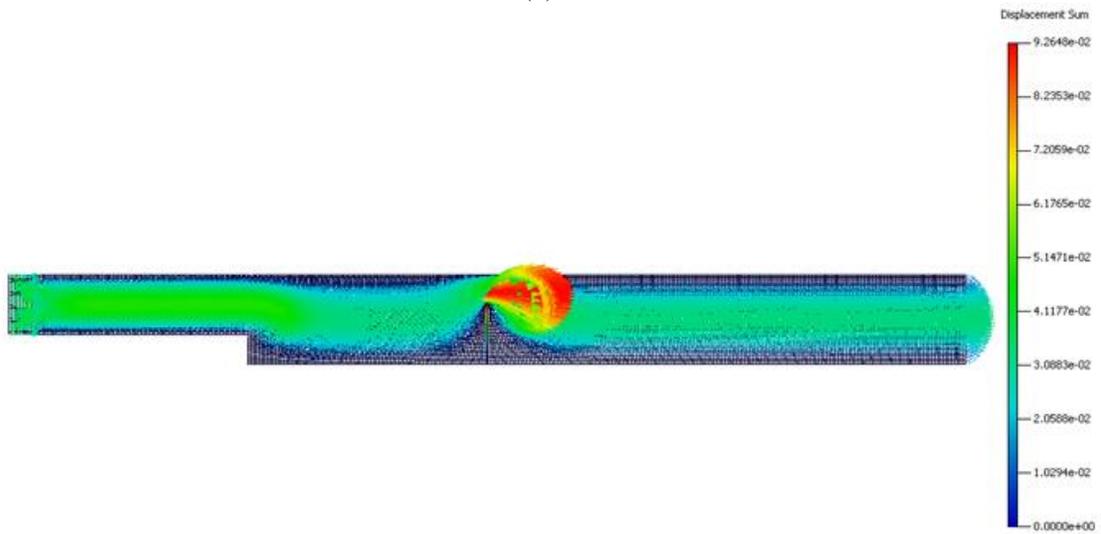


(b)

Figure 3.10 Color contour plot of fluid velocity and displacement distribution in steady FSI analysis (Re = 1): (a) velocity distribution of steady flow; (b) displacement of cantilever beam
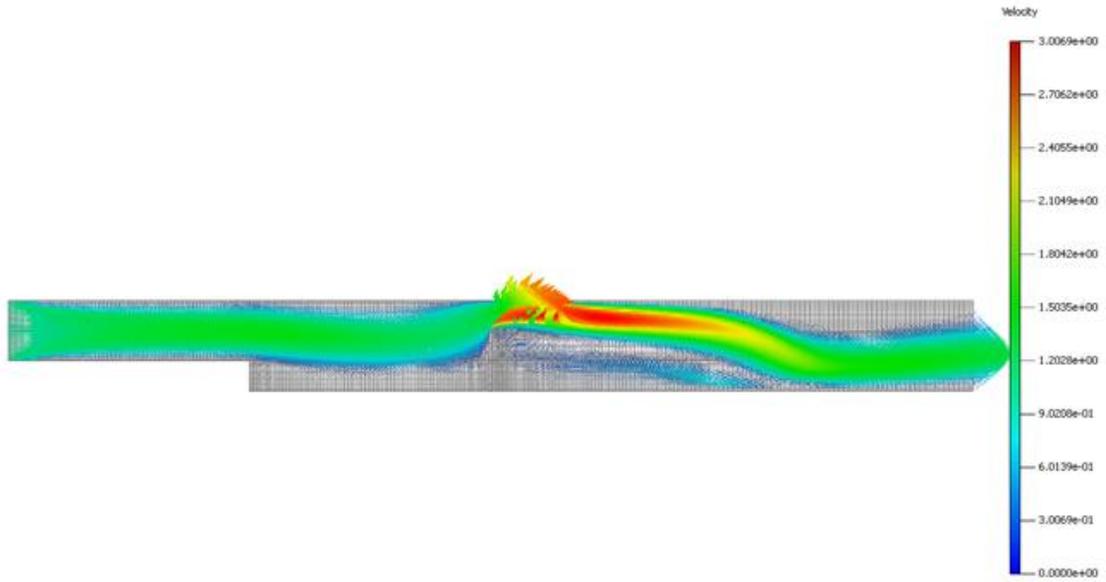
(a)
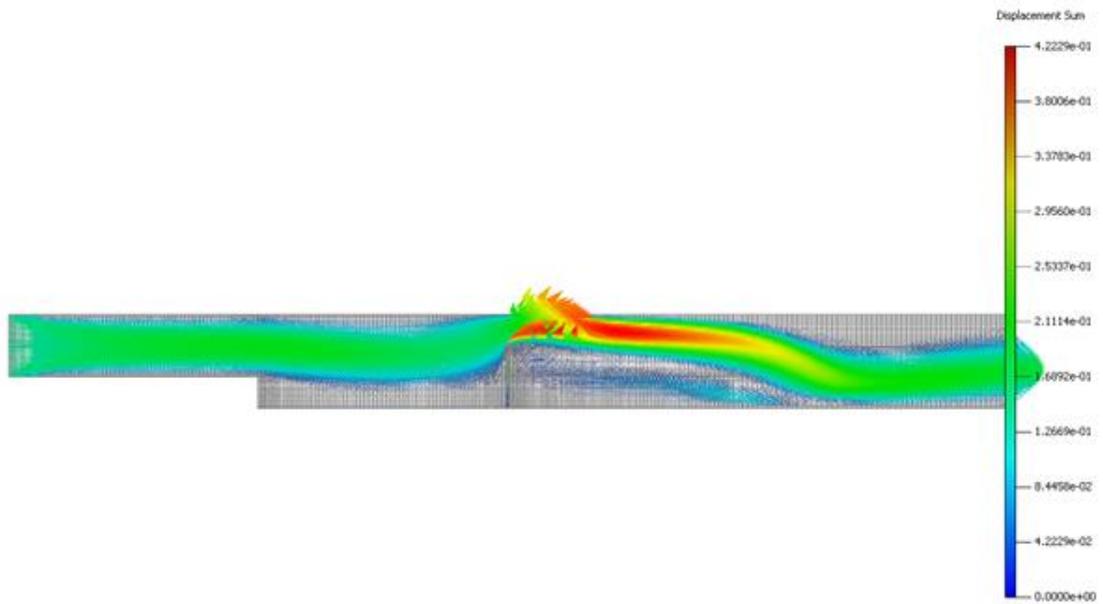


(b)

Figure 3.11 Color contour plot of fluid velocity and displacement distribution in steady FSI analysis (Re = 100): (a) velocity distribution of steady flow; (b) displacement of cantilever beam
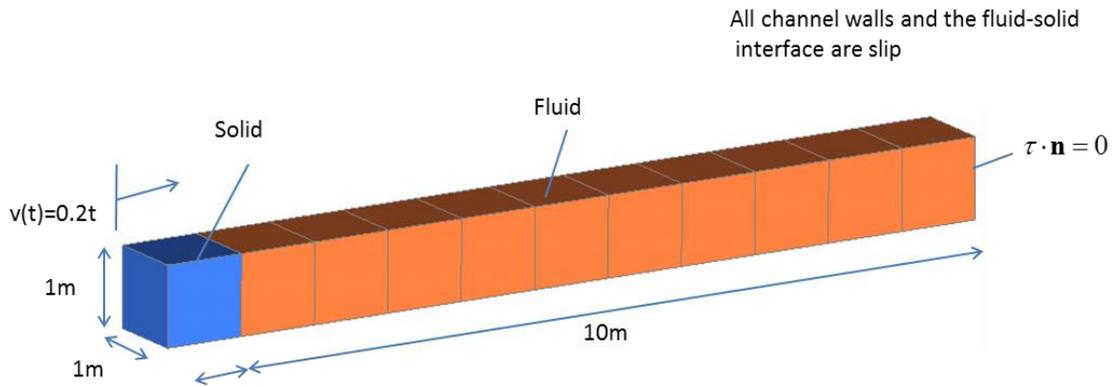
Figure 3.12 3D FSI model for testing transient strong coupling flow
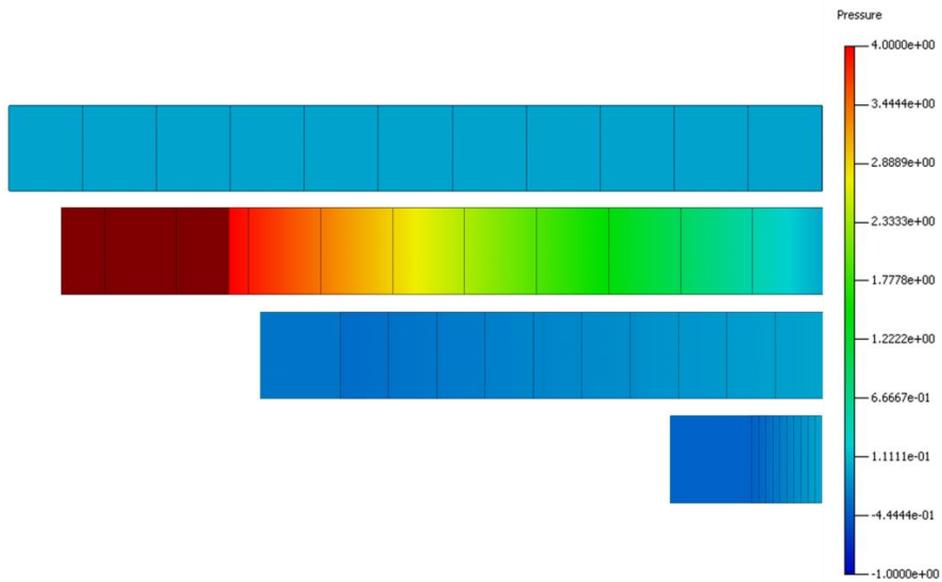


Figure 3.13 Color contour plot of fluid pressure distributions at $t = 0.0, 3.0, 6.0,$ and 9.5 s in transient strong coupling flow test
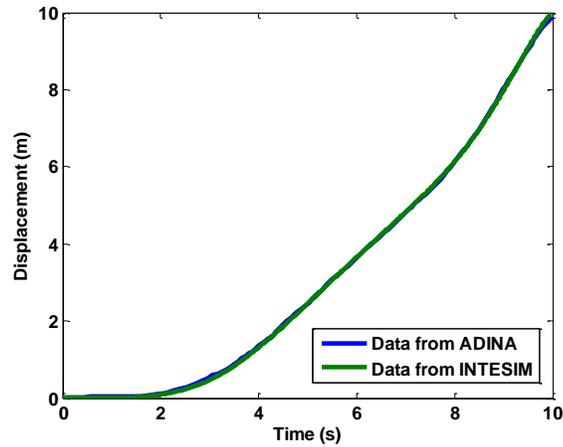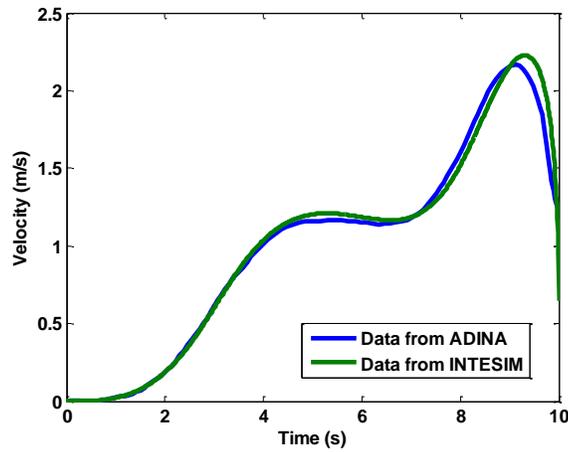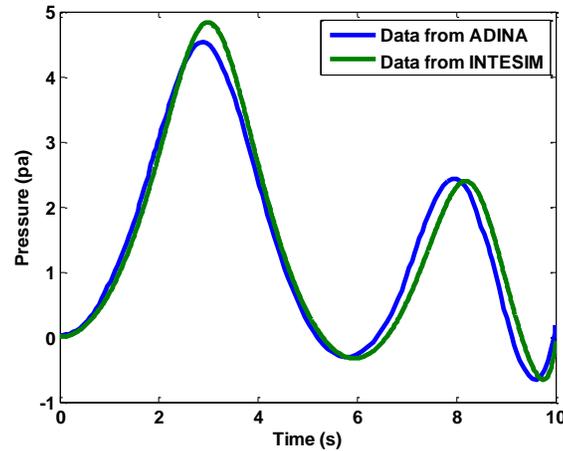
Figure 3.14 Simulation study results from two FSI models (ADINA data are from Bathe [2007]) for transient strong coupling flow test: (a) interface displacement time history; (b) interface velocity time history; (c) interface pressure time history

# Chapter 4: Bio-inspired vibration sensor design with tunable sensing characteristics

*4.1 Introduction*

3D Printing is about to transform our lives by producing complex objects directly from computer aided digital designs. It can be likened to clicking on the print button on a computer and sending a digital file, such as a letter, to a printer sitting on an office desk. The difference is that in a 3D printer the material or ink is deposited in successive, thin layers on top of each other to build-up a solid 3D object. The layers are defined by software that takes a series of digital cross-sections through a computer-aided design. Descriptions of the slices are then sent to the 3D printer to construct the respective layers. 3D printers have traditionally been used by large companies to produce fit and form concept prototypes ('rapid prototyping') before production. In recent years however there has been a move to adopt the technology as full-scale manufacturing solution. With the proliferation of 3D printers such as the Reprap and Fab@Home, 3D printers have also facilitated an individualized or personalized approach to manufacturing, where objects can be customized and produced by an individual to their own specifications. This uptake in usage has been coupled with a demand for printing technology and materials able to print functional elements such as electronic sensors (Leigh et al. 2012). One of the most unique advantages of 3D printing technologies is their ability to create complex geometrical shapes that would be impossible to do with any other method of manufacturing (e.g.,

biological organ with irregular internal shapes in Fig. 4.2). In the case of complex shapes, subtractive manufacturing methods often run into the problems of tool clearance, the amount of space required for a tool to reach the cutting area of a part. Tool clearance is usually overcome through joining (i.e., the use of nails, screws, adhesives, welding, etc. to couple multiple parts), but joining creates structural weaknesses and is not always possible depending on the application, especially when manufacturing small or delicate parts. Other methods including molding and casting exist, but for certain objects of complex shapes, it can be difficult or impossible to create a mold for or to remove the object from one (Lou and Grosvenor 2012).

With advancement of 3D printing technology, it is possible to make sensors with custom-adjusted sensing specifications using 3D printers and smart materials, simply from available digital sensor design drawings. In the past decade or so, sensors made of piezoelectric materials have gained increasing popularities in the field of structural health monitoring. Piezoelectric materials can be broadly classified into three major categories: ferroelectric ceramics, piezoelectric polymers (e.g., PVDF), and piezoelectric composites. Because of their electro-mechanical coupling property, piezoelectric materials have been widely used for sensing and actuation applications (e.g., Polla & Francis, 1998; Niezrecki et al., 2001; Gautschi, 2002; Damjanovic, 2001). Piezoelectric ceramics are perhaps the most popular piezoelectric materials for sensing purpose. As of today, most piezoelectric sensors are made of piezoelectric ceramics such as lead-zirconate-titanate (PZT). By taking advantage of the advancement in the 3D printing technology and piezoelectric sensing material, a new bio-inspired sensor design is presented in this chapter, which serves as a case

study to demonstrate the use of 3D printing technology in implementing bio-inspired sensor design typically involving complex shape and configuration.

## 4.2 Morphology study and numerical simulation on octopus macula/statolith

### 4.2.1 Morphology study

The inspiration for this sensor design is from the study of morphological structure of the cephalopod's macula/statolith system (see Chapter 2). After removing the statolith from the octopus statocyst, a microscopic view of the macula epithelium is provided in Figure 4.1a. A close look at this picture suggests that the kinocilia bundles are encased in statolith-like aragonite residuals sticking to part of the macula epithelium (see Figure 4.1b). A histological transverse section view part of cephalopod's macula by Budelmann (1979) is shown in Figure 4.2. It is seen that the statolith is not connected to the kinocilia bundles. It is therefore the endolymph flow that pushes the kinocilia bundle to deform whenever the statolith moves and the bending of the kinocilia bundle would stimulate the underlying hair cell and thus trigger the neurotransmission process.

### 4.2.2 Description of the numerical model

The kinocilia/hair cell is the mechanosensory part in the macula/statolith system and its dynamic feature is investigated through numerical simulation. To study the interaction between the endolymph and the kinocilia bundle, the FSI analysis software INTESIM is utilized for numerical simulation in this study. The simplified model of the kinocilia bundle and its surrounding parts are illustrated schematically in Figure 4.3, in which the bundle is shown to be in a cavity filled with endolymph fluid

covered by the statolith. The supporting cell and microvilli are assumed to have little effect on the mechanical sensing characteristics and they are neglected in the simplified FSI model. Based on this configuration, a simplified 2D macula/statolith numerical model (the out-of-plane dimension is set to 0.66 µm) that represents one kinoclilia bundle module on the macula is shown in Figure 4.4a. This 2D FSI model comprises a beam representing the kinocilia bundle, the overlying statolith, which is immersed in endolymph fluid. Since the kinocilia bundle is modeled as an upright cantilever beam, the reaction force at its base can be recorded for response analysis during the FSI process. The statolith is modeled using solid elements as a floating object that would move only in horizontal direction. The endolymph fluid fills up the space surrounding the kinocilia bundle and statolith and this fluid space is confined within a rectangular boundary. The gap between the kinocilia bundle and statolith is denoted as inner gap. On the other hand, the gap between the epithelium and the statolith is identified as the outer gap. The material properties of each part used for the model are listed in Table 4.1. Figure 4.4b shows a typical velocity contour when the statolith is moving away from its initial position. Because the Reynolds number in this simulation study is much lower than 1.0, the laminar flow condition dominates in this FSI problem. This is also evidenced in the velocity contour plot which is characterized by constant fluid motion and no turbulent flow is observed within the gap region.

4.2.3 Numerical analysis of kinocilia bundle

The actual kinocilia bundles, statolith, and macula epithelium have been demonstrated in Figure 4.2. It is seen that the inner gap size and outer gap size vary

between different kinocilia bundles, and such difference may cause varying kinocilia bundles' response when the endolymph flows through these gaps. In this study, three inner gap size values (0.33 μm, 0.80 μm and 1.33 μm) and three outer gap size values (0.3 μm, 1.0 μm and 2.0 μm) were selected for the numerical model to investigate their effect on the kinocilia bundle's response. In addition to the gap size, another noticeable feature is that the angles between the kinocilia bundle and the macula epithelium in the macula/statolith system are different from each other, and this inclined angle could reach as large as 60 degrees according to the study by Budelmann (1979). The effect of the kinocilia bundle's inclined angle on the frequency response will also be discussed in this section.

### 4.2.3.1 Reference model response analysis

A reference model is first built to study the kinocilia bundle's frequency response characteristics when it is subjected to the fluid pressure caused by statolith motion. The sinusoidal statolith movement is set to be +/-0.001 μm in amplitude; the inner gap and outer gap dimensions are 0.33 μm and 1.0 μm respectively (see Model Pk in Table 4.2). A plot of the reaction force at the kinocilia bundle base and the frequency of the harmonic statolith motion is shown in Figure 4.5a. In the low frequency range (e.g., below 20 Hz), the reaction force increases linear proportionally with growing frequency. Meanwhile, in the higher frequency range starting at 100 Hz, the reaction force appears to saturate and remains relatively constant. It is also noted that the slope of this frequency response curve begins to drop above approximately 20 Hz, which is defined as cut-off frequency in this study.

By dividing the frequency response curve for constant displacement in Figure 4.5a with circular frequency $\omega$ of $2\pi$ rad./s., its frequency response curve to harmonic velocity excitation of constant amplitude (velocity amplitude equals 0.001 μm/s) can be derived, as shown in Figure 4.5b. Figure 4.5b shows that the horizontal reaction force at the kinocilia bundle base keeps almost constant below a cut-off frequency of approximately 20 Hz, after which it decreases with increasing frequency. This implies that the sensitivity of the kinocilia bundle base reaction force to velocity stimulus applied at the statolith is relatively unchanged in the low frequency range while it decreases at higher frequency values.

4.2.3.2 Effect of inner gap size

The second group of FSI models are designed to examine the effect of inner gap size values on the frequency response characteristics of the kinocilia bundle base reaction to statolith movement. Details of these models (Model Pk, Model Ak1 and Model Ak2) can be found in Table 4.2. The frequency response curves of the kinocilia bundle base reaction to harmonic statolith displacement and harmonic statolith velocity are displayed in Figure 4.6a and Figure 4.6b, respectively. The cut-off frequency corresponding to the turning point observed in the frequency response curve of the reference model are also seen in all three frequency response curves, suggesting that they follow similar trend, while the exact location of the turning point appears to be dependent on the inner gap size. Corresponding to the three inner gap sizes (i.e., 0.33 μm, 0.80 μm and 1.33 μm) considered for this study, the approximate cut-off frequency values at these turning points are read from the figure as: 20 Hz, 50 Hz and 100 Hz, respectively. This finding indicates that increasing inner gap size can

change the kinocilia bundle's frequency response characteristics by both shifting the cut-off frequency towards the higher frequency value and slightly changing the gain. Therefore, by adjusting the inner gap size, the frequency bandwidth can be tuned. This is a very useful feature in 3D printable sensor design because now sensor frequency bandwidth can be adjusted by controlling the inner gap dimensions.

Furthermore, the gain of the frequency response curve for the kinocilia bundle base reaction to velocity stimulus at the statolith can be changed by adjusting the inner gap size. As shown in Figure 4.6b, with three different inner gap size values (i.e., 0.33 μm, 0.80 μm and 1.33 μm), the corresponding gain below the cut-off frequencies of those turning points are 6.21e-7 N*s/m, 2.07e-7 N*s/m and 8.12e-8 N*s/m. This indicates that by increasing inner gap size, the sensitivity factor of the kinocilia bundle base reaction force to the applied velocity stimulus can be reduced. Therefore, for larger sensitivity, a smaller inner gap size would be desirable, but this increased sensitivity is achieved by paying a price of reduced frequency bandwidth.

4.2.3.3 Effect of outer gap size

The third group of numerical models are intended to study the effect of varying outer gap size values on the frequency response characteristics of the kinocilia bundle base reaction to statolith motion. The details of the three models used in this study (denoted as Model Bk1, Model Pk and Model Bk2) are given in Table 4.2. Based on the sine sweep excitation analysis, the kinocilia bundle base reactions to statolith displacement and velocity are shown in Figures 4.7a and 4.7b. It is seen from the figures that the cut-off frequency of the turning points appears to be around 5 Hz, 20 Hz and 50 Hz in the respective models with corresponding outer gap sizes

(0.3 μm, 1.0 μm and 2.0 μm). This suggests that by increasing outer gap size the lower cut-off frequency of its frequency band can be shifted to higher frequency values.

Additionally, the effect of the outer gap is also seen in the variation of frequency response gain for the kinocilia bundle's reaction to velocity stimulus at statolith. As shown in Figure 4.7b, below the cut-off frequency of the turning point, increasing outer gap size drops the frequency response gain to a lower level, suggesting an inverse relationship between the outer gap size and the sensitivity of the kinocilia bundle's reaction to the statolith velocity.

### 4.2.3.4 Effect of tilt angle

Dependent on the study of the macula kinocilia bundle in cephalopods (Budelmann, 1979), it is known the kinocilia bundle tilts different angles away from the upright direction. A model with inclined kinocilia bundle (Model Tk) is utilized in this section to see whether inclined bundle would have some impact on the kinocilia bundle's base reaction response. The frequency response curves of the kinocilia bundle base reaction to statolith displacement and velocity are shown in Figure 4.8a and Figure 4.8b respectively. With the cut-off frequency of the turning points identified as 50 Hz in both curves, the model with inclined kinocilia bundle (inclined angle equals 20° from its upright position) shows a similar trend as the model with upright bundle. Given the same inner gap and outer gap dimensions in two models (Model Ak1 and Tk), the comparison between these two frequency response curves means the inclination angle does not obviously affect the kinocilia bundle frequency response.

*4.3 Conceptualization of bio-inspired sensor design*

4.3.1 Model description

The frequency response characteristics of the FSI model mimicking the octopus macula/statolith system reveals that the kinocilia bundle's frequency response is tunable by varying the geometry and dimensions of the kinocilia bundle and its surrounding environment. Inspired by this observation, this section presents the concept of a bio-inspired sensor design that can be realized with 3D printed parts. A schematics of the configuration of this conceptualized sensor design is shown in Figure 4.9, which consists of a number of 3D printed components, viscous fluid that fills the chamber, and a strain sensing element (e.g., piezoresistive or piezoelectric patch).

Based on their position and function, the four 3D printed components are identified as base mount, inner beam, shear layer and outer case, respectively. Among them, the inner beam, base mount, and outer case intend to mimic the kinocilia bundle, macula epithelium and statolith in the octopus's macula/statolith system, and engineering plastic is chosen as the material for these three parts; on the other hand, the shear layer, is made of soft material (e.g., silicone rubber) to accommodate the case motion when the sensor is in operation. Because these materials are available as commonly used 3D printing materials, (see Table 4.3) all the components can be fabricated with current 3D printing technology. The viscous fluid, which is designed to mimic the endolymph fluid in the macula/statolith system, will fill the chamber surrounding the inner beam. The piezoelectric sensing element, which converts the

physical strain at the inner beam base into corresponding electrical charge signal, is the active element of the sensor that mimics neuron cell responding to external stimulus.

A simplified 2D numerical model (the out-of-plane dimension is 0.35 mm) that captures the basic features of the proposed bio-inspired sensor design is created in the FSI software INTESIM, as shown in Figure 4.10. In this simplified FSI model, a horizontal harmonic displacement and the vertical DOF restraint are applied at the top of the sensor while the base mount is fixed at its bottom surface. With these boundary conditions, the relative movement between the top and the bottom of the sensor will cause the bio-inspired sensor to deform in a pure shear mode, and the viscous fluid is pressured to flow through the gap over the inner beam. Because of the FSI effect, the inner beam would deflect and the strain of the inner beam base can be measured with the piezoelectric strain sensing element. Since the electrical signal generated in the piezoelectric sensing element is linearly related with the deflection amplitude of the elastic inner beam, the inner beam top deflection is used as one of the response indicators in this study.

4.3.2 Mechanical model of proposed sensor design

Based on the macula/statolith analysis, it is found that the reaction force at the kinocilia bundle base increases proportionally with growing frequency in the low frequency range and remains relatively constant in the higher frequency range. This phenomenon, has also been observed in most viscoelastic materials, which can be described with the Maxwell model. Since the proposed bio-inspired sensor model behaves similarly as the kinocilia bundle (demonstrated in the following study), the

Maxwell model is selected here to quantitatively describe the frequency response characteristics of the proposed bio-inspired sensor.

The Maxwell unit is comprised of a spring and dashpot connected in series, as shown in Figure 4.11. When a unit displacement is applied across the two ends of the Maxwell unit, the force in the unit is defined as its stiffness, which can be expressed as,

$$K = \frac{k^2 \eta^2 \omega^2}{\eta^2 \omega^2 + k^2} \tag{4.1}$$

where $k$ and $\eta$ are positive constants representing the spring stiffness and the dashpot damping coefficient, respectively (Tschoegl, 1989).

### 4.3.3 Reference model study

#### 4.3.3.1 Response analysis

A reference model study was first conducted to reveal the bio-inspired sensor's frequency response characteristics through sine sweep excitation. The harmonic displacement excitation with three different amplitudes (0.25 mm, 0.5 mm and 1.0 mm) were applied at the top of the bio-inspired sensor. The inner beam top point deflection was recorded simultaneously to display the bio-inspired sensor response. For instance, an inner beam top point deflection to the 5 Hz harmonic excitation at the amplitude of 1.0 mm is displayed in Figure 4.12, and it shows a steady sinusoidal response at the applied sensor motion. By recording the deflection amplitudes at different excitation frequencies, the frequency response curve of the inner beam top point deflection to the harmonic excitation is shown in Figure 4.13a. Over the considered frequency range, the turning point defining the rising portion and

flat portion in the frequency response curve in the prior macula/statolith FSI model simulation is also seen in the frequency response curves of this bio-inspired sensor, suggesting that the bio-inspired design captures the interesting frequency response behavior of the octopus's macula/statolith system. It is also noted that the amplitudes of all three frequency response curves are proportional to the corresponding displacement input amplitudes while having the same cut-off frequency at around 20 Hz. This indicates that for displacement input amplitude range considered, the frequency responses of the bio-inspired sensor are independent of the input displacement amplitude. The frequency response curve of the sensor to velocity input could be derived by dividing the curve shown in Figure 4.13a with circular frequency $2\pi$ rad/s. Figure 4.13b shows that the inner beam's deflection keeps constant below the cut-off frequency at 20 Hz and begins to decrease starting from this cut-off frequency.

4.3.3.2 Hysteresis feature

Since the inner beam tip deflection is proportionally related to its base reaction force, the frequency response of the bio-inspired sensor can be expressed in term of the horizontal inner beam base reaction force. After this transformation, the hysteresis loop which is usually displayed in the viscoelastic materials can be used to demonstrate the relationship between the base reaction force and the applied harmonic displacement in the reference bio-inspired sensor design, as shown in Figure 4.14a. The hysteresis loops for the two cases with excitation frequencies of 1 Hz and 10 Hz (below the cut-off frequency of the turning point in the frequency response curve) exhibit a strong viscous feature associated with the base reaction

90

force, in which the base reaction force lags behind the displacement motion by 85° and 75° in phase. On the other hand, the hysteresis loops of the cases with excitation frequency of 100 Hz and 1000 Hz (above the cut-off frequency) show a significant increase of the elastic stiffness and the diminishing trend of the viscous effect associated with the base reaction force. The phase difference between the base reaction force and the displacement motion consequently decreases to 34° and 3° respectively. The above comparison between these two distinctive groups of hysteresis loops, explains the different dynamic response behavior of the bio-inspired sensor design observed on the two sides of the cut-off frequency in its frequency response curve.

4.3.3.3 Fluid distribution

The deflection of the inner beam is caused by the interaction between the inner beam and viscous fluid flowing past it, which can be utilized to tune the frequency response characteristics of the bio-inspired sensor by adjusting its cut-off frequency and gain. In order to understand the effect of viscous fluid-inner beam interaction on the bio-inspired sensor sensing characteristics, the velocity distribution of the viscous fluid at varying frequencies of the harmonic displacement input with constant amplitude is shown in Figure 4.14b. It is seen that, as the sensor is dynamically displaced away from its initial position, the fluid distribution displays two different patterns with varying excitation frequencies. Specifically, with low excitation frequency values (i.e., 1 Hz and 10 Hz), the analyzed viscous fluid shows a laminar flow characteristics (Re number is less than 1.0) through the gap area, and the highest flow velocity value is observed to be located above the inner beam tip within

91

the gap area; with higher excitation frequency values (i.e., 100 Hz and 1,000 Hz), the flow condition through the gap area shown in the lower excitation is intended to disperse into a larger area around the inner beam. In the meanwhile, the highest flow velocity zone also shifts towards the inner beam tip. This observation reveals the underlying physics that causes the observed frequency response characteristics due to the FSI process.

4.3.3.4 Maxwell model representation

The frequency response curves of inner beam tip displacement shown in Figure 4.13 could also be transformed from inner beam deflection to base reaction force, and the frequency response functions of the inner beam base reaction to the excitation displacement and velocity applied at the outer case top surface are shown in Figure 4.15a and Figure 4.15b respectively. Since the viscoelastic behaviors displayed by these curves could be described by the Maxwell model, a Maxwell unit with a spring stiffness $k$ of 0.105 N/m and damping coefficient $\eta$ of 3.0e-4 N*s/m is used to fit the frequency response curve of the prototype bio-inspired sensor design. A comparison between the Maxwell model and the discrete frequency response relationship derived from FSI model simulation in Figure 4.15 demonstrates that they agree very well with each other, suggesting that the dynamic response behavior of the concerned bio-inspired sensor design could be described with a simplified model represented by the Maxwell unit. Using the calibrated Maxwell model, FSI simulation is no longer needed to examine the sensing performance of the proposed bio-inspired sensor design.

4.3.4 Parametric study

In this section, three control parameters are varied to investigate their effect on the frequency response characteristics (focused on frequency band and gain in this study) of the proposed bio-inspired sensor design.

4.3.4.1 Effect of gap size

3D printing technology can be used to fabricate custom-designed bio-inspired sensor with desired frequency response characteristics for its ease in manufacturing components with tunable geometry and dimensions. A parametric study of bio-inspired sensors with three different inner gap sizes are considered in this section and the model details (Model Ps, Model Bs1 and Model Bs2) are given in Table 4.4. By recording the base reaction force from a swept sine analysis, the frequency response characteristics of the inner beam base reaction to the harmonic displacement and harmonic velocity input are shown in Figure 4.16a and Figure 4.16b respectively. The observed cut-off frequencies are around 5 Hz, 20 Hz and 50 Hz for the three models with varying inner gap sizes (i.e., 0.6 mm, 1.5 mm and 2.4 mm) respectively, indicating that the increasing inner gap size shifts the bio-inspired sensor's cut-off frequency to a higher value. A comparison with corresponding Maxwell models also shows increasing size of inner gap reduces the dashpot damping coefficient in the equivalent Maxwell unit (see Table 4.5).

4.3.4.2 Effect of fluid viscosity

The other parameter that may affect the frequency response feature of the bio-inspired sensor is the viscous fluid property. The viscosity, which is the property arising from collision between neighboring particles in a fluid, play an important role

93

in the FSI analysis. Since the response of the bio-inspired is dependent on the interaction between inner beam and surrounding fluid, the values of chosen viscosity will directly impact on the sensor response. Three viscous coefficient values (i.e., 1 Pa-sec, 10 Pa-sec and 100 Pa-sec) are considered for the bio-inspired sensor models.. The effect of different viscosity coefficients on the frequency response curves are shown in Figure 4.17a and Figure 4.17b respectively. In the low frequency range, the frequency response curves of the base reactions to the displacement and velocity input have amplified gain with increasing fluid viscosity values. Meanwhile, the gain of these three curves with different fluid viscosity values remains relatively unchanged in the higher frequency range.

The other effect of the fluid viscosity is demonstrated by the change of the bio-inspired sensor's cut-off frequency in its frequency response curves. Specifically, the cut-off frequency values of the bio-inspired sensor are read from the figure to be around 2 Hz, 20 Hz and 200 Hz for fluid viscosity coefficients of 1 Pa-sec, 10 Pa-sec and 100 Pa-sec, respectively. A comparative study of these discrete frequency response points derived from FSI simulation and the corresponding curves from Maxwell model fitting, indicates the effect of the viscosity coefficient change could be equivalently represented with the damping coefficient change in the Maxwell unit (see Table 4.5).

### 4.3.4.3 Effect of shear layer

Since the shear layer in the sensor configuration is intended to accommodate the shear deformation, rubber-like material is chosen in this study. Commonly-used rubber-like 3D printable material has the Young's modulus ranging from 1 MPa to 10

MPa. To investigate the stiffness effect, another higher stiffness material (E = 100 MPa) is also chosen in this parametric study.

The frequency responses to the harmonic displacement and harmonic velocity excitation at the outer case top surface are shown in Figure 4.18a and Figure 4.18b. It can be seen that the response frequency curves of the first two rubber-like models almost overlap with each other. Even with a higher stiffness value (E = 100 MPa), the difference between these response curves is still small. Hence, for the studied material range, the shear layer material is not considered to have a major effect on the bio-inspired sensor's frequency response characteristics.

*4.4 Conclusion*

In this chapter, based on the configuration of the octopus's macula/statolith system, a simplified 2D macula/statolith model is used to simulate the frequency response of the kinocilia bundle. The findings in the simulation indicate that the dynamic response behavior of the kinocilia bundle could be affected by its geometry, which provides the inspiration for the bio-inspired sensor design. The bio-inspired sensor consists of a number of 3D printed components, viscous fluid and a strain sensing element. The following parametric studies on the bio-inspired sensor reveal the effects of varying the three control design parameters (inner gap size, fluid viscosity and shear layer material) on the frequency response characteristics of the concerned bio-inspired sensor. Through a comparative study with the Maxwell unit, it is also concluded that different inner gap sizes and fluid viscosity coefficient have significant impacts on the frequency response characteristics of the bio-inspired sensor and the sensor could be described by an equivalent Maxwell unit.

Table 4.1 Material property of the macula/statolith model in FSI simulation study

|  | Young's Modulus (Pa) | Density (kg/m$^3$) |
|---|---|---|
| Kinocilia bundle (solid) | 9.0e4 | 1,300 |
| Statolith (solid) | 2.0e10 | 2,000 |
|  | Viscosity (Pa-sec) | Density (kg/m$^3$) |
| Endolymph fluid | 0.003 | 1,000 |

Table 4.2 Parameters of the macula/statolith models in FSI simulation study

| Model | Inner gap (μm) | Outer gap (μm) | Tilt angle ( ° ) | Displacement excitation amplitude (μm) |
|---|---|---|---|---|
| Pk* | 0.33 | 1.00 | 0 | 0.001 |
| Ak1 | 0.80 | 1.00 | 0 | 0.001 |
| Ak2 | 1.33 | 1.00 | 0 | 0.001 |
| Bk1 | 0.33 | 0.30 | 0 | 0.001 |
| Bk2 | 0.33 | 2.00 | 0 | 0.001 |
| Tk | 0.80 | 1.00 | 20 | 0.001 |

* Pk is the reference model

Table 4.3 Material property of 3D printing materials used for bio-inspired sensor simulation study

| Material | Young's Modulus (MPa) | Poisson Ratio |
|---|---|---|
| Engineering Plastic | 2500.0 | 0.35 |
| Soft Material (e.g., silicone rubber) Type 1 | 10.0 | 0.45 |
| Soft Material Type 2 | 1.0 | 0.45 |

Table 4.4 Parameters of the bio-inspired sensor design model for FSI simulation study

| Model | Inner gap (mm) | Fluid viscosity (Pa-sec) | Young' modulus of shear layer material (Pa) | Applied displacement amplitude (mm) |
|---|---|---|---|---|
| Ps* | 1.5 | 10 | 1.0e7 | 1.00 |
| As1 | 1.5 | 10 | 1.0e7 | 0.50 |
| As2 | 1.5 | 10 | 1.0e7 | 0.25 |
| Bs1 | 0.6 | 10 | 1.0e7 | 1.00 |
| Bs2 | 2.4 | 10 | 1.0e7 | 1.00 |
| Cs1 | 1.5 | 1 | 1.0e7 | 1.00 |
| Cs2 | 1.5 | 100 | 1.0e7 | 1.00 |
| Ds1 | 1.5 | 10 | 1.0e6 | 1.00 |
| Ds2 | 1.5 | 10 | 1.0e8 | 1.00 |

Ps* is the reference model


Table 4.5 Parameters of the equivalent Maxwell model bio-inspired sensor design

| Model | Spring stiffness $k$ (N/m) | Damping coefficient $\eta$ (N*s/m) |
|---|---|---|
| Ps | 0.105 | 3.0e-4 |
| As1 | 0.105 | 3.0e-4 |
| As2 | 0.105 | 3.0e-4 |
| Bs1 | 0.090 | 2.5e-3 |
| Bs2 | 0.150 | 1.3e-4 |
| Cs1 | 0.195 | 3.2e-5 |
| Cs2 | 0.105 | 3.0e-3 |
| Ds1 | 0.105 | 3.0e-4 |
| Ds2 | 0.090 | 2.5e-4 |
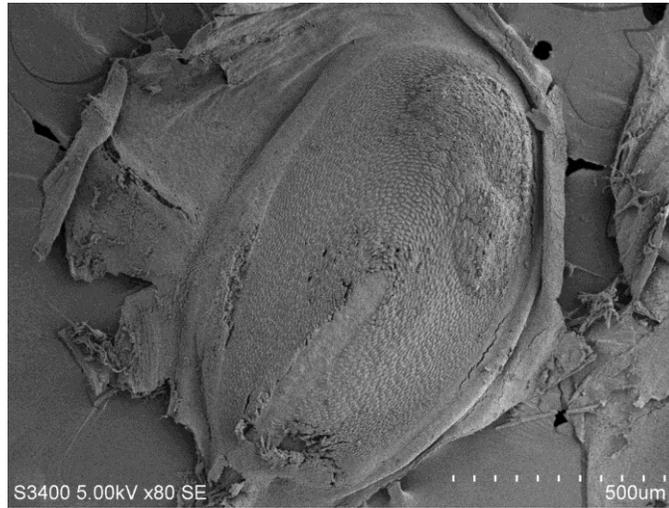
(a)
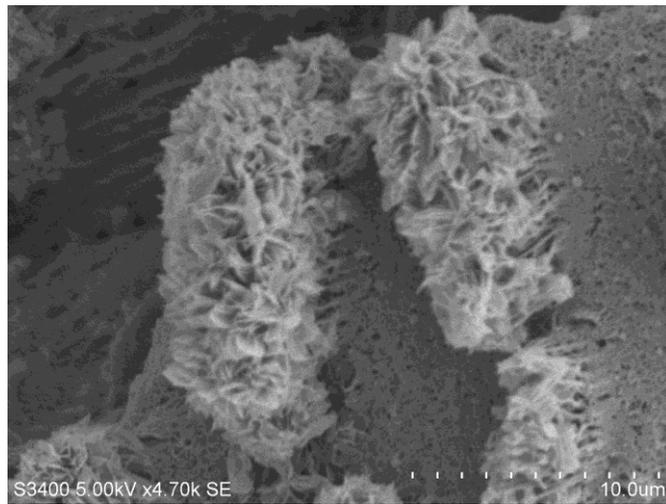


(b)

Figure 4.1 Morphology study of kinocilia bundle in the macula of *Octopus vulgaris*:
(a) macula epithelium after removing the statolith; (b) kinocilia bundles wrapped by
the residual statolith (courtesy of Professor Jiakun Song, Shanghai Ocean University,
China)
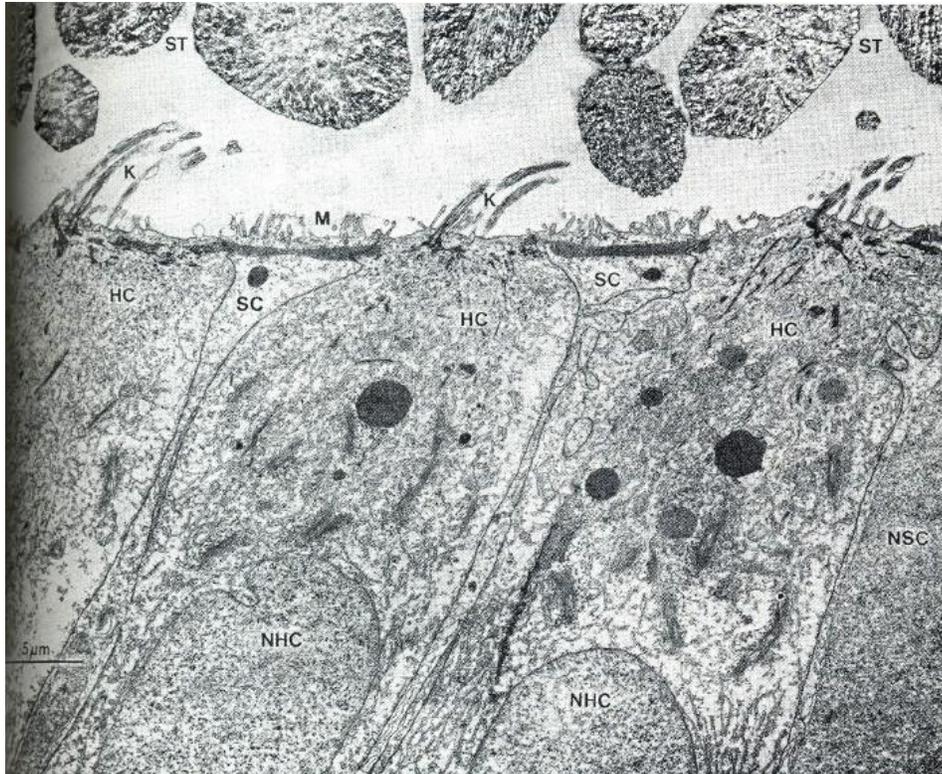
Figure 4.2 Transverse section through the macula of the statocyst of *Loligo vulgaris*. HC = hair cell; K = Kinocilia bundle; M = Microvilli; NHC = nucleus of hair cell; NSC = nucleus of supporting cell; SC = supporting cell; ST = statoconia. (Budelmann, 1979)
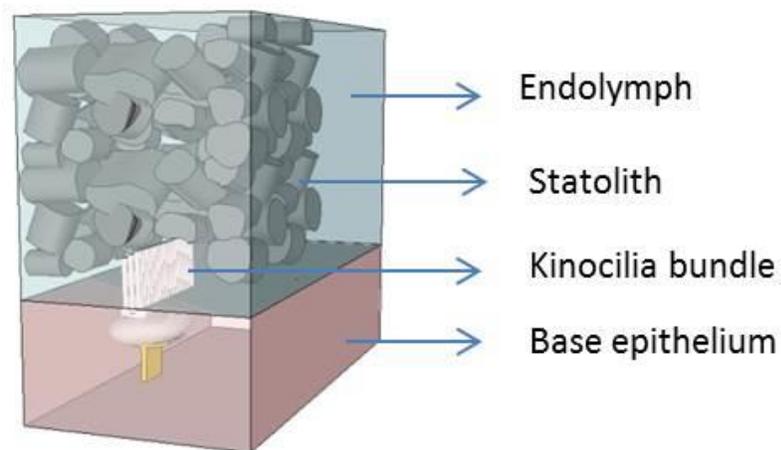


Figure 4.3 Schematic illuastration of the kinocilia bundle and its surrounding environment
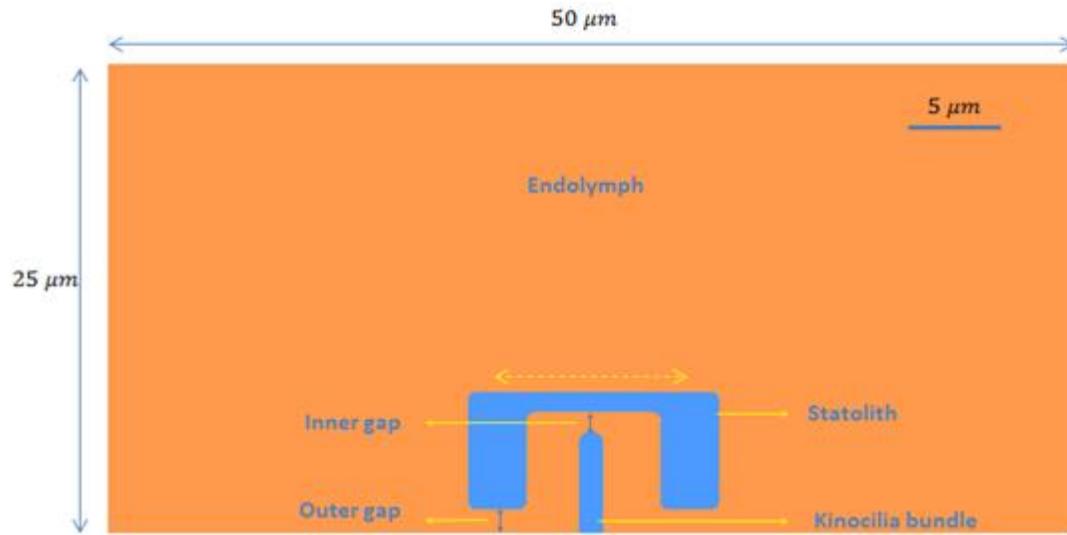
(a)
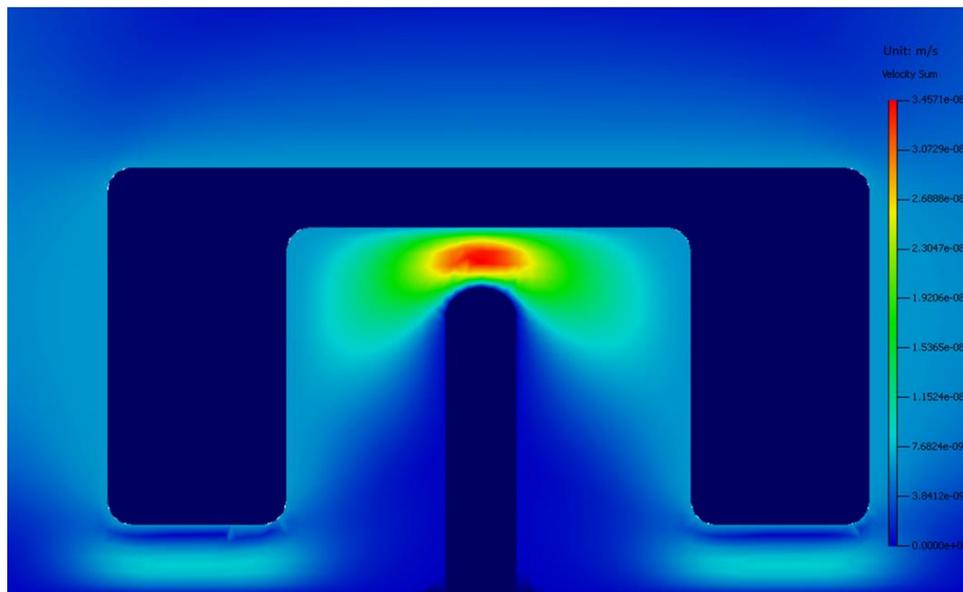


(b)

Figure 4.4 Simplified FSI numerical model (created and analyzed using the FSI software – INTESIM) of the kinocilia bundle interaction with statolith in the macula/statolith system of cephalopod (termed as macula/statolith model hereafter): (a) model dimensions and geometry; (b) contour plot of velocity distribution of the endolymph flow when the statolith is about to move away from its initial position
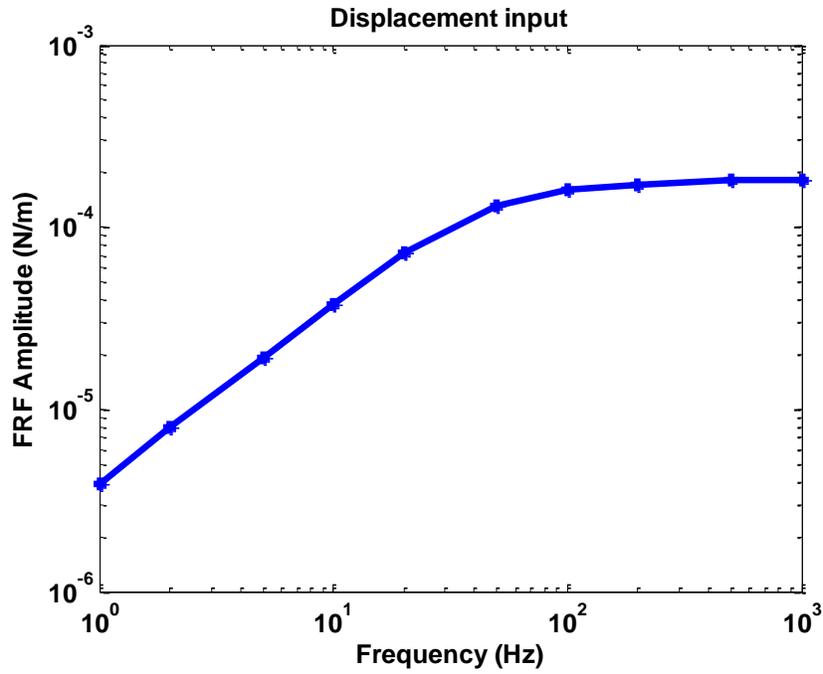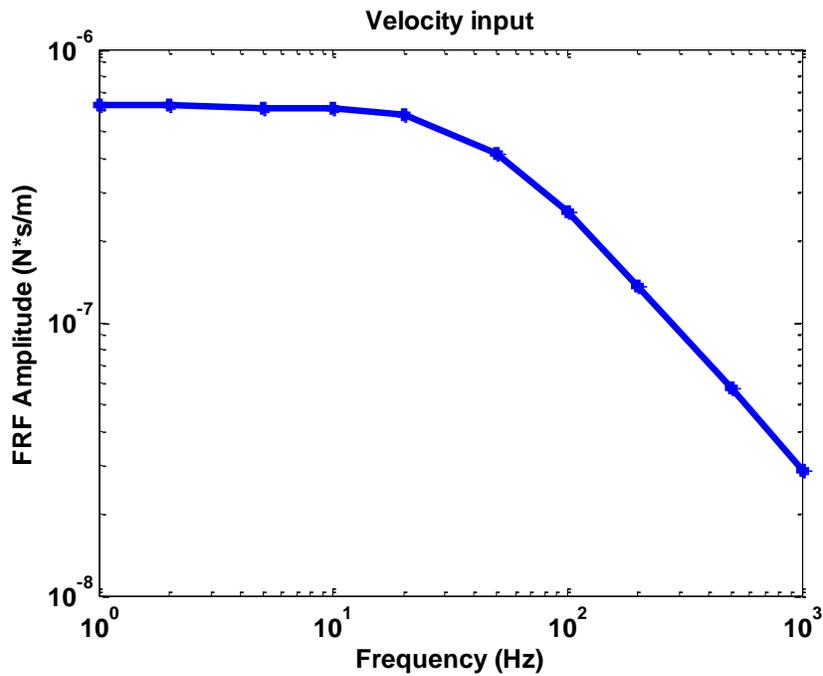
Figure 4.5 Frequency response of reference macula/statolith model derived from FSI simulation: (a) kinocilia bundle base reaction force to statolith displacment excitation; (b) kinocilia bundle base reaction force to statolith velocity excitation
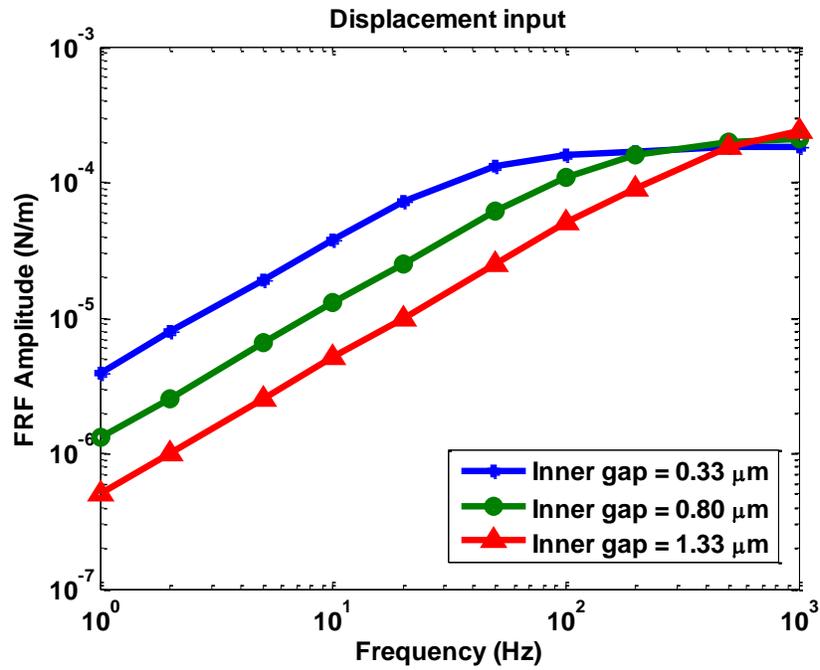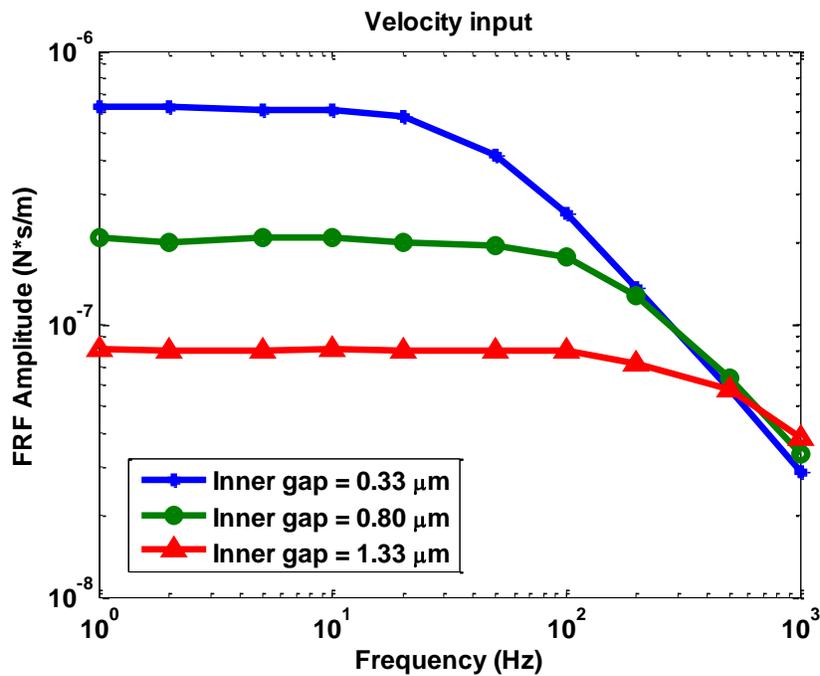
Figure 4.6 Frequency response of macula/statolith models with three inner gap sizes derived from FSI simulation: (a) kinocilia bundle base reaction force to statolith displacement excitation; (b) kinocilia bundle base reaction force to statolith velocity excitation
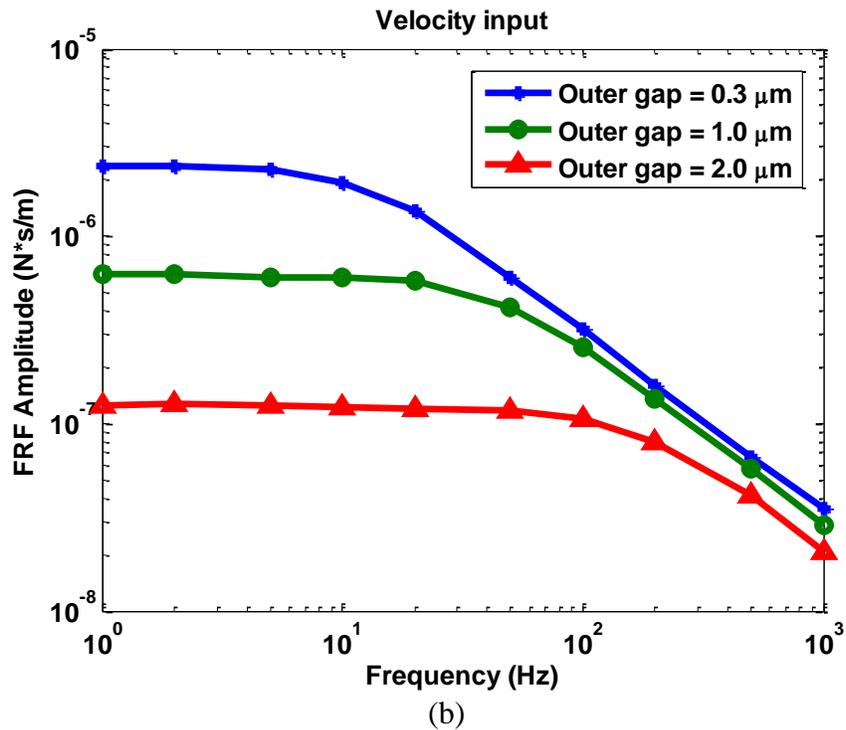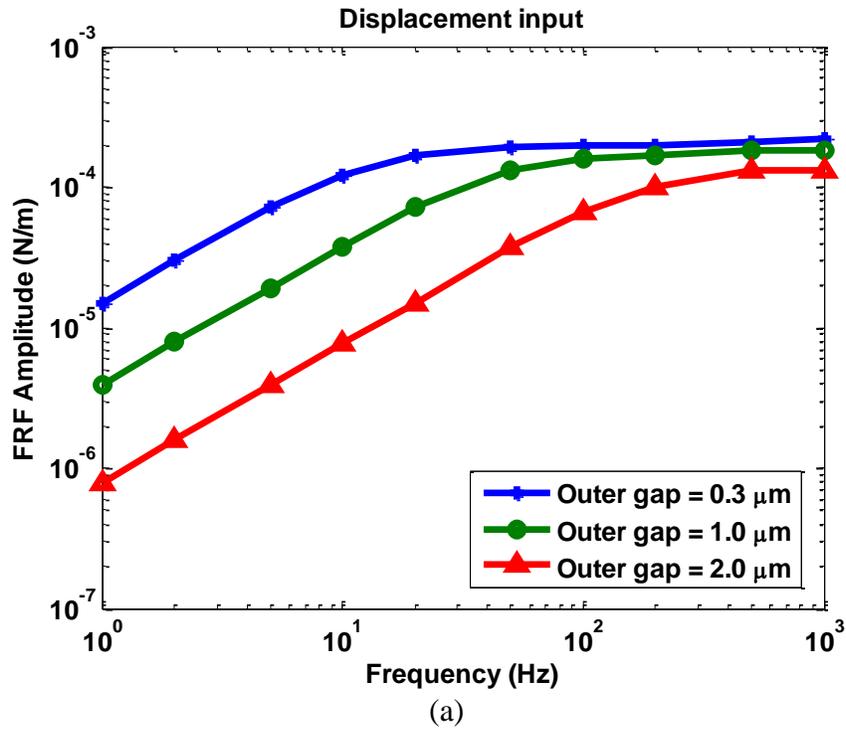
Figure 4.7 Frequency response of macula/statolith model with three outer gap sizes derived from FSI simulation: (a) kinocilia bundle base reaction force to statolith displacement excitation; (b) kinocilia bundle base reaction force to statolith velocity excitation
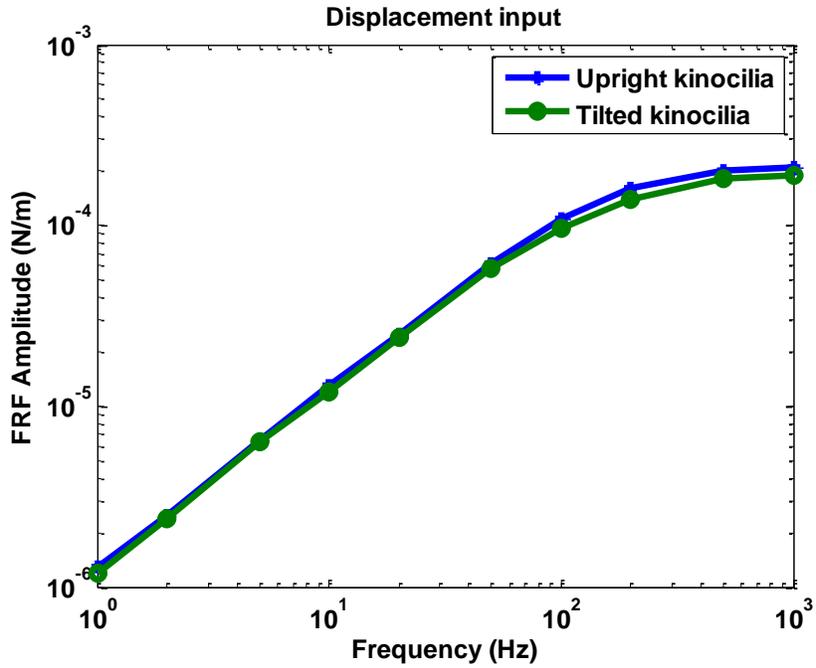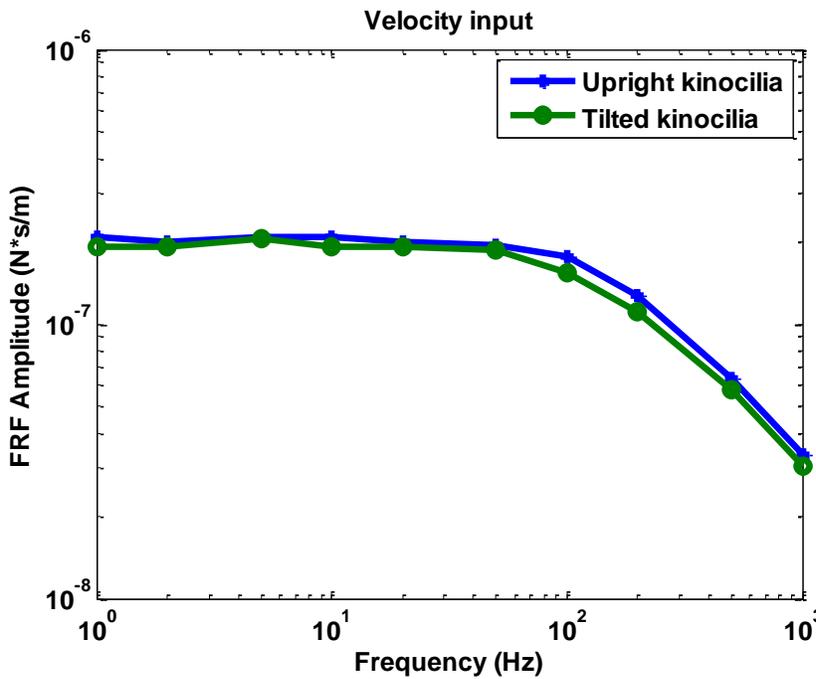
Figure 4.8 Frequency response of macula/statolith models with upright kinocilia and tilted kinocilia bundle (tilt angle = 20°) derived from FSI simulation: (a) kinocilia bundle base reaction force to statolith displacement excitation; (b) kinocilia bundle base reaction force to statolith velocity excitation
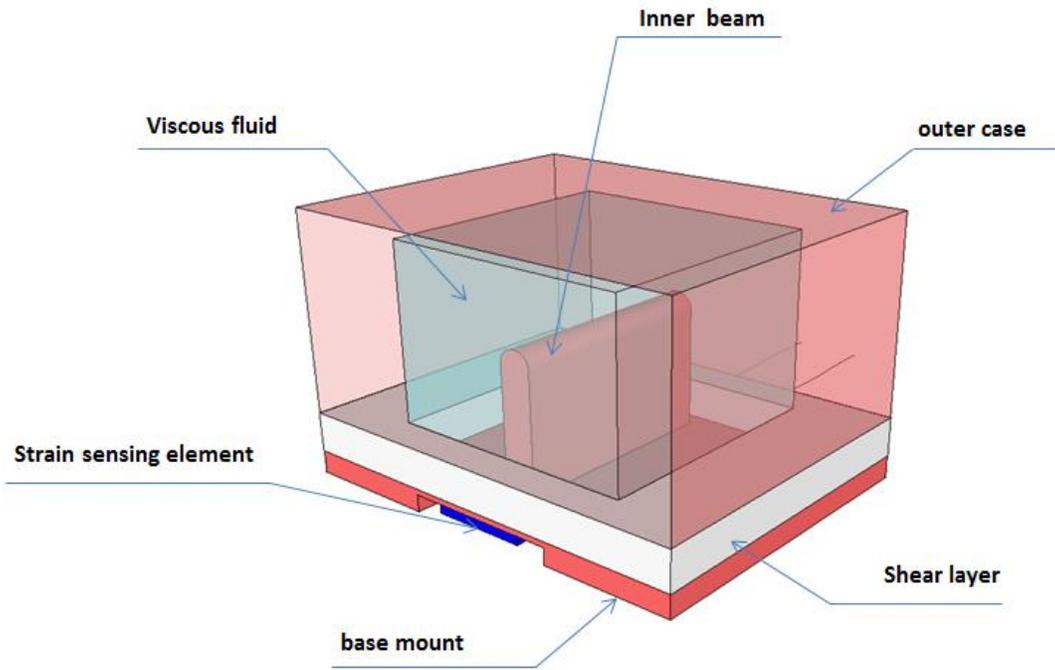
Figure 4.9 Schematic illustration of the proposed bio-inspired vibration sensor design
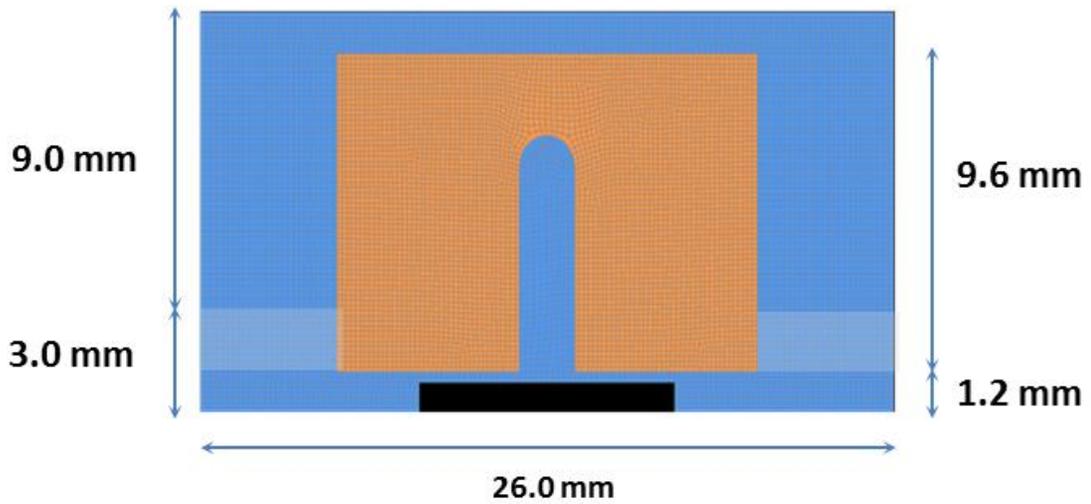


Figure 4.10 Simplified FSI numerical model of the bio-inspired sensor design created and analyzed in FSI software - INTESIM
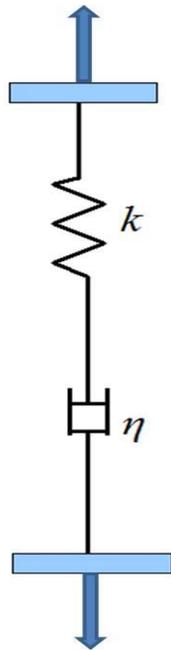
Figure 4.11 Illustration of Maxwell unit model ($k$ = the spring stiffness; $\eta$ = the dashpot's damping coefficient)
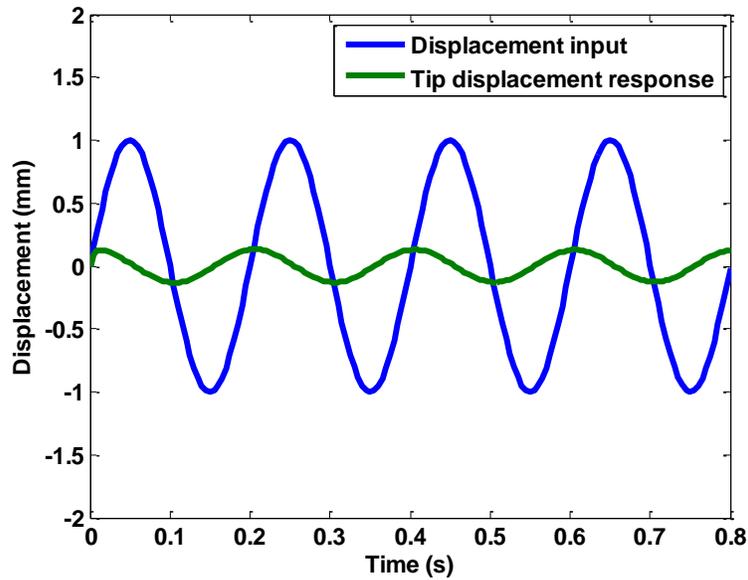


Figure 4.12 Time histories of inner beam tip deflection under harmonic displacement excitation with an excitation frequency of 5 Hz at sensor top
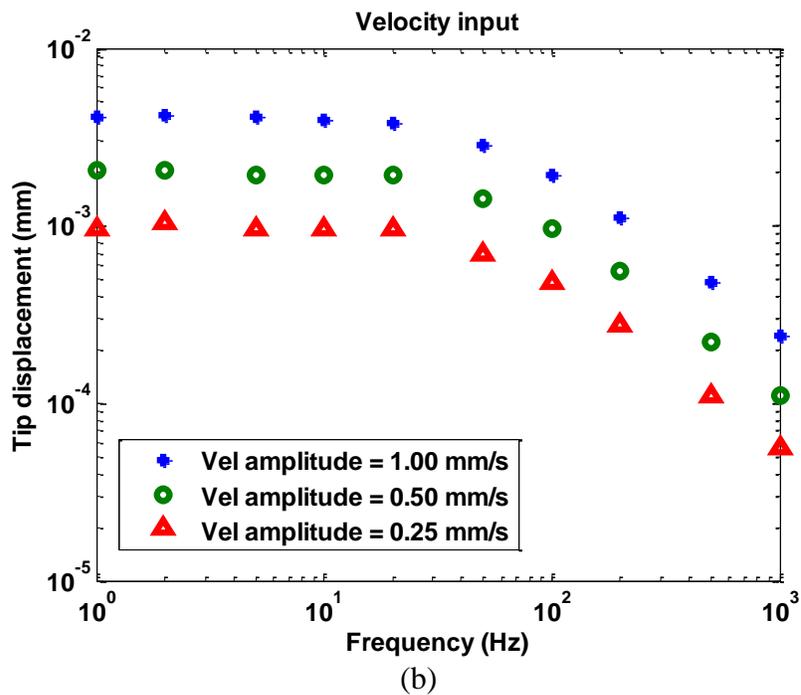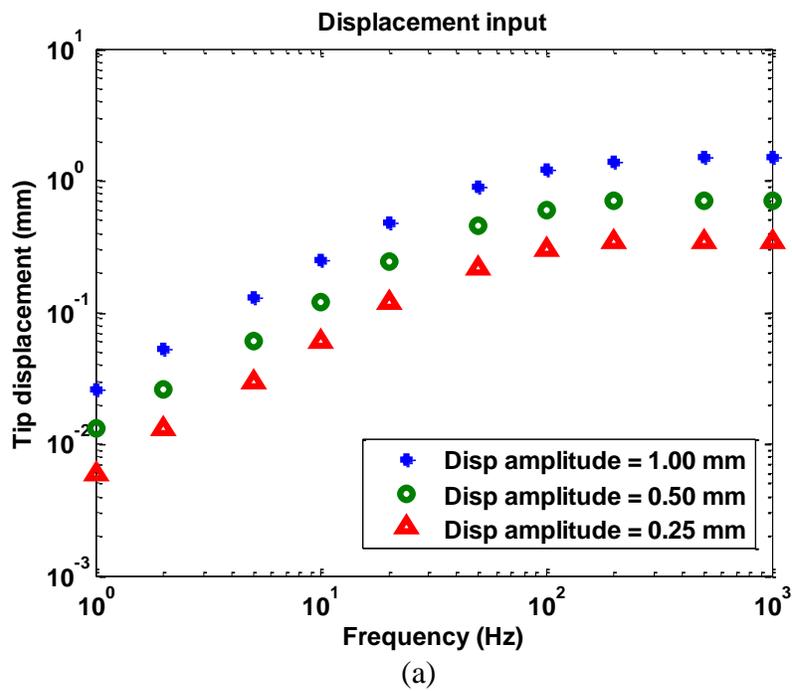
Figure 4.13 Frequency response of bio-inspired sensor under harmonic excitation with different stimulus amplitudes: (a) inner beam tip displacement to harmonic constant displacement at sensor top; (b) inner beam tip displacement to harmonic constant velocity excitation at sensor top
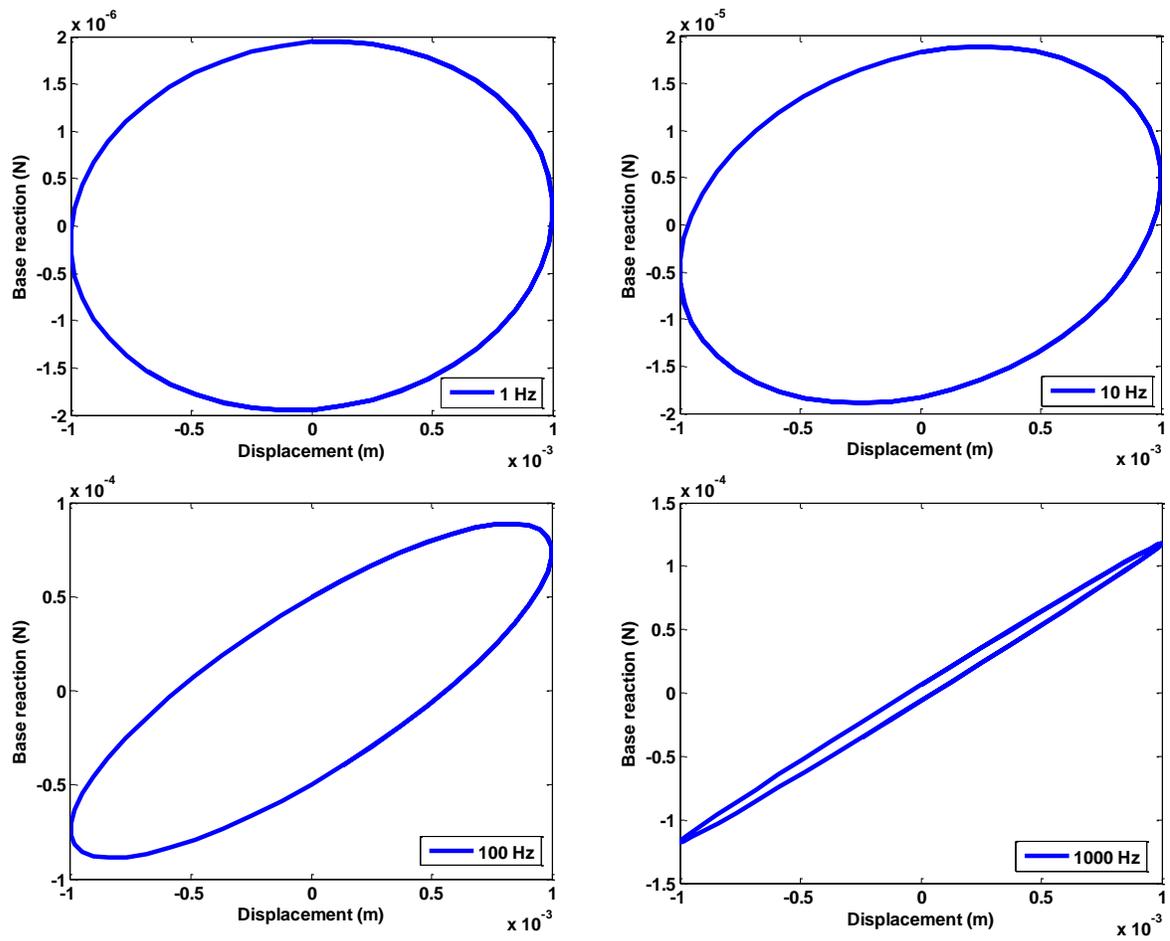
(a)

Figure 4.14 (continued)

1 Hz

10 Hz

100 Hz

1000 Hz

(b)
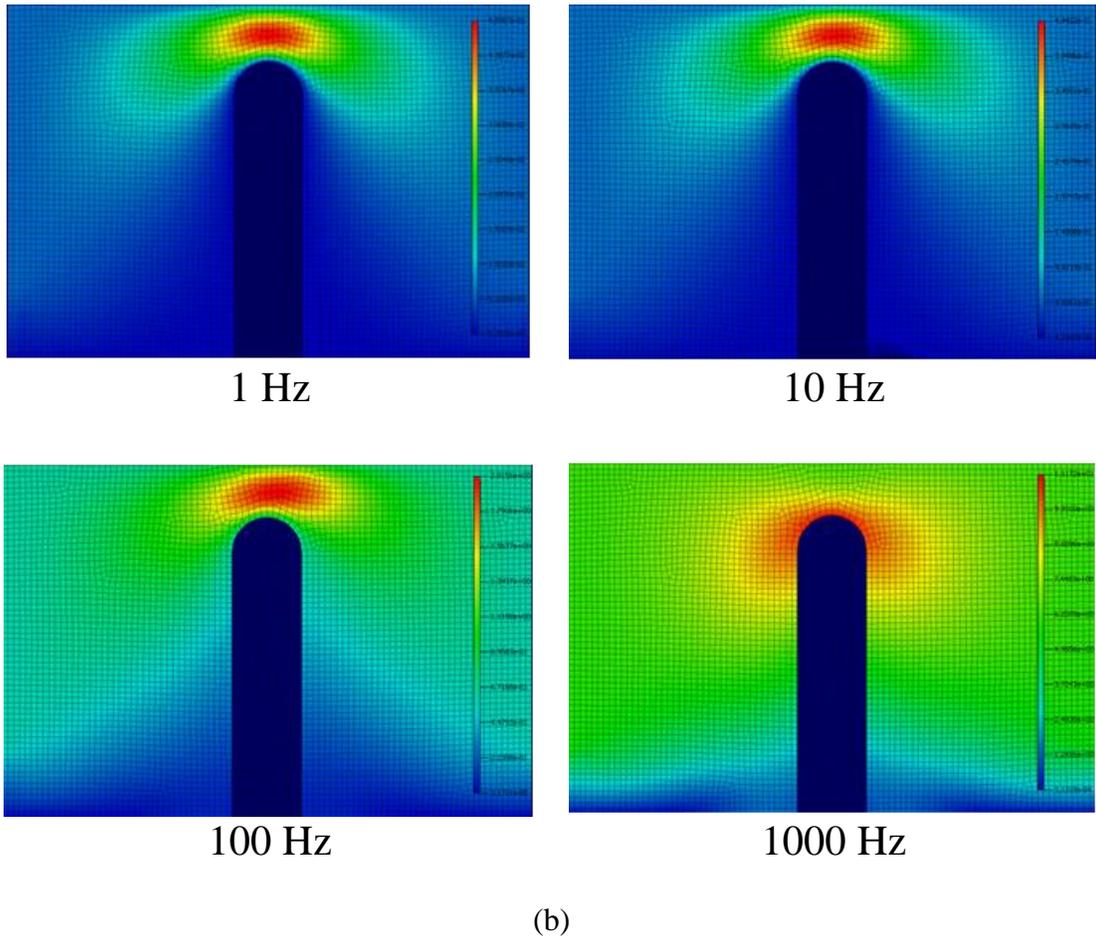
Figure 4.14 Response of reference bio-inspired sensor under harmonic displacement excitation with excitation frequency of 1 Hz, 10 Hz, 100 Hz and 1000 Hz respectively: (a) hysteresis loops; (b) contour plot of fluid velocity distributions in the bio-inspired sensor when the outer case is about to move away from its initial position
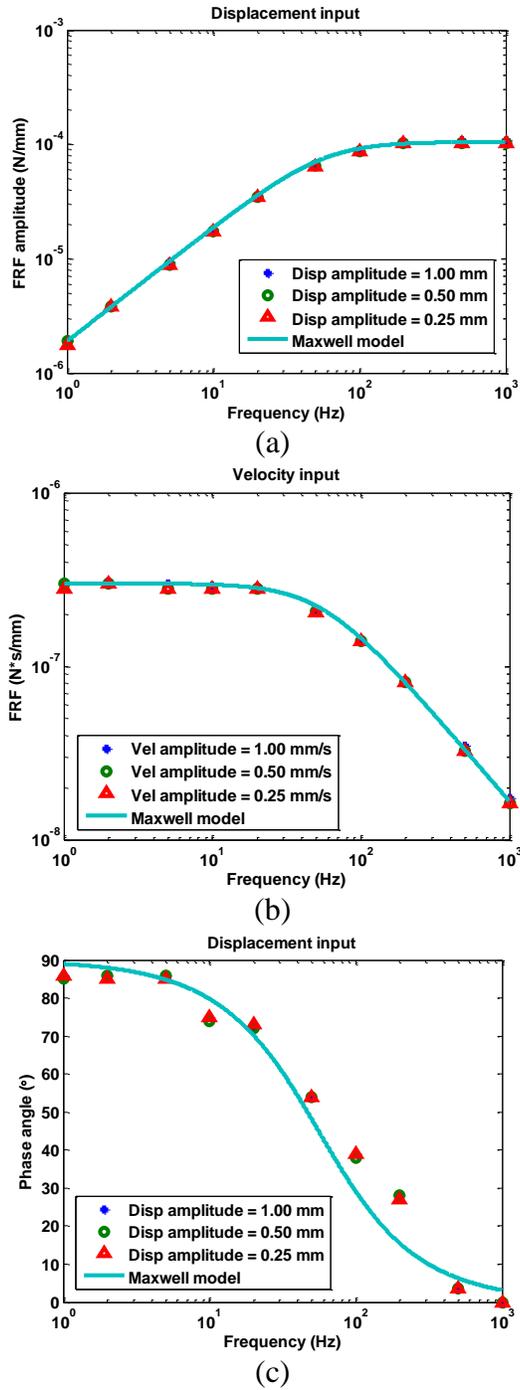
Figure 4.15 Frequency response of the bio-inspired sensor under different stimulus (harmonic excitation at outer case top) amplitudes (dots derived from FSI simulation; solid line from equivalent Maxwell model prediction): (a) base reaction force to constant amplitude harmonic displacement excitation; (b) base reaction force to constant harmonic velocity excitation; (c) phase angle to constant amplitude harmonic displacement excitation
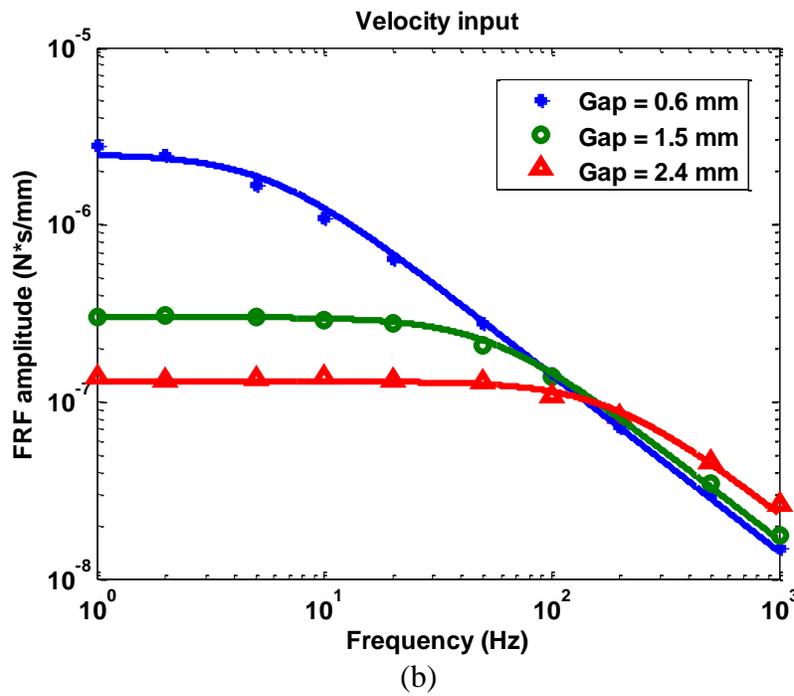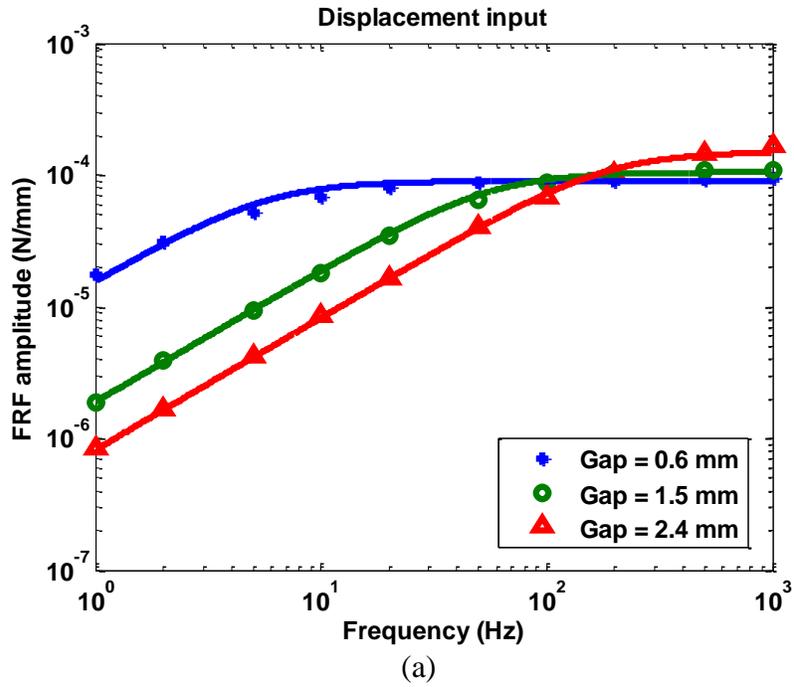
Figure 4.16 Frequency response of the bio-inspired sensor with three gap sizes (dots derived from FSI simulation; solid line from equivalent Maxwell model prediction): (a) base reaction force to constant amplitude harmonic displacement excitation; (b) base reaction force to constant harmonic velocity excitation
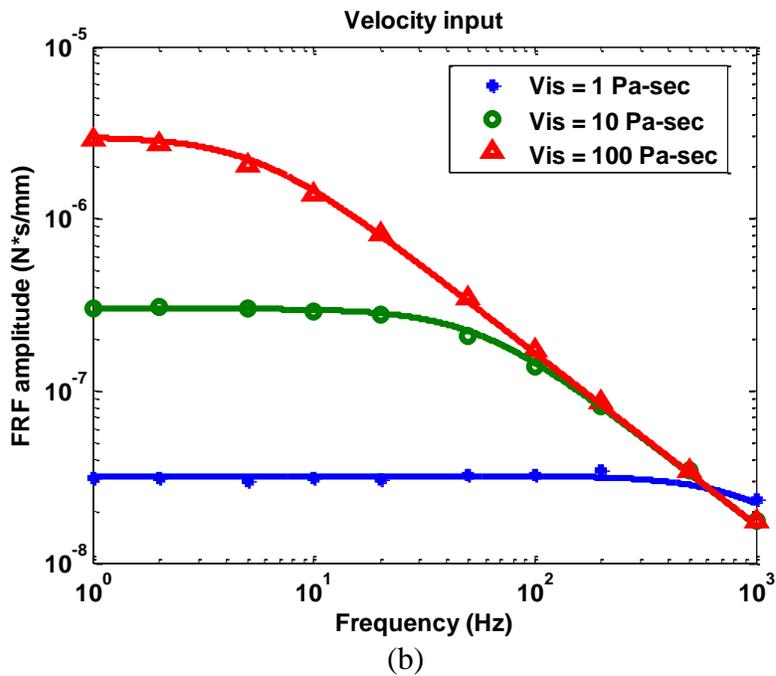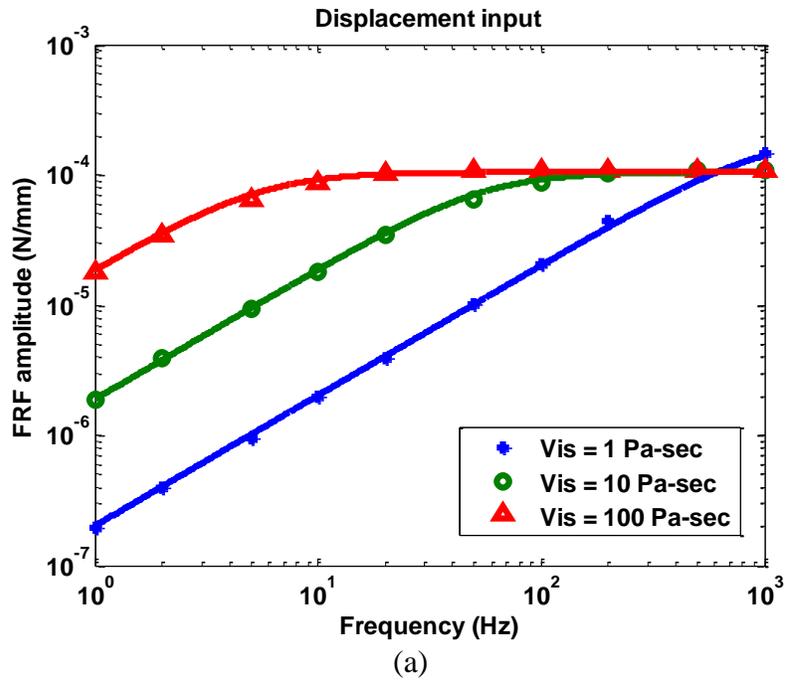
Figure 4.17 Frequency response of the bio-inspired sensor with three fluid viscosity coefficient values (dots derived from FSI simulation; solid line from equivalent Maxwell model prediction): (a) base reaction force to constant amplitude harmonic displacement excitation; (b) base reaction force to constant harmonic velocity excitation
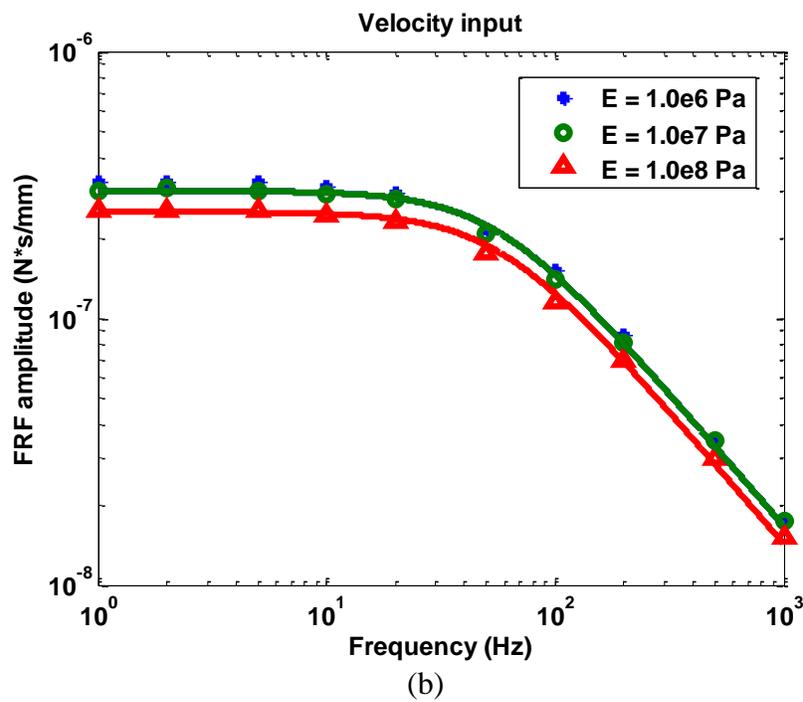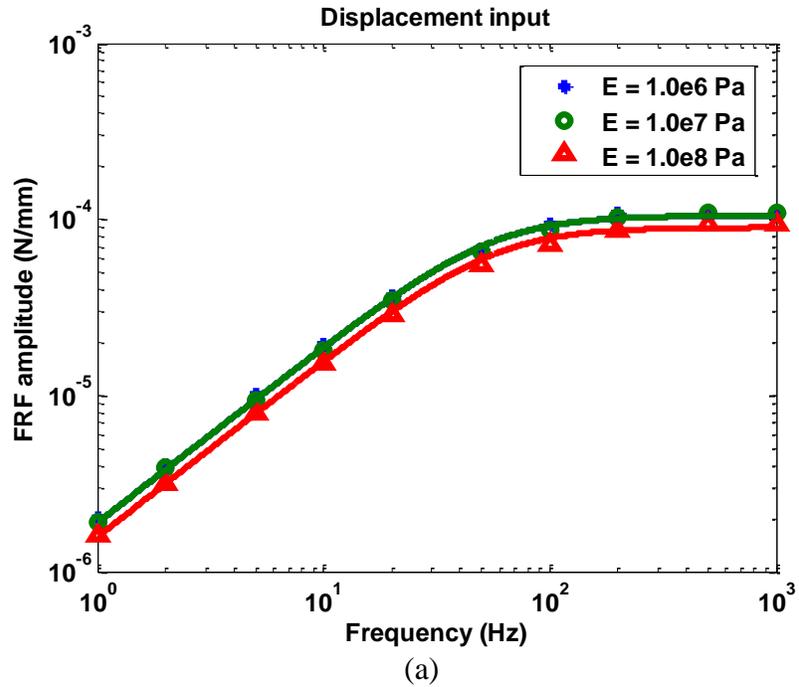
Figure 4.18 Frequency response of the bio-inspired sensor with three values for shear layer material's Young Modulus (dots derived from FSI simulation; solid line from equivalent Maxwell model prediction): (a) base reaction force to constant amplitude harmonic displacement excitation; (b) base reaction force to constant harmonic velocity excitation

# Chapter 5: Experiment study on the bio-inspired sensor

## 5.1 Introduction

The frequency response characteristics of the bio-inspired sensor design were studied in Chapter 4 by 2D FSI numerical simulation and Maxwell model. In this chapter, the bio-inspired sensor design is further investigated through prototype fabrication and experimental testing. The prototype sensor was designed and fabricated in the lab, which is comprised of 3D printed plastic (ABS) components, a shear layer made of silicone gel, filling silicone oil and the piezoelectric patch based dynamic strain sensing element. For the testing part, shake table test was conducted to experimentally examine the dynamic response behavior of the prototype sensor, and the experimental test results were compared with the numerical simulation data. Lastly, the sensing mechanism of the bio-inspired sensor is described, and two potential applications (jerk sensor and velocity sensor) of the bio-inspired sensor are presented.

## 5.2 Prototype sensor design and fabrication

### 5.2.1 Sensor design

The dimensions of the prototype sensor are shown in Figure 5.1a. Based on the location of the strain sensing element, illustrations of the two alternative sensor designs with slight difference (Type A and Type B) are schematically shown in Figure 5.1b and Figure 5.1c, respectively. In Design A, the piezoelectric strain

sensing element was bonded to the side surface of the inner beam; in Design B, the piezoelectric strain sensing element was placed on the bottom surface of the base mount. All other parts of the sensor keep the same dimension and configuration in both designs, which are described as follows.

The ABS components, indicated as red in Figure 5.1, include three main parts: the base mount, the inner beam and the outer case. In this experimental study, the inner beam and the base mount were separately printed and connected with each other using M-Bond 200 adhesive, while the base mount and outer case were connected together through the use of a silicone gel based shear layer.

The shear layer, highlighted in grey color in Figure 5.1, is designed to accommodate the relative motion between the outer case and base mount through its shear deformation when the sensor is excited. Ecoflex 0020, a platinum-catalyzed silicone, was used for the shear layer. This silicone gel material has a Young's modulus of 5.5e4 Pa. Because of the low Young's modulus value, the shear deformation between the base mount and the outer case will be the dominant deformation mode in the sensor when being excited.

A key part in the bio-inspired sensor is the silicone oil that fills the fluid chamber surrounding the inner beam. The silicone oil, highlighted in turquoise color in Figure 5.1, is used to engage the outer case and inner beam through FSI. Specifically, when the sensor is in operation, the relative movement between the outer case and the base mount of the sensor would pressurize the filling silicone oil and the FSI would deflect the inner beam. The strain in the deflected inner beam was then measured by the piezoelectric strain sensing element. In the experiment, a low

115

viscosity silicone oil (viscosity coefficient = 0.346 Pa-sec) was used for ease of handling. The silicone oil was injected into the chamber with a syringe and sealed at the top of the outer case. Due to silicone oil's electrically non-conductive property, the immersed piezoelectric strain sensing element and wires were allowed to function properly without short circuit problem in Design A.

The prototype sensor was subsequently assembled for testing by connecting the ABS components and silicone gel shear layer, bonding the piezoelectric patch strain sensing element and injecting the silicone oil.

### 5.2.2 3D printing of ABS components

3D printing refers to the process of making a three-dimensional object from a digital model primarily through additive manufacturing process in which successive layers of material are laid down under computer control. Dependent on the materials, several different 3D printing technologies are available for use: fused deposition modeling (FDM), granular materials binding, laminated object manufacturing and so on. Among them, the fused deposition modeling provides an economical and proved 3D printing approach to fabricating 3D objects from thermoplastics like ABS. In this study, the FDM based 3D printer (model #: Maker-Bot Replicator, as shown in Figure 5.2a) were used.

To fabricate the plastic components of the sensor, the ABS components were first designed using the software Google SketchUp, as shown in Figure 5.1. After uploading these model files into the Maker-Bot Replicator companion software, the 3D printer fed the ABS filament to the heated extrusion nozzle head. By depositing the extruded ABS filament through the nozzle, the component was formed layer by

layer with hardened ABS material. Such processes can be clearly seen in Figure 5.2b, where the highest degree near the nozzle head is around 150 Celsius degree and the temperature of the platform is 130 Celsius degree. The printed ABS components are shown in Figure 5.2c.

### 5.2.3 Piezoelectric strain sensing element

#### 5.2.3.1. Sensing principle of piezoelectric film

The piezoelectric strain sensing elements are used to transform the strain signal into an electric charge signal. Without loss of generality, it is assumed here that piezoelectric strain sensing film is only subjected to unidirectional strain in its film plane. The dielectric displacement D3 is related to the generated electric charge by the following relationship,

$$q = \iint D_3 \mathrm{d}A_3 \tag{5-1}$$

where $\mathrm{d}A_3$ is the differential electrode area in the 1-2 plane of the piezoelectric strain sensing film. The electric charge generated by the sensor can be expressed as,

$$q = d_{31} Y_C b_C \int_{lc} \varepsilon_1 dl \tag{5-2}$$

where $Y_C$ is the Young's modulus of the piezoelectric paint, $l_c$ and $b_c$ are length and width of the piezoelectric paint sensor, respectively.

Piezoelectric strain sensing films (e.g., PZT wafer or PVDF film) are usually bonded to the surface of the host structure. Piezoelectric strain sensing films can be used as strain sensor or strain rate sensor due to the electro-mechanical coupling property of piezoelectric materials. Lee and O'Sullivan (1991) investigated piezoelectric strain rate gages used for measuring dynamic friction force variation and

in strain rate control of flexible structure. When a current amplifier is used as the signal conditioning circuit, the voltage output of the sensor can be expressed as,

$$V_{out}(t) = -R_f \dot{q} = -R_f d_{31} Y_C b_C \int_{lc} \dot{\varepsilon}_1 dl \qquad (5\text{-}3)$$

the output voltage is proportional to the integral of time derivative of the in-plane strain in 1-direction.

Sirohi and Chopra (2000) studied the behavior of PZT and PVDF strain sensor over a frequency range of 5 Hz to 500 Hz. In their work, a typical piezoelectric patch strain sensor is considered as a parallel plate capacitor, which stores the electric charge generated by the piezoelectric sensor when mechanical deformation is applied. A charge amplifier was used in their investigation as the signal conditioning circuit to measure the charge generated by the sensor, which is proportional to the mechanical strain at the host structure location of the sensor. Thus, if a charge amplifier is connected to the sensor electrode, the output voltage is

$$V_{out}(t) = -\frac{q}{C_f} = -\frac{d_{31} Y_C b_C}{C_f} \int_{lc} \varepsilon_1 dl \qquad (5\text{-}4)$$

In this study, piezoelectric sensing films are used as a strain sensor and a charge amplifier is designed and described in next section.

5.2.3.2. Material properties of piezoelectric sensing element

One of the commonly used piezoelectric materials for sensor applications is Lead Zirconate Titanates (PZTs), which are solid solutions of lead zirconate and lead titanate and often doped with other elements to obtain specific properties (Sirohi & Chopra, 2000). While individual manufacturers of PZT use proprietary formulas for each composition, in general, PZT-5 is NB-doped, PZT-6 is Cr-doped, PZT-7 is La-

118

doped, and PZT-4 is Fe-doped (Tressler et al., 1998). In this study, PZT-5A based piezoelectric ceramic disc (model #: SMD05T02S412 STEMINC) was used in the bio-inspired sensor and its material properties are provided in Table 5.1. The 5 mm (diameter) x 0.2 mm (thickness) PZT-5A disc was first bonded to a backing film using epoxy, followed by connecting two lead wires to PZT-5A disc's two electrodes, as shown in Figure 5.3. With the lead wires connected to the preamplifer circuit, the strain signals measured by the piezoelectric sensing element could be acquired using a voltage receiving data logger.

### 5.2.4 Signal conditioning circuit

Generally speaking, the charge signal from the piezoelectric sensing element is weak and would attenuate rapidly along a transmission cable. In order to improve the signal-noise-ratio of the weak signal, a conditioning circuit is needed to amplify the signal and filter the noise (Zhou, 2013). The first part of the conditioning circuit in this study was a custom designed 45-dB amplification circuit using a LM6171 op amp – high speed low power low distortion voltage feedback optional amplifier. In order to enhance the signal-to-noise ratio, the second part of the conditioning circuit, a low-pass analogue filter was connected to the amplifier. As the shake table tests were operated in the low frequency range (10 Hz to 200 Hz), the high cut-off frequency of this filer was set as 2 kHz. During the tests, the 12-V DC power supply for the conditioning circuit was bypassed by placing a 0.1-μF capacitor to provide signal stability. The schematics of the conditioning circuit are shown in Figure 5.4a, and circuit boards are displayed in Figure 5.4b and 5.4c. To further reduce the

environmental electromagnetic noise, a steel box was used to provide the EMI shield for the conditioning circuit.

### 5.3 Experiment testing and results discussion

#### 5.3.1 Test setup for sensor characterization

The sensing characteristics of the prototype bio-inspired sensor were investigated with shake table tests in this study. The test setup for the sensor characterization experiment is shown in Figure 5.5a, in which the APS 400 dynamic shaker was the shake table, and an Agilent function generator was connected to the power amplifier of the shake table system in order to provide the sinusoidal input signal. The shake table is an open-loop system that does not have feed-back control of its motion. In order to achieve the desired excitation levels (i.e., 0.02 g, 0.05 g or 0.1 g in acceleration) at different frequencies (varied between 10  and 200 Hz), an ICP accelerometer (model #: 393B04, sensitivity factor = 1015 mV/g) made by PCB PIEZOTRONICS company was employed to measure the shake table's acceleration amplitude.

In the experimental test, when the shake table vibrated in harmonic motion, the base mount of the prototype bio-inspired sensor which is fixed to the shake table surface would be set into motion accordingly. The lag in the response of the outer case from the base mount's movement resulted in the FSI interaction in the sensor and the signals collected from the piezoelectric strain sensing element mounted to the prototype sensor were acquired by a digital oscilloscope (Tektronix Model # TDS2000).

5.3.2 Test results

The first test series was to investigate the effect of the filling silicone oil on the sensor response. Four sensors were fabricated in the lab for this test series, including two prototype sensors of Design A with or without silicone oil, and two prototype sensors of Design B with or without silicone oil. The acceleration amplitude of the shake table motion was set as 0.05 g and the frequency range was varied from 10 to 200 Hz.

Based on the test data (see Figure 5.6), it can be concluded that the silicone oil has a similar effect on sensors of both Design A and Design B. Specifically, for the cases without silicone oil, no FSI would occur and the inner beam's deformation would be isolated from the outer case movement, and thus the sensor response only depends on the dynamic characteristics of the inner beam. Because the inner beam is a very stiff cantilever structure with a much higher natural frequency (over 1000 Hz) compared with the excitation frequency applied to the shake table, the deflection of the inner beam remains low. Consequently, the signal measured by the piezoelectric strain sensing element shows a relatively flat frequency response, which is consistent with the classical vibration theory. On the contrary, with the silicone oil filling the fluid chamber in the bio-inspired sensor, the response signal is seen to vary substantially with the dynamic excitation frequency, as shown in Figure 5.6. It is seen that with growing frequency, the response signal initially increases below 100 Hz and then starts to drop above 100 Hz, while the peak response occurs around 100 Hz.

The second test series was designed to check the linearity of the bio-inspired sensor's response to varying excitation acceleration amplitudes. In this test series, the

prototype bio-inspired sensors of both Design Type A and Design Type B were filled with silicone oil (model # 350 cst Chemistry Store). Three acceleration amplitude levels (0.02 g, 0.05 g and 0.10 g) were specified for the shake table test and the frequency response curves of the prototype bio-inspired sensors are displayed in Figure 5.7. Over the tested frequency range, the prototype sensor's frequency response curves under all three acceleration amplitude levels show an increasing trend below 100 Hz and decreasing trend above 100 Hz, (100 Hz is believed to be the resonant frequency of the prototype sensor). It is also observed that the sensor response's magnitude is linearly proportional to the amplitude of stimulating acceleration.

In the third test series, a steel mass that weighs 10.5 g was placed atop the prototype sensor of Design Type B. The excitation acceleration amplitude was set as 0.05 g for the shake table test and the test results are shown in Figure 5.8. It is seen that adding the mass to the prototype sensor shifts the peak frequency of the sensor from 100 Hz to 50 Hz. Compared with the frequency response of the prototype sensor of Design Type B (see Figure 5.7b), the peak response amplitude is twice greater than the sensor without the additional steel mass, and the response amplitude variation near the peak response is also sharper, suggesting reduced damping ratio due to increased mass.

5.3.3 Numerical simulation study

To better understand the experiment test results, numerical models of the prototype bio-inspired sensor were created for FSI analysis and are presented in this section. The two critical factors that affect the response behavior of the prototype bio-

inspired sensor are: the movement of outer case as a second order dynamic oscillator and the coupling of the inner beam's deflection with the outer case through FSI effect. In this section, numerical simulation studies were conducted to examine the effect of these two factors.

The dynamic response behavior of the outer case part of the prototype bio-inspired sensor was studied by running a model created using generic finite element analysis software – ANSYS Workbench V14. In this numerical model, silicone oil was not included in the sensor's inner fluid chamber to exclude the FSI effect, while other parts of the sensor model are identical to the tested prototype sensors including dimensions and material property. From the modal analysis of the numerical model (see Figure 5.9), the first deformation mode of the numerical model is close to the shear deformation along the excitation direction and the corresponding frequency is 105 Hz. The second mode is close to the shear deformation in the other orthogonal direction perpendicular to the excitation and the third mode is the torsional mode. Since the excitation direction in the experiment is the same as the shear direction in the first mode, the second and the third mode deformations are considered trivial response in the experiment. The fourth mode of the prototype sensor, with a frequency of 260 Hz, is shown as a vertical movement mode in Figure 5.9d. Considering the excitation frequency ranging from 10 Hz to 200 Hz in the experiment test, the fourth mode and higher modes contribution to the sensor response are assumed to be negligible. Therefore, the frequency response of the prototype bio-inspired sensor subjected to base excitation in the experiment test would be dominated by the first mode response, and a SDOF second order dynamic oscillator

with its natural frequency at 105 Hz, can be utilized to describe the dynamic response behavior of the outer case's motion when subjected to base excitation.

According to the structural dynamics theory, the displacement frequency response function of this SDOF second order dynamic oscillator can be expressed as,

$$u_{t0}(\omega) = \frac{\ddot{x}_g(\omega)}{\omega_n^2} \frac{1}{\sqrt{[1-(\omega/\omega_n)^2]^2 + [2\zeta(\omega/\omega_n)]^2}} \tag{5-5}$$

Where $\ddot{x}_g(\omega)$ is the base excitation acceleration; the natural and excitation frequencies are $\omega_h = $ sqrt ($k/m$) (k is the stiffness and m is the mass of oscillator) and $\omega$ respectively; $u_{t0}(\omega)$ is the relative displacement amplitude between the outer case top surface and base; the viscous damping ratio is denoted as $\zeta$. Assuming $\ddot{x}_g = 0.05g$ and damping ratio $\zeta$ value 0.6 (estimated with experimental data), the frequency response of the second order dynamic oscillator between the relative displacement and base excitation is shown in Figure 5.10.

After determining the dynamic response behavior of the outer case part, an equally important task is to understand the relationship between the outer case movement and the inner beam's deformation due to FSI effect. This task is accomplished in this study by creating and running analysis of a 2D FSI numerical model in the FSI software INTESIM (see Figure 5.11). In this sensor model, the bottom of the base mount is fixed and the top of the sensor was pushed and pulled cyclically with a sinusoidal displacement in the horizontal direction. The displacement transfer function, defined as the ratio between the outer case top displacement and the inner beam's free tip deflection, is used to study the coupling effect due to FSI. The numerical simulation results given in Figure 5.12 indicate that

the displacement transfer function is linear with excitation frequency. Quantitatively, the inner beam's tip displacement can be expressed as,

$$u_{i0}(\omega) = \bar{k}\omega \, u_{t0}(\omega) \tag{5-6}$$

where $u_i$ is the inner beam's tip displacement amplitude, $\bar{k}$ is a scaling factor equal to the slope of the displacement transfer function, $\omega$ is the frequency of the outer case motion, and $u_{t0}(\omega)$ is the displacement at the top of the sensor.

By convolving Equation 5.5 and Equation 5.6, the frequency response function of the inner beam's tip displacement in the prototype sensor is expressed as,

$$u_{i0}(\omega) = \frac{\ddot{x}_g(\omega)}{\omega_n^2} \frac{\bar{k}\omega}{\sqrt{[1-(\omega/\omega_n)^2]^2 + [2\zeta(\omega/\omega_n)]^2}} \tag{5-7}$$

Since the strain response signal measured at the inner beam of the prototype sensor is linearly proportional to the inner beam's tip displacement (inner beam is designed to deform linear elastically), Equation 5.7 provides the frequency response function that describes the dynamic response of the prototype bio-inspired sensor if the piezoelectric sensing element has a flat frequency response over the operation frequency range. By substituting the base acceleration and damping ratio values into Equation 5.7, a typical bio-inspired sensor's frequency response curve (assuming the strain sensing element has a flat frequency response) is shown in Figure 5.13 for base acceleration excitation with constant amplitude.

### 5.3.4 Comparison between experimental and simulation results

A comparison between the experimental test result and the simulated sensor frequency response will be very helpful in further our understanding of the sensor

behavior, which is presented in this section. By setting the natural frequency to 105 Hz (same as sensor's first modal frequency) and damping ratio as 0.6 (estimated from curving fitting of the experimental frequency response data) In Equation 5.7, typical bio-inspired sensor's frequency response curve is shown in turquoise color, overlapped with experiment data from the second test series in Figure 5.14. The experiment data is normalized by dividing by the amplitude of the base excitation acceleration. It is seen that the numerical model curve fit well with the experiment test data points, which reveals the peak response is controlled by the sensor's resonance peak at its natural frequency. Comparing the experimental data and the simulated curve shows that the frequency response of the sensor keeps increasing below its natural frequency and decreasing above the natural frequency.

In order to study the added mass' effect on the sensor response in the third test series, a numerical model was created in ANSYS Workbench V14 as shown in Figure 5.15. Because of the added mass at the sensor top, the natural frequency of the bio-inspired sensor is shifted from 105 Hz to 50 Hz while the modal deformation remains unchanged. Substituting the natural frequency with 50 Hz in Equation 5.3, the simulated result of the bio-inspired sensor also agrees well with the experimental data points in Figure 5.15. Through these comparisons, it is demonstrated that the experiment results can be explained by the described numerical model.

*5.4 Application of the bio-inspired sensor design*

5.4.1 Jerk sensor

The time derivative of acceleration, sometimes called a jerk, plays an important role in the vibration control (Miu & Bhat, 1991; Mizoshita et al., 1996;

Youn, 1996), ride comfort evaluation (Liu, 1999), and earthquake engineering (Yang, 2008; Tong & Lee, 1999). By using the prospective value of the jerk, it is seen that the control system can improve the response of the system and avoid excessive input of acceleration to the body (Fujiyoshi et al., 2002). In earthquake engineering, recent study shows the relationship between peak ground acceleration and peak ground velocity at near-source ground motion may be determined by the jerk, which could be used to analyze potential near-source characteristics (Yang, 2008).

The conventional method to determine jerk is to measure the acceleration and differentiate it with a differentiation circuit. The problem of this method is that it can cause large errors because of the amplified noise (especially at higher frequency) when the differentiation of the acceleration signal is made. In that case, a device that could directly measure the jerk is desirable. Based on the mechanics model in Equation 5.7, by substituting acceleration $\ddot{x}_g$ with $\ddot{x}_g = \dfrac{\dddot{x}_g}{\omega}$, the relationship between the inner beam deflection and jerk excitation at the sensor base can be expressed as,

$$u_{i0}(\omega) = \frac{\dddot{x}_g(\omega)}{\omega_n^2} \frac{\overline{k}}{\sqrt{[1-(\omega/\omega_n)^2]^2 + [2\zeta(\omega/\omega_n)]^2}} \tag{5.8}$$

When subjected to jerk excitation, typical frequency response curve of the bio-inspired sensor is derived from the above equation, as shown in Figure 5.17. It is seen that the bio-inspired sensor's response keeps at a constant level below its natural frequency and the amplitude of this flat response is proportional to the amplitude of jerk excitation (see Equation 5.8). These features indicate the bio-inspired sensor can be used as a jerk sensor whose operating frequency band is from DC to its natural

frequency if the strain sensing element has a flat frequency response over this frequency range.

### 5.4.2 Velocity sensor

By substituting acceleration $\ddot{x}$ with velocity expression $\ddot{x} = \omega \dot{x}$ in Equation 5.7, the relationship between the inner beam's displacement and the excitation velocity can be expressed in Equation 5.9.

$$u_{i0}(\omega) = \frac{\omega^2 \dot{x}_g(\omega)}{\omega_n^2} \frac{\bar{k}}{\sqrt{[1-(\omega/\omega_n)^2]^2 + [2\zeta(\omega/\omega_n)]^2}} \tag{5.9}$$

A typical frequency response under the velocity excitation is shown in Figure 5.18, in which a constant level occurs above the bio-inspired sensor's natural frequency. From the expression of Equation 5.9, it is seen that the amplitude of this constant level is proportional to the velocity's amplitude. Based on these features, the bio-inspired sensor can be used as a velocity sensor when the desired frequency band is above its natural frequency.

## 5.5 Conclusion

This chapter presents the experimental test results of the prototype bio-inspired sensor and prospective application as jerk sensor and velocity sensor. The fabrication process for the main parts of this sensor (ABS plastic components, silicone oil, silicone gel layer, and piezoelectric dynamic strain sensing element) and the subsequent assembling process demonstrates its potential advantages of ease in custom design. Depending on the locations of the piezoelectric sensing element, two designs (Design A and Design B) of this bio-inspired sensor were investigated through a series of shake table tests.

The comparison test between the sensors with and without silicone oil indicates the effect of the silicone oil, which facilitates the interaction between the ABS outer case and the inner beam through FSI. The experimental test of the prototype sensor subjected to base acceleration excitation with different amplitude levels suggests a linear relationship between the measured strain signal and the excitation acceleration amplitude at varying frequencies. The experimental test of the sensors with and without additional steel mass on the top manifests the natural frequency of this sensor could be easily changed by changing the top mass, which can be used to change the desired frequency bandwidth. Both Design A and Design B display similar frequency response trend as observed from these three test series.

A numerical model indicates the response of the bio-inspired sensor can be analytically determined by performing convolution of a second order dynamic oscillator's (the sensor without silicone oil) top displacement response and the transfer function of the inner beam deflection subject to the outer case motion. The comparison between this numerical model and experiment data shows this model could explain the sensor behavior observed in the shake table tests. Based on this study, two prospective sensor applications (jerk sensor and velocity sensor) are proposed.

Table 5.1 Properties of piezoelectric ceramic disc transducer
(model #: SMD05T02S412 STEMINC)

| Dimensions: | 5 mm (diameter) ✕ 0.2 mm (thickness) |
|---|---|
| Resonant frequency | 445 kHz +/- 5 kHz |
| Piezoelectric constant $d_{33}$ | 450e-12 m/v |
| Piezoelectric constant $d_{31}$ | -190e-12 m/v |
| Piezoelectric constant $g_{33}$ | 25.6e-3 Vm/N |
| Piezoelectric constant $g_{31}$ | -12.6e-3 Vm/N |
| Elastic constant $Y_{33}$ | 5.6e10 N/m$^2$ |
| Elastic constant $Y_{11}$ | 7.6e10 N/m$^2$ |
| Dielectric constant @ 1 kHz | 1850 |
| Dissipation factor @ 1 kHz | 1.2 % |
| Curie Temperature | 320 °C |
| Density | 7.8 g/cm$^3$ |
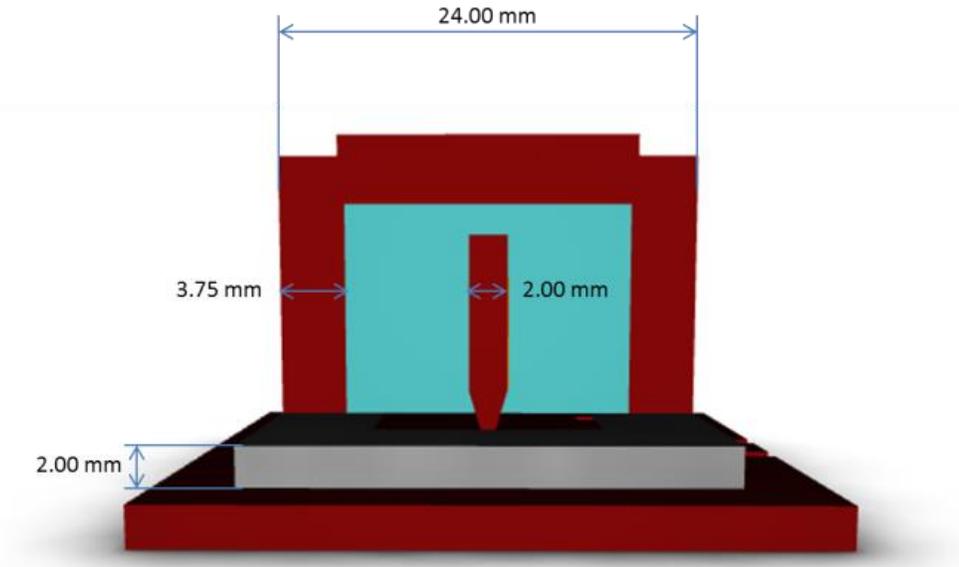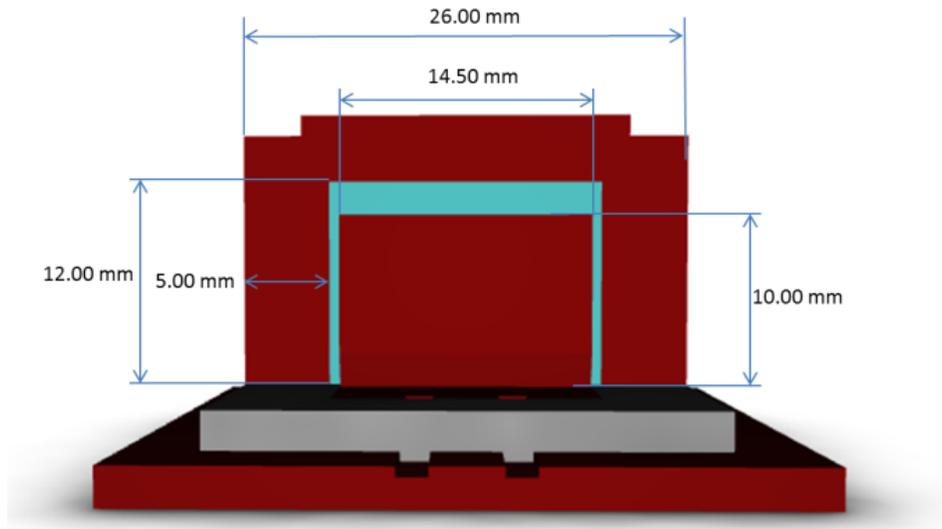
(a)

Figure 5.1 (continued)

(b)

Figure 5.1 (continued)

Silicone oil

Outer case

Silicone gel shear layer

PZT sensing element

Sealing cover

Filling cover

Silicone oil

Outer case

Silicone gel shear layer

Inner beam

PZT sensing element

Base mount
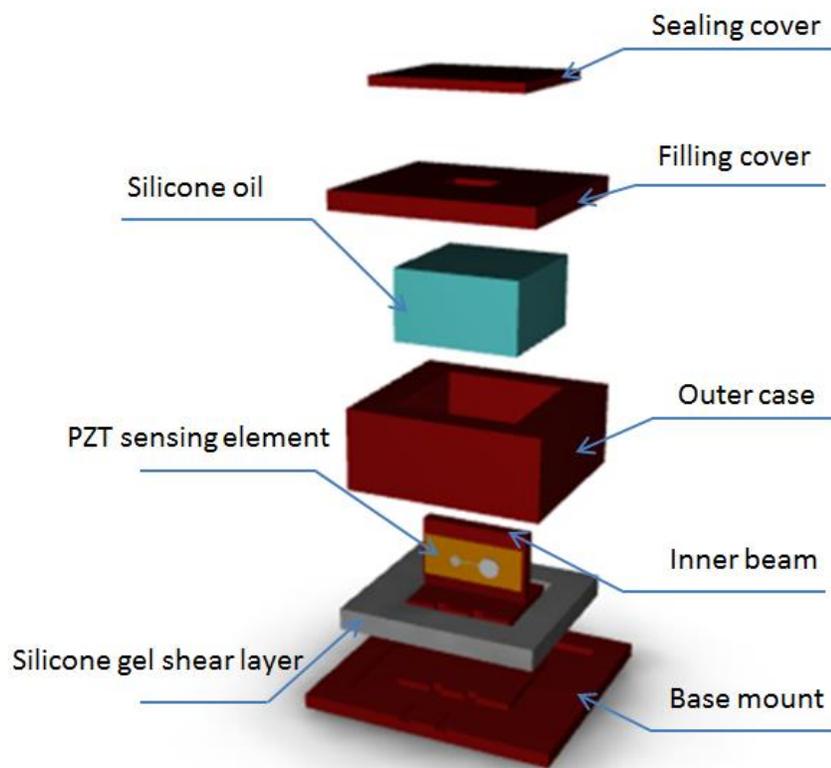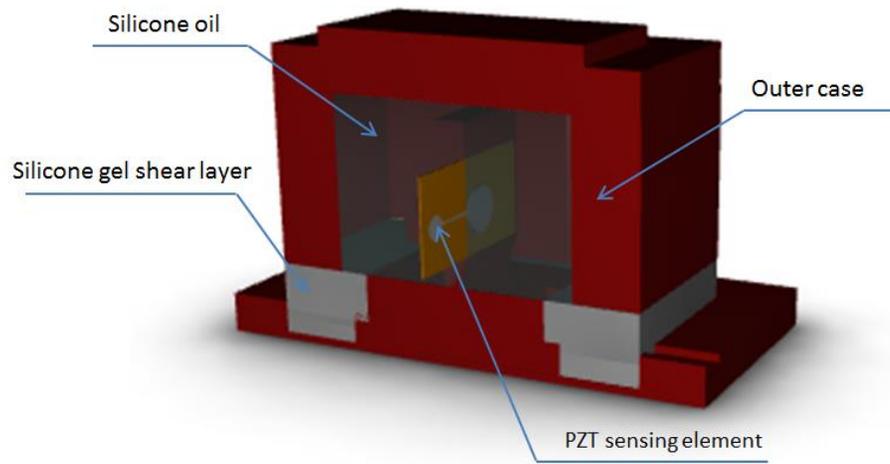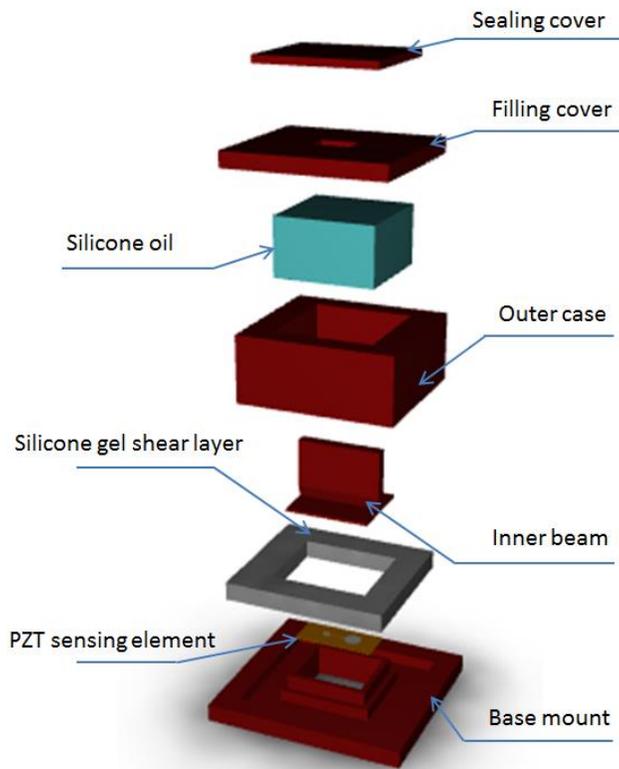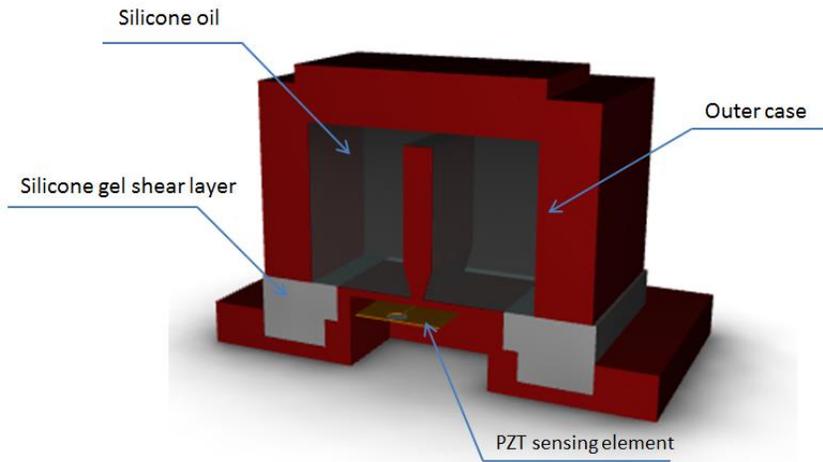
(c)

Figure 5.1 Schematics of the prototype bio-inspired motion sensor design: (a) section view and dimensions;  (b) sensor design of Type A; (c) sensor design of Type B
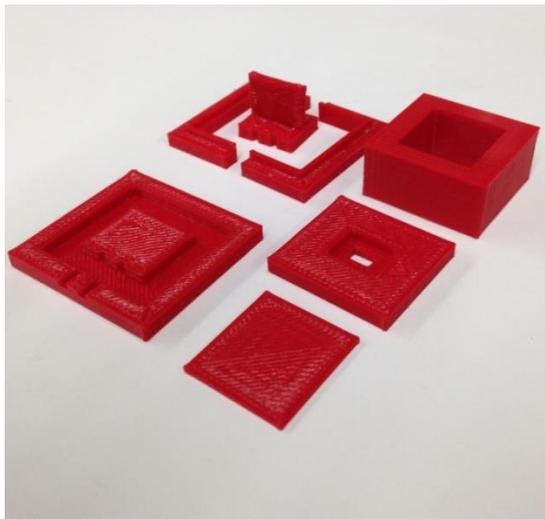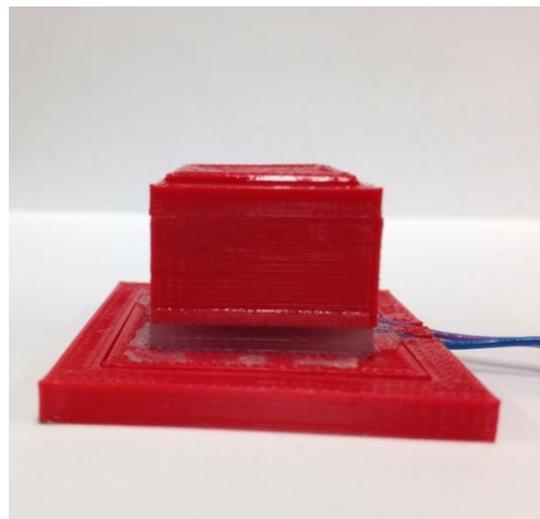
Figure 5.2 3D printing of prototype sensor parts: (a) MakerBot Replicator 3D printer; (b) thermal image of printing head in operation; (c) printed ABS sensor components before assembling; (d) close-up view of the assembled prototype sensor

(a)
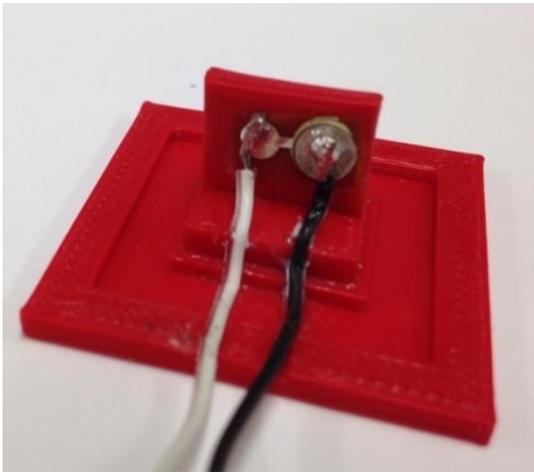


(b)



(c)

Figure 5.3 Piezoelectric strain sensing element in proposed sensor: (a) components of piezoelectric sensing element; (b) piezoelectric sensing element in design A; (c) piezoelectric sensing element in design B
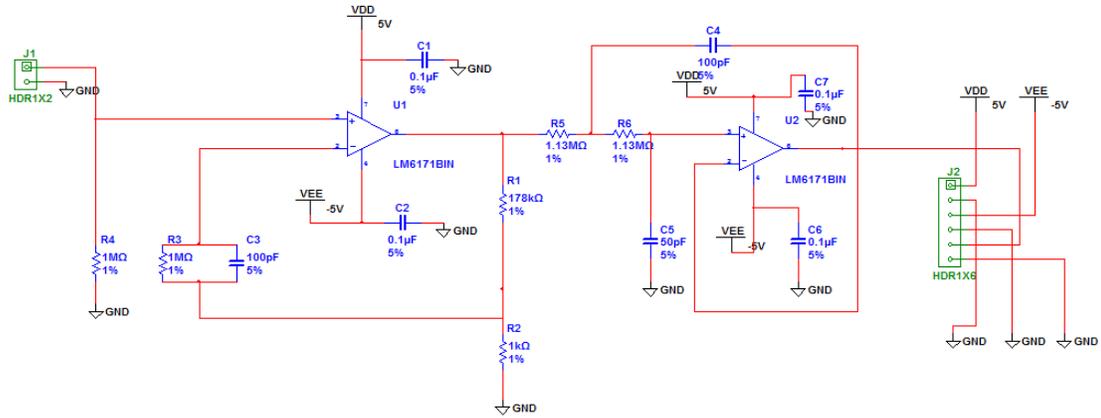
(a)
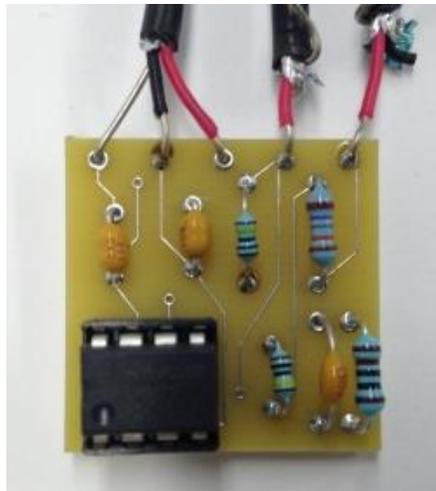


(b)
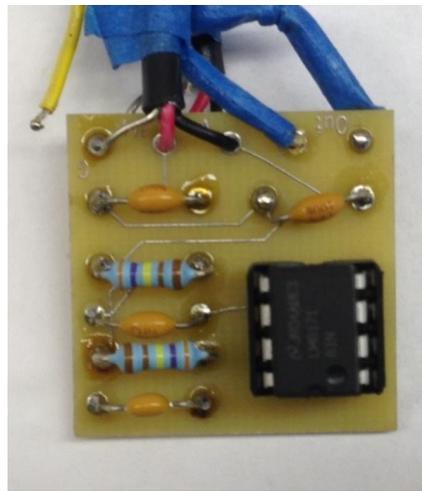


(c)

Figure 5.4 Signal conditioning (preamplifying and filtering) circuit for the prototype sensor: (a) conditioning circuit design; (b) 45 dB amplifier; (c) low-pass filter with a 2 kHz cutoff frequency
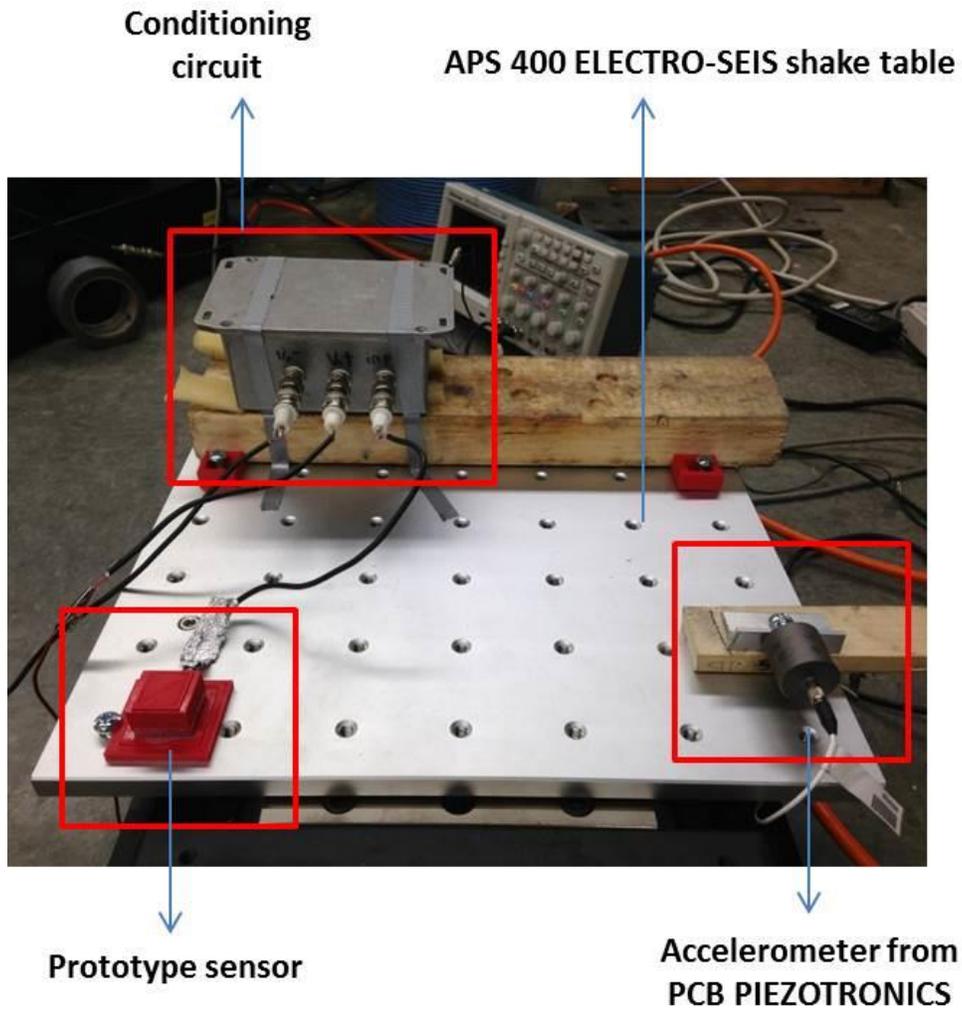
(a)

Figure 5.5 (continued)

40 Hz

80 Hz

110 Hz

150 Hz

(b)



(c)
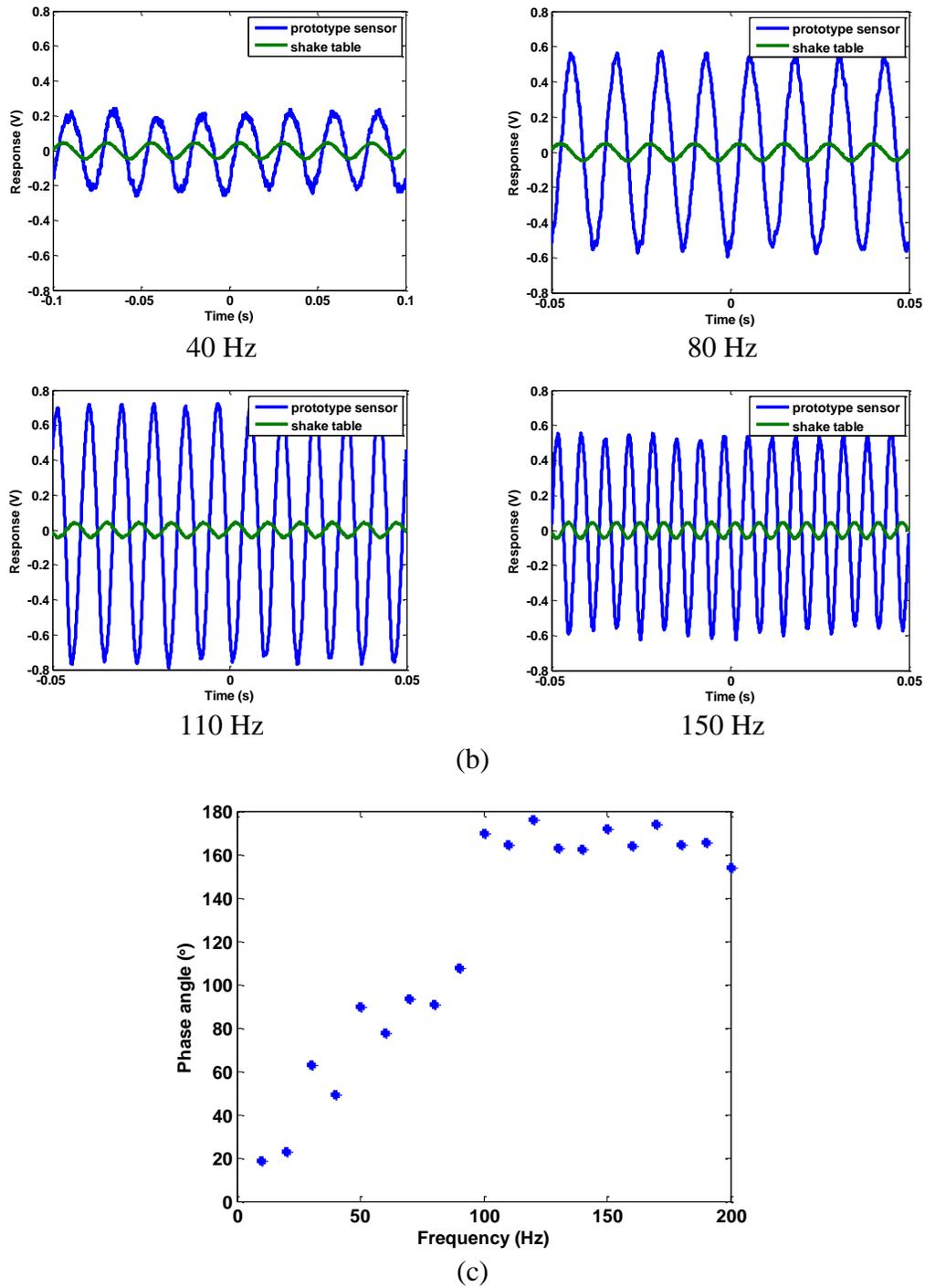
Figure 5.5 Experimental test on the prototype sensor: (a) test setup for sensor characterization with electrodynamic shake table; (b) time history response comparison between prototype sensor and shake table acceleration input (amplitude = 0.05 g) excitation; (c) phase angle between prototype sensor and input acceleration in sensor of Type A
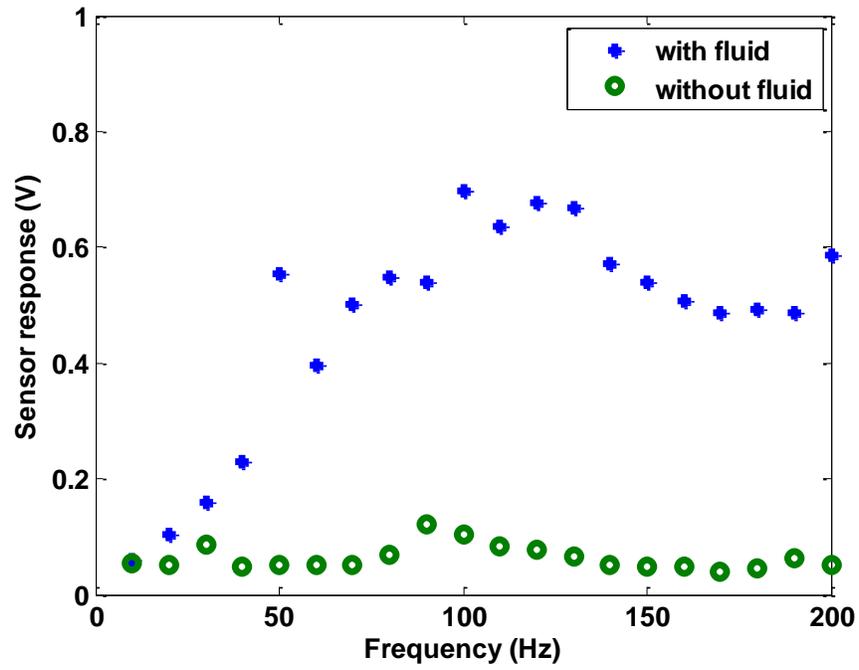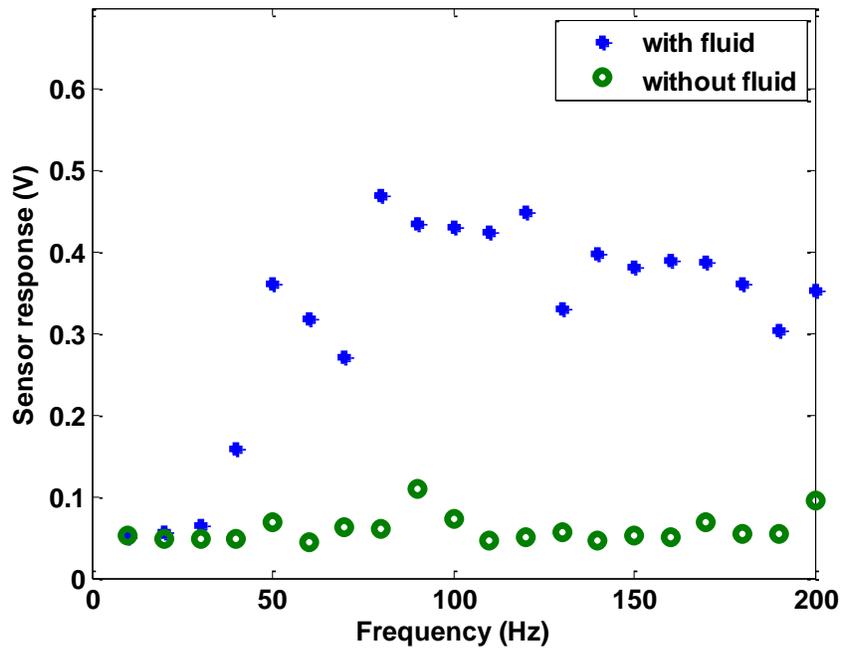
Figure 5.6 Experimentally measured frequency response (in direct sensor output) of prototype bio-inspired sensor with and without filling fluid: (a) sensor design of Type A; (b) sensor design of Type B
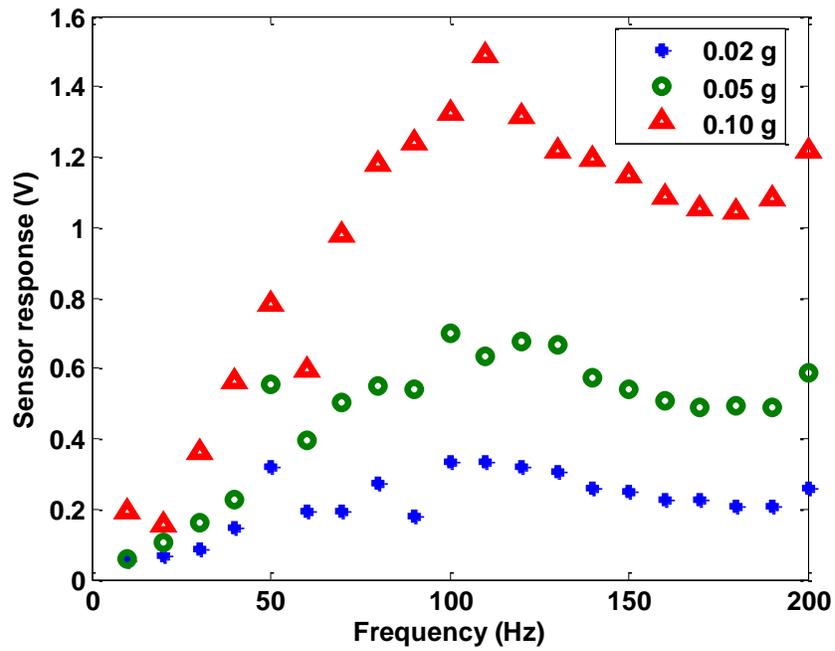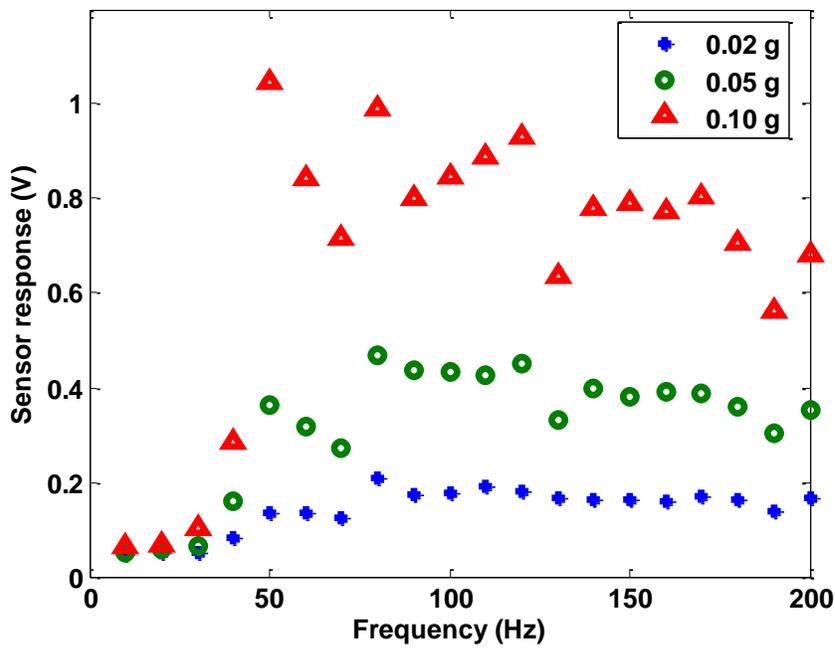
Figure 5.7 Experimentally measured frequency response (in direct sensor output) of prototype bio-inspired sensor under excitation acceleration at three amplitude levels: (a) sensor design of Type A; (b) sensor design of Type B

140
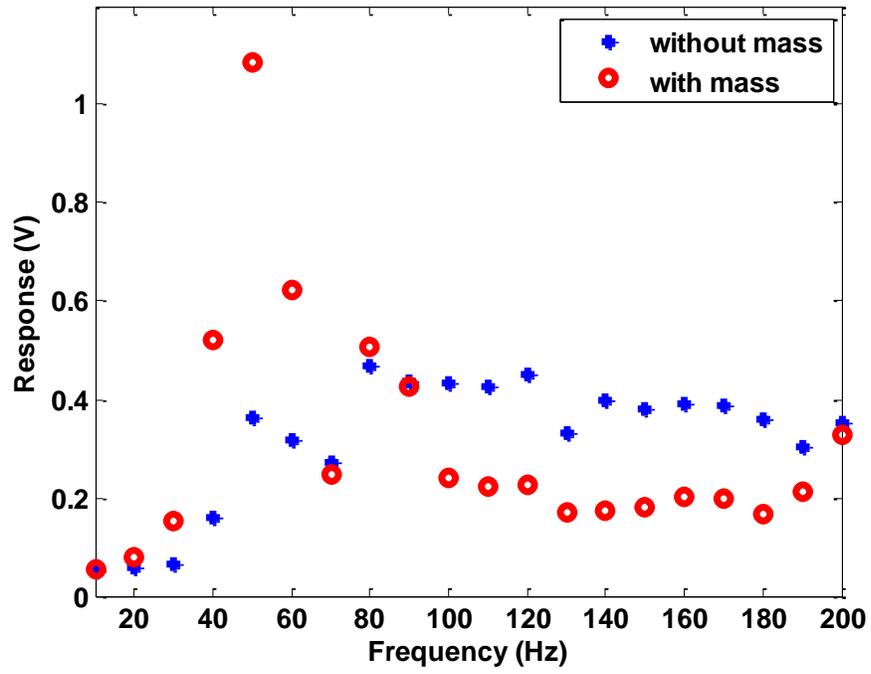
Figure 5.8 Experimentally measured frequency response (in direct sensor output) of prototype bio-inspired sensor with and without additional steel mass
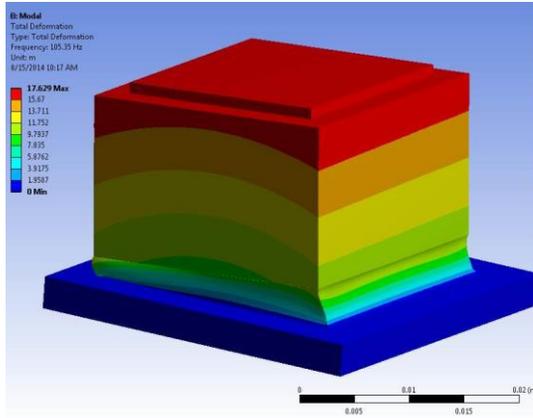
(a)
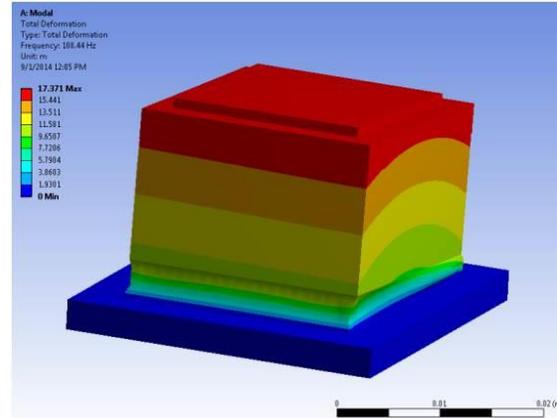


(b)
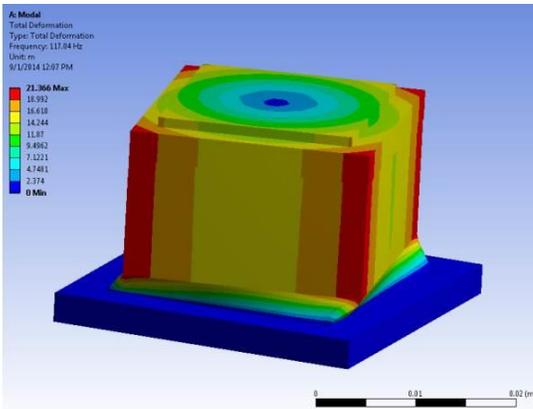


(c)
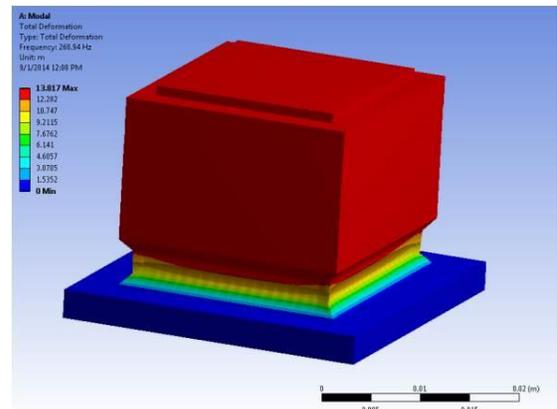


(d)

Figure 5.9 Deformation shape of the first four vibration modes: (a) first mode
(frequency = 105 Hz); (b) second mode (frequency = 108 Hz); (c) third mode
(frequency = 117 Hz); (d) fourth mode (frequency = 261 Hz)
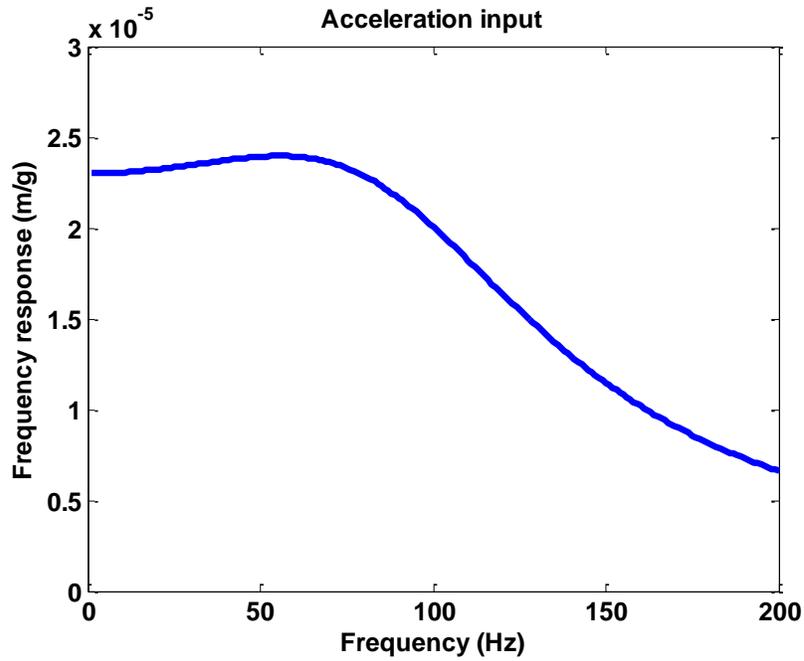
Figure 5.10 Frequency response (transfer function) of sensor top displacement to base acceleration excitation in the equivalent SDOF dynamic oscillator model of the bio-inspired sensor outer case (i.e., without fluid)



| (a) | (b) |
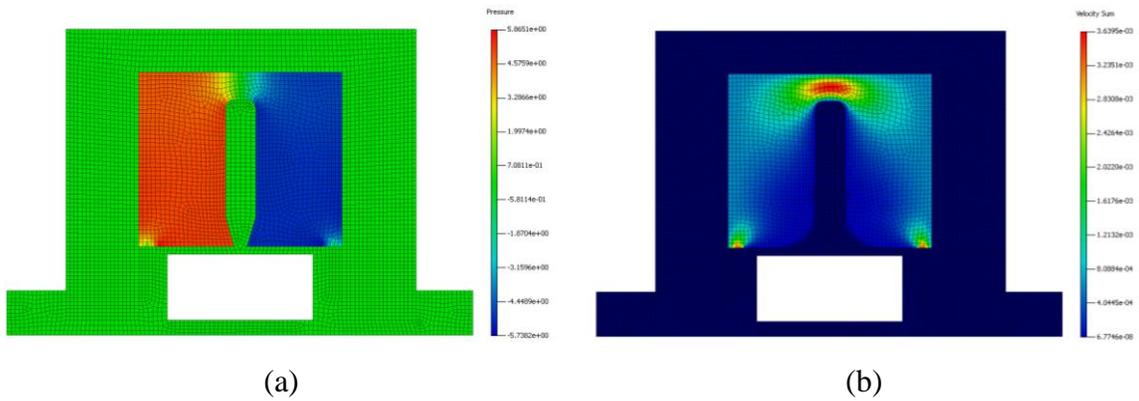
Figure 5.11 FSI numerical model in INTESIM: (a) pressure distribution with outer case moving away from its initial position; (b) velocity distribution with outer case moving away from its equilibrium position
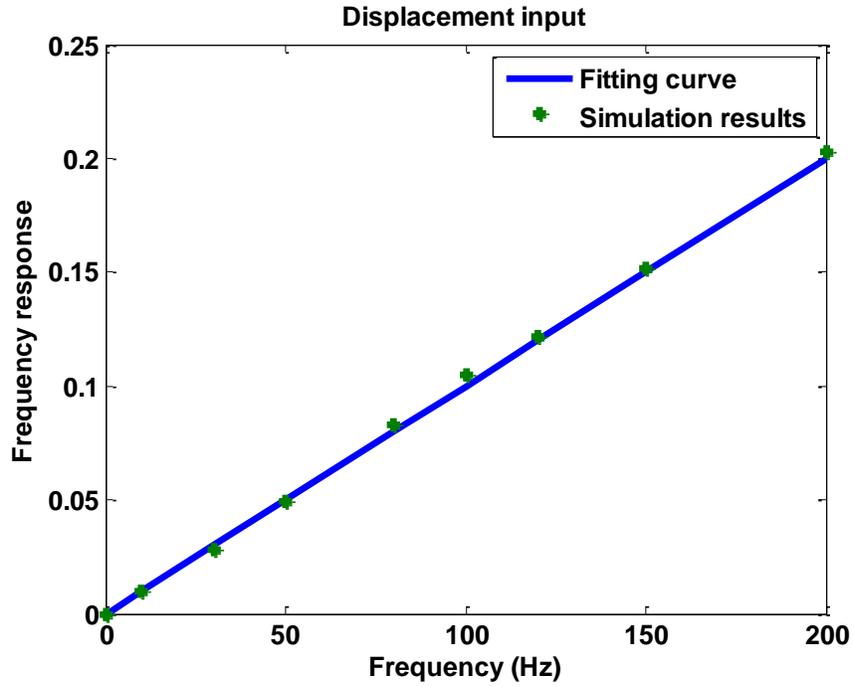
Figure 5.12 Transfer function of inner beam tip deflection to the displacment input at the top of the sensor outer case
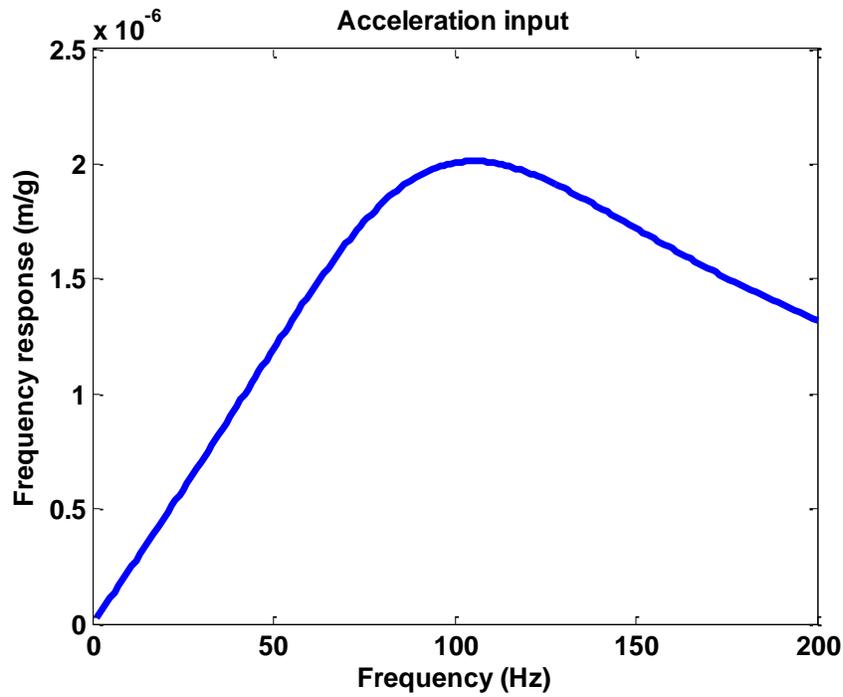


Figure 5.13 Frequency response of prototype bio-inspired sensor's inner beam tip deflection to base acceleration excitation
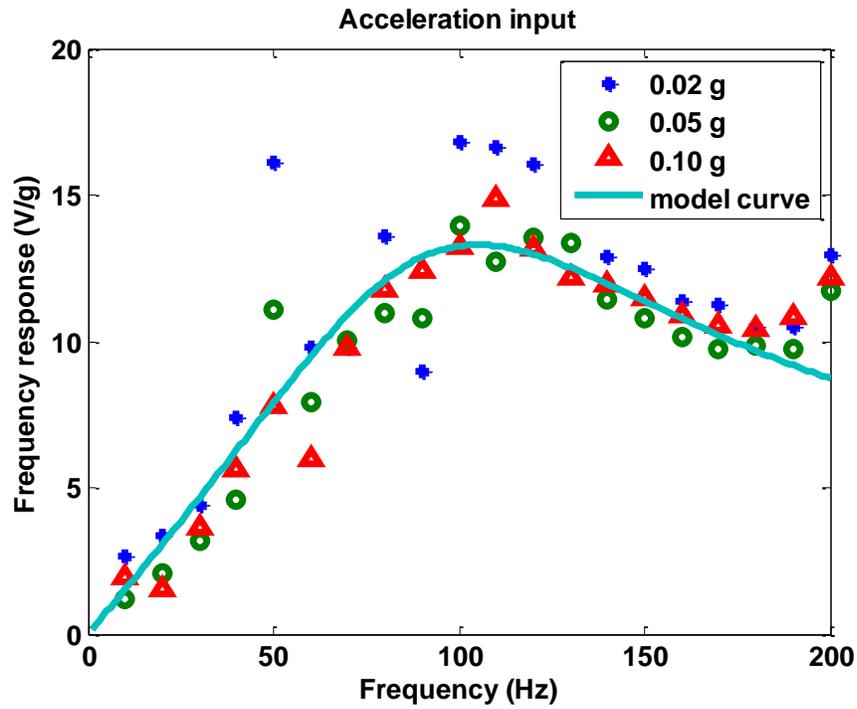
(a)
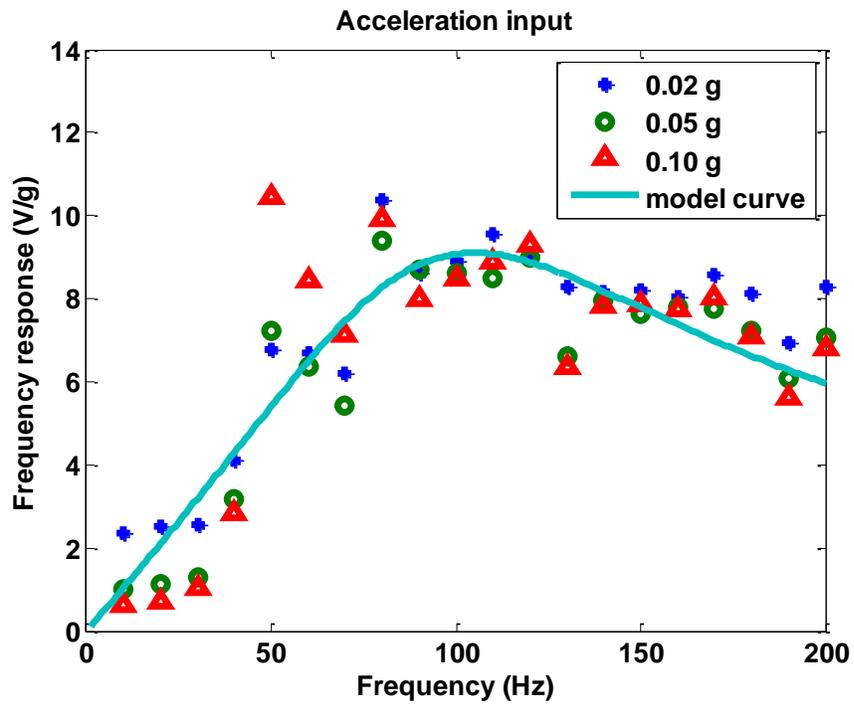


(b)

Figure 5.14 Frequency response of prototype bio-inspired sensor from experimental measurements and theoretical model prediction (parameters calibrated with experimental data): (a) sensor design of Type A; (b) sensor design of Type B

(a)                                                 (b)
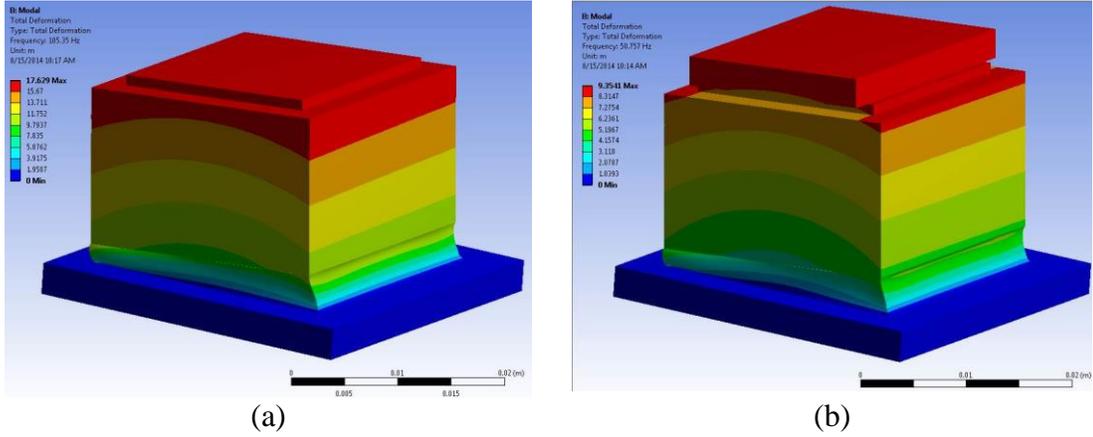
Figure 5.15 Modal deformation shape of prototype bio-inspired sensors: (a) sensor (no fluid) without steel mass (frequency = 105 Hz); (b) sensor (no fluid) with additional steel mass (frequency = 51 Hz)
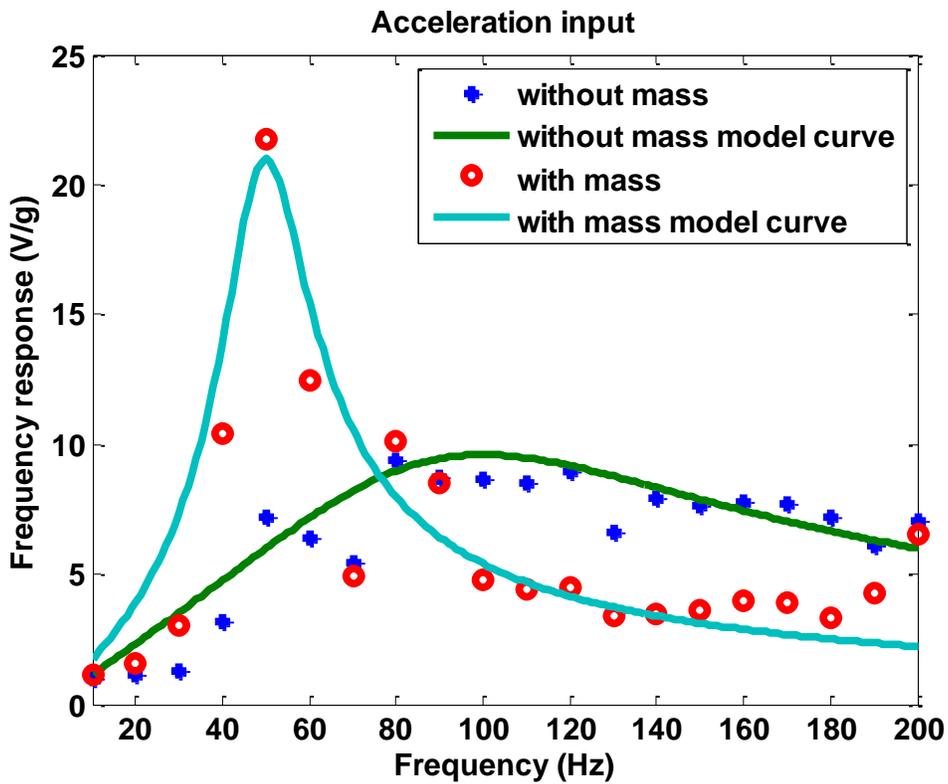


Figure 5.16 Frequency response of prototype bio-inspired sensors from experimental measurements and data and theoretical model prediction (parameters calibrated with experimental data) with and without additional steel mass
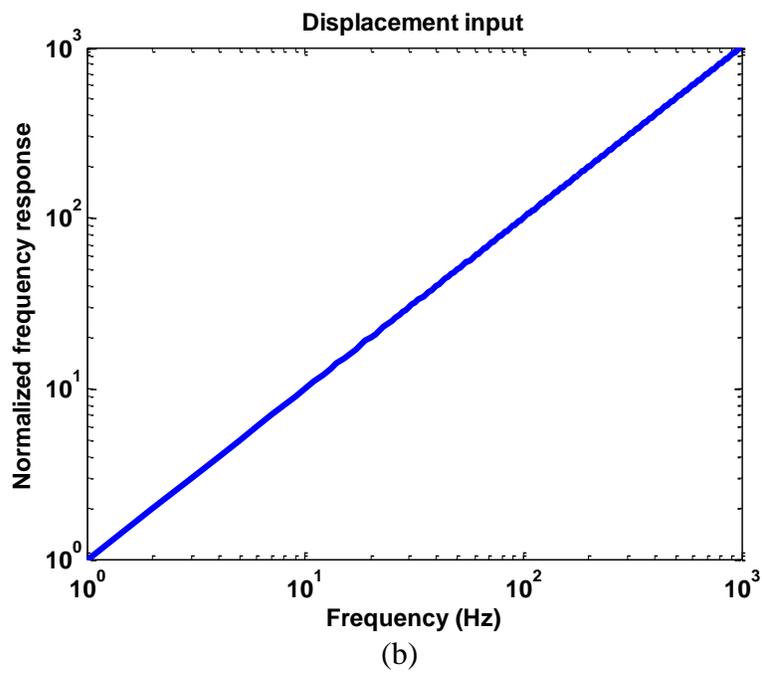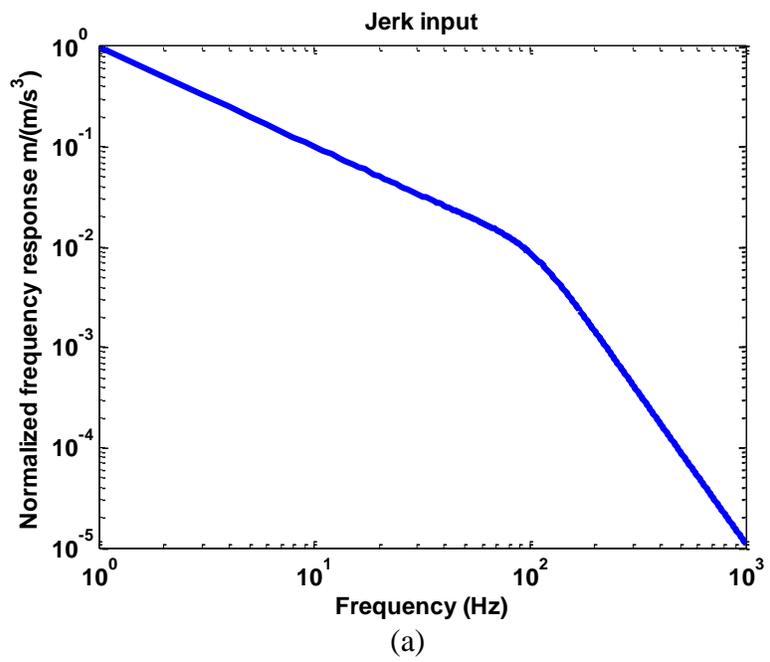
Figure 5.17 (continued)
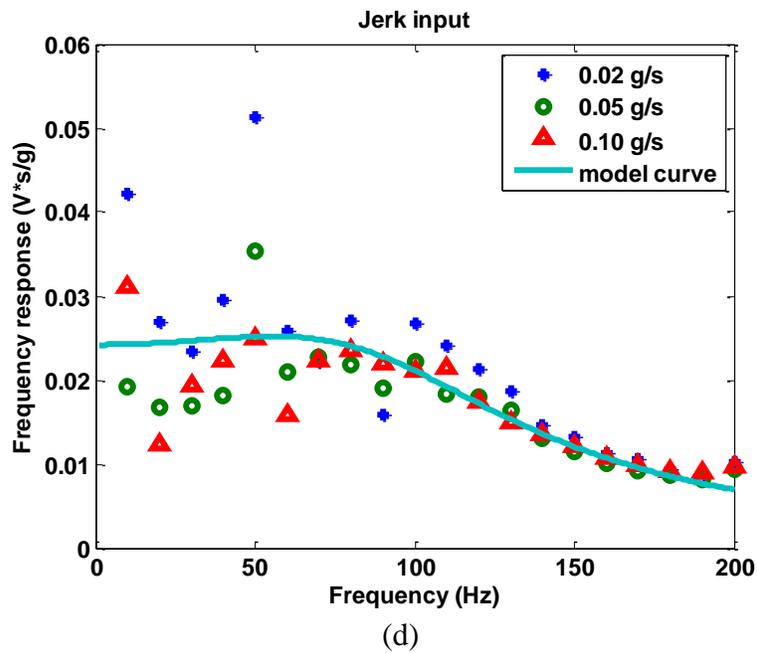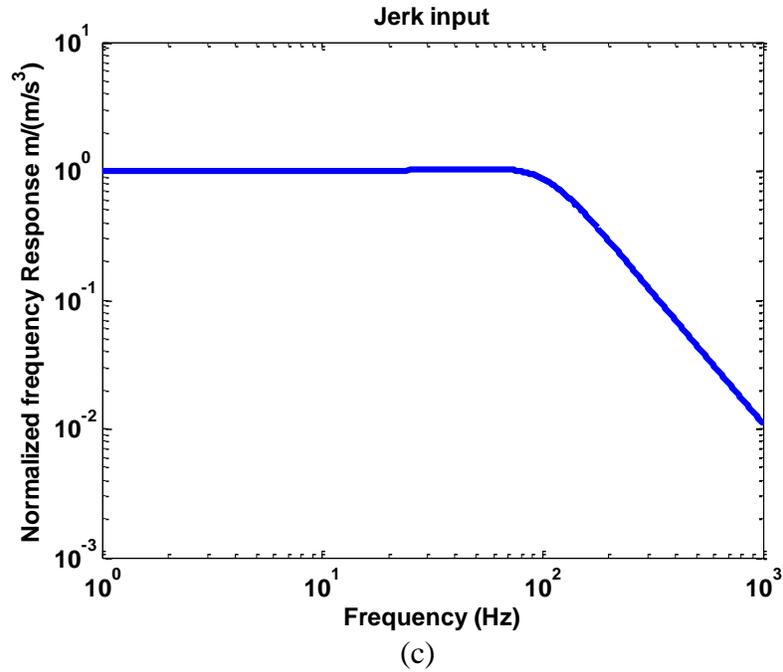
Figure 5.17 Frequency response of proposed bio-inspired jerk sensor: (a) transfer function of outer case displacement to base jerk input; (b) inner beam deflection to displacement input at outer case top surface; (c) frequency response of jerk sensor after convolution of frequency response function presented in (a) and (b); (d) theoretical model and experiment data comparison expressed by jerk input (design type A)

(a)



(b)
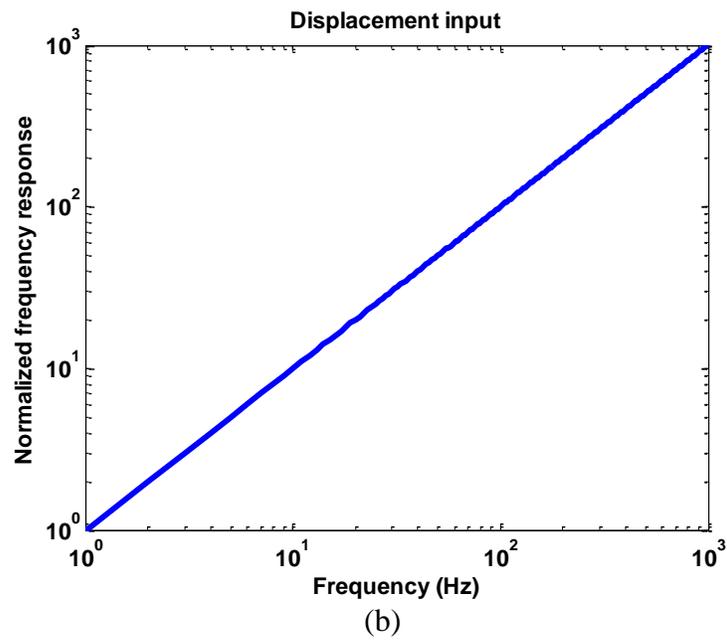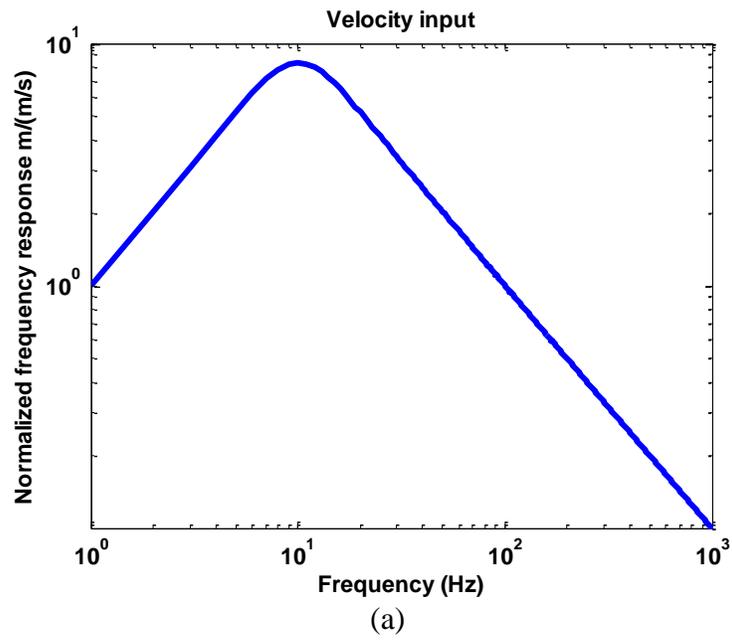
Figure 5.18 (continued)
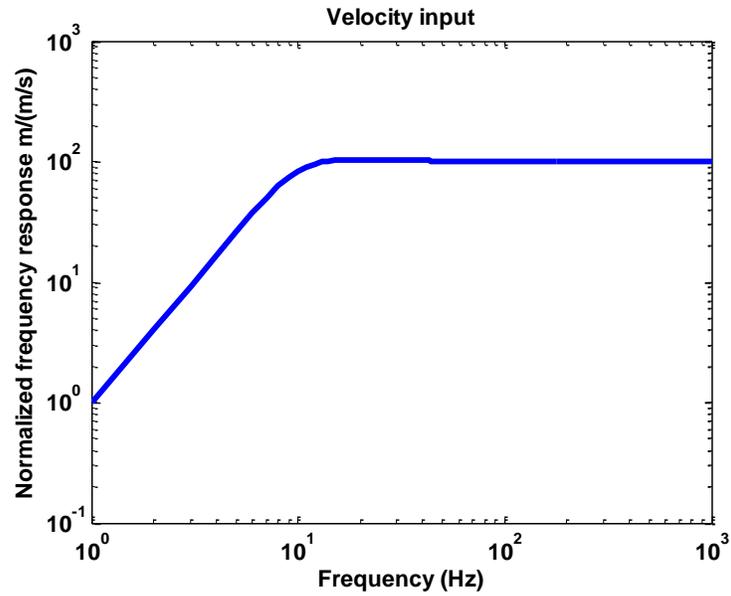
(c)
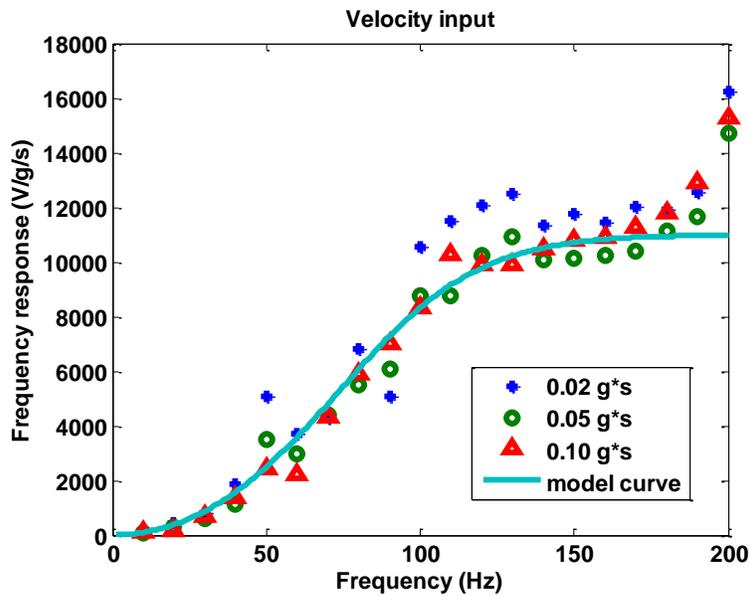


(d)

Figure 5.18 Frequency response of proposed bio-inspired velocity sensor: (transfer function of outer case displacement to base velocity input; (b) inner beam deflection to displacement input at outer case top surface (c) frequency response of velocity sensor after convolution of frequency response function presented in (a) and (b); (d) theoretical model and experiment data comparison expressed by velocity input (design type A)

# Chapter 6: Bio-inspired isolator

## 6.1 Introduction

The pressing need of high-precision measurement for instruments and minimizing vibration interference for machines calls on the development of vibration isolation. In the past few decades, a variety of vibration isolators have been developed for distinct environmental disturbances including seismic ground motion, traffic induced ground vibration, aircraft flyover and rotary equipment vibrations (Xu et al., 2003; Yoshioka et al., 2002; Daley et al., 2006). Generally, these isolators can be categorized into the following three groups: passive isolator, active isolator and semi-active isolator (Choi et al., 2005). Active and semi-active vibration isolators are used in cases where low frequency vibration isolation is required while large static deformations of the low frequency passive vibration isolators are undesirable or unacceptable (Rivin, 2003). Considering the cost and power requirement of active and semi-active vibration isolators, passive isolators are still very popular in an overwhelming majority of applications (Rivin, 2003).

## 6.2 Conceptual study of isolation modular element

By taking advantage of passive vibration isolator's simplicity and thus reliability, this study presents the concept of a novel passive modular vibration isolation element. This modular vibration isolation element consists of three core components: an outer case encasing an inside fluid chamber, a base mount with an

inner beam, and viscous fluid filling up the inside chamber. The configuration of the modular vibration isolation element has been inspired from the macula/statolith system in the *octopus vulgaris*, as shown in Figure 6.1c. The outer case, base mount, inner beam and viscous fluid are intended to mimic the mucus layer, macula epithelium, kinocilia bundle and endolymph in the macula/statolith system respectively. Among these components, the outer case is made of laminated rubber/steel layers to allow for deformation; the base mount and inner beam uses metal such as steel for greater stiffness; highly viscous fluid is used to fill the inside fluid chamber. The outer case is designed to accommodate primarily all the lateral displacement through shear deformation while the fluid-structure-interaction (FSI) effect between the viscous fluid and inner beam provides the desired damping to the vibration isolation element.

A numerical simulation based parametric study presented in this chapter reveals that the built-in viscoelastic damping capability of the bio-inspired vibration isolation element would help to reduce the vibration isolator's lower frequency response without impairing its isolation performance over higher frequency range. By carefully selecting the outer case material, the viscous fluid, and the gap size between the inner beam and outer case, the stiffness and damping characteristics of the proposed bio-inspired isolation element can be adjusted towards a favorable transmissibility relationship over a broad frequency range. Furthermore, the modular isolation element has certain advantage in scaling up the system of arrayed modular vibration isolation elements.

In order to aid the design process, an analysis model that can accurately predict the mechanical behavior of the proposed bio-inspired vibration isolator element is desired. Similar to the bio-inspired sensor described in the prior chapters, this modular vibration isolator element can be modeled with a Standard Linear Solid model that exhibits viscoelastic behavior.

### 6.3.1 Viscoelastic damping

The viscoelastic property of the modular vibration isolation element can be expressed using a complex modulus model. The real part of the complex term (storage modulus) relates to the isolation element's elastic behavior, while the imaginary component (loss modulus) relates to the viscous behavior (Jones, 2001). Several characteristic variables are defined to quantify its viscoelastic property of the modular vibration isolation element. One such variable is the isolated object's moving displacement, which is expressed as Equation 6.1,

$$D = \bar{d} \sin(\omega t) \tag{6.1}$$

where $\bar{d}$, $\omega$ and $t$ are the displacement amplitude, the circular frequency and time. The other characteristic variable is the reaction force at the bottom of the isolation element as expressed in Equation 6.2 as,

$$P = P_0 \sin(\omega t + \phi) \tag{6.2}$$

where $P_0$ is the reaction force amplitude and $\phi$ is the phase angle between the reaction force and applied stimulus (e.g., motion of the outer case at its top surface).

Under the steady state condition, the dissipated energy for each cycle motion can be derived as Equation 6.3.

$$W_d = \pi P_0 \bar{d} \sin(\phi)$$ (6.3)

After introducing the storage stiffness $K_1$ and loss stiffness $K_2$ as Equation 6.4,

$$K_1 = \frac{P_0}{\bar{d}} \cos(\phi) \quad , \quad K_2 = \frac{P_0}{\bar{d}} \sin(\phi)$$ (6.4)

Equation 6.2 could be rewritten as Equation 6.5,

$$P = K_1 D + \frac{K_2}{\omega} \dot{D}$$ (6.5)

where the first term represents the force due to the elastic stiffness and the second term is the force due to the viscosity. By dividing the loss stiffness $K_2$ with storage stiffness $K_1$, the loss factor is defined as

$$\eta_l = \frac{K_2}{K_1} = \tan \phi$$ (6.6)

The values of viscous damping ratio can be expressed as:

$$\zeta = \frac{\eta_l}{2}$$ (6.7)

During the whole process, the dependence of mechanical properties on temperature is assumed not significant.

### 6.3.2 Standard Linear Solid model

The Standard Linear Solid (SLS) model, which is widely used to characterize the stiffness functions of linear viscoelastic media, is adopted to describe the viscoelastic property of the bio-inspired isolation element. Placing a spring in parallel with the Maxwell unit gives a schematic of the SLS model as shown in Figure 6.2.

This spring has stiffness $k_e$, so named because it provides an "equilibrium" stiffness that remains after the force in the Maxwell unit has relaxed away as the dashpot extends (Jones, 2001).

The stiffness derived from the SLS model is given by

$$K(t) = k_e + k e^{-tk/\eta} \tag{6.8}$$

where $k_e$, $k$ and $\eta$ are all positive constants representing the equilibrium stiffness, the spring stiffness and the dashpot damping coefficient in the Maxwell unit, respectively. By substituting the time-domain function with the corresponding function in frequency, in the SLS model, the storage $K_1$ and the loss stiffness $K_2$ are expressed as (Tschoegl, 1989)

$$K_1 = k_e + \frac{k\eta^2\omega^2}{\eta^2\omega^2 + k^2} \tag{6.9}$$

$$K_2 = \frac{k^2\eta\omega}{\eta^2\omega^2 + k^2} \tag{6.10}$$

## *6.4 Simulation results discussion*

### 6.4.1 Model description

A simplified 2D numerical model (the out-of plane dimension is 7 mm) was created to analyze the behavior of the bio-inspired modular isolation element in FSI software INTESIM, as shown in Figure 6.3. In this FSI numerical model, the vertical degree of freedom (DOF) of the nodes at the top surface of the isolation element was constrained and all DOFs of the nodes at the bottom surface were constrained. With such defined boundary conditions, shear deformation would dominate when

horizontal displacement is applied as stimulus to the isolator at its top surface. Figure 6.4 show the fluid velocity and pressure contour in steady state, which corresponds to the time instants with maximum velocity and maximum displacement at the top surface, respectively. At the maximum velocity point, the fluid pressure difference between the two sides of the inner beam reaches its peak value and the fluid is forced to flow through the gap between inner beam and outer case. On the contrary, at the maximum displacement moment, the pressure difference, which has its minimum value, would not cause obvious flow through the gap. During this whole process, the energy can be dissipated by pushing the fluid flow back and forth through the gap between the inner beam and outer case.

In the following section, a reference model of the bio-inspired modular isolation element was studied under sweep sine excitations to get its typical frequency response curve. Next, FSI numerical models with different control parameter values (gap size, fluid viscosity, outer case stiffness and inner beam stiffness) were considered to investigate each parameter's effect on the frequency response characteristics. In the numerical simulation study, a series of horizontal harmonic displacements were applied at the top surface of the isolation element and reaction forces at the bottom surface were recorded as the response variable.

6.4.2 Reference model study

6.4.2.1 Hysteresis behavior

Four hysteresis loops of the reference bio-inspired isolation element model (Model P in Table 6.2) are displayed in Figure 6.5a. It is seen that, under the same displacement amplitude (5.0 mm) applied to the top of the isolation element, these

elliptical hysteresis loops display different features with varying frequency values for harmonic displacement excitation. Specifically, from 0.2 Hz to 0.5 Hz, it shows an increase of hysteresis area and a similar inclined slope in the two hysteresis loops, indicating an increasing viscous damping capacity and unchanged elastic stiffness in the bio-inspired isolation element respectively. With frequency climbing to 5.0 Hz, the hysteresis loop tends to be elliptical in shape rather than pointed, suggesting the increase of the viscous damping effect in the isolation element. As the excitation reaches 50 Hz, the hysteresis loop shrinks in area while the slope of the hysteresis loop still shows an increase compared with the case of 5.0 Hz hysteresis loop. These findings indicate that, over the considered frequency range, the viscous damping capacity of the bio-inspired isolation element is initially proportional to the frequency followed by a decreasing trend after crossing a characteristic frequency. In the meanwhile, the elastic stiffness, which keeps unchanged in the low frequency range (0.2 Hz and 0.5 Hz), gradually increases in the higher frequency range (5 Hz and 50 Hz).

6.4.2.2 Comparison with Standard Linear Solid model

The viscous damping capacity and elastic stiffness of the bio-inspired vibration isolation element can be respectively represented by the loss stiffness and storage stiffness in the complex modulus. Over the concerned frequency range, by converting the hysteresis parameters into the complex modulus (expressed in Equations 6.1 to 6.7), the storage stiffness, the loss stiffness and the loss factor of the reference isolation element are presented using green dots in Figures 6.6a to 6.6c, respectively. In the meanwhile, the SLS model is displayed as a blue curve in each

figure. A comparison between the simulation data and curves derived from the SLS model shows that, the SLS model (67,000 N/m for its equilibrium stiffness, 110,000 N/m for the spring constant and 5,000 N*s/m for the dashpot damping coefficient) fit very well with the FSI numerical simulation data.

In Figure 6.6a, the storage stiffness of the isolation element maintains at the equilibrium level in the low frequency range and the value of the equilibrium level is equal to the outer case stiffness. With the frequency increasing to 1 Hz, the storage stiffness starts to increase rapidly until a new plateau level is reached at 10 Hz. This pattern of storage stiffness change reveals that the elastic stiffness change displayed in the hysteresis loops occurs primarily over the frequency range from 1 Hz and 10 Hz. Furthermore, the frequency response characteristic of the imaginary component in the complex modulus can be seen in Figure 6.6b, in which the loss stiffness shows an increasing trend in the low frequency range and decreasing trend for the higher frequency range. The maximum value of the loss stiffness occurs in the same frequency range where the storage stiffness rapidly increases. By dividing the loss stiffness with corresponding storage stiffness, the same frequency dependent response behavior is also seen in the loss factor, shown in Figure 6.6c. The loss factor of the isolation element reaches the highest value around 2.3 Hz, suggesting that the bio-inspired modular vibration isolation element has the highest energy dissipation capacity at this particular frequency. Since the loss factor changes in the frequency range between 2 Hz and 3 Hz is trivial, it is concluded that this particular bio-inspired modular isolation element design has the highest damping capacity in this frequency range. In summary, the performance of the bio-inspired vibration isolation element

are closely related to its operating frequency and this frequency dependent response behavior can be described by the SLS model as shown in Figures 6.6a, to 6.6c. By using the calibrated SLS model, FSI simulation is no longer needed to study the performance of the proposed modular vibration isolation element, which could significantly simplify the analysis.

6.4.2.3 Transmissibility

Based on the frequency dependent loss factor of the bio-inspired vibration isolation element (see Figure 6.6c), it is noted that the damping capacity of the proposed vibration isolation element shows a decreasing trend in the higher frequency range and such feature is generally desired in the isolator application. In other words, the isolator's transmissibility could be improved by properly designing the bio-inspired isolation element such that its damping capacity decreases with frequency in higher frequency range. For instance, by setting the maximum loss factor frequency equal to the isolated object's natural frequency (2.3 Hz), the transmissibility curve of the reference isolation element model is shown in Figure 6.7. It is seen that in the low frequency range, the transmissibility of the isolation element is almost identical to an equivalent viscous model with a viscous damping ratio of 29%. While the transmissibility curve of the isolation element in higher frequency range (after 4 Hz in this case; it is worth noting that this frequency is tunable) is much lower than the transmissibility curve of a 29% viscous damped isolator. It is concluded that the bio-inspired isolation element has promising transmissibility performance across its entire operating frequency range.

6.4.2.4 Effect of shear strain

In addition to the case with 5-mm displacement amplitude (stimulus at the top surface of the isolator element), another two cases with different displacement amplitude values (2.5 mm and 10.0 mm) were considered for the reference isolation element. Since the isolation element is deformed into a pure shear mode, the corresponding displacement amplitude (2.5 mm, 5.0 mm and 10.0 mm) can be converted into equivalent shear strain of 3%, 6% and 12% respectively after dividing by the height of the isolation element. Based on FSI simulation results, the effects of varying the shear strain levels can be seen in Figures 6.8a to 6.8c. Frequency responses are overlapping with each other in all three figures, indicating that the frequency response functions (storage stiffness, loss stiffness and loss factor) of the bio-inspired isolation element are not dependent on the shear strain level for the strain range considered.

6.4.3 Parametric study

6.4.3.1 Effect of gap size

One important design parameter of the bio-inspired vibration isolation element is its gap size between the inner beam and the outer case. To study this effect, another three additional models with different gap sizes (see Model A1, Model A2 and Model A3 in Table 6.1) were created for FSI simulation study under sweep sine excitations. The frequency response of the base reaction force to the displacement stimulus at the sensor top is converted into the complex modulus form by using Equations 6.1 to 6.7, and the results are shown in Figures 6.9a to 6.9c. Given the various gap sizes, the general shape of the frequency response curves (storage

160

stiffness, loss stiffness and loss factor) are similar to that of the reference model, while the exact location of the turning points for different frequency response curves are different. Increasing the gap size would shift the frequency response turning point towards higher frequency values and slightly decreases the peak gain values. This finding implies that changing the gap size offers a means to tune the frequency response characteristics of the bio-inspired vibration isolation element. In engineering practice, altering the gap size in the bio-inspired isolation element could provide a simple and economical approach to adjusting its operating frequency band in order to achieve good transmissibility.

The effect of varying gap size on the response behavior of bio-inspired isolation element can also be predicted using the SLS model. By keeping the equilibrium stiffness unchanged and tuning the values of spring constant and dashpot damping coefficient, the SLS model curves fit very well with the FSI simulation results, as shown in Figure 6.9. The values of these SLS model parameters are listed in Table 6.2 (for Model A1, Model P, Model A2 and Model A3, with varying gap sizes). Compared with the slight drop in spring constant $k$, the reduction in the dashpot damping coefficient $\eta$ values is more significant with increasing gap size. In other words, increasing the gap size of the vibration isolation element is comparable to decreasing the dashpot damping coefficient in the SLS model.

6.4.3.2 Effect of fluid viscosity

In order to achieve greater energy dissipation capacity at the resonance frequency range, highly viscous fluid could be chosen to reduce the resonance vibration (Makris et al., 1990; Arima et al., 1988). In this section, three values of the

viscous fluid's viscosity coefficient (200 Pa-sec, 500 Pa-sec and 1,000 Pa-sec) were considered in the vibration isolation element models to investigate their effect on its frequency response and the model details are given in Table 6.1 (Model B1, Model P and Model B2). Based on the sweep sine excitation analysis, the frequency response curves, expressed in terms of storage stiffness, loss stiffness and loss factor, are respectively shown in Figures 6.10a, Figure 6.10b and Figure 6.10c. It is seen from these figures that these frequency response curves with similar trend to that of the reference model are shifted towards lower frequency range when higher viscosity fluid is used in the isolation element. Compared with the effect of gap size between the inner beam and outer case, the viscosity does not appear to affect the peak gain values of the presented frequency response curves. These observations suggest that the operating frequency range of the proposed bio-inspired vibration isolation element can be adjusted by selecting proper viscous fluid viscosity value and such adjustment does not seem to change the maximum stiffness (storage and loss stiffness) values.

The parameter values of the SLS models (from curve fitting of simulation data points) are given in Table 6.2 (Model B1, Model P and Model B2). As the fluid viscosity increases, the dashpot damping coefficient increases proportionally while the equilibrium stiffness and spring stiffness values remain unchanged. This indicates that the effect of the viscous fluid's viscosity can be quantitatively described by altering the dashpot damping coefficient value in the SLS model.

6.4.3.3 Effect of outer case stiffness

The laminated rubber/steel layer, which is commonly used in conventional vibration isolator, is also proposed to be used for the outer case material in the bio-

inspired vibration isolator. Three models of the vibration isolation element with different values of outer case materials are considered in this study and the model details are given in Table 6.1 (Model C1, Model P and Model C2). With increasing Young's modulus of the outer case, the frequency responses of these three models shown in Figure 6.11a and Figure 6.11b displays a trend of shifting towards higher values in both frequency and stiffness gain. In contrast with the storage and loss stiffness changes, higher Young's modulus value shifts the loss factor frequency response towards the high frequency range without increasing the gain of the loss factor. In particular, the maximum loss factor values of the first two models (E = 1.0e7 Pa and E =1.0e8 Pa) maintain the same level while the maximum loss factor value of the third model (E =1.0e9 Pa) drops. This indicates that the stiffness change of the outer case can also be utilized to adjust the operating frequency range of the concerned vibration isolation element, but its damping capacity could be impacted accordingly.

The frequency response curves of the corresponding SLS models (Model C1, Model P and Model C2) are shown in the Figure 6.11a, Figure 6.11b and Figure 6.11c and the model details are given in Table 6.2. The good agreement between the curves predicted by the SLS models and data points from FSI simulation demonstrates the ability of the SLS model in describing the response behavior of the isolation element. From the listed parameter values of the SLS models are in Table 6.2, the values of the equilibrium stiffness and spring constant significantly increase with the rising Young's modulus value of the outer case, while change in the dashpot damping coefficient appears to be negligibly small. This finding reveals that the effect of outer

163

case is comparable to changing the equilibrium stiffness and spring constant in the SLS model.

### 6.4.3.4 Effect of inner beam stiffness

A comparative study on models with varying stiffness values of inner beam ($E_i$ = 2e11, $E_i$ = 2e10 and $E_i$ = 2e9) was also conducted (Model P, Model D1 and Model D2 in Table 6.2) as shown in Figures 6.12a to 6.12c. In each of the three frequency response functions (storage stiffness, loss stiffness and loss factor), the maximum gain values are positively correlated with the inner beam stiffness value. It is also noted that, over the considered frequency range, the gain of the loss factor with larger inner beam stiffness are always greater or at least equal to the loss factor gain of the models with lower inner beam stiffness. This indicates that the damping effect of the isolation element is notably reduced due to reduced inner beam stiffness values.

Furthermore, the SLS models are used to fit the simulation data points shown in Figure 6.12. The curve fitting results, along with parameter values in the SLS model (see Table 6.2), suggest that the effect of inner beam is comparable to varying the spring constant of the SLS model. It is also noted that the fitting accuracy between the FSI simulation results and the theoretical curve of the SLS model with higher stiffness inner beam ($E_i$ = 2e11 Pa and $E_i$ = 2e10 Pa) is better than the model with lower stiffness inner beam ($E_i$ = 2e9 Pa). This is because the inner beam deflection caused by the interaction between the inner beam and viscous fluid through FSI could be amplified due to reduced inner beam stiffness and this amplified deflection could again interact with the FSI inside the isolation element.

From Figures 6.9 to 6.12, it is concluded that the SLS model is very effective in predicting the response behavior of the bio-inspired vibration isolation element while computing is greatly simplified compared with FSI simulation.

*6.5 conclusion*

Inspired from the octopus's macula/statolith system, the concept of a novel bio-inspired vibration isolation element is proposed in this chapter. 2D FSI numerical models created in the FSI software INTESIM were used to investigate its dynamic response behaviors when the vibration isolator is subjected to displacement stimulus at the isolator top surface. The FSI numerical simulation results reveal that the bio-inspired vibration isolation element exhibits a viscoelastic characteristic which is very promising to enhance the isolator transmissibility performance, especially over higher frequency ratio range. Based on the results from comprehensive parametric studies and curve fitting using the SLS model, it is concluded that the dynamic response behavior of the proposed bio-inspired vibration isolation element are primarily controlled by four design parameters (gap size, fluid viscosity, outer case and inner beam stiffness). Among them, the gap size, fluid viscosity and outer case could be tuned to adjust isolation element's working frequency without notably reducing the maximum loss factor in the investigated cases, while the adjustment of working frequency by changing the inner beam's stiffness could significantly reduce the isolation element's maximum loss factor. These effects could be measured by comparing the parameter value change of the corresponding SLS model.

Table 6.1 Parameter values of vibration isolation element models

| Model No. | Gap (mm) | Outer case Modulus (MPa) | Inner beam modulus (GPa) | Fluid viscosity (Pa-sec) | Top displacement amplitude (mm) |
|---|---|---|---|---|---|
| P* | 3.3 | 100 | 200 | 1000 | 5.0 |
| A1 | 2.5 | 100 | 200 | 1000 | 5.0 |
| A2 | 5.0 | 100 | 200 | 1000 | 5.0 |
| A3 | 6.6 | 100 | 200 | 1000 | 5.0 |
| B1 | 3.3 | 100 | 200 | 500 | 5.0 |
| B2 | 3.3 | 100 | 200 | 2000 | 5.0 |
| C1 | 3.3 | 10 | 200 | 1000 | 5.0 |
| C2 | 3.3 | 1000 | 200 | 1000 | 5.0 |
| D1 | 3.3 | 100 | 2 | 1000 | 5.0 |
| D2 | 3.3 | 100 | 20 | 1000 | 5.0 |
| E1 | 3.3 | 100 | 200 | 1000 | 2.5 |
| E2 | 3.3 | 100 | 200 | 1000 | 10.0 |

P* is the reference model

Table 6.2 SLS model parameter values of vibration isolation element models in Table 6.1

| Model No. | Spring stiffness $k$ (N/m) | Damping coefficient $\eta$ (N*s/m) | Equilibrium stiffness $k_e$ (N/m) |
|---|---|---|---|
| P | 110,000 | 5,000 | 67,000 |
| A1 | 120,000 | 9,000 | 67,000 |
| A2 | 100,000 | 2,000 | 67,000 |
| A3 | 94,000 | 800 | 67,000 |
| B1 | 112,000 | 2,500 | 67,000 |
| B2 | 110,000 | 10,000 | 67,000 |
| C1 | 11,000 | 5,000 | 6,700 |
| C2 | 700,000 | 5,500 | 670,000 |
| D1 | 22,000 | 5,500 | 67,000 |
| D2 | 76,000 | 5,500 | 67,000 |
| E1 | 110,000 | 5,000 | 67,000 |
| E2 | 110,000 | 5,000 | 67,000 |

(a)



(b)



**Steel plate connected with isolated object**

**Outer case**

**Steel mount and inner beam**

**Viscous fluid**
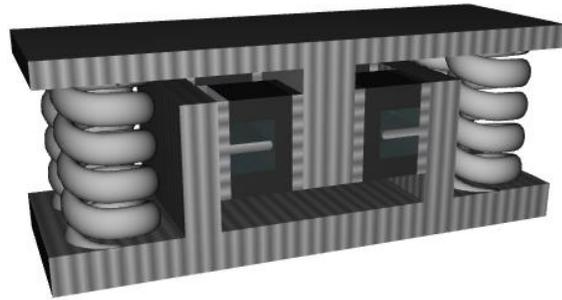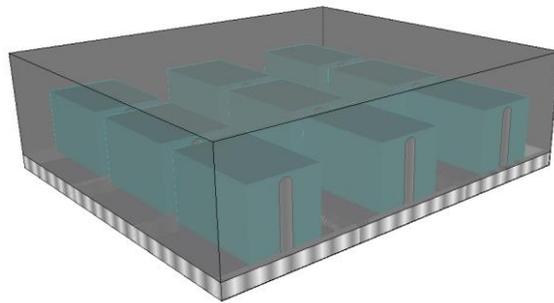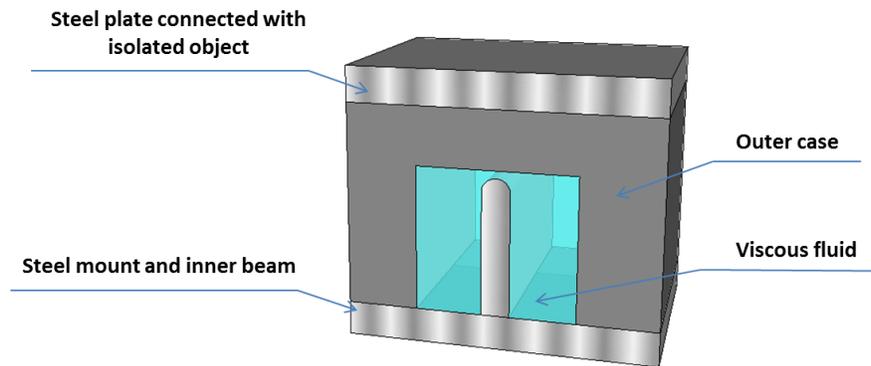
(c)

Figure 6.1 Schematic illustration of proposed modular vibration isolation element: (a) vertical isolator; (b) horizontal isolators with arrayed modular isolation elements; (c) section view of modular isolation element
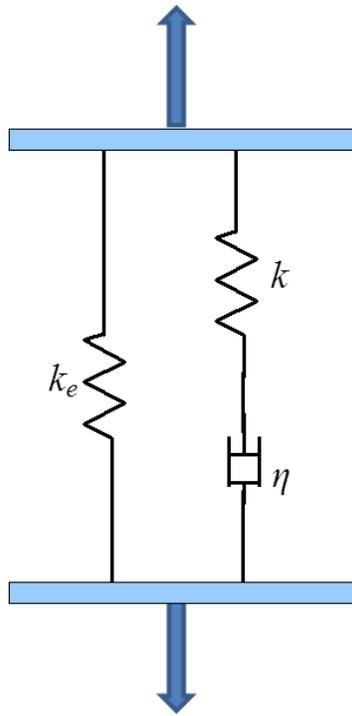
Figure 6.2 Schematic representation of the Standard Linear Solid model
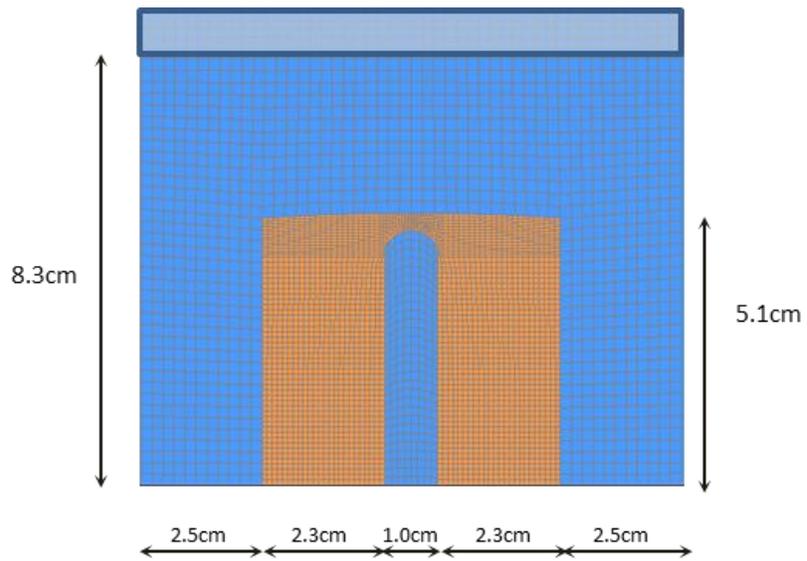


Figure 6.3 2D numerical model of modular isolation element for FSI analysis
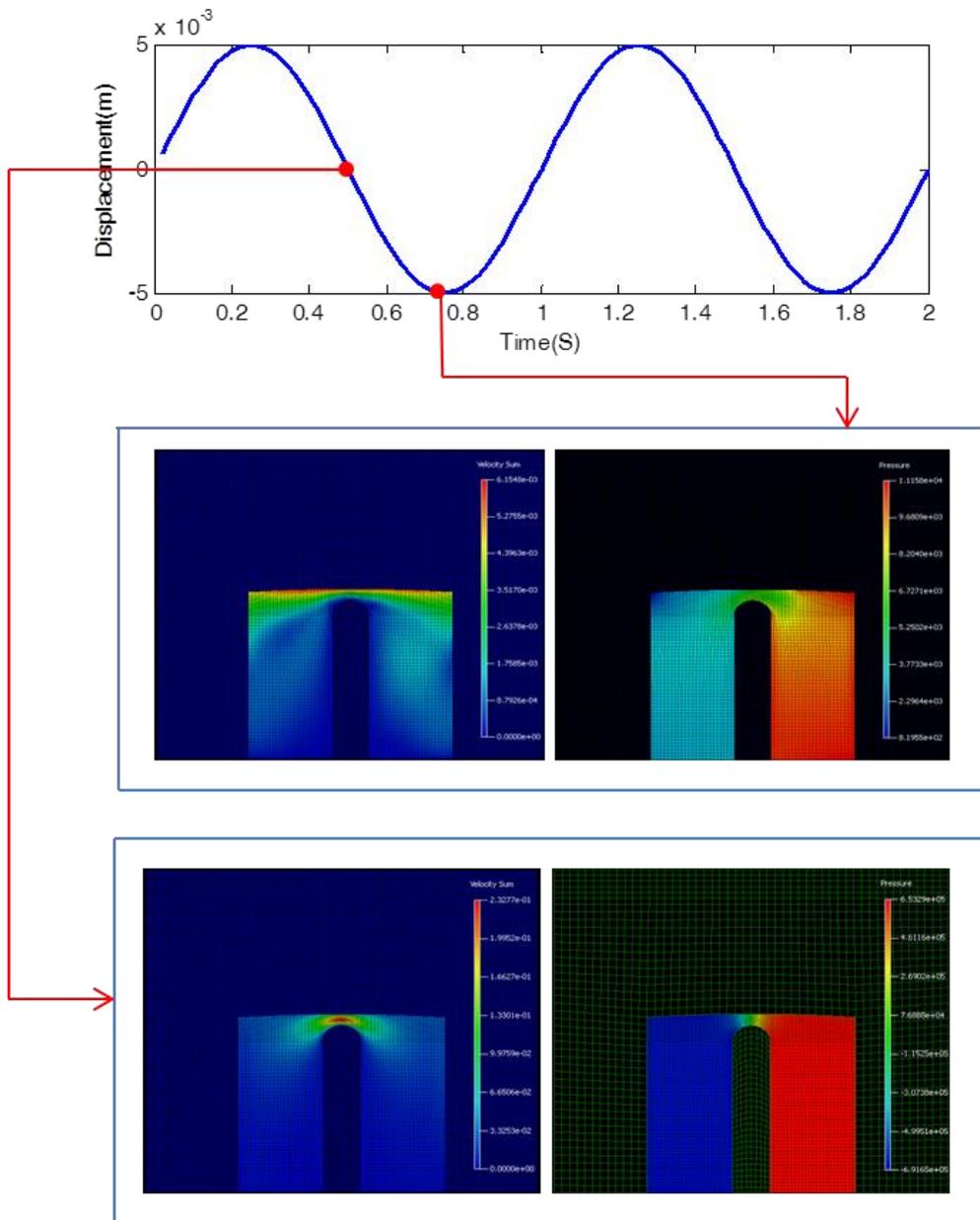
Figure 6.4 Contour plots of fluid velocity and pressure distribution corresponding two distinctive displacement levels at different time points
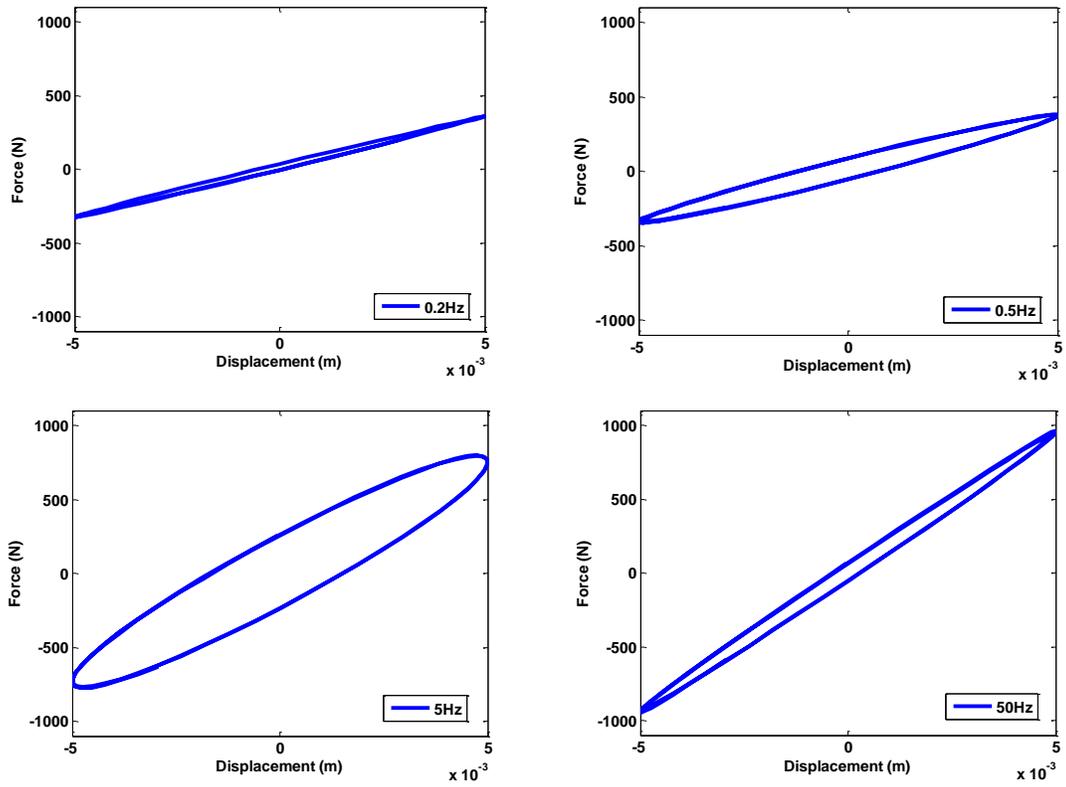
Figure 6.5 Hysteresis loops (force vs. displacement) of vibration isolation element under harmonic displacement excitation with excitation frequency of 0.2 Hz, 0.5 Hz, 5.0 Hz and 50 Hz
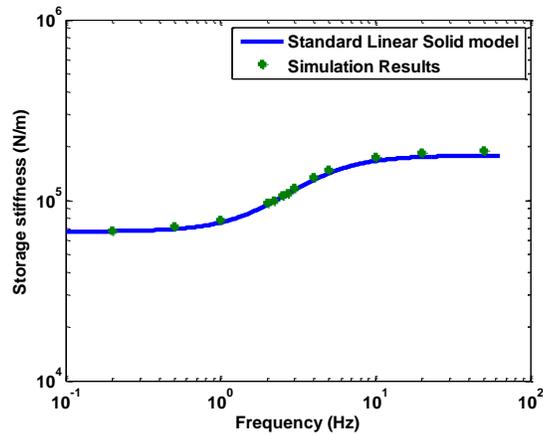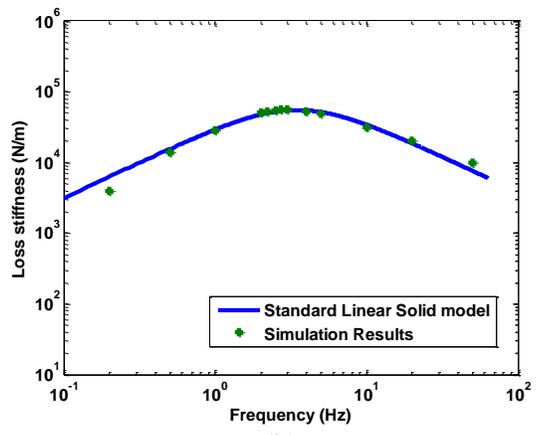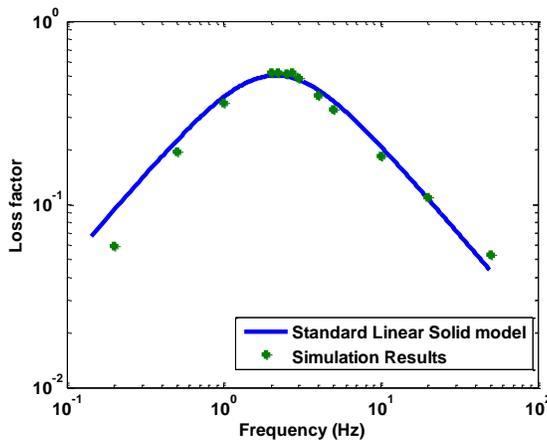
Figure 6.6 Frequency response of reference vibration isolation element from FSI simulation and SLS model analysis: (a) storage stiffness; (b) loss stiffness; (c) loss factor
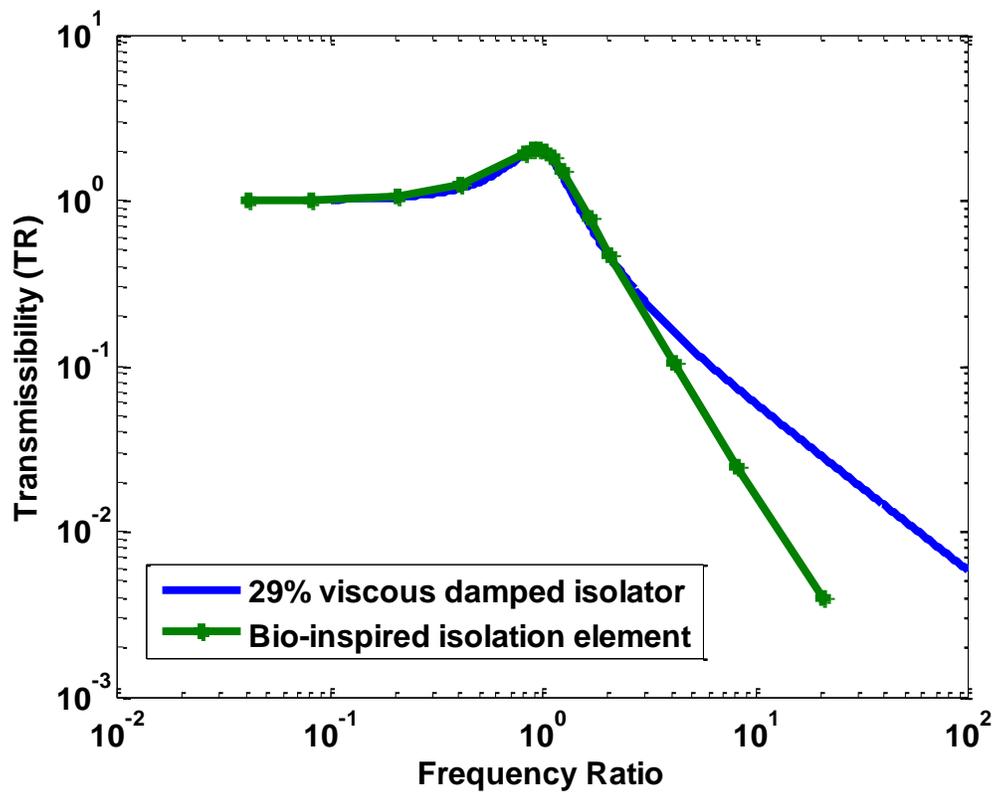
Figure 6.7 Normalized transmissibility of reference vibration isolation element and equivalent viscous damped isolator
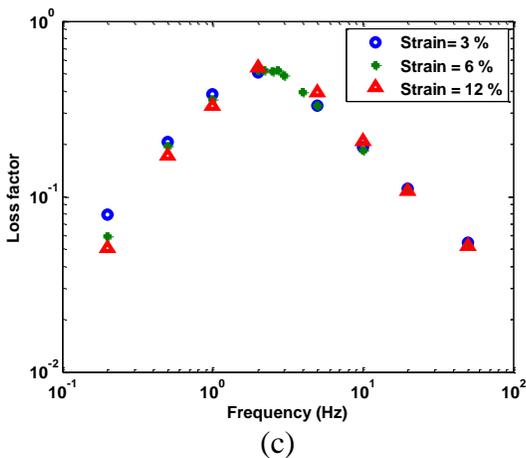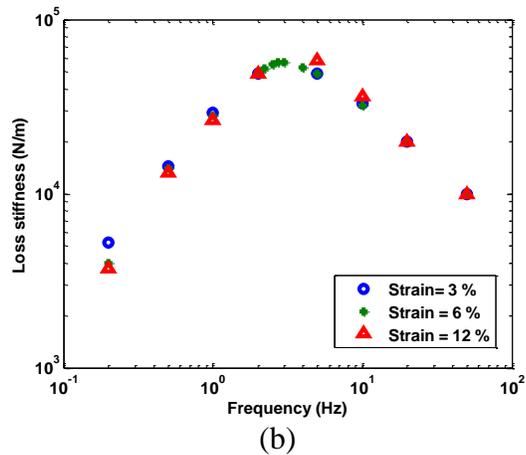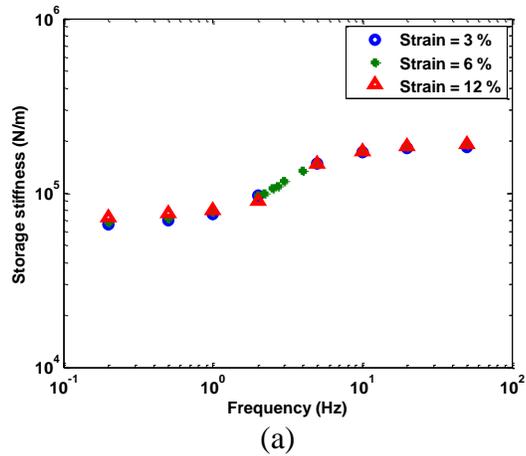
Figure 6.8 Frequency response of reference vibration isolation element from FSI simulation subjected to different shear strain magnitudes: (a) storage stiffness; (b) loss stiffness; (c) loss factor
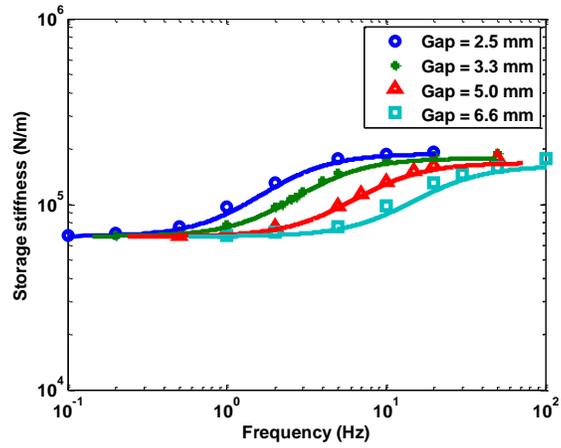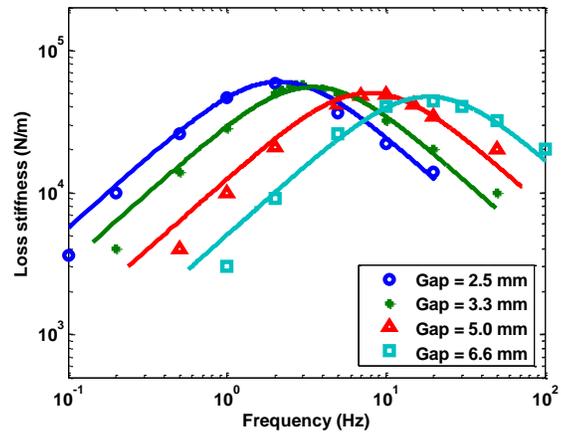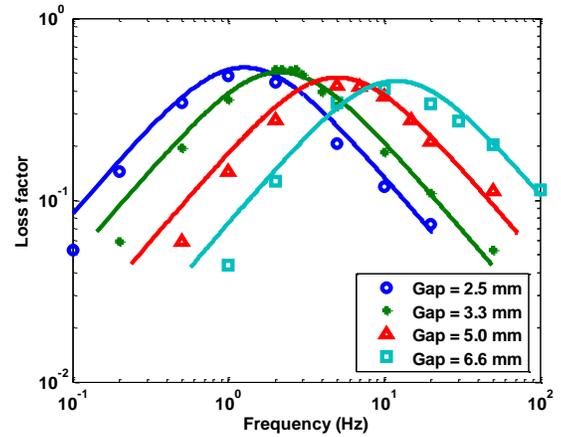
Figure 6.9 Frequency response of vibration isolation element from FSI simulation and SLS model analysis with four gap size values: (a) storage stiffness; (b) loss stiffness; (c) loss factor
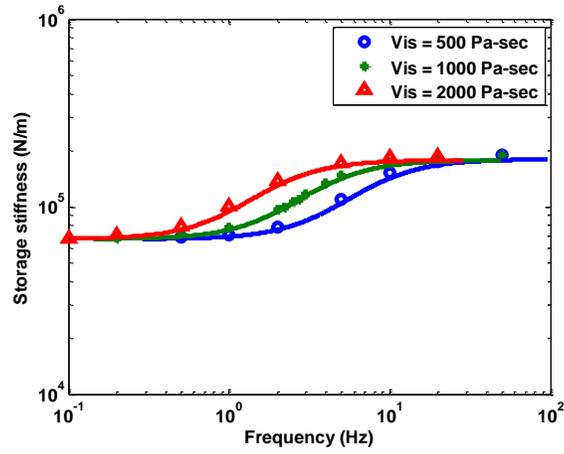
(a)
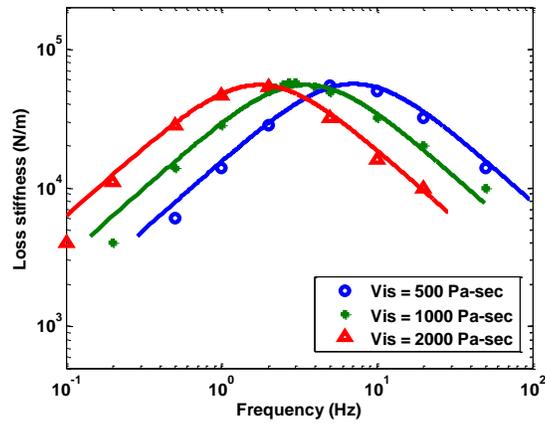


(b)
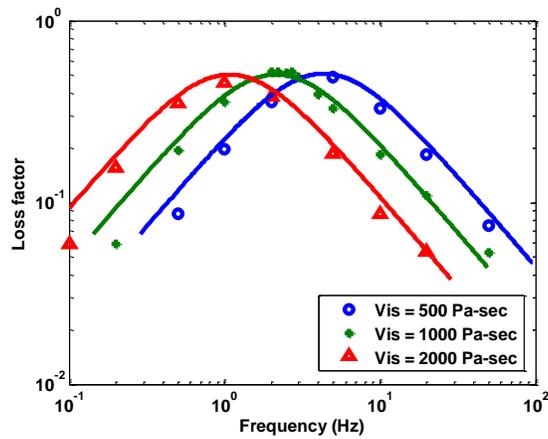


(c)

Figure 6.10 Frequency response of vibration isolation element from FSI simulation and SLS model analysis with three fluid viscosity coefficient values: (a) storage stiffness; (b) loss stiffness; (c) loss factor
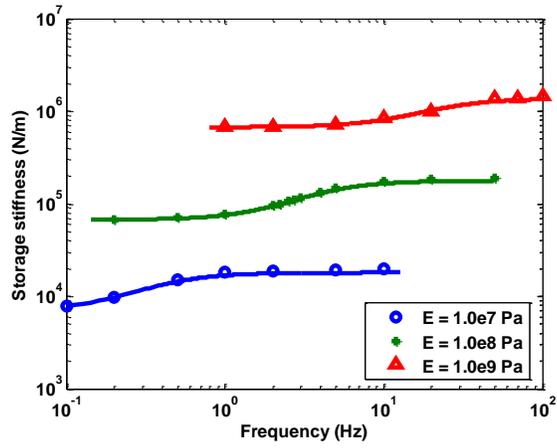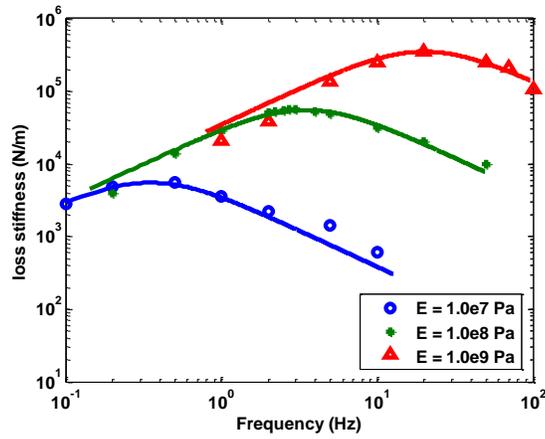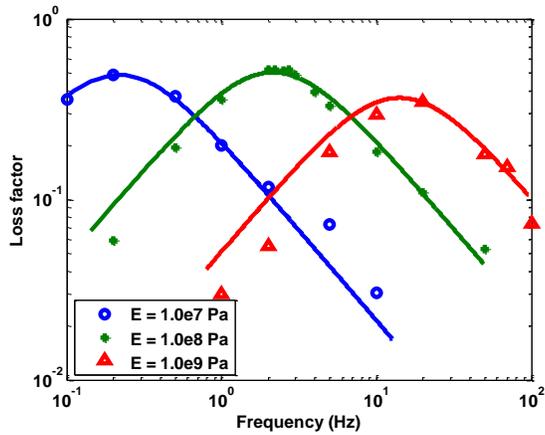
Figure 6.11 Frequency response of vibration isolation element from FSI simulation and SLS model analysis with three values of outer case material's Young's Modulus E: (a) storage stiffness; (b) loss stiffness; (c) loss factor
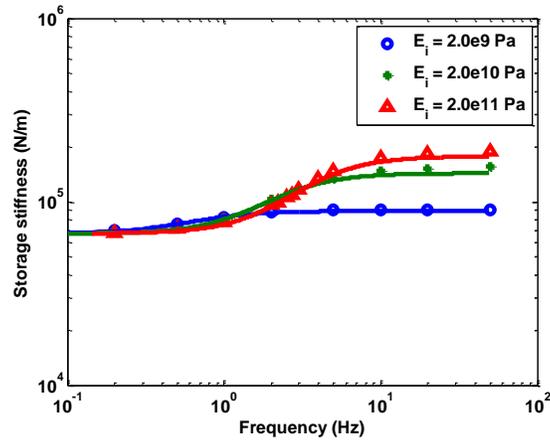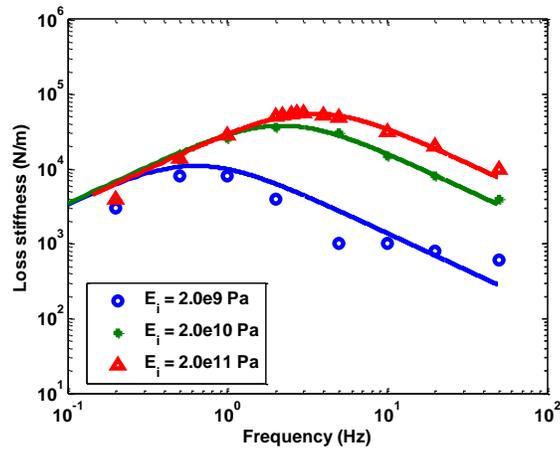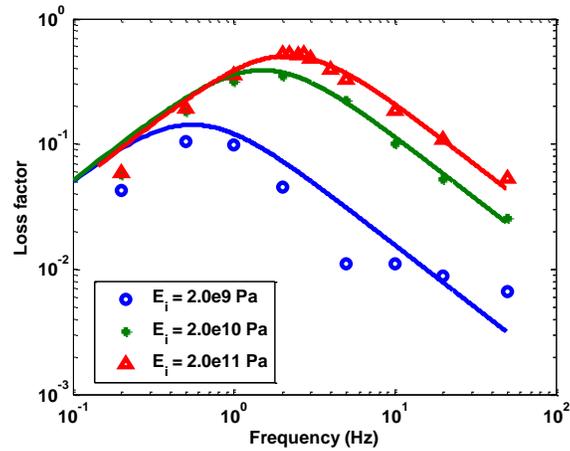
Figure 6.12 Frequency response of vibration isolation element from FSI simulation and SLS model analysis with three values of inner beam materials' Young's modulus $E_i$: (a) storage stiffness; (b) loss stiffness; (c) loss factor

# Chapter 7: Summary, conclusions and future works

## 7.1 Research summary

Humans have always sought to understand and utilize the function displayed in the living organisms which have evolved well-adapted structures over geological time through natural selection. A number of approaches have helped humans understand the related phenomena and associated principles in the living organisms. Among them, morphology deals with the form and structure of organisms and their particular structural features ("morphology," 2015); biomechanics is the study of the structure and function of biological systems by means of the methods of mechanics ("biomechanics," 2015); biomimetics is the imitation of the models and elements of nature for the purpose of solving complex human problems ("biomimetics," 2015). This study delves into these three fields with an aim of investigating the octopus's balancing and water particle sensing organ – the macula/statolith part of its statocyst and its biomimetic implications to innovative vibration sensor design.

This research started with the morphology study of three species of cephalopod's statocyst to gain insight into the function and sensing mechanism of the macula/statolith part of the statocyst in the cephalopods. Next, biomechanics model of the macula/statolith part of the octopus's statocyst was created to characterize and understand the functionality of this interesting sensing organ through numerical simulation and theoretical analysis. As an integral part of this research, the frequency response characteristics of the kinocilia bundle interacting with statolith via fluid-

178

structure-interaction (FSI) were also studied by experimental testing and simulation study of prototype bio-inspired vibration sensor and vibration isolation element from biomimetics-based engineering design. Specifically, the following research works have been performed,

- Previous study has suggested that cephalopod detects water particle motion by the macula/statolith part of its statocyst. A second order dynamic oscillator model is first employed here to study the cephalopod's frequency response characteristics. However, it is found that further work needs to be done to include the special sensing feature of the kinocilia bundle interaction with the statolith in the overall sensing characteristics of the macula/statolith in the statocyst. Research of this interaction phenomenon is the first of its kind.

- Experimentally measured acceleration detection threshold data for the three cephalopods species (*Octopus vulgaris, Sepia officinalis and Loligo vulgaris*) were used to calibrate the proposed dynamic oscillator model by regression analysis.

- To interpret the phenomenon of kinocilia bundle interaction with statolith through fluid structure interaction (FSI), kinocilia bundle from the macula part in the statocyst of *Octopus vulgaris* was modeled as FSI numerical model in a FSI computing software INTESIM. Parametric study of the FSI numerical model mimicking the kinocilia bundle and statolith by varying the dimensions and geometry was

179

conducted in order to improve our understanding of the sensing mechanism of the kinocilia bundle interaction with the statolith.

- Inspired by the interaction phenomenon between the kinocilia bundle and statolith through FSI, a bio-inspired vibration sensor design was conceptually developed. In order to fully understand the sensing characteristics of this bio-inspired sensor design, numerical simulation based parametric study of a few key sensor design parameters (i.e., gap size, fluid viscosity and shear layer stiffness) was conducted using FSI models created in the software INTESIM.

- By taking advantage of 3D printing technology, prototype bio-inspired vibration sensors were fabricated in the lab and subsequently tested to validate and characterize its sensing behavior. The prototype sensor is comprised of 3D-printed plastic components, injected silicone oil, silicone gel shear layer and piezoelectric strain sensing element. A series of shake table tests were carried out to characterize the frequency response behavior of the prototype sensors.

- By mimicking the macula part in the octopus's statocyst, a bio-inspired vibration isolator was conceptually developed. Its transmissibility function was established by both FSI simulation study and equivalent Standard Linear Solid (SLS) modeling. To provide design guidance, parametric study of the vibration isolator's key design parameters and their variation effect on the vibration isolator performance were also performed.

*7.2 Outcomes and conclusions*

Based on the conducted research works, the major findings are summarized as follows,

- Through the comparison study between the model predictions and experimentally measured acceleration detection threshold spectra for the three cephalopod species, it is seen that the $2^{nd}$-order dynamic oscillator model for the macula/statolith part in the statocyst is generally good in predicting the acceleration detection threshold curve over certain frequency range, but may have limitations in predicting the frequency response curves in other frequency ranges, especially in lower frequency range.

- Based on the modeling analysis of the macula/statolith part in the octopus's statocyst, it is found that the cephalopods are most sensitive to the water particle motion in the low frequency range (below 10 Hz), while the detection threshold rapidly increases with rising frequency after 10 Hz.

- The FSI simulation study of the kinocilia bundle interaction with statolith reveals that a notable turning point exists in the frequency response curve of the kinocilia bundle interacting with the statolith through FSI effect. Below the cut-off frequency corresponding to this turning point, the gain linearly increases with frequency to constant amplitude displacement excitation while maintaining a constant level with varying frequency under constant velocity excitation; above this

cut-off frequency, the frequency response gain approaches to a constant value for the cases with constant displacement excitation while decreasing with frequency under constant velocity excitation. The value of this cut-off frequency can be tuned by changing the dimensions of the inner gap and outer gap in the model, while the tilt angle of the kinocilia bundle appears to have negligible effect on the frequency response behaviors for the tilt angle values considered.

- The numerical analysis on the bio-inspired vibration sensor design reveals that the frequency response behavior observed in the kinocilia bundle model in FSI analysis are also seen in the model for the proposed sensor design. Since the cut-off frequency corresponding to the turning point in the frequency response curve is notably affected by the gap size and fluid viscosity, the frequency band of this vibration sensor design could be adjusted to desired operation frequency range by properly choosing the material and geometry parameter values.

- The frequency response characteristics of the bio-inspired vibration sensor design can be described by the Maxwell model. The effect of varying key design parameters (i.e., gap size, fluid viscosity and shear layer material) in the sensor design is found to be equivalent to the change of the spring stiffness and damping coefficient in the Maxwell unit.

- The shake table tests of the prototype bio-inspired vibration sensor demonstrate that the frequency response gain is proportional to the

amplitude of the acceleration input, and the peak value of the frequency response gain can be tuned by changing the additional mass.

- The comparison between the experimental data and predictions from a theoretical model suggests that the frequency response function of the bio-inspired sensor design can be derived from the convolution of that of a $2^{nd}$-order dynamic oscillator and the sensor's inner beam. This unique frequency response characteristics of the proposed bio-inspired vibration sensor design enables the development of analogue jerk sensor (its frequency band is below the cut-off frequency) and velocity sensor (its frequency band is above the cut-off frequency) respectively. This is potentially appealing to practical sensor application because this analogue sensor design could be made into compact size with improved noise rejection capability (by eliminating the need for the differentiation circuit to derive jerk from acceleration measurements).

- The numerical analysis on the proposed bio-inspired isolation element indicates that the isolator's transmissibility curve can be tuned by changing the key design parameters over the concerned frequency range. The dynamic response behavior of the isolation element can be fairly accurately described with the SLS model, in which the isolator design parameters can be modeled by the three parameters (i.e., the equilibrium stiffness, spring stiffness and dashpot damping coefficient) of the equivalent SLS unit.

Future works is expected to advance the following fundamental knowledge gap and technology know-how,

- The bio-inspired sensor design was fabricated by assembling the 3D printed components and piezoelectric sensing element in this study. With the development of the 3D printing technology, the piezoelectric sensing element could also be created from the 3D printer, which will significantly simplify the manufacture of the proposed sensing design. One of the future works could be focused on the fabrication of the bio-inspired sensor entirely by advanced 3D printing technology including 3D printable sensing materials like piezoelectric paint or piezoresistive paste based strain sensor.

- The concepts of jerk sensor and velocity sensor are proposed in this study. However, neither of these sensor designs is made into compact size by employing MEMS (Microelectromechanical systems) fabrication technology. Future works could be extended to the development of these two promising vibration sensor designs, especially how to make tiny-sized sensors.

- The proposed bio-inspired vibration isolator was studied in its modular element. While large scale vibration isolator can be made by forming arrays of these modular vibration isolation element, further study including prototype fabrication and experimental characterization still need to be done. The conception of the jerk sensor and velocity sensor

are provided in this study. However, neither of them is described in detail, especially on their manufacture process. Hence, one of the future works could focus on the development of these two potential sensors, and compare their experimental results with the dynamic feature shown in this study.

# Bibliography

Albert, J., Friedrich, O., Dechant, H. E., & Barth, F. (2001). Arthropod touch reception: spider hair sensilla as rapid touch detectors. *Journal of Comparative Physiology A*, *187*(4), 303-312.

Anderson, J. D. (1995). *Computational fluid dynamics* (Vol. 206). New York, NY: McGraw-Hill.

Andersson, M. H. (2011) Offshore wind farms − Ecological effects of noise and habitat alteration on fish. Doctoral dissertation, Department of Zoology, Stockholm University, Stockholm, Sweden.

Andre M, Sole M, Lenoir M *et al*. (2011). Low-frequency sounds induce acoustic trauma in cephalopods. *Frontiers in Ecology and the Environment* 9, 489–93.

Ansys, C.F.X. (2012). Solver Theory Guide, Release 14.5. *Ansys Inc., Canonsburg*.

Arima, F., Miyazaki, M., Tanaka, H., & Yamazaki, Y. (1988) A study on buildings with large damping using viscous damping walls. In *Proceedings of the 9th World Conference on Earthquake Engineering* (Vol. 821). Tokyo

Badia, S., Quaini, A., & Quarteroni, A. (2008). Splitting methods based on algebraic factorization for fluid-structure interaction. *SIAM Journal on Scientific Computing*, *30*(4), 1778-1805.

Barber, V. C. (1966). The fine structure of the statocyst of *Octopus vulgaris*. *Zeitschrift für Zellforschung und Mikroskopische Anatomie 70*(1), 91–107.

Barber, V. C. (1968). The structure of mollusc statocysts, with particular reference to cephalopods. In *Symp. Zool. Soc. Lond* (Vol. 23, pp. 37-62).

Bar-Cohen, Y. (2006). *Biomimetics: biologically inspired technologies*. Boca Raton, FL: Taylor and Francis

Bathe, K. J. (2012). ADINA Theory and Modeling Guide Volume III: ADINA CFD & FSI. *ADINA System*, *8*.

Bathe, K. J., & Ledezma, G. A. (2007). Benchmark problems for incompressible fluid flows with structural interactions. *Computers & structures*, *85*(11), 628-644.

Bathe, K. J., & Zhang, H. (2004). Finite element developments for general fluid flows with structural interactions. *International Journal for Numerical Methods in Engineering*, *60*(1), 213-232.

Bazilevs, Y., Calo, V. M., Zhang, Y., & Hughes, T. J. (2006). Isogeometric fluid–structure interaction analysis with applications to arterial blood flow. *Computational Mechanics*, *38*(4-5), 310-322.

Bazilevs, Y., Hsu, M. C., Kiendl, J., Wüchner, R., & Bletzinger, K. U. (2011). 3D simulation of wind turbine rotors at full scale. Part II: Fluid–structure interaction modeling with composite blades. *International Journal for Numerical Methods in Fluids*, *65*(1-3), 236-253.

Bechert, D. W. (1999). *U.S. Patent No. 5,971,326*. Washington, DC: U.S. Patent and Trademark Office.

Bechert, D. W., Hoppe, G., & Reif, W. E. (1985). On the drag reduction of the shark skin. *AIAA paper*, *85*, 0546.

Belytschko, T., & Mullen, R. (1976). Mesh partitions of explicit-implicit time integration. *Formulations and computational algorithms in finite element analysis*, 673-690.

Biomimetics. (n.d.). In *Wikipedia*. Retrieved March 10, 2015 http://en.wikipedia.org/wiki/Biomimetics

Budelmann, B. U. (1975). Gravity receptor function in cephalopods, with particular reference to *Sepia officinalis*. *Fortschritte der Zoologie* 23, 84–96.

Budelmann, B. U. (1976). Equilibrium receptor systems in molluscs. In: Mill PJ, ed. *Structure and Function of Proprioceptors in the Invertebrates*. Chapman and Hall, London, pp. 529–66.

Budelmann, B. U. (1979). Hair cell polarization in the gravity receptor systems of the statocysts of the cephalopods *Sepia officinalis* and *Loligo vulgaris*. *Brain Research* 160, 261–70.

Budelmann, B. U., Barber, V. C., & West, S. (1973). Scanning electron microscopical studies of the arrangements and numbers of hair cells in the statocysts of *Octopus vulgaris*, *Sepia officinalis* and *Loligo vulgaris*. *Brain Research* 56, 25–41.

Budelmann, B. U., & Bonn, U. (1982). Histochemical evidence for catecholamines as neurotransmitters in the statocyst of Octopus vulgaris. *Cell Tissue Research* 227, 475–83.

Budelmann, B. U., Sachse, M., & Staudigl., M. (1987). The angular acceleration receptor system of the statocyst of *Octopus vulgaris*: Morphometry, ultrastructure, and neuronal and synaptic organization. *Philosophical Transactions of the Royal Society of London Series B: Biological Sciences* 315, 305–43.

Budelmann, B. U., & Williamson, R. (1994). Directional sensitivity of hair cell afferents in the octopus statocyst. *Journal of Experimental Biology* 187, 245–59.

Budelmann, B. U. (2000). Kinociliary Mechanoreceptors in the Equilibrium Receptor Organs of Cephalopods. In *Cell and Molecular Biology of the Ear* (pp. 3-17). Springer US

Burman, E., & Fernández, M. A. (2007). Stabilized explicit coupling for fluid–structure interaction using Nitsche's method. *Comptes Rendus Mathematique*, *345*(8), 467-472.

Čanić, S., Tambaca, J., Guidoboni, G., Mikelic, A., Hartley, C. J., & Rosenstrauch, D. (2006). Modeling viscoelastic behavior of arterial walls and their interaction with pulsatile blood flow. *SIAM Journal on Applied Mathematics*, *67*(1), 164-193.

Čanić, S., Hartley, C. J., Rosenstrauch, D., Tambača, J., Guidoboni, G., & Mikelić, A. (2006). Blood flow in compliant arteries: an effective viscoelastic reduced model, numerics, and experimental validation. *Annals of Biomedical Engineering*, *34*(4), 575-592.

Causin, P., Gerbeau, J. F., & Nobile, F. (2005). Added-mass effect in the design of partitioned algorithms for fluid–structure problems. *Computer methods in applied mechanics and engineering*, *194*(42), 4506-4527.

Chadwick, W. W., Dziak, R. P., Haxel, J. H., Embley, R. W., & Matsumoto, H. (2012). Submarine landslide triggered by volcanic eruption recorded by in situ hydrophone. *Geology* 40, 51–4.

Chaplin, C. R., Gordon, J. E., & Jeronimidis, G. (1983). *U.S. Patent No. 4,409,274*. Washington, DC: U.S. Patent and Trademark Office.

Checkley, D. M., Dickson, A. G., Takahashi, M., Radich, J. A., Eisenkolb, N., & Asch, R. (2009). Elevated $CO_2$ enhances otolith growth in young fish. *Science*, *324*(5935), 1683-1683.

Choi, Y. T., Wereley, N. M., & Jeon, Y. S. (2005). Semi-active vibration isolation using magnetorheological isolators. *Journal of Aircraft*, *42*(5), 1244-1251.

Chopra, A. K. (1995). *Dynamics of structures* (Vol. 3). New Jersey: Prentice Hall.

Cook, R. D. (2007). *Concepts and applications of finite element analysis*. New York: John Wiley & Sons.

Crawley, E. F. (1994). Intelligent structures for aerospace-A technology overview and assessment. *AIAA journal*, *32*(8), 1689-1699.

Daley, S., Hätönen, J., & Owens, D. H. (2006). Active vibration isolation in a "smart spring" mount using a repetitive control approach. *Control Engineering Practice*, *14*(9), 991-997.

Dambly-Chaudière, C., Sapède, D., Soubiran, F., Decorde, K., Gompel, N., & Ghysen, A. (2003). The lateral line of zebrafish: a model system for the analysis of morphogenesis and neural development in vertebrates. *Biology of the Cell*, *95*(9), 579-587.

Damjanovic, D., Muralt, P., & Setter, N. (2001). Ferroelectric sensors. *IEEE sensors journal*, *1*(3), 191-206.

De Rosis, A., Ubertini, S., & Ubertini, F. (2014). A partitioned approach for two-dimensional fluid–structure interaction problems by a coupled lattice

Boltzmann-finite element method with immersed boundary. *Journal of Fluids and Structures*, *45*, 202-215.

De Vries, H. L. (1950). The mechanics of the labyrinth otoliths. *Acta oto-laryngologica*, *38*(3), 262-273.

Dechant, H. E., Rammerstorfer, F., & Barth, F. (2001). Arthropod touch reception: stimulus transformation and finite element model of spider tactile hairs. *Journal of Comparative Physiology A*, *187*(4), 313-322.

Deparis, S., Fernández, M. A., & Formaggia, L. (2003). Acceleration of a fixed point algorithm for fluid-structure interaction using transpiration conditions. *ESAIM: Mathematical Modelling and Numerical Analysis*, *37*(04), 601-616.

Dijkstra, M., Van Baar, J. J., Wiegerink, R. J., Lammerink, T. S. J., De Boer, J. H., & Krijnen, G. J. M. (2005). Artificial sensory hairs based on the flow sensitive receptor hairs of crickets. *Journal of micromechanics and microengineering*, *15*(7), S132.

Dilly, P. N. (1976). The structure of some cephalopod statoliths. *Cell and tissue research*, *175*(2), 147-163.

Donea, J., Giuliani, S., & Halleux, J. P. (1982). An arbitrary Lagrangian-Eulerian finite element method for transient dynamic fluid-structure interactions. *Computer methods in applied mechanics and engineering*, *33*(1), 689-723.

Donea, J., Huerta, A., Ponthot, J. P., & Rodríguez-Ferran, A. (2004). Arbitrary lagrangian–eulerian methods. *Encyclopedia of computational mechanics*. New York: John Wiley & Sons.

Fan, Z., Chen, J., Zou, J., Li, J., Liu, C., & Delcomyn, F. (2002, June). Development of artificial lateral-line flow sensors. In *Proc. Solid-State Sensor, Actuator and Microsystems Workshop* (pp. 169-172).

FAO (2009). Global Production Statistics, 1950–2007. [Cited 8 November 2009.] Available from URL: http://www.fao.org/fishery/statistics/global-production.

Farhat, C., & Lesoinne, M. (2000). Two efficient staggered algorithms for the serial and parallel solution of three-dimensional nonlinear transient aeroelastic problems. *Computer methods in applied mechanics and engineering*, *182*(3), 499-515.

Felippa, C. A., & Park, K. C. (1980). Staggered transient analysis procedures for coupled mechanical systems: formulation. *Computer Methods in Applied Mechanics and Engineering*, *24*(1), 61-111.

Felippa, C. A., Park, K. C., & Farhat, C. (2001). Partitioned analysis of coupled mechanical systems. *Computer methods in applied mechanics and engineering*, *190*(24), 3247-3270.

Fernández, M. A., Gerbeau, J. F., & Grandmont, C. (2006). A projection algorithm for fluid–structure interaction problems with strong added-mass effect. *Comptes Rendus Mathematique*, *342*(4), 279-284.

Fluent, A.N.S.Y.S. (2012). 13: Flow Modeling Software. *Ansys Inc*.

Fujiyoshi, M., Nonomura, Y., Arai, F., & Fukuda, T. (2002). A new micro jerk sensor with viscous coupling. In *Micromechatronics and Human Science, 2002. MHS 2002. Proceedings of 2002 International Symposium on* (pp. 219-222). IEEE.

Fung, Y. C. (1990). Biomechanics. New York: Springer.

Galante, T., Frank, J., Bernard, J., Chen, W., Lesieutre, G. A., & Koopmann, G. H. (1999). Design, modeling, and performance of a high force piezoelectric inchworm motor. *Journal of intelligent material systems and structures*, *10*(12), 962-972.

Gautschi, G. (2002). *Piezoelectric sensorics: force, strain, pressure, acceleration and acoustic emission sensors, materials and amplifiers*. Berlin, New York: Springer.

Gordon, J. (1985). The New Science of Strong Materials or Why You Don't Fall through the Floor. *American Journal of Physics*, *53*(5), 508-509.

Guide, ANSYS. (2012). ANSYS Release 14.0. *Swanson Analysis Systems, Houston*.

Harvey, P. S., & Gavin, H. P. (2013). The nonholonomic and chaotic nature of a rolling isolation system. *Journal of Sound and Vibration*, *332*(14), 3535-3551.

Hazel, J., Stone, M., Grace, M. S., & Tsukruk, V. V. (1999). Nanoscale design of snake skin for reptation locomotions via friction anisotropy. *Journal of biomechanics*, *32*(5), 477-484.

Heil, M. (2004). An efficient solver for the fully coupled solution of large-displacement fluid–structure interaction problems. *Computer Methods in Applied Mechanics and Engineering*, *193*(1), 1-23.

Holzapfel, G. A. (2000). *Nonlinear solid mechanics* (Vol. 24). Chichester, New York: Wiley.

Hou, G., Wang, J., & Layton, A. (2012). Numerical methods for fluid-structure interaction—a review. *Commun. Comput. Phys*, *12*(2), 337-377.

Hron, J., & Mádlík, M. (2007). Fluid-structure interaction with applications in biomechanics. *Nonlinear analysis: real world applications*, *8*(5), 1431-1458.

Hron, J., & Turek, S. (2006). *A monolithic FEM/multigrid solver for an ALE formulation of fluid-structure interaction with applications in biomechanics* (pp. 146-170). Springer Berlin Heidelberg.

Hu, M. Y., Yan, H. Y., Chung, W. S., Shiao, J. C., & Hwang, P. P. (2009). Acoustically evoked potentials in two cephalopods inferred using the auditory brainstem response (ABR) approach. *Comparative Biochemistry and Physiology Part A: Molecular & Integrative Physiology*, *153*(3), 278-283.

Hübner, B., Walhorn, E., & Dinkler, D. (2004). A monolithic approach to fluid–structure interaction using space–time finite elements. *Computer methods in applied mechanics and engineering*, *193*(23), 2087-2104.

Hudspeth, A. J. (1989). How the ear's works work. *Nature*, *341*(6241), 397-404.

Hudspeth, A. J. (2008). Making an effort to listen: mechanical amplification in the ear. *Neuron*, *59*(4), 530-545.

Hudspeth, A. J., & Jacobs, R. (1979). Stereocilia mediate transduction in vertebrate hair cells (auditory system/cilium/vestibular system). *Proceedings of the National Academy of Sciences*, *76*(3), 1506-1509.

Hughes, T. J. (2012). *The finite element method: linear static and dynamic finite element analysis*. Courier Publications.

Hughes, T. J. R., & Liu, W. K. (1978). Implicit-explicit finite elements in transient analysis: stability theory. *Journal of Applied Mechanics*, *45*(2), 371-374.

INTESIM2014 Theory Manual, Dalian, China; 2014

Ishihara, D., & Yoshimura, S. (2005). A monolithic approach for interaction of incompressible viscous fluid and an elastic body based on fluid pressure Poisson equation. *International Journal for Numerical Methods in Engineering*, *64*(2), 167-203.

Jones, D. I. (2001). *Handbook of viscoelastic vibration damping*. Chichester, New York: John Wiley & Sons.

Kaifu, K., Akamatsu, T., & Segawa, S. (2011). Preliminary evaluation of underwater sound detection by the cephalopod statocyst using a forced oscillation model. *Acoustical Science and Technology*, *32*(6), 255-260.

Kaifu, K., Akamatsu, T., & Segawa, S. (2008). Underwater sound detection by cephalopod statocyst. *Fisheries Science*, *74*(4), 781-786.

Kalro, V., & Tezduyar, T. E. (2000). A parallel 3D computational method for fluid–structure interactions in parachute systems. *Computer Methods in Applied Mechanics and Engineering*, *190*(3), 321-332.

Karlsen, H. (1992). The inner ear is responsible for detection of infrasound in the perch (Perca fluviatilis). *Journal of experimental biology*, *171*(1), 163-172.

Kassiotis, C. (2009). *Nonlinear fluid-structure interaction: a partitioned approach and its application through component technology* (Doctoral dissertation, Université Paris-Est).

Kawai, H. (1969). The piezoelectricity of poly (vinylidene fluoride). *Japanese Journal of Applied Physics*, *8*(7), 975.

Keil, T. A. (1997). Functional morphology of insect mechanoreceptors. *Microscopy research and technique*, *39*(6), 506-531.

King, M. J., Vincent, J. F., & Harris, W. (1996). Curling and folding of leaves of monocotyledons—a strategy for structural stiffness. *New Zealand Journal of Botany*, *34*(3), 411-416.

La Rocca, M., Galluzzo, D., Saccorotti, G., Tinti, S., Cimini, G. B., & Del Pezzo, E. (2004). Seismic signals associated with landslides and with a tsunami at Stromboli volcano, Italy. *Bulletin of the Seismological Society of America*, *94*(5), 1850-1867.

Landolfa, M. A., & Jacobs, G. A. (1995). Direction sensitivity of the filiform hair population of the cricket cereal system. *Journal of Comparative Physiology A*,*177*(6), 759-766.

Lee, C. J. K., Noguchi, H., & Koshizuka, S. (2007). Fluid–shell structure interaction analysis by coupled particle and finite element method. *Computers & structures*, *85*(11), 688-697.

Lee, C. K., & O'Sullivan, T. C. (1991). Piezoelectric strain rate gages. *The Journal of the Acoustical Society of America*, *90*(2), 945-953.

Lee, H., Lee, Y., Statz, A. R., Rho, J., Park, T. G., & Messersmith, P. B. (2008). Substrate-independent layer-by-layer assembly by using mussel-adhesive-inspired polymers. *Advanced Materials*, *20*(9), 1619-1623.

Leigh, S. J., Bradley, R. J., Purssell, C. P., Billson, D. R., & Hutchins, D. A. (2012). A simple, low-cost conductive composite material for 3D printing of electronic sensors. *PloS one*, *7*(11), e49365.

LeVeque, R. J. (2002). *Finite volume methods for hyperbolic problems* (Vol. 31). Cambridge, New York: Cambridge university press.

Le Tallec, P., & Mouro, J. (2001). Fluid structure interaction with large structural displacements. *Computer Methods in Applied Mechanics and Engineering*, *190*(24), 3039-3067.

Liang, Y., Cao, J., Zhang, D., Wang, R., & Pan, Q. (2010). A biologically inspired sensor wakeup control method for wireless sensor networks. *Systems, Man, and Cybernetics, Part C: Applications and Reviews, IEEE Transactions on*, *40*(5), 525-538.

Lim, K., & Park, S. (2009). A mechanical model of the gating spring mechanism of stereocilia. *Journal of biomechanics*, *42*(13), 2158-2164.

Liu, C., & Herman, R. (1999). Road profile, vehicle dynamics, and ride quality rating. *Journal of transportation engineering*, *125*(2), 123-128.

Liu, C., Gazis, D. C., & Kennedy, T. W. (1999). Human judgment and analytical derivation of ride quality. *Transportation science*, *33*(3), 290-297.

Liu, S. C., Chong, K. P., & Singh, M. P. (1995). Civil infrastructure systems research: hazard mitigation and intelligent material systems. *Smart Materials and Structures*, *4*(1A), A169.

Lou, A., & Grosvenor, C. (2012). Selective laser sintering, birth of an industry. *University of Texas: Mechanical Engineering Department*.

Mahadevan, L., Daniel, S., & Chaudhury, M. K. (2004). Biomimetic ratcheting motion of a soft, slender, sessile gel. *Proceedings of the National Academy of Sciences*, *101*(1), 23-26.

Makris, N., & Constantinou, M. C. (1990). Viscous dampers: testing, modeling and application in vibration and seismic isolation.

Martin, P., Mehta, A. D., & Hudspeth, A. J. (2000). Negative hair-bundle stiffness betrays a mechanism for mechanical amplification by the hair cell. *Proceedings of the National Academy of Sciences*, *97*(22), 12026-12031.

McConney, M. E., Anderson, K. D., Brott, L. L., Naik, R. R., & Tsukruk, V. V. (2009). Bioinspired material approaches to sensing. *Advanced Functional Materials*, *19*(16), 2527-2544.

Michler, C., Hulshoff, S. J., Van Brummelen, E. H., & De Borst, R. (2004). A monolithic approach to fluid–structure interaction. *Computers & fluids*, *33*(5), 839-848.

Miu, D. K., & Bhat, S. P. (1991). Minimum power and minimum jerk position control and its applications in computer disk drives. *Magnetics, IEEE Transactions on*, *27*(6), 4471-4475.

Mizoshita, Y., Hasegawa, S., & Takaishi, K. (1996). Vibration minimized access control for disk drives. *Magnetics, IEEE Transactions on*, *32*(3), 1793-1798.

Morphology. (n.d.). In *Wikipedia*. Retrieved March 10, 2015, from http://en.wikipedia.org/wiki/Morphology_%28biology%29

Neinhuis, C., & Barthlott, W. (1997). Characterization and distribution of water-repellent, self-cleaning plant surfaces. *Annals of Botany*, *79*(6), 667-677.

Neumeister, H., & Budelmann, B. U. (1997). Structure and function of the Nautilus statocyst. *Philosophical Transactions of the Royal Society of London. Series B: Biological Sciences*, *352*(1361), 1565-1588.

Niezrecki, C., Brei, D., Balakrishnan, S., & Moskalik, A. (2001). Piezoelectric actuation: state of the art. *The shock and vibration digest*, *33*(4), 269-280.

Nobile, F., & Vergara, C. (2012). Partitioned algorithms for fluid-structure interaction problems in haemodynamics. *Milan journal of mathematics*, *80*(2), 443-467.

Oñate, E., Idelsohn, I., & Dvorkin, E. (1998). Computational mechanics new trends and applications. *Computational mechanics new trends and applications*.

Packard, A., Karlsen, H. E., & Sand, O. (1990). Low frequency hearing in cephalopods. *Journal of Comparative Physiology A*, *166*(4), 501-505.

Peltola, S. M., Melchels, F. P., Grijpma, D. W., & Kellomäki, M. (2008). A review of rapid prototyping techniques for tissue engineering purposes. *Annals of medicine*, *40*(4), 268-280

Polla, D. L., & Francis, L. F. (1998). Processing and characterization of piezoelectric materials and integration into microelectromechanical systems. *Annual review of materials science*, *28*(1), 563-597.

Popper, A. N. (2003). Effects of anthropogenic sounds on fishes. *Fisheries*, *28*(10), 24-31.

Proctor Jr, T. M. (1982). An improved piezoelectric acoustic emission transducer. *The Journal of the Acoustical Society of America*, *71*(5), 1163-1168.

Ramm, E., & Wall, W. A. (2001). Interaction of fluids and thin structures. In *Proceedings of the 2nd European Conference on Computational Mechanics, Cracow*.

Reddy, J. N., & Gartling, D. K. (2010). *The finite element method in heat transfer and fluid dynamics*. Boca Raton, FL: CRC press.

Rengier, F., Mehndiratta, A., von Tengg-Kobligk, H., Zechmann, C. M., Unterhinninghofen, R., Kauczor, H. U., & Giesel, F. L. (2010). 3D printing

based on imaging data: review of medical applications. *International journal of computer assisted radiology and surgery*, 5(4), 335-341.

Rivin EI (2003). *Passive vibration isolation*. New York: ASME Press.

Roylance, D. (2001). Engineering viscoelasticity. *Department of Materials Science and Engineering–Massachusetts Institute of Technology, Cambridge MA*, *2139*, 1-37

Rugonyi, S., & Bathe, K. J. (2001). On finite element analysis of fluid flows fully coupled with structural interactions. *CMES- Computer Modeling in Engineering and Sciences*, *2*(2), 195-212.

Sallen, R. P., & Key, E. L. (1955). A practical method of designing RC active filters. *Circuit Theory, IRE Transactions on*, *2*(1), 74-85.

Sand, O., & Karlsen, H. E. (1986). Detection of infrasound by the Atlantic cod.*Journal of Experimental Biology*, *125*(1), 197-204.

Sand, O., & Karlsen, H. E. (2000). Detection of infrasound and linear acceleration in fishes. *Philosophical Transactions of the Royal Society of London. Series B: Biological Sciences*, *355*(1401), 1295-1298.

Shangguan, W. B., & Lu, Z. H. (2004). Experimental study and simulation of a hydraulic engine mount with fully coupled fluid–structure interaction finite element analysis model. *Computers & structures*, *82*(22), 1751-1771.

Sheldon, J. P. (2012). *A Comparison of Fluid-Structure Interaction Coupling Algorithms Using the Finite Element Method* (Master's Thesis, The Pennsylvania State University).

Shimozawa, T., Kumagai, T., & Baba, Y. (1998). Structural scaling and functional design of the cercal wind-receptor hairs of cricket. *Journal of Comparative Physiology A*, *183*(2), 171-186.

Sieber, G. (2002). *Numerical simulation of fluid-structure interaction using loose coupling methods* (Doctoral dissertation, TU Darmstadt).

Sirohi, J., & Chopra, I. (2000). Fundamental understanding of piezoelectric strain sensors. *Journal of Intelligent Material Systems and Structures*, *11*(4), 246-257.

Spyrakos, C. C., & Raftoyiannis, J. (1997). Linear and nonlinear finite element analysis in engineering practice. Pittsburgh, Pennsylvania: Algor Publishing Division.

Takizawa, K., Moorman, C., Wright, S., Spielman, T., & Tezduyar, T. E. (2011). Fluid–structure interaction modeling and performance analysis of the Orion spacecraft parachutes. *International Journal for Numerical Methods in Fluids*,*65*(1-3), 271-28

Tang, A. Y., & Amin, N. (2014, February). Some Numerical Approaches to Solve Fluid Structure Interaction Problems in Blood Flow. In *Abstract and Applied Analysis* (Vol. 2014). Hindawi Publishing Corporation.

Tata, U., Deshmukh, S., Chiao, J. C., Carter, R., & Huang, H. (2009). Bio-inspired sensor skins for structural health monitoring. *Smart Materials and Structures*, *18*(10), 104026.

Temam, R. (1984). *Navier--Stokes Equations*. American Mathematical Soc..

Tong, M., & Lee, G. C. (1999). 3D temporal characteristics of earthquake ground motion at single point. *Journal of engineering mechanics*, *125*(10), 1099-1105.

Tressler, J. F., Alkoy, S., & Newnham, R. E. (1998). Piezoelectric sensors and sensor materials. *Journal of Electroceramics*, *2*(4), 257-272.

Tschoegl, N. W. (1989). The phenomenological Theory of Linear Viscoelastic Behavior. Berlin, New York: Springer.

Unger, R., Haupt, M. C., & Horst, P. (2007). Application of Lagrange multipliers for coupled problems in fluid and structural interactions. *Computers & structures*, *85*(11), 796-809.

Version, A.B.A.Q.U.S. (2011). 6.11 Documentation. *Dassault Systemes Simulia Corp., Providence, RI, USA*.

Vincent, J. F. V. (2000). Smart by name, smart by nature. *Smart materials and structures*, *9*(3), 255.

Wall, W. A., Genkinger, S., & Ramm, E. (2007). A strong coupling partitioned approach for fluid–structure interaction with free surfaces. *Computers & Fluids*, *36*(1), 169-183.

Wang, Q., Gossweiler, G. R., Craig, S. L., & Zhao, X. (2014). Cephalopod-inspired design of electro-mechano-chemically responsive elastomers for on-demand fluorescent patterning. *Nature communications*, *5*.

Wang, W., Deng, T., & ZHAO, S. G. (2004). Determination for Material Constants of Rubber Mooney-Rivlin Model [J]. Special Purpose Rubber Products, 4, 003.

Wicaksono, D. H. B. (2008). *Learning from nature: biologically-inspired sensors*. TU Delft, Delft University of Technology.

Williamson, R., & Chrachri, A. (2007). A model biological neural network: the cephalopod vestibular system. *Philosophical Transactions of the Royal Society B: Biological Sciences*, *362*(1479), 473-481.

Williamson, R. (1991). Factors affecting the sensory response characteristics of the cephalopod statocyst and their relevance in predicting swimming performance. *The Biological Bulletin*, *180*(2), 221-227.

Xu, Y. L., Yang, Z. C., Chen, J., & Liu, H. J. (2003). Microvibration control platform for high technology facilities subject to traffic-induced ground motion. *Engineering structures*, *25*(8), 1069-1082.

Yang, X., Qi, X., Lee, C., Mai T. & Cao, J. (2008). Jerk and Jerk Sensor. In *The 14th World Conference on Earthquake Engineering October* (pp. 12-17).

Yamada, T., & Yoshimura, S. (2008). Line search partitioned approach for fluid-structure interaction analysis of flapping wing. *Computer Modeling in Engineering and Sciences*, *24*(1), 51.

Yoon, G. H. (2010). Topology optimization for stationary fluid–structure interaction problems using a new monolithic formulation. *International journal for numerical methods in engineering*, *82*(5), 591-616.

Yoshioka, H., Ramallo, J. C., & Spencer Jr, B. F. (2002). "Smart" base isolation strategies employing magnetorheological dampers. *Journal of engineering mechanics*, *128*(5), 540-551.

Youn, I. (1996). *Optimal preview control design of active and semi-active suspension systems including jerk* (No. 960936). SAE Technical Paper.

Young, J. Z. (1960). The statocysts of Octopus vulgaris. *Proceedings of the Royal Society of London. Series B. Biological Sciences*, *152*(946), 3-29.

Young, J. Z. (1989). The angular acceleration receptor system of diverse cephalopods. *Philosophical Transactions of the Royal Society B: Biological Sciences*, *325*(1227), 189-237.

Yu, C., Li, Y., Zhang, X., Huang, X., Malyarchuk, V., Wang, S., ... & Rogers, J. A. (2014). Adaptive optoelectronic camouflage systems with designs inspired by cephalopod skins. *Proceedings of the National Academy of Sciences*, *111*(36), 12998-13003

Zhang, Q., & Zhu, B. (2012). An integrated coupling framework for highly nonlinear fluid-structure problems. *Computers & Fluids*, *60*, 36-48.

Zhang, Q., & Hisada, T. (2004). Studies of the strong coupling and weak coupling methods in FSI analysis. *International Journal for Numerical Methods in Engineering*, *60*(12), 2013-2029.

Zhang, Y. (2006). In situ fatigue crack detection using piezoelectric paint sensor. *Journal of Intelligent Material Systems and Structures*, *17*(10), 843-852.

Zhou, C. (2013). Fatigue crack monitoring with coupled piezoelectric film acoustic emission sensors (Doctoral dissertation, University of Maryland).

# Nomenclature

In summary, following notation is used in this dissertation:

$a$      :    amplitude of water particle acceleration

$a_{min}$    :    minimum detectable acceleration

$A_3$     :    electrode area

$\mathbf{b}$      :    body force in Eulerian description

$\mathbf{b}_\kappa$     :    body force in ALE description

$\mathbf{B}$      :    body force in Lagrangian description

$b_c$     :    width of the piezoelectric material

$c$      :    viscous damping coefficient

$c_w$     :    speed of sound in water

$\mathbf{C}$      :    strain invariant

$d_{min}$    :    minimum detectable displacement

$d_{31}$     :    piezoelectric coefficient

$\bar{d}$      :    displacement amplitude of isolated object

$D$      :    displacement of isolated object

$\dot{D}$      :    velocity of isolated object

$D_3$     :    dielectric displacement

$E$      :    Young's modulus

$\mathbf{E}$      :    Green-Lagrange strain tensor

$\mathbf{F}$      :    deformation gradient from Lagrangian description to Eulerian description

$\mathbf{F}_m$     :    deformation gradient from ALE description to Eulerian description

$\mathbf{I}$      :    identity tensor

$J$      :    determinant of deformation gradient $\mathbf{F}_m$

$j_{min}$     :    minimum detectable jerk

$k$      :    stiffness

$k_e$     :    equilibrium stiffness

| | | |
|---|---|---|
| $\overline{k}$ | : | slope of displacement transfer function |
| $K$ | : | stiffness of Maxwell unit |
| $K_1$ | : | storage stiffness |
| $K_2$ | : | loss stiffness |
| $l_c$ | : | length of piezoelectric material |
| $m_{am}$ | : | added mass |
| $m_e$ | : | effective mass of statolith |
| $m_s$ | : | mass of statolith |
| $\mathbf{n}$ | : | outward unit |
| $\overline{\mathbf{N}}^{\,j}$ | : | $j^{th}$ interpolation basis function |
| $p$ | : | pressure in Eulerian description |
| $p_{ref}$ | : | reference pressure |
| $p_{rms}$ | : | root-means-square sound pressure |
| $p_\kappa$ | : | pressure in ALE description |
| $P$ | : | reaction force of isolator |
| $P_0$ | : | reaction force amplitude of isolator |
| $\mathbf{P}$ | : | first Piola-Kirchhoff stress tensor |
| $q$ | : | electric charge generate by piezoelectric material |
| $\mathbf{S}$ | : | second Piola-Kirchhoff stress tensor |
| $t$ | : | time |
| $\mathbf{t}$ | : | traction force on  boundary |
| $\mathbf{T}$ | : | stress tensor action on structure boundary |
| $u$ | : | Lamé's second parameter |
| $u_i$ | : | inner beam tip displacement |
| $u_{t0}$ | : | relative displacement between outer case and base mount in vibration sensor |
| $\mathbf{u}_m$ | : | fluid mesh displacement |
| $\mathbf{U}$ | : | displacement in Lagrangian description |

| | | |
|---|---|---|
| $\boldsymbol{\upsilon}$ | : | velocity in Eulerian description |
| $\boldsymbol{\upsilon}_m$ | : | fluid mesh velocity |
| $\boldsymbol{\upsilon}_\kappa$ | : | velocity in ALE description |
| $\boldsymbol{\upsilon}_D$ | : | boundary velocity |
| $V$ | : | statolith volume |
| $\mathrm{V}_{out}$ | : | voltage output |
| $\mathbf{V}$ | : | velocity in Lagrangian description |
| $\hat{\mathbf{V}}$ | : | arbitrary weight function |
| $v_{min}$ | : | minimum detectable velocity |
| $W_d$ | : | dissipated energy |
| $x$ | : | displacement of statolith relative to equilibrium position |
| $x_{min}$ | : | minimum detectable displacement of statolith |
| $x_g$ | : | base displacement |
| $\dot{x}_g$ | : | base velocity |
| $\ddot{x}_g$ | : | base acceleration |
| $\dddot{x}_g$ | : | base jerk |
| $Yc$ | : | Young's modulus of piezoelectric material |
| $\Gamma_D$ | : | Dirichlet boundary |
| $\Gamma_N$ | : | Neumann boundary |
| $\Gamma_F$ | : | boundary of fluid domain in Eulerian description |
| $\Gamma_{F\kappa}$ | : | boundary of fluid domain in ALE description |
| $\Gamma_S$ | : | boundary of solid domain in Lagrangian description |
| $\lambda$ | : | Lamé's first parameter |
| $\mu$ | : | fluid dynamic viscosity |
| $\nu$ | : | Poisson's ratio |
| $\zeta$ | : | damping ratio |
| $\eta$ | : | dash pot damping coefficient |

| | | |
|---|---|---|
| $\rho$ | : | mass density |
| $\rho_s$ | : | mass density of statolith or mass density of solid |
| $\rho_w$ | : | mass density of water |
| $\rho_f$ | : | mass density of fluid |
| $\boldsymbol{\sigma}$ | : | Cauchy stress tensor in Eulerian description |
| $\boldsymbol{\sigma}_\kappa$ | : | Cauchy stress tensor in ALE description |
| $\phi$ | : | phase angle |
| $\psi$ | : | strain energy function |
| $\omega$ | : | angular frequency |
| $\omega_n$ | : | resonance frequency |
| $\Omega_F$ | : | fluid domain in Eulerian description |
| $\Omega_{F\kappa}$ | : | fluid domain in ALE description |
| $\Omega_S$ | : | solid domain in Lagrangian description |